Development of a dynamic LES model for turbulent diffusion flames

Giunio de Luca

université PARIS-SACLAY

Développement de modèles dynamiques pour la simulation aux grandes échelles de la combustion turbulente non-prémélangée

Development of a dynamic LES model for turbulent diffusion flames

Thèse de doctorat de l'université Paris-Saclay

École doctorale n° 579 :
sciences mécaniques et énergétiques, matériaux et géoscience (SMEMAG)
Spécialité de doctorat: Combustion
Unité de recherche : Université Paris-Saclay, CNRS, CentraleSupélec,
Laboratoire EM2C, 91190, Gif-sur-Yvette, France.
Référent : CentraleSupélec

Thèse présentée et soutenue à Paris-Saclay, le 21/06/2021, par

Giunio DE LUCA

Composition du Jury

Pascale DOMINGO Directrice de recherche, CNRS, CORIA	Présidente
Bénédicte CUENOT Ingénieur de recherche, CERFACS	Rapporteur & Examinatrice
Amsini SADIKI Professeur, TU Darmstadt	Rapporteur & Examinateur
Olivier COLIN Ingénieur de recherche, IFPEN	Examinateur

Direction de la thèse

Denis Veynante Directeur de recherche, CNRS, EM2C	Directeur
Thomas SCHMITT Chargé de recherche, CNRS, EM2C	Co-encadrant

Thèse de doctorat

NNT : 2021UPAST053

Remerciements

Je remercie tout d'abord ma famille de m'avoir soutenu tout au long de mes études.
Je remercie également mes amis, mes collègues du Clean-Gas et du laboratoire EM2C. Je remercie Giampaolo et Stefano pour le soutien et les échanges de bon matin devant la machine à café, grâce auxquels j'ai eu les intuitions qui m'ont permis d'avancer le travail de recherche de manière significative.
Je remercie tout le personnel technique du laboratoire EM2C, en particulier Jean-Michel Dupays pour sa disponibilité, son amabilité et son professionnalisme.
Un remerciement particulier va aussi à tout le personnel administratif du laboratoire, aux secrétaires Nathalie, Noï et Brigitte.
Je remercie tous les membres du jury, la présidente, les rapporteurs et les examinateurs, pour l'intérêt scientifique montré envers mes travaux.
Je remercie mon directeur de thèse pour les corrections et les remarques très directes, grâce auxquelles j'ai pu mener un travail de qualité. Je remercie mon co-encadrant pour les idées et les intuitions apportées au travail de recherche, et pour sa disponibilité malgré son emploi du temps très chargé.
En général j'adresse un grand merci à tous les gens avec lesquels j'ai échangé pendant ce parcours.

Abstract

The present study is about the formulation of a dynamic LES model to simulate turbulent diffusion flames. For such flames, fuel and oxidizer do not mix before entering the combustion chamber. Compared to premixed flames, diffusion flames are easier to design and safer to operate since there is no risk of flashbacks. On the other hand, they are well known to be highly pollutant and low efficient. Those flames are present in glass furnaces, rocket engines, or even in gas turbines under particular operating conditions.
Nowadays, simulation has become of utmost importance in juxtaposing experiments and helping the design of modern burners. Despite the computational power growth, direct simulations of the entire spectrum of turbulence (DNS) are still not affordable for practical applications. Large Eddy Simulation represents a good compromise in terms of information retrieved and computational cost. The basic idea is to solve the filtered Navier-Stokes equations so that the most energetic structures are computed through the calculus grid, while the effects of the sub-grid scale structures are modeled according to the equilibrium hypothesis between the eddies and the wrinkling of the flame surface (flamelet models).
A model broadly validated for turbulent application is the so called 'Thickened Flame Model' for Large Eddy Simulation (TFLES). Initially formulated for premixed flame, this approach consists in thickening the flame front to solve it with a coarse grid by preserving the flame speed. Nevertheless, it has also been successfully used in predicting the qualitative behavior of non-premixed turbulent flame without clear theoretical foundations.
In the present work, the TFLES model is then used for a laminar diffusion counter-flow flame to analyze the model's impact on such flame.
A second part of the present study focuses on analyzing a dynamic formulation to predict the flame surface in turbulent diffusion flames. The accuracy of such predictions depends mainly on the model of the flame surface's wrinkling effects at the non-resolved scales. In real turbulent flames, the equilibrium between turbulence and flame wrinkling is not always verified as the flame is laminar at an early stage and progressively wrinkled by turbulent motions. Classical LES combustion models are based on algebraic expressions. Others assume an additional balance equation for concerned variables. The drawback of these formulations is that they depend on constants that, in turn, strongly depend

on the specific scale range and application.
A promising alternative recently developed consists in using a dynamic model to automatically adjust the flame wrinkling factor from the knowledge of resolved scales. This modeling approach has been widely used to described unresolved turbulent transport. Recent studies of the dynamic wrinkling factor formulation coupled with different combustion models for large eddy simulation of turbulent premixed combustion have shown the capabilities to predict a wide range of phenomenon.
In the present work, the dynamic formulation is coupled with the TFLES model, and its implications on non-premixed flames are investigated for a planar turbulent jet.

Synthése

La présente étude porte sur le développement d'un modèle pour la simulation aux grandes échelles des flammes turbulentes non-prémélangées. Ces flammes, dans lesquelles combustible et comburant arrivent séparément dans la zone de réaction, sont plus faciles à concevoir que les flammes prémélangées (pas de mélange préalable des réactifs dans des proportions compatibles avec les limites d'inflammabilité) et sont plus sûres puisqu'il n'y a pas de risque de remontée de flamme (« flashback »), ce qui motive leur utilisation dans un certain nombre de situations (fours industriels, moteurs-fusée, ...). En revanche, elles sont globalement moins performantes tandis que l'impossibilité de contrôler leur température maximale, déterminée par les conditions stoechiométriques, favorise la formation des oxydes d'azote.

La simulation numérique est devenue aujourd'hui incontournable pour aider à la conception de brûleurs performants. Malgré la croissance continue de la puissance des moyens de calcul, les simulations numériques directes (DNS), sans modélisation de l'interaction flamme / turbulence, restent hors de portée pour des chambres de combustion d'intérêt pratique. A l'inverse, les approches de type RANS (Reynolds averaged Navier-Stokes simulation) ne donnent accès qu'à la connaissance de l'écoulement moyen. La simulation aux grandes échelles (LES) représente alors un bon compromis en termes d'informations récupérées, notamment le comportement instationnaire des flammes, et de coûts de calcul. Elle consiste à résoudre les équations de Navier-Stokes filtrées pour calculer explicitement les structures les plus grandes et les plus énergétiques de la turbulence, tandis que les effets des structures les plus petites, non-résolues sur le maillage de calcul, sont modélisés.

Un des modèles de combustion les plus utilisés en simulation aux grandes échelles est le modèle dit « de flamme épaissie » (« thickened flame model »). Initialement développé pour les flammes prémélangées, il consiste à épaissir artificiellement le front de flamme afin de permettre sa résolution sur le maillage de calcul, tout en préservant la vitesse de flamme laminaire, tandis que la surface de flamme perdue par le processus d'épaississement est modélisée par un facteur de plissement. Ce modèle a également été utilisé avec succès pour les flammes turbulentes non-prémélangées malgré l'absence de fondements théoriques clairs. L'objectif de ce travail est d'étudier plus en détail le comportement du modèle pour ces dernières. Une étude analytique développée sous

l'hypothèse d'une densité constante et confirmée par des simulations prenant en compte les variations de densité, montre que le taux de réaction total est significativement affecté par la procédure d'épaississement, y compris, mais dans une moindre mesure, si l'épaississement est limité à la zone de réaction par l'introduction d'un senseur. Pour une cinétique chimique suffisamment rapide, le taux de réaction d'une flamme non-prémélangée laminaire est controlée par la diffusion moléculaire des réactifs. Modifier cette diffusion influe donc directement la prédiction du taux de réaction.
Une seconde partie de ce travail consiste à examiner la capacité d'une formulation dynamique à prédire la surface de flamme non-résolue dans la simulation en exploitant la connaissance des échelles résolues. Ce formalisme permet ici l'ajustement automatiquement en cours de calcul du paramètre d'un modèle de plissement de type fractal. Cette approche permet de s'affranchir de l'hypothèse d'équilibre entre structures turbulentes et plissement de la surface de flamme des modèles algébriques usuels, pas toujours vérifiée en pratique, sans devoir résoudre une équation pour la surface de flamme. Un cas idéal de jet planaire turbulent bidimensionnel a été étudié pour reproduire des conditions de chimie infiniment rapide, y compris après épaississement, et permettre une simulation directe de référence (i.e. suffisamment résolue pour se passer d'un modèle d'interaction flamme / turbulence). Le modèle TFLES est ensuite appliqué sans modèle de plissement. Enfin, après une vérification du comportement fractale de la flamme, le modèle TFLES a pu être couplé avec une modélisation dynamique du plissement de surface de flamme de sous-mailles basé sur une formulation fractale. Le modèle dynamique s'avère robuste et permet de prédire correctement la surface de flamme totale. Malheureusement, la surestimation du taux de réaction par unité de surface de flamme induite par la procédure d'épaississement conduit à surestimer les taux de réaction totaux. Ce résultat suggère de coupler le formalisme dynamique avec une modélisation de type « flammelette » de la structure locale de la flamme. Le modèle TFLES pourrait toutefois donner de bons résultats pour les flammes non-prémélangées dans les situations où le taux de réaction est essentiellement contrôlé par le transport turbulent des réactifs.

Contents

Nomenclature

Latin Characters :

$[X_k]$	Molar concentration of specie k [mol/m^3]
F	Thickening factor $[\,-\,]$
$\mathcal{M}_k$	name of the specie k
$\mathcal{Q}_i$	Progress rate of reaction i
a	strain rate
A	cross-sectional area $[m^2]$
A_T	instantaneous flame surface of turbulent flame $[m^2]$
A_i	pre-exponential constant for the forward reaction i
B	Fractal dimension $[\,-\,]$
c	Progress variable $[\,-\,]$
C_{pk}	Specific heat capacity at constant pressure of specie k $[J/(kg\,K)]$
C_{vk}	Specific heat capacity at constant volume of specie k $[J/(kg\,K)]$
d_w	Distance to the closest wall
D	Molecular diffusion coefficient $[m/s]$
D_k	Molecular Diffusion coefficient of specie k $[m/s]$
D_T	Thermal diffusion coefficient $[m/s]$
e_k	Mass energy of specie k $[J/kg]$
E	Total non-chemical energy of the mixture $[J/kg]$
E_{ai}	Activation energy for the reaction i [cal/mol]
h_k	Mass enthalpy of specie k $[J/kg]$
H	Total non-chemical enthalpy of the mixture $[J/kg]$
$J_{i,k}$	i component of molecular diffusive flux of the specie k $[kg/(m^2/s)]$
k	Wavenumber $[m^{-1}]$
k_B	Boltzmann constant $[J/K]$
K_{eq^i}	Equilibrium reaction constant for the reaction i
l_f	mean free path of the particle $[m]$
l_t	Integral length scale $[m]$
m	mass of the mixture $[kg]$
m_k	Mass of specie k $[kg]$
n	number of moles [mol]
n_k	number of moles of specie k [mol]
p	Total pressure of the mixture $[N/m^2]$
p_k	Partial pressure of specie k $[N/m^2]$
Q	Heat Released by the reaction per unit mass $[J/kg]$

q_i	i-component of energy flux $[J/(m^2 s)]$
R	Ideal gas constant $[J/(\text{mol}K)]$
s	Mass stoichiometric ratio $[-]$
S_L	Laminar flame speed $[m/s]$
S_T	Turbulent flame speed $[m/s]$
T	Temperature of the mixture $[K]$
u^i	i-component of velocity vector $[m/s]$
u'	Turbulent velocity fluctuation $[m/s]$
u'_Δ	Sub-grid scale turbulent velocity $[m/s]$
V_i^c	i-component of correction velocity $[m/s]$
V	Volume of the mixture $[m^3]$
W_k	Molar mass of specie k $[kg/\text{mol}]$
W	Mean molecular weight of the mixture $[kg/\text{mol}]$
X_k	Molar fraction of specie k $[-]$
Y_k	Mass fraction of specie k
Z	Mixture fraction $[-]$

Greek Characters :

β_i	Temperature exponent for the forward reaction i $[-]$
δ_i	Reference flame thickness
δ_L^0	Thermal flame thickness $[m]$
δ_c	Inner cut-off flame scale $[m]$
δ_{ij}	Kronecker delta $[-]$
Δ_x	Grid spacing $[m]$
Δ	Combustion filter size $[m]$
$\hat{\Delta}$	Test filter size $[m]$
$\check{\Delta}$	Effective test filter size $[m]$
Δ_{avg}	Average filter size $[m]$
$\Delta h_{f,k}^0$	Mass enthalpy of formation of the specie k at temperature reference $T_0 = 0K$ $[J/kg]$
η_k	Kolmogorov length scale $[m]$
θ_F	Flame sensor
γ	Ratio between effective test and filter combustion filter sizes $[-]$
Γ_Δ	Efficiency function $[-]$
$\dot{\omega}_k$	Mass reaction rate of specie k $[kg/(m^3\,s)]$
$\dot{\Omega}_k$	Mass reaction rate per unit area of specie k $[kg/(m\,s)]$
$\dot{\omega}_T$	Heat release due to combustion $[J/(m^3\,s)]$
λ	Heat conduction coefficient $[J/(mKs)]$
μ	Dynamic (shear viscosity) $[kg/(m\,s)]$
ν	Kinematic viscosity $[m^2/s]$
ν_{sgs}	Sub-grid scale turbulent viscosity $[m^2/s]$
ν'_{ki}	Molar stoichiometric coefficient of specie k for the forward reaction i $[-]$
ν''_{ki}	Molar stoichiometric coefficient of specie k for the backward reaction i $[-]$
ϕ	Equivalence ratio $[-]$
ρ	Density of the mixture $[kg/m^3]$
ρ_k	Density of specie k $[kg/m^3]$
Σ	Flame Surface density $[1/m]$
τ_{ij}	Viscous stress tensor $[N/m^2]$
τ_k	Kolmogorov time scale $[s]$
τ_c	Chemical time scale $[s]$
τ_t	Integral time scale $[s]$
Ξ_Δ	Sub-grid wrinkling factor $[-]$
ζ	non-dimensional axial cordinate $[-]$

Non-dimensional numbers:

Da	Damköhler number
Da^{fl}	Damköhler number for diffusion flame
Ka	Kalovitz number
Kn	Knudsen number
Le_k	Lewis number of specie k
Pr	Prandtl number
Re	Reynolds number
Re_t	Reynolds turbulent number

Re_Δ	Sub-grid scale Reynolds turbulent number
Sc_k	Schmidt number of specie k

Abbreviations:

CF	Counter-flow
CFD	Computational Fluid Dynamics
CFL	Courant-Friedrichs-Lewy
DNS	Direct Numerical Simulation
FSD	Flame Surface Density
F-TACLES	Filtered TAbulated Chemistry for Large Eddy Simulation
LES	Large Eddy Simulation
LFA	Linear Flamelet Assumption
LHS	Left Hand Side
RANS	Reynolds-Averaged Navier-Stokes
RHS	Right Hand Side
SGS	Sub-grid Scale
TFLES	Thickened Flame model for Large Eddy Simulation
QSS	Quasi-Steady State

Introduction

The work is part of the CLEAN-Gas project, a Marie-Curie Innovative training network (http://www.cleang-gas.polimi.it). The scientific goal is to investigate the natural gas combustion, which is of great interest to the European Energy policy. The network consists of four academic partner institutions (Politecnico di Milano, Université Libre de Bruxelles, École CentraleSupélec and Technische Universität Darmstadt), three industrial partners (Ansaldo Energia, Rolls Royce Deutschland, Numeca) and the T.I.M.E. Association from four different countries.

Energy and Combustion

The role of combustion in the energy supply is of utmost importance. According to the Inernational Energy Agency (2016), in the European Union, combustion accounts for almost 80% of energy consumption, as shown in figure 1. Despite the growing environmental impact, combustion is not supposed to decrease in the next future. The reason is found in the physical and chemical properties of liquid hydrocarbons, particularly the density of energy in terms of unit volume and mass make them well suitable for ground and air transportation. Till today it is the only practicable means to concentrate the energy required for long distances. Furthermore, combustion still plays a vital role in electrical energy production, despite renewable energy sources' growth. However, combustion processes produce pollutant chemical species that have harmful effects on human health and the environment, such as carbon monoxide CO, nitrogen oxide pollutants NOx, unburnt hydrocarbons HC and soot. Besides, the only fact that combustion produces carbon dioxide contributes to global warming (Sawyer, 2009).
In every application, from transportation to energy production, a combustion chamber should face environmental constraints, and the interest in understanding and optimize combustion processes is crucial.

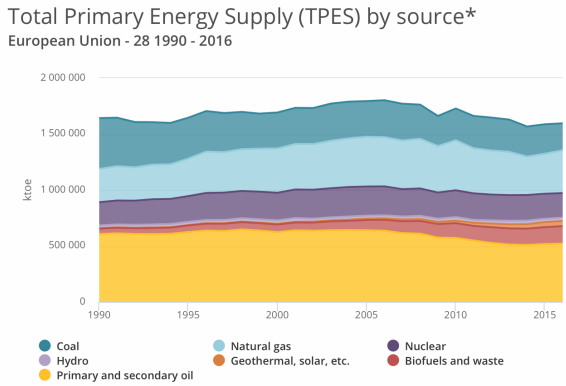

(a)

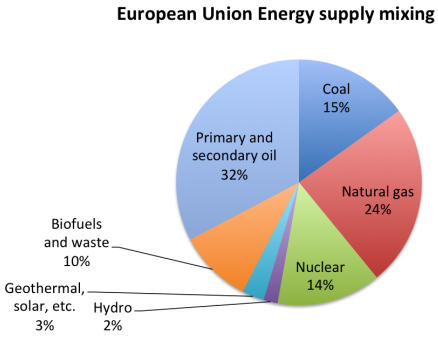

(b)

Figure 1 – *Total Primary Energy Supply (TPLES) in the European Union in kilotonne of oil equivalent (ktoe). Energy supply mix of coal, oil, natural gas, nuclear, hydraulic, biofuel and waste, Geothermal-solar: (a) evoluation of global TPES from 1990 to 2016; (b) share of global TPES in 2016 (Inernational Energy Agency, 2016);*

Computational Fluid Dynamics CFD

The thesis work is carried out in the context of computational fluid dynamics (CFD). In the last decades, with the increasing of the computational performances (as predicted by Meuert et al. (2018), figure 2), the role of CFD in the preliminary design is becoming of utmost importance in basic research and in supporting the design of combustion systems (examples in figure 3). Today almost all the flowfield of engineering applications can be adequately handled by CFD, such as reacting flows in a combustion chamber, flame-wall interaction, combustion instabilities, deflagrations, explosions, and more.
In addition to economic advantages, CFD offers the opportunity to retrieve detailed information of the flowfield, some of which can be difficult to measure. However, the CFD results are only as valid as the physical model incorporated in the governing equations, and therefore are subject to error, especially for

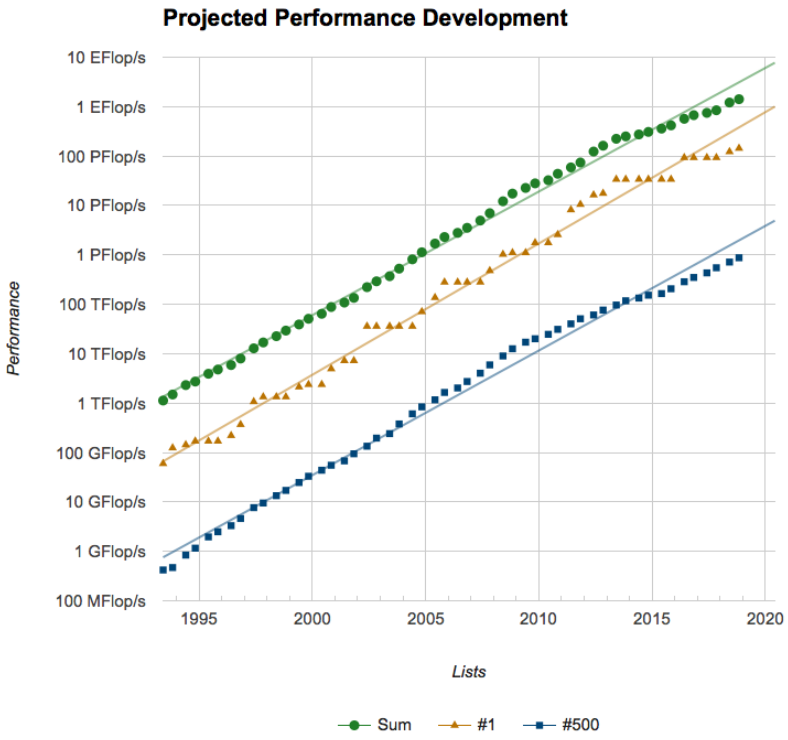

Figure 2 – *Performance of computational resources development over the time in [Flop/s] (Floating point operations per second). Green symbols: sum of the performance of the first 500 powerful computer in world; yellow symbols: performance of the most powerful computer; blue symbol performance of the 500th most powerful computer. Continuous lines: projected performance development (Meuert et al., 2018)*

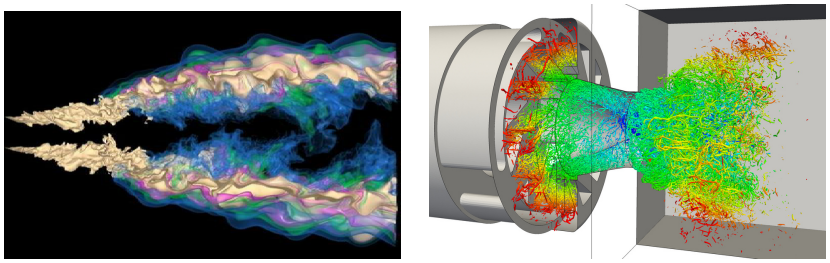

(a) (b)

Figure 3 – *examples of CFD applications in combustion systems. (a) Direct numerical simulation of flame stabilization in a lifted hydrogen flame. Image shows the mixture fraction iso-surface (tan colour) and volume rendering of the OH radical concentration (Kothe, 2007) ; (b) LES and DNS of a lean premixed swirl flame (Moureau et al., 2011)*

turbulent flows (Morton, 1993). Regrettably, it is essential to point out that CFD cannot reproduce physics inadequately included in the problem formulation. The most notable example is turbulence. Today, most CFD solutions of turbulent flows contain turbulence models that are just approximations of actual physics, which depend on empirical data for various constants considered in the turbulence model.

Work Contributions

In the context of Large Eddy Simulation, the most energetic scales of the flow are directly resolved by the numerical grid, while the smallest ones' effects need to be modeled. However, the flame front is still too thin to be resolved with the computational mesh, and several approaches have been developed to overcome the problem. Examples are flame fronts tracking techniques, such as the G-equation (Kerstein et al., 1988; Raman and Pitsch, 2007), adoption of filters larger than the mesh size (Boger et al., 1998) and the TFLES approach (Colin et al., 2000) in which diffusion and pre-exponential factors are modified to thicken the flame artificially. The present work adopts this last strategy. Initially designed for premixed flame regimes, the TFLES model has also been used for non-premixed (Legier et al., 2000; Schmitt et al., 2007) and partially premixed flames (Sengissen et al., 2007) without theoretical support.
The present manuscript investigates in detail the behavior of the model in turbulent non-premixed flames.
Furthermore, the non-resolved sub-grid terms require taking into account the interaction between the flame and the turbulence. Several models are used in literature which include sub-grid turbulent flame speed (Poinsot and Veynante, 2012; Pitsch, 2006), which is directly related to the flame front wrinkling factor (Colin et al., 2000; Charlette et al., 2002a) or to the sub-grid flame surface density (Boger et al., 1998). Usual algebraic models assume equilibrium between turbulent motions and flame surface, unlikely verified in transient situations. A way to overcome this problem can be to solve an additional balance equation for the filtered surface density (Richard et al., 2007; Hawkes and Cant, 2000) or the wrinkling factor (Weller et al., 1998). However, new unclosed terms appear and need to be modeled. The alternative is to develop dynamic models that model the sub-grid scale contributions by using the resolved ones' information. The approach consists of filtering the resolved field with a test filter scale larger than the original LES filter. This strategy has been widely used, and the basic idea was first applied to describe sub-grid momentum transport (Germano et al., 1991) with the so-called Germano identity. In combustion modeling, the dynamic approach is used to determine the sub-grid scale flame/turbulence interaction. When the Germano-like identity is averaged all over the domain, the parameter is uniform and evolves with time (global formulation). Over a finite volume instead, the parameter evolves both in time and space (local formula-

tion). Charlette et al. (2002b) proposed a dynamic global formulation for the exponent parameter of a fractal wrinkling factor expression coupled with the TFLES model. Wang et al. (2012) and Wang et al. (2011) used the dynamic formulation for a jet flame and a transient ignition of a flame kernel under several operating conditions. Schmitt et al. (2015) and Schmitt et al. (2013) adopted the dynamic formulation to the wrinkling factor expression coupled with the tabulated chemistry F-TACLES method, simulating the Tecflam turbulent swirl burner and the turbulent Bunsen flames.
Volpiani et al. (2016) simulate a pilot stabilized jet flame by using a dynamic formulation for the wrinkling factor combined with the TFLES model. They also investigated the influence of physical (flame wrinkling, inner cut-off length scale) and numerical (test width, averaging procedure, updating frequency) characteristics. Furthermore, the dynamic formulation has also been applied to predict combustion instabilities for the PRECCINSTA burner (Volpiani et al., 2017b).
Other uses of dynamic formalism involve variances and scalar dissipation rates of a mixtures that describe non-premixed combustion model (Réveillon and Vervisch, 1998; Pierce and Moin, 1998, 2004; Balarac et al., 2008; Kaul et al., 2013). These approaches can be denoted as "indirect" to differ from the previous ones that involve reaction rates directly.
Hence another objective of the present work is to extend the direct dynamic formulation to non-premixed configurations and investigate its behavior.
To sum up, the main contributions of the manuscript are:

- theoretical investigation of the TFLES for the non-premixed flame in laminar and turbulent regimes. The analysis goes through the effect of the model for a simple laminar counterflow configuration;
- investigation and choice of a proper chemical mechanism for diffusion flames;
- application of the dynamic formulation to a planar turbulent diffusion flame used as reference.

Structure of the manuscript

The manuscript is organized into two parts and one annex. Part I includes the conservation equations of reacting flows, the basic theory of laminar non-premixed flame, and the state of the art of dynamic modeling. Part II explains the theoretical work done on the laminar configuration, and the modeling concepts of the dynamic formulation are applied to a planar turbulent diffusion flame. The annex contains an analysis of reduced chemical mechanisms for methane and an analytical approach explaining the relation between thickened and filtered diffusion thickness of a laminar non-premixed flame.

Part I

General Concepts

Chapter 1

Conservation equations

This chapter explains the fundamental equations of multi-species reacting flows with an insight into the laminar non-premixed flame theory. The Navier-Stokes equations, the species balance, and the energy conservation are used by considering a Newtonian fluid in a continuum space. The chapter aims to help the reader deeply understand the nature of the problem from a mathematical perspective since combustion involves multiple species reacting through multiple chemical reactions. The derivation of the fundamental equations of reacting flows can be found in classic books such as Kuo (2005); Williams (1985); Poinsot and Veynante (2012), while Peters (1988); Linan and Crespo (1976); Bilger (1988, 1989) cover the theory of the laminar non-premixed flame.

Contents

1.1 Primitive and Thermochemical Variables

In a mixture, species are characterized through their mass fractions Y_k for $k = 1...N$ where N is the number of species in the reacting mixture. The mass fraction for each specie Y_k is defined as:

$$Y_k = \frac{m_k}{m} \tag{1.1}$$

where m_k is the mass of specie k present in a given volume V and m is the total mass of the mixture within the volume.
The primitive variables that define the system are:

- density $\rho = m/V$
- three velocity field components u_i
- one variable for energy (or pressure)
- mass fractions Y_k of the N reacting species

The solution of a reacting flow for combustion requires N + 5 variables. Since most chemical schemes involve a large number of species (N is larger than 50 for most simple hydrocarbon fuels), the number of conservation equations to solve represents a substantial computational effort.

The molar fraction X_k is defined as the ratio between the number of moles of k-species (n_k) in a volume V and the total number of moles n in the same volume:

$$X_k = \frac{n_k}{n} = \frac{W}{W_k} Y_k \tag{1.2}$$

where W is the mean molecular weight and W_k is the molar mass of the species k.
The molar concentration $[X_k]$ is number of mole of species k per unit volume:

$$[X_k] = \frac{n_k}{V} = \rho \frac{Y_k}{W_k} = \rho \frac{X_k}{W} \tag{1.3}$$

In a mixture of perfect gas the total pressure p is the sum of the partial pressures p_k of the species:

$$p = \sum p_k \qquad p_k = \rho_k \frac{R}{W_k} T \tag{1.4}$$

where $\rho_k = Y_k \rho$ is the partial density of the species, $R = 8.314 J/(mol\, K)$ is the gas constant and T the temperature of the system. So the state equation is reduced to:

$$p = \rho \frac{R}{W} T \tag{1.5}$$

Information about the energetic status of the system can be taken into account with several variables. Considering the species k, the most used are the energy e_k and the enthalpy h_k per unit mass defined as the sum of a sensible and a chemical part:

$$e_k = \underbrace{\int_{T_0}^{T} C_{vk} dT - RT_0/W_k}_{\text{sensible}} + \underbrace{\Delta h^0_{f,k}}_{\text{chemical}} \tag{1.6}$$

$$h_k = \underbrace{\int_{T_0}^{T} C_{pk} dT}_{\text{sensible}} + \underbrace{\Delta h^0_{f,k}}_{\text{chemical}} \tag{1.7}$$

Form	Energy	Enthalpy
Sensible	$e_s = \int_{T_0}^{T} C_v dT - RT_0/W_k$	$h_s = \int_{T_0}^{T} C_p dT$
Sensible + Chemical	$e = e_s + \sum_{k=1}^{N} \Delta h^0_{f,k}$	$h = h_s + \sum_{k=1}^{N} \Delta h^0_{f,k}$
Total Chemical	$e_t = e + \frac{u_i^2}{2}$	$h_t = h + \frac{u_i^2}{2}$
Total non-Chemical	$E = e_s + \frac{u_i^2}{2}$	$H = h_s + \frac{u_i^2}{2}$

Table 1.1 – *Enthalpy and energy forms used in conservation equations (Poinsot and Veynante, 2012)*

where $\Delta^0_{f,k}$ is mass enthalpy formation of the specie k at temperature T_0. C_{vk} and C_{pk} are the heat capacity of the species respectively at constant volume and constant pressure. Those two quantities are related:

$$e_k = h_k - \frac{p_k}{\rho_k} \tag{1.8}$$

there are multiple ways to express energy and enthalpy of a mixture. Different forms are summarized in table 1.1. The heat capacities of the mixture are given by:

$$C_p = \sum_{k=1}^{N} C_{pk} Y_k \tag{1.9}$$

$$C_v = \sum_{k=1}^{N} C_{vk} Y_k \tag{1.10}$$

1.2 Governing Equations

It is possible to describe the flow of particles at different levels of detail. In order to model a flowfield, it is important to consider the distribution of particle in the space in term of mean free path l_f which is the average distance travelled by a moving particle between two collisions which modify its direction or energy or other particle properties (Laurendeau, 2005). For a Boltzmann gas, the mean free path can be calculated as:

$$l_f = \frac{k_B T}{\sqrt{2}\pi d^2 P} \tag{1.11}$$

where $k_B = 1.38\,10^{-23} J/K$ is the Boltzmann constant, T is the thermodynamic temperature, d is the particle hard-shell diameter and P is the total pressure. Considering the mean free path l and the characteristic length of the flow L, the Knudsen number is defined as:

$$\mathrm{Kn} = \frac{l_f}{L} = \frac{k_B T}{\sqrt{2}\,\pi\sigma^2\,P_0 L} \tag{1.12}$$

For a relatively small Knudsen number ($\mathrm{Kn} < 0,01$) the system is considered continuous and flow is viscous. A compressible reaction flow is so described by

the Navier-Stokes equations as (Williams, 1985):

$$\frac{\partial \rho u_i}{\partial t} + \frac{\partial}{\partial x_i}(\rho u_i u_j) = -\frac{\partial}{\partial x_j}\left[P\delta_{ij} - \tau_{ij}\right] \tag{1.13}$$

$$\frac{\partial \rho E}{\partial t} + \frac{\partial}{\partial x_j}\left(\rho E u_j\right) = -\frac{\partial}{\partial x_j}\left[u_i\left(P\delta_{ij} - \tau_{ij}\right) + q_j\right] + \dot{\omega}_k \tag{1.14}$$

$$\frac{\partial \rho Y_k}{\partial t} + \frac{\partial}{\partial x_j}\left(\rho Y_k u_j\right) = -\frac{\partial}{\partial x_j}\left[J_{j,k}\right] + \dot{\omega}_k \tag{1.15}$$

Equations 1.13-1.15 are the conservation laws respectively for momentum, total energy and species; ρ is the density, u_i is the component i of the velocity vector and E is the total energy per unit mass.
The stress tensor τ_{ij}, the diffusive flux for the species $J_{j,k}$, the heat flux vector q_j the species source $\dot{\omega}_k$ and the energy source term $\dot{\omega}_T$ have to be defined to close the system of equations.
In vector notation, it writes as:

$$\frac{\partial \mathbf{w}}{\partial t} + \nabla \cdot \mathbf{F} = \mathbf{s} \tag{1.16}$$

where $\mathbf{w} = (\rho u, \rho v, \rho w, \rho E, \rho Y_k)^T$ is the state vector, $\mathbf{F}$ is the flux tensor and $\mathbf{s}$ is the source term. The flux tensor can be decomposed into an inviscid and a viscous term:

$$\mathbf{F} = \mathbf{F}^I(\mathbf{w}) + \mathbf{F}^V(\mathbf{w}, \nabla\mathbf{w}) \tag{1.17}$$

Inviscid Term

The components of the inviscid flux $\mathbf{F}^I(\mathbf{w})$ are:

$$\bar{\mathbf{f}^I} = \begin{pmatrix} \rho u^2 + P \\ \rho uv \\ \rho uw \\ (\rho E + P)u \\ \rho Y_k u \end{pmatrix} \tag{1.18}$$

$$\bar{\mathbf{g}^I} = \begin{pmatrix} \rho uv \\ \rho uv^2 + P \\ \rho vw \\ (\rho E + P)v \\ \rho Y_k v \end{pmatrix} \tag{1.19}$$

$$\bar{\mathbf{h}^I} = \begin{pmatrix} \rho uw \\ \rho vw \\ \rho w^2 + P \\ (\rho E + P)w \\ \rho Y_k w \end{pmatrix} \tag{1.20}$$

Viscous terms

The viscous term $\mathbf{F}^V(\mathbf{w}, \nabla\mathbf{w})$ is:

$$\bar{\mathbf{f}^V} = \begin{pmatrix} -\tau_{xx} \\ -\tau_{xy} \\ -\tau_{xz} \\ -(u\tau_{xx} + v\tau_{xy} + w\tau_{xz}) + q_x \\ J_{x,k} \end{pmatrix} \tag{1.21}$$

$$\bar{\mathbf{g}^V} = \begin{pmatrix} -\tau_{xy} \\ -\tau_{yy} \\ -\tau_{yz} \\ -(u\tau_{xy} + v\tau_{yy} + w\tau_{yz}) + q_y \\ J_{y,k} \end{pmatrix} \tag{1.22}$$

$$\bar{\mathbf{h}^V} = \begin{pmatrix} -\tau_{xz} \\ -\tau_{yz} \\ -\tau_{zz} \\ -(u\tau_{xz} + v\tau_{yz} + w\tau_{zz}) + q_y \\ J_{z,k} \end{pmatrix} \tag{1.23}$$

where τ_{ij} is the stress tensor, $J_{i,k}$ the diffusive flux of species k in the i-direction and q_i the heat flux vector.

Viscous Stress Tensor

The stress tensor τ_{ij} for a Newtonian fluid is:

$$\tau_{ij} = -\frac{2}{3}\mu\frac{\partial u_k}{\partial x_k}\delta_{ij} + \mu\left(\frac{\partial u_i}{\partial x_j} + \frac{\partial u_j}{\partial x_i}\right) \tag{1.24}$$

where μ is the shear viscosity and δ_{ij} is the Kronecker symbol (for $i = j$, $\delta_{ij} = 1$, otherwise $\delta_{ij} = 0$). Some notations gather the pressure tensor with the viscous term to obtain:

$$\sigma_{ij} = \tau_{ij} - p\delta_{ij} = -p\delta_{ij} - \frac{2}{3}\mu\frac{\partial u_k}{\partial x_k}\delta_{ij} + \mu\left(\frac{\partial u_i}{\partial x_j} + \frac{\partial u_j}{\partial x_i}\right) \tag{1.25}$$

Species diffusion flux

In multi-species flows the total mass conservation implies that:

$$\sum_{k=1}^{N} Y_k V_{k,i} = 0 \qquad \sum_{k=1}^{N} \dot{\omega}_k = 0 \tag{1.26}$$

where V_k, i are the components in the i-direction of the diffusion velocity of the specie k. It is often expressed as a function of the species gradient using the approximation by Hirschfelder and Curtiss (1954):

$$X_k V_{k,i} = -D_k \frac{\partial X_k}{\partial x_i} \tag{1.27}$$

where X_k is the molar fraction and D_k is the diffusion coefficients for the specie k. Considering the mass fraction, equation 1.27 becomes:

$$Y_k V_{k,i} = -D_k \frac{W_k}{W} \frac{\partial X_k}{\partial x_i} \tag{1.28}$$

The influence of the temperature gradients on the diffusion (know as Soret effect) and the molecular transport due to the pressure gradients (Giovangigli, 1999) are neglected.
By summing equation 1.28 for all the species, the mass conservation 1.26 is not achieved. A correction diffusion velocity V_i^c is so added to the convection velocities $V_{k,i}$ to ensure the global mass conservation (Poinsot and Veynante, 2012):

$$V_i^c = \sum_{k=1}^{N} D_k \frac{W_k}{W} \frac{\partial X_k}{\partial x_i} \tag{1.29}$$

The diffusive species flux for the specie k is:

$$J_{k,i} = \rho Y_k (V_{k,i} + V_i^c) = -\rho \left(D_k \frac{W_k}{W} \frac{\partial X_k}{\partial x_i} - Y_k V_i^c \right) \tag{1.30}$$

Heat flux vector

In muti-species flows, the heat flux is given by the conduction and by the species gradients, so that the total heat flux vector is:

$$q_i = -\lambda \frac{\partial T}{\partial x_i} + \sum_{k=1}^{N} J_{k,i} h_{sk} \tag{1.31}$$

$$q_i = \underbrace{-\lambda \frac{\partial T}{\partial x_i}}_{\text{conduction}} \underbrace{-\rho \sum_{k=1}^{N} \left(D_k \frac{W_k}{W} \frac{\partial X_k}{\partial x_i} - Y_k V_i^c \right) h_{sk}}_{\text{species diffusion}} \tag{1.32}$$

where λ is the heat conduction coefficient of the mixture.

Transport coefficients

The dynamic viscosity μ depends on several variables such as species concentration, temperature and pressure. However, it is commonly assumed to depend only on the temperature with a small induced error. A typical approximation is the Sutherland's law (Sutherland, 1893), which relates the dynamic viscosity to the temperature as follows:

$$\mu = \mu_{\text{ref}} \left(\frac{T}{T_{\text{ref}}} \right)^{3/2} \frac{T_{\text{ref}} + S}{T + S} \tag{1.33}$$

where μ_{ref} is the viscosity measured at reference temperature T_{ref} and S is the Sutherland temperature. Values for the reference temperature and the Sutherland temperature are $T_{\text{ref}} = 273K$ and $S = 110.4K$.

The heat conduction is related to the Prandtl number, assumed constant in time and space ($\text{Pr} = 0.7$), so:

$$\lambda = \frac{\mu C_p}{\text{Pr}} \tag{1.34}$$

One can write the thermal diffusion as:

$$D_T = \frac{\mu}{\rho \text{Pr}} = \frac{\lambda}{\rho C_p} \tag{1.35}$$

The determination of the species diffusion coefficients D_k is not straightforward. Those are written as a function of the binary coefficients D_{ij} obtained from the kinetic theory (Hirschfelder and Curtiss, 1954) and write as (Bird, 1961):

$$D_k = \frac{1 - Y_k}{\sum_{j \neq k}^{N} X_j / D_{jk}} \tag{1.36}$$

where D_{ij} are complex function of collision integrals and thermodynamic variables. However in most industrial application using large eddy simulation a complex transport is not necessary. Thus, a simplified approximation for D_k is adopted. The Schmidt numbers Sc_k of the species are assumed to be constant in time and space. So the binary diffusion coefficient for each specie is computed as:

$$D_k = \frac{\mu}{\rho \text{Sc}_k} \tag{1.37}$$

The thermal heat diffusivity D_T and the species diffusion coefficient D_k are related by the Lewis number of the specie Le_k:

$$\text{Le}_k = \frac{D_T}{D_k} = \frac{\text{Sc}_k}{\text{Pr}} \tag{1.38}$$

In simple turbulent model it is can assumed that the thermal and molecular diffusivity are equal so the Lewis number is equal to unity.

Source Term

The source term **s** on the RHS of equation 1.16 is:

$$\mathbf{s} = \begin{pmatrix} 0 \\ 0 \\ 0 \\ \dot{\omega}_T \\ \dot{\omega}_k \end{pmatrix} \tag{1.39}$$

where $\dot{\omega}_T$ is the rate of heat release and $\dot{\omega}_k$ the reaction rate of the specie k. Considering N species $\mathcal{M}_k$ reacting through M reactions, a chemical mechanism can be written as:

$$\sum_{k=1}^{N} \nu'_{ki} \mathcal{M}_k \leftrightarrow \sum_{k=1}^{N} \nu''_{ki} \mathcal{M}_k \ , \qquad i = 1, ..., M \tag{1.40}$$

where ν'_{ki} and ν''_{ki} are the molar stoichiometric coefficients of the specie k for the reaction i. The total reaction rate of specie k, $\dot{\omega}_k$ is the sum of the reaction rate $\dot{\omega}_{ki}$ produced by the all the M reactions:

$$\dot{\omega}_k = \sum_{i=1}^{M} \dot{\omega}_{ki} = W_k \sum_{i=1}^{M} \nu_{ki} \mathcal{Q}_i \tag{1.41}$$

where $\nu_{ki} = \nu'_{ki} - \nu''_{ki}$ and $\mathcal{Q}_i$ is the rate progress of reaction i and it is written as:

$$\mathcal{Q}_i = \underbrace{K_{fi} \prod_{k=1}^{N} \left(\frac{\rho Y_k}{W_f} \right)^{\nu'_{ki}}}_{k_{fi}} - \underbrace{K_{ri} \prod_{k=1}^{N} \left(\frac{\rho Y_k}{W_k} \right)^{\nu''_{ki}}}_{k_{ri}} \tag{1.42}$$

K_{fi} and K_{ri} are the respectively the forward and reverse rates of reaction i. They are commonly modelled with the Arrhenius's law (Arrhenius, 1889):

$$K_{fi} = A_i T^{\beta_i} \exp\left(\frac{E_{ai}}{RT} \right) \tag{1.43}$$

A_i is the pre-exponential constant, β_i is the temperature exponent and E_{ai} is the activation energy of reaction i. The terms k_{fi} and k_{ri} are commonly referred respectively as forward and reverse reaction rates for the reaction i. The reverse rates K_{ri} are computed from the forward rates and the equilibrium constant K^i_{eq}:

$$K_{ri} = \frac{K_{fi}}{K^i_{\text{eq}}} \tag{1.44}$$

The K_{eq}^i terms depend only on the temperature and on the thermodynamic data of the system and can be computed as (Kuo, 2005):

$$K_{\text{eq}}^i = \left(\frac{p_a}{RT}\right)^{\sum_{k=1}^{N} \nu_{kj}} \exp\left(\frac{S_i^0}{R} - \frac{H_i^0}{RT}\right) \tag{1.45}$$

H_i^0 and S_i^0 are respectively the enthalpy and entropy changes when passing from reactants to products for the reaction i. Then the heat release by the reaction is calculated as:

$$\dot{\omega}_T = -\sum_{k=1}^{N} \dot{\omega}_k \Delta h_{f,k}^0 \tag{1.46}$$

where $\Delta h_{f,k}^0$ is the mass enthalpy of formation of the specie k at the reference temperature of $T_0 = 0K$.
The source term due to the radiation effects is not taken into account in the present work.

1.3 Laminar non-premixed flame

The non-premixed or diffusion flames constitute a class of specific flames where fuel and oxidiser enter the combustion chamber separately without premixing. Literature on non-premixed flame is abundant (Linan and Crespo, 1976; Bilger, 1988, 1989).
Figure 1.1 shows a simple configuration; it is important to do some considerations. First, away on each side of the flame, the mixture is too rich or too lean to burn so that the chemical reactions can happen only in a limited region. The flame is steady only if a strain is applied when oxidiser and fuel are pushed against each other. Unlike the premixed flame, the diffusion flame does not exhibit any flame speed neither a reference flame thickness. From an industrial point of view, these flames are simpler to design and to build because they do not require any premixing with a given equivalence ratio. They do not propagate so they are relatively safer to operate, compared to premixed flames, but in turn, the efficiency is reduced .
The following assumptions are considered for the analysis:

- a single step chemical reaction with N species $\mathcal{M}_k$:

$$\sum_{k=1}^{N} \nu_k' \mathcal{M}_k \rightleftharpoons \sum_{k=1}^{N} \nu_k'' \mathcal{M}_k \tag{1.47}$$

- constant thermodynamic pressure and low Mach numbers

- all the diffusion coefficients of the species D_k are constant and equal to D. The Fick's law is used for diffusion velocities

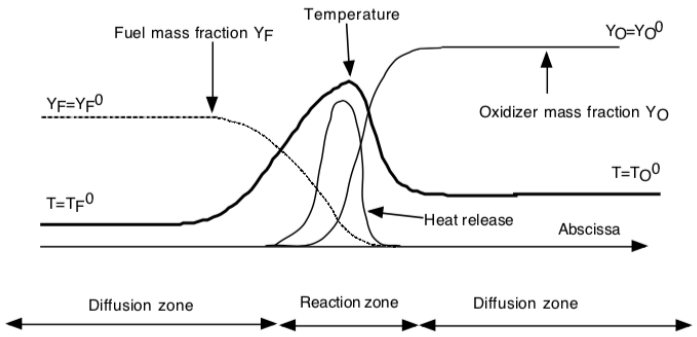

Figure 1.1 – *Laminar non-premixed Flame structure (Poinsot and Veynante, 2012).*

- heat capacities C_{pk} of chemical species are equal and independent of the temperature, $C_{pk} = C_p$

The balance equation of mass fraction (eq. 1.15) of the species Y_k rewrites to:

$$\frac{\partial \rho Y_k}{\partial t} + \frac{\partial}{\partial x_i}(\rho u_i Y_k) = \frac{\partial}{\partial x_i}\left(\rho\, D \frac{\partial Y_k}{\partial x_i}\right) + \dot{\omega}_k \tag{1.48}$$

and the energy equation (from eq. 1.14 and 1.35),:

$$\frac{\partial \rho T}{\partial t} + \frac{\partial}{\partial x_i}(\rho u_i T) = \frac{\partial}{\partial x_i}\left(\frac{\lambda}{\rho C_p}\frac{\partial T}{\partial x_i}\right) + \dot{\omega}_T \tag{1.49}$$

where λ is the heat conduction coefficient.
By considering the case where the reaction (1.47) involves only fuel (F), oxidiser (O) and products (P):

$$\nu_F F + \nu_O O \rightleftharpoons \nu_P P \tag{1.50}$$

By assuming the case of reaction (1.50), it is possible to link the reaction rate of the fuel $\dot{\omega}_F$ and the oxidiser $\dot{\omega}_O$ as:

$$\dot{\omega}_O = s\,\dot{\omega}_F \quad \text{with} \quad s = \frac{\nu_O W_O}{\nu_F W_F} \tag{1.51}$$

where s is the mass stoichiometric ratio and W_F and W_O are the molecular weights of fuel and oxidiser respectively.
By considering the reaction rate for the temperature equation (eq. 1.46) and the the heat released per unit mass by the reaction Q as:

$$Q = \sum_{k=1}^{N}\left(\Delta h^0_{f,k}\frac{W_k \nu_k}{W_F \nu_F}\right) \tag{1.52}$$

it is possible to retrieve the source term of the energy equation:

$$\dot{\omega}_T = Q\dot{\omega}_F \tag{1.53}$$

By using these relations, the conservation equations for fuel, oxidiser and temperature become:

$$\frac{\partial \rho Y_F}{\partial t} + \frac{\partial}{\partial x_i}(\rho u_i Y_F) = \frac{\partial}{\partial x_i}\left(\rho D \frac{\partial Y_F}{\partial x_i}\right) + \dot{\omega}_F \tag{1.54}$$

$$\frac{\partial \rho Y_O}{\partial t} + \frac{\partial}{\partial x_i}(\rho u_i Y_O) = \frac{\partial}{\partial x_i}\left(\rho D \frac{\partial Y_O}{\partial x_i}\right) + s\,\dot{\omega}_F \tag{1.55}$$

$$\frac{\partial \rho T}{\partial t} + \frac{\partial}{\partial x_i}(\rho u_i T) = \frac{\partial}{\partial x_i}\left(\frac{\lambda}{C_p}\frac{\partial T}{\partial x_i}\right) + \frac{Q}{C_p}\dot{\omega}_F \tag{1.56}$$

where λ is the thermal conductivity. Combining equations 1.54, 1.55 and 1.56 and assuming unity Lewis numbers ($\mathrm{Le} = \lambda/(\rho C_p D) = 1$), the following quantities:

$$Z_1 = sY_F - Y_O \quad ; \quad Z_2 = \frac{C_p T}{Q} + Y_F \quad ; \quad Z_3 = \frac{C_p T}{Q} + Y_O \tag{1.57}$$

follow the same balance equation:

$$\frac{\partial \rho Z_j}{\partial t} + \frac{\partial}{\partial x_i}(\rho u_i Z_j) = \frac{\partial}{\partial x_i}\left(\rho D \frac{\partial Z_j}{\partial x_i}\right) \tag{1.58}$$

where Z is a passive scalar and changes because of diffusion and convection but not because of reaction. The normalized variables z_j:

$$z_j = \frac{Z_j - Z_j^O}{Z_j^F - Z_j^O} \tag{1.59}$$

follow the same convection/diffusion equation:

$$\frac{\partial \rho z_j}{\partial t} + \frac{\partial}{\partial x_i}(\rho u_i z_j) = \frac{\partial}{\partial x_i}\left(\rho D \frac{\partial z_j}{\partial x_i}\right) \tag{1.60}$$

and with the same boundary conditions $z_j = 1$ in the fuel and $z_j = 0$ in the oxidiser stream, all those variable are equal:

$$z_1 = z_2 = z_3 = z \tag{1.61}$$

Expressing z with equations 1.59 and the boundary conditions of table 1.2

$$z = \frac{sY_F - Y_O + Y_O^0}{sY_F^0 + Y_O^0} = \frac{\frac{C_p}{Q}(T - T_O^0) + Y_F}{\frac{C_p}{Q}(T_F^0 - T_O^0) + Y_F^0} = \frac{\frac{sC_p}{Q}(T - T_O^0) + Y_O - Y_O^0}{\frac{sC_p}{Q}(T_F^0 - T_O^0) - Y_O^0} \tag{1.62}$$

where Y_O^0 and T_O^0 are the oxidiser mass fraction and temperature at the oxidiser tank, Y_F^0 and T_F^0 are the fuel mass fraction and temperature at the fuel tank.

Variable	Fuel side	Oxidiser side
Fuel Mass fraction	Y_F^1	0
Oxidiser Mass fraction	0	Y_O^0
Temperature	T_1	T_0
Mixture fraction z	1	0

Table 1.2 – *Boundary conditions for species mass fractions, temperature and the mixture fraction z defined by eq. 1.59.*

Another important quantity in diffusion flame is the scalar dissipation rate χ defined as:

$$\chi = 2D\left(\frac{\partial z}{\partial x_i}\frac{\partial z}{\partial x_i}\right) \tag{1.63}$$

The variable χ has the dimension on an inverse time, and it is related to the gradient of z and the fluxes of the species towards the flame front and vice-versa. Furthermore, the quantity of $\sqrt{D/\chi}$ represents an estimation of the mixing layer thickness.

A common assumption for diffusion flame is that all the species and temperature depends on the mixture fraction z and on the time t

$$T = T(z,t) \quad \text{and} \quad Y_k = Y_k(z,t) \tag{1.64}$$

This assumption means that the gradients along the flame front are neglected compared to the gradients normal to the flame front (Williams, 1985; Peters, 2000). In a multi-dimensional flow, this requires that the flame be thin compared to other flow and wrinkling scales. So each element of the flame can be viewed as a small laminar flame called *flamelet*.

So, the balance equation (1.48) and energy equation (1.49) can be rewritten as follows (Poinsot and Veynante, 2012):

$$\rho\frac{\partial Y_k}{\partial t} = \dot{\omega}_k + \frac{1}{2}\rho\chi\frac{\partial^2 Y_k}{\partial z^2} \tag{1.65}$$

$$\rho\frac{\partial T}{\partial t} = \dot{\omega}_T + \frac{1}{2}\rho\chi\frac{\partial^2 T}{\partial z^2} \tag{1.66}$$

Equations 1.65 and 1.66 are so called *flamelet equations*.
Another significant quantity to define the structure of a diffusion flame is the stoichiometric mixture fraction z_{st}. In infinitely fast chemistry assumption the reaction takes places at $z = z_{\text{st}}$, since fuel and oxidiser can not coexists in the same location [1].

[1] Because their combustion rate is infinitely fast compared to all other scales in the flame.

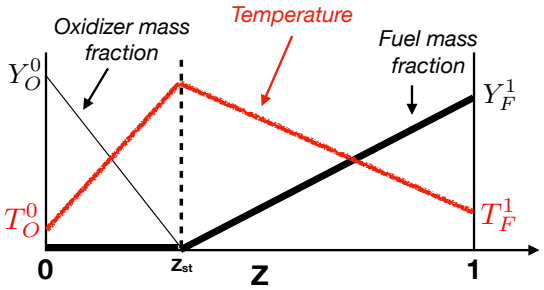

Figure 1.2 – *Diffusion flame structure in the mixture fraction z diagram for irreversible infinitely fast chemistry (Burke and Schumann, 1928).*

The flame structure can be defined (Burke and Schumann, 1928) on the fuel side ($z > z_{st}$) as:

$$\begin{aligned} Y_F(z) &= Y_F^0 \frac{z - z_{st}}{1 - z_{st}} \\ Y_O(z) &= 0 \\ T(z) &= zT_F^1 + (1-z)T_O^0 + \frac{QY_F^0}{C_p} z_{st} \frac{1-z}{1-z_{st}} \end{aligned} \tag{1.67}$$

and on the oxidiser side ($z < z_{st}$):

$$\begin{aligned} Y_F(z) &= 0 \\ Y_O(z) &= Y_O^0 (1 - \frac{z}{z_{st}}) \\ T(z) &= zT_F^1 + (1-z)T_O^0 + \frac{QY_F^0}{C_p} z \end{aligned} \tag{1.68}$$

The stoichiometric mixture fraction z_{st} can be retrieved from equation (1.62) as the position where both Y_F and Y_O are zero:

$$z_{\text{st}} = \frac{1}{1 + \frac{sY_F^0}{Y_O^0}} \tag{1.69}$$

1.3.1 Steady strained one-dimensional diffusion flame

The counter flow steady strained diffusion flame is a representative configuration for the diffusion regime (figure 1.3). Experimentally it can be created by sending a stream of fuel against a stream of oxidiser. The flame is stable because the flow is strained and z depends only on the the axial cordinate.

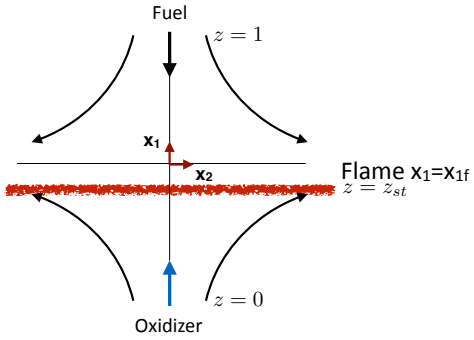

Figure 1.3 – *Planar counter flow flame domain.*

Assuming constant density, the velocity field can be written as potential flow-field:

$$u_1 = -ax_1 \qquad \text{and} \qquad u_2 = ax_2 \tag{1.70}$$

The strain rate a, which has a dimension of time^{-1} is assumed to be constant. By considering unity Lewis number for all the species and constant diffusion, the continuity equation can be reduced to (Poinsot and Veynante, 2012):

$$-ax_1 \frac{\partial z}{\partial x_1} = D \frac{\partial^2 z}{\partial x_1^2} \tag{1.71}$$

replacing x_1 by $\zeta = x_1\sqrt{a/2D}$ one can write:

$$\frac{\partial^2 z}{\partial \zeta^2} + 2\zeta \frac{\partial z}{\partial \zeta} = 0 \tag{1.72}$$

with boundary conditions: $z(+\infty) = 1$ and $z(-\infty) = 0$, the solution of equation (1.72) is:

$$z = \frac{1}{2}\left[1 + \text{erf}(\zeta)\right] = \frac{1}{2}\left[1 + \text{erf}\left(\, x_1\sqrt{\frac{a}{2FD}}\right)\right] \tag{1.73}$$

and its gradient:

$$\frac{\partial z}{\partial \zeta} = \frac{\exp\left(-\zeta^2/F\right)}{\sqrt{\pi\, F}} \qquad \text{and} \qquad \frac{\partial z}{\partial x_1} = \sqrt{\frac{a}{2\pi FD}}\exp\left(-x_1^2\frac{a}{2FD}\right) \tag{1.74}$$

The fuel reaction rate per unit area $\dot{\Omega}$, representative of the heat released by the flame,can be expressed integrating equation 1.54 between x_f^- and x_f^+ which are two points located at both sides of the front x_f infinitely close to it:

$$\dot{\Omega} = \int_{x_{1f}^-}^{x_{1f}^+} \dot{\omega}_F dx_1 = -\left[\rho D \frac{\partial Y_F}{\partial x_1}\right]_{x_{1f}^-}^{x_{1f}^+} = \rho D \left[\frac{\partial Y_F}{\partial x_1}\right]_{x_1 = x_{1f}^+} \tag{1.75}$$

By assuming infinitely fast chemistry, the fuel mass fraction can be recast as (Poinsot and Veynante, 2012; Burke and Schumann, 1928):

$$Y_F = Y_F^0 \frac{z - z_{\text{st}}}{1 - z_{\text{st}}} \tag{1.76}$$

so that:

$$\frac{\partial Y_F}{\partial x_1} = \frac{\partial Y_F}{\partial z}\frac{\partial z}{\partial x_i} \tag{1.77}$$

By considering equations (1.74), (1.76) and (1.77), eq 1.75 rewrites as:

$$\dot{\Omega}_F = \rho \frac{Y_F^0}{1 - z_{\text{st}}} \sqrt{\frac{a\,D}{2\pi}} \exp\left(-\zeta_f^2\right) \tag{1.78}$$

where ζ_f correspond to the flame location where $z > z_{st}$ and from Eq. (1.73) it is computed as:

$$\zeta_f = x_{1f}\sqrt{\frac{a}{2\,D}} = \text{erf}^{-1}(1 - 2z_{\text{st}}) \tag{1.79}$$

The scalar dissipation can be directly related to the strain rate a by considering the solution of z distribution (eq. 1.73):

$$\chi = 2\,D\left(\frac{\partial z}{\partial x_1}\right)^2 = \frac{a}{\pi}\exp\left(-\frac{a}{D}x_1^2\right) \tag{1.80}$$

Combining eq. 1.73 and 1.80 gives:

$$\chi = \frac{a}{\pi}\exp\left(-2\left[\text{erf}^{-1}(1-2z)\right]^2\right) = \chi_0 \exp\left(\text{erf}^{-1}(1-2z)\right) = \chi_0 F(z) \tag{1.81}$$

where χ_0 is the maximum value of the scalar dissipation corresponding to the stagnation plane.
For infinitely fast irreversible chemistry its value on the flame front is:

$$\chi_f = \frac{a}{\pi}\left[-2\left(\text{erf}^{-1}\left(1 - 2z_{\text{st}}\right)\right)^2\right] = \chi_0 F(z_{st}) \tag{1.82}$$

The solution of relation (1.82) is shown in figure 1.4 for a methane air counter flow laminar flame.

1.4 Conclusion

The basic concepts of primitive and thermochemical variables describing a system's thermodynamic state have been given. Furthermore, the governing equations to describe a multi-species flowfield have been explained (Williams,

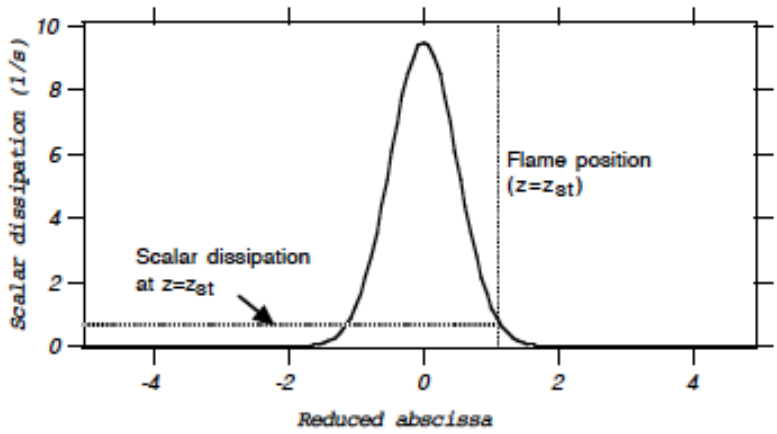

Figure 1.4 – *Scalar dissipation rate χ versus reduced abscissa ζ in a constant density methane/air flame (strain rate $a = 30s^{-1}$).*

1985; Kuo, 2005; Poinsot and Veynante, 2012). Finally, the attention has focused on the basic definitions and equations for a simplified laminar diffusion flame (Linan and Crespo, 1976; Bilger, 1988, 1989; Peters, 2000; Poinsot and Veynante, 2012). Simplifications (such as constant pressure, constant density, single-step chemical reaction, constant diffusion) allows retrieving simple relations to understand the physics of a real diffusion flame. However, the following chapter focuses on the turbulent diffusion flames.

Chapter 2

Turbulent Flame Modeling

Since full-resolved simulations are still not affordable for a real industrial combustion system, the Large Eddy Simulation (LES) represents an interesting compromise between the flow field and the computational cost. It is now widely used, and it consists of filtering the Navier-Stokes equations to directly resolve the most significant structure of the turbulent spectrum and model the effects of the smallest ones.
This chapter describes the numerical modeling of turbulent flames in the context of LES.
The combustion models for the sub-grid terms are classified according to their basic concept formulation into three main groups: flame surface, statistical descriptions, and turbulent mixing. A particular focus is given to the models used for non-premixed flames.

Contents

2.1 Turbulence Characterization

A turbulent flow is a fluid motion characterized by chaotic changes in pressure and velocity (Batchelor, 2000). A traditional description, used mainly for theoretical modeling, consists of a mean flow, created by pressure gradients or other forces, does work on the large-scale motions of the turbulence, thereby increasing their energy turbulence production (Ferziger, 1999). Through various other processes, including vortex, stretching, the energy is transferred to ever smaller scales until, eventually, it reaches the scales small enough for viscosity to dissipate the energy into the fluid's internal energy. The distribution of energy over the scales of turbulence is usually described in terms of wavenumber k of the perturbation, defined as:

$$k = \frac{U_p}{f} \tag{2.1}$$

where U_p is the speed at which the perturbation is propagating, which can be the mean flow speed, and f is the frequency of propagation. Related to the wavenumber, a wavelength λ can be defined as:

$$\lambda = \frac{1}{k} \tag{2.2}$$

For homogeneous flows, it is possible to represent the velocity field as a Fourier series as:

$$u(x) = \Sigma \hat{u}(k) e^{ikx} \tag{2.3}$$

so the energy spectrum as:

$$E(k) = \frac{1}{2} u(k) u^*(k) \tag{2.4}$$

where the superscript * denotes the complex conjugate of the quantity. The energy spectrum gives the distribution of the turbulence energy in terms of wavenumber.
So according to (Kolmogorov, 1941), the three-dimensional energy spectrum in such a region must have the form:

$$E(k) = C_K \epsilon^{2/3} k^{-5/3} \tag{2.5}$$

where $E(k)$ is the three dimensional energy spectrum, so $E(k)dk$ is the amount of energy in a spherical shell of thickness dk in three dimensional wave-number space, ϵ is the rate of energy dissipation, and C_K is the Kolmogorov constant deduced from experimental measurements. The energy spectrum 2.5 can be obtained in many ways, and it has been experimentally verified numerous times. Figure 2.1 shows a typical energy spectrum of turbulence in logarithmic coordinates.

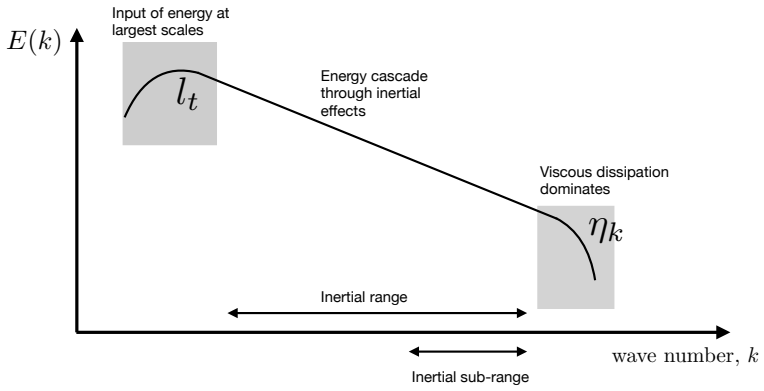

Figure 2.1 – *Turbulence energy cascade over the wavenumber. Both scales are logarithmic. Most energetic scales l_t (integral length scales), smallest scales η_k (Kolmogorov length scales).*

However, several length scales can be figured out in the spectrum of a turbulent flow. Of these the most important are the integral or outer scale and the Kolmogorov scale. The inertial range lie in between, where there is no production, and the rate at which energy is transferred to the smaller scales must equal the rate at which it is dissipated at the smallest scales.
Generally, the integral length scales l_t (with integral time scales τ_t) correspond to the peak in the energy spectrum. They represent, therefore, the characteristic length-scale of the energy-containing scales. The Kolmogorov scales η_k (with time scales τ_k) are the ones at which the dissipation takes place and thus the smallest scales of interest in a turbulent flow. By assuming that they are determined entirely by the rate of dissipation of the energy transported by the turbulence and the viscosity ν, it is possible to show that (Benocci and Olivari, 2014):

$$\eta_k = \left(\frac{\nu^3}{\epsilon}\right)^{3/4} \tag{2.6}$$

where η_k is the Kolmogorov scale and ϵ is the rate of dissipation. One can demonstrate that, these scales are related by:

$$\frac{l_t}{\eta_k} = \mathrm{Re}_L^{3/4} \tag{2.7}$$

where:

$$\mathrm{Re}_L = \frac{U l_t}{\nu} \tag{2.8}$$

and U is the characteristic velocity of the large scales.

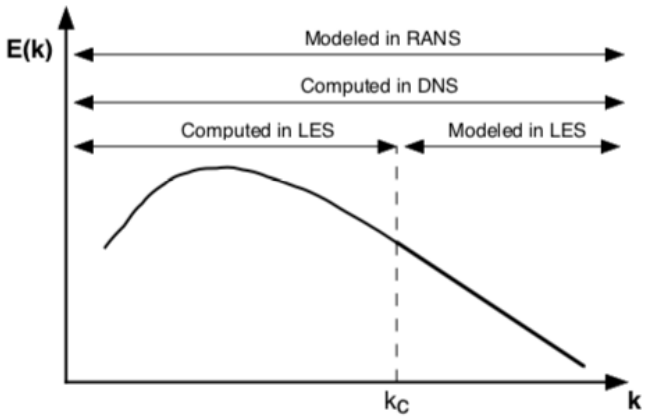

Figure 2.2 – *Turbulence energy spectrum plotted as a function of wave numbers. RANS, LES and DNS are summarised in terms of spatial frequency range. k_c is the cut-off wave number used in LES (log-log diagram) (Poinsot and Veynante, 2012).*

Equation 2.7 is useful to estimate the cost of the simulation for the specific application. For example, for the Sandia D flame three-dimensional flow at $\mathrm{Re}_L = 22400$ (Barlow and Frank, 2007), the resolution of the entire spectrum requires at least $\mathrm{Re}_L^{9/4} = 6.1$ billions grid points which is definitely impracticable with the present computational resources.

Inside the inertial range it is possible to define an inertial sub-range at which the eddies are significantly affected by the viscosity. The characteristic length of those scales is defined as the Taylor length microscale $\lambda_{\mathrm{Taylor}}$ (Tennekes, 1972). Its size can be computed from the turbulent Reynolds number, based on the integral length scale l_t and its corresponding turbulent velocity fluctuations u' (van Beeck and Benocci, 2014):

$$\lambda_{\mathrm{Taylor}} \approx L\sqrt{15/\mathrm{Re}_t} \tag{2.9}$$

where Re_t is the turbulent Reynolds number:

$$\mathrm{Re}_t = \frac{u' l_t}{\nu} \tag{2.10}$$

2.1.1 Computational approaches for turbulent flows

The approaches adopted to simulate turbulent flows differ in term of length scale modelling as shown in figure 2.2.

- **Direct Numerical Simulation DNS** consists in solving the Navier-Stokes equations directly. In principle, this is a good idea but, in practice, the computational time can be exorbitant, especially if one attempts to simulate flows of industrial interest. A further difficulty is

that of generating the initial and the boundary conditions required to define the problem completely.

- **Large Eddy Simulation LES** computes the behaviour of the large scales explicitly but models the effect of the small scales on them. In order to obtain the equations for the larger scales, the equations are filtered;

- **Reynolds averaged Navier-Stokes Simulation RANS** is the most commonly used approach to predict turbulent flows. The Reynolds averaging operation is based on the idea of decomposing the flow into a mean flow and a turbulent fluctuation. This technique is appropriate steady flows where the controlling conditions does not change in time.

2.2 Diffusion flames

For finite rate chemistry, the flow effects on the diffusion flame structure can be quantified with the Damköhler number (Poinsot and Veynante, 2012) Da^{fl}, which is defined as the ratio between the flow τ_f and chemical time scale τ_c:

$$\mathrm{Da}^{fl} = \frac{\tau_f}{\tau_c} \tag{2.11}$$

In order to define the flow time τ_f, it is common practice to refer to the scalar dissipation rate, which measures the mixture fraction gradients and it is directly related to the strain rate. The idea is to consider τ_f as a mixing time scale so it can be estimated as the inverse of the scalar dissipation rate at stoichiometric position: $\tau_f \approx 1/\chi_{st}$.
Several expressions of the Damköhler number for diffusion flames Da^{fl} can be found in literature from he asymptotic analysis (Liñán, 1974; Cuenot and Poinsot, 1996; Vervisch and Poinsot, 1998). For example, the most relevant form, relies the Da^{fl} to the fuel Y_F^0 and oxidizer Y_O^0 mass fraction in the fuel and oxidizer stream respectively and to the scalar dissipation rate at stoichiometric point χ_{st} (Poinsot and Veynante, 2012):

$$\mathrm{Da}^{fl} = f\left(Y_F^0, Y_O^0, \chi_{st}\right) \tag{2.12}$$

This quantity is useful to estimate the quenching of the flame due to the strain. In order to develop models for diffusion flames, it becomes necessary to identify combustion regimes that characterise the flame. Compared to the premixed flame, the description in diffusion flames is more complex since the length scales varies with time and space.
Unfortunately, the thickness of a non-premixed flame is not constant, and it depends on the flow motions. However, a reference flame thickness can be

	Length scale	Velocity scale
Flame	$\delta_i = (1/\lvert\nabla z\rvert)_{z=z_{st}}$	δ_i/τ_c
Vortex	r	u'
Ratio	r/δ_i	$u'\tau_c/\delta_i$

Table 2.1 – *Characteristic length and velocity scaled introduced to analyse DNS flame/vortex interaction (Poinsot and Veynante, 2012)*

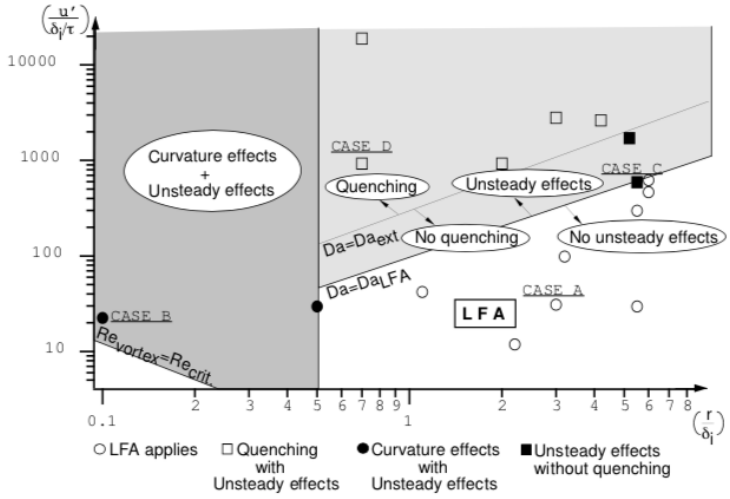

Figure 2.3 – *Laminar diffusion flame/vortes interaction spectral log-log diagram. Regime plotted versus velocity and length scale ratios refined in table 2.1 (Cuenot and Poinsot, 1994)*

estimated as (Cuenot and Poinsot, 1994):

$$\delta_i = \left(\frac{1}{|\nabla z|}\right)_{z=z_{st}} = \sqrt{\frac{2D_{st}}{\chi_{st}}} \tag{2.13}$$

where χ_{st} is the scalar dissipation rate at the stoichiometric position $z = z_{st}$ and D_{st} is the molecular diffusion coefficient at the stoichiometric value. A chemical time scale τ_c can be defined from asymptotic theories (Liñán, 1974; Cuenot and Poinsot, 1996; Vervisch and Poinsot, 1998).

$$\tau_c = \frac{1}{\chi_{st}\mathrm{Da}^{fl}} \tag{2.14}$$

When dealing with flame vortex interaction, a reference flame velocity can be computed as $u_f = \delta_i/\tau_c$. By considering r, the characteristic size of the vortex and u' the characteristic velocity, a length scale ratio and a velocity ratio can be defined respectively as r/δ_i and u'/u_f.

In table 2.1 the characteristic length scales r/δ_i and velocity scales $u'\tau_c/\delta_i$ for a diffusion flame are listed.
The flame vortex interaction regime is represented in a log-log diagram based on the velocity and length scale ratios as shown in figure 2.3. Two characteristic lines can be identified:

- a constant Damköhler number Da, comparing vortex and chemical times:

$$\mathrm{Da} = \frac{r/u'}{\tau_c} = \frac{r}{\delta_i}\left(\frac{u'}{\delta_i/\tau_c}\right)^{-1} \tag{2.15}$$

  which corresponds to a line of slope +1 in a log-log diagram

- a vortex Reynolds number defined as:

$$\mathrm{Re}_{\mathrm{vortex}} = \frac{u'r}{\nu} = \frac{\tau_d}{\tau_c}\left(\frac{u'}{\delta_i/\tau_c}\right)\left(\frac{r}{\delta_i}\right) \tag{2.16}$$

  where $\tau_d = \delta_i^2/\nu$ is the diffusion time. Constant vortex Reynolds number correspond to lines of slopes -1.

In a work of Cuenot and Poinsot (1994), a two-dimensional direct numerical simulation has been performed to investigate the interaction between a vortex and the laminar diffusion flame front.
Figure 2.3 show various regimes that can be identified and analysed. Four typical situations result from DNS with two transition Damköhler numbers ($\mathrm{Da}_{\mathrm{LFA}}$ and $\mathrm{Da}_{\mathrm{ext}}$):

- for sufficiently large Damköhler numbers ($\mathrm{Da} > \mathrm{Da}_{\mathrm{LFA}}$), the flame front behaves like a laminar flame element with the same scalar dissipation rate, so the steady laminar flamelet assumption (LFA) can be adopted (case A in figure 2.3);

- for small length scale ratio, a strong curvature of the flame front is remarked and the heat and molecular diffusion along the tangential direction to the flame front are not negligible anymore (case B in figure 2.3);

- for sufficiently large length scale and by decreasing the Damköhler number (increasing the vortex speed u') to a certain value ($\mathrm{Da}_{\mathrm{ext}} < \mathrm{Da} < \mathrm{Da}_{\mathrm{LFA}}$), the chemical time is no more negligible compared to the time of the vortex, so the chemistry is not able to instantaneously follow the flow changes as in LFA. Unsteady effects can be observed (case C in figure 2.3);

- when the turbulent velocity further increases, induces a strain on the

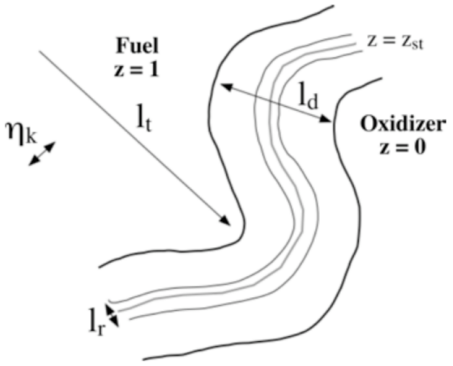

Figure 2.4 – *Characteristical length scales in turbulent non-premixed combustion (Poinsot and Veynante, 2012)*

flame front that becomes too strong ($\mathrm{Da} < \mathrm{Da}_{\mathrm{ext}}$) and quenching occurs (case D in figure 2.3).

2.2.1 Combustion turbulent diffusion flames regimes

The characterisation of the turbulent combustion regimes can be done only with the identification of reference length scales. For homogeneous and isotropic turbulence, the scales considered are the integral length scale l_t and the Kolmogorov scales η_k. Two main length scales characterise the flame front of a non-premixed flame:

- the diffusion layer thickness l_d, defined as the thickness of the zone of variation of the mixture fraction ($0 < z < 1$). In mixture fraction space the thickness is $\Delta z = 1$
- the reaction zone thickness l_r which corresponds to the region where the reaction rate is non zero. In mixture fraction space this layer has thickness Δz_r and it lies around the stoichiometric iso-surface z_{st}

Unlike for the premixed flame, those quantities are not constant and depend on time and flow conditions, and can vary independently.
However, a local laminar diffusive layer thickness can be always estimated with Eq. 2.13. By extending this analysis to turbulent non-premixed flames the diffusive layer thickness, can be computed as:

$$l_d \approx \sqrt{D_{\mathrm{st}}/\tilde{\chi}_{\mathrm{st}}} \tag{2.17}$$

where $\tilde{\chi}_{\mathrm{st}}$ is defined as:

$$\bar{\rho}\tilde{\chi}_{\mathrm{st}} = 2\left(\overline{\rho D \left|\nabla z\right|^2 | z_{\mathrm{st}}}\right) \tag{2.18}$$

	Thickness	Time	Reference velocity
Diffusive layer	$l_d \approx \sqrt{D_{\rm st}/\tilde{\chi}_{\rm st}}$	$\tau_f \approx 1/\tilde{\chi}_{\rm st} = l_d^2/D_{\rm st}$	l_d/τ_f
Reactive layer	$l_r = l_d({\rm Da}^{fl})^{-1/a}$	$\tau_c = 1/({\rm Da}^{fl}\tilde{\chi}_{\rm st})$	l_r/τ_c

Table 2.2 – *Characteristic length scales in turbulent non-premixed flame.* $Da^{fl} = (\tau_c\tilde{\chi}_{st})^{-1}$ *(Poinsot and Veynante, 2012).*

where $(\overline{Q|z_{\rm st}})$ denotes a conditional average of Q on the stoichiometric surface $z = z_{\rm st}$.
The mean scalar dissipation rate $\tilde{\chi}_{\rm st}$ is generally unknown. By assuming that the turbulent motion controls the flame structure, the local diffusion layer can be viewed as a steady constant density diffusion layer, and $\tilde{\chi}$ and $\tilde{\chi}_{\rm st}$ can be directly related (Poinsot and Veynante, 2012).
The knowledge of $\tilde{\chi}_{\rm st}$ can be used to estimate a diffusion time scale τ_f:

$$\tau_f \approx (\tilde{\chi}_{\rm st})^{-1} \tag{2.19}$$

Then the local flame Damköhler number is:

$${\rm Da}^{fl} = \tau_f/\tau_c \approx (\tilde{\chi}_{\rm st}\tau_c)^{-1} \tag{2.20}$$

Furthermore, with asymptotic theories, a reactive layer thickness l_r can be related to the diffusive thickness l_d and the Damköhler number. For a single step chemical reaction of fuel F and oxidizer O as $\nu_F\ F\ +\ \nu_O O\ \longrightarrow\ P$ (Liñán, 1974):

$$l_r/l_d \approx \left({\rm Da}^{fl}\right)^{-1/a} \tag{2.21}$$

where $a = \nu_F + \nu_O + 1$. The higher is the Damköhler number, the thinner is the reaction zone
In order to describe the non-premixed turbulent flame regimes, further assumptions have to be done. The classification is possible by comparing the chemical time τ_c with a turbulent time which has to be identified. By assuming homogeneous isotropic turbulence, the maximum strain rates and the shortest turbulent time depend on the Kolmogorov scale. The diffusive thickness l_d and the time $1/\tilde{\chi}_{\rm st}$ are assumed to be constant and controlled by the Kolmogorov motions of size η_k and time τ_k so:

$$l_d \approx \eta_k \qquad \text{and} \quad \tau_f = (\tilde{\chi}_{\rm st})^{-1} \approx \tau_k \tag{2.22}$$

At the Kolmogorov scales, the Reynolds number is one, so:

$$\frac{\eta_k u_k}{D_{\rm st}} = \frac{\eta_k^2}{D_{\rm st}\tau_k} = \frac{l_d^2}{D_{\rm st}\tau_f} = 1 \tag{2.23}$$

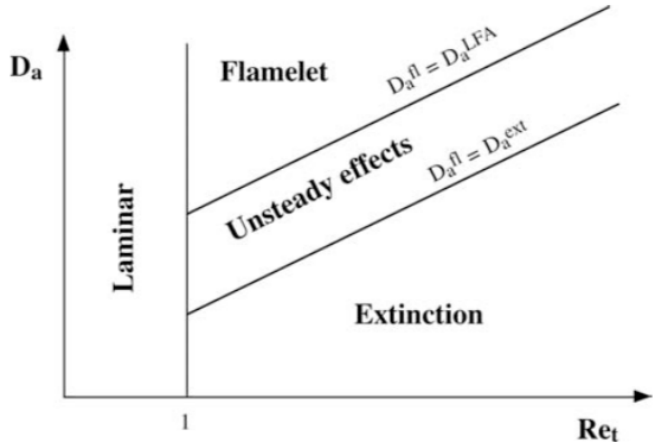

Figure 2.5 – *Regimes for turbulent non-premixed combustion as a function of the Damköhler number $Da = \tau_t/\tau_c$ (based on the turbulence integral time scale τ_t and chemical time scale τ_c) and turbulent Reynolds number $Re_t = u' l_t/\nu$ (Poinsot and Veynante, 2012). The line $Da = Da^{LFA}$ represent the lower limit for which the flame is expected to have laminar flame structure, while the line $Da = Da^{ext}$ is the limit of the extinction.*

The integral length scale l_t is the order of the mean mixing zone thickness l_z estimated from the mean mixture fraction gradient:

$$l_t \approx l_z \approx (|\nabla \tilde{z}|)^{-1} \tag{2.24}$$

The combustion regime and the flame structure depend on the chemical time scale τ_c. As shown in figure 2.5 for fast chemistry (low τ_c and large Da), the flame is sufficiently thin ($l_r << l_d \approx \eta_k$) to be identified to a laminar flame element ("flamelet"). For larger values of chemical time τ_c the reaction thickness l_r becomes of the same of order of the Kolmogorov scale η_k and unsteady effects are expctected, and by further increasing τ_c (Da decreasing) extinction takes place.
By considering the integral time scale τ_t, the Damköhler number can be recast as function of the local flame Damköhloer number Da^{fl} and the turbulent Reynolds number Re_t (Poinsot and Veynante, 2012):

$$\mathrm{Da} = \frac{\tau_t}{\tau_c} = \frac{\tau_t}{\tau_k}\frac{\tau_k}{\tau_c} \approx \frac{\tau_t}{\tau_k}\frac{2}{\tilde{\chi}_{\mathrm{st}}\tau_c} \approx 2\sqrt{\mathrm{Re}_t}\,\mathrm{Da}^{fl} \tag{2.25}$$

Constant local laminar Damköhler number Da^{fl} correspond to lines of slope 1/2 in a log-log (Da,Re_t) diagram. According to Cuenot and Poinsot (1994), for $\mathrm{Da}^{fl} \geq \mathrm{Da}^{LFA}$ the flame is expected to have laminar flame structure (LFA) and extinction occurs for large chemical times ($\mathrm{Da}^{fl} \geq \mathrm{Da}^{\mathrm{ext}}$).
The diagram depicted in figure 2.5 should be carefully used for several reasons.

First, because the local flame thickness depends on the local flow conditions such as local strain rates and can be affected by unsteady effects. Then the local diffusion thickness l_d and time τ_f are supposed to be controlled by the Kolmogorov length scales, but this assumption needs to be validated. In the literature, several diagrams are present, and they introduce various parameters such as the scalar dissipation rate or the mixture fraction variance $\widetilde{z''^2}$ (Borghi, 1988; Peters, 2000).

2.3 Large Eddy Simulation formulation

The present work is based on the flame modeling in the context of Large Eddy Simulation, which consists in resolve the filtered equation of the flow field. LES are based on the use of filtering operation: a filtered (or resolved, or large-scale) variable, denoted by an overbar, is defined as (Leonard, 1975):

$$\bar{f}(\mathbf{x}) = \int_\Omega f(\mathbf{x}')G(\mathbf{x},\mathbf{x}',\Delta)d\mathbf{x}' \qquad \text{with} \qquad \int_\Omega G(\mathbf{x},\mathbf{x}',\Delta)d\mathbf{x}' = 1 \quad (2.26)$$

where Ω is the entire domain and G is the spatial filter function. The filter function determines the size and the structure of the small scales. The size of the smallest eddies is related to the filter width Δ. In order to accurately represent the eddies, the grid size h should be sufficiently fine. The filter width Δ is a key factor in modelling the unresolved stresses, and the determination of a proper value have been largely discussed in literature (McMillan and Ferziger, 1979; Ghosal, 1996; Geurts and Fröhlich, 2002; Meyers et al., 2005).
The most commonly-used filter functions are

- the sharp Fourier cutoff filter, defined in the wavenumber space[1]:

$$\hat{G}(k) = \begin{cases} 1 \text{ if } k \leq \pi/\Delta \\ 0 \text{ if otherwise} \end{cases} \quad (2.27)$$

- the Gaussian filter,

$$G(\mathbf{x}) = \left(\frac{6}{\pi\Delta}\right)^{\frac{3}{2}} \exp\left(-\frac{6\mathbf{x}^2}{\Delta^2}\right) \quad (2.28)$$

- and the top-hat filter in the real space:

$$G(\mathbf{x}) = \begin{cases} 1/\Delta^3 & \text{if } |\mathbf{x}| \leq \Delta/2 \\ 0 & \text{otherwise} \end{cases} \quad (2.29)$$

[1] in thie case, the quantity denoted by a caret $\hat{.}$ is the complex Fourier coefficient of the original quantity

The filtered quantity $\bar{f}$ represent the resolved turbulent structures. The contribution of the non resolved structures are:

$$f'(\mathbf{x},t) = f(\mathbf{x},t) - \overline{f(\mathbf{x},t)} \tag{2.30}$$

To account for density fluctuations, the density weighted Favre-filtering is adopted (Favre, 1969):

$$\bar{\rho}\tilde{f}(\mathbf{x}) = \int \rho f(\mathbf{x}')G(\mathbf{x}-\mathbf{x}')d\mathbf{x}' \qquad \text{or} \qquad \tilde{f} = \frac{\overline{\rho f}}{\bar{f}} \tag{2.31}$$

However, several other filters can be found in literature (Lele, 1992; Lund, 1999; Vasilyev et al., 1998; Haselbacher and Vasilyev, 2003). It is important to note that a priori:

$$\bar{\bar{f}} \neq \bar{f} \qquad \text{and} \qquad \overline{f'} \neq 0 \tag{2.32}$$

2.4 Filtered equation for reactive flows

The balance equations for large simulations are obtained by filtering the instantaneous balance equations 1.13-1.15:

$$\frac{\partial\left(\bar{\rho}\tilde{u}_i\right)}{\partial t} + \frac{\partial}{\partial x_j}\left(\bar{\rho}\tilde{u}_i\tilde{u}_j\right) + \frac{\partial}{\partial x_j}\bar{\rho}\left(\widetilde{u_iu_j} - \tilde{u}_i\tilde{u}_j\right) = -\frac{\partial\bar{P}\delta_{ij}}{\partial x_j} + \frac{\partial\bar{\tau}_{ij}}{\partial x_j} \tag{2.33}$$

$$\frac{\partial\bar{\rho}\tilde{E}}{\partial t} + \frac{\partial}{\partial x_j}\left(\bar{\rho}\tilde{u}_j\tilde{E}\right) + \frac{\partial}{\partial x_j}\bar{\rho}(\widetilde{u_jE} - \tilde{u}_j\tilde{E}) = -\frac{\partial}{\partial x_j}\left[\overline{u_i\left(P\delta_{ij}-\tau_{ij}\right)} + \bar{q}_j\right] + \bar{\dot{\omega}}_T \tag{2.34}$$

$$\frac{\partial\bar{\rho}\tilde{Y}_k}{\partial t} + \frac{\partial}{\partial x_j}\left(\bar{\rho}\tilde{Y}_k\tilde{u}_j\right) + \frac{\partial}{\partial x_j}\bar{\rho}\left(\widetilde{u_jY_k} - \tilde{u}_j\tilde{Y}_k\right) = -\frac{\partial\bar{J}_{j,k}}{\partial x_j} + \bar{\dot{\omega}}_k \tag{2.35}$$

which in vector notation is:

$$\frac{\partial\bar{\mathbf{w}}}{\partial t} + \nabla\cdot\bar{\mathbf{F}} = \bar{\mathbf{s}} \tag{2.36}$$

with $\bar{\mathbf{w}} = (\rho\tilde{u}, \rho\tilde{v}, \bar{\rho}\tilde{w}, \rho\tilde{E}, \rho\tilde{Y}_k)^T$ being the state vector, $\bar{\mathbf{s}}$ is the filtered source terms. $\bar{\mathbf{F}}$ is the flux vector that can be divided in three parts: the resolved inviscid part $\bar{\mathbf{F}}^I$, the viscous part $\bar{\mathbf{F}}^V$ and the sub-grid scale turbulent part $\bar{\mathbf{F}}^{\mathrm{SGS}}$. The effect of the unresolved scales on the resolved field are unknown and they need to be modelled, namely:

- **Unresolved Reynolds stresses** $\bar{\tau}^{\mathrm{sgs}_{ij}} = \bar{\rho}(\widetilde{u_iY_k} - \tilde{u}_i\tilde{Y}_k)$, which represents the impact of the unresolved motions on the resolved ones.

- **Unresolved species fluxes** $\bar{J}_{j,k}^{\text{sgs}} = \bar{\rho}(\widetilde{u_i Y_k} - \tilde{u}_i \tilde{Y}_k)$
- **Unresolved energy fluxes** $\bar{q}_i^{\text{sgs}} = \bar{\rho}(\widetilde{u_i E} - \tilde{u}_i \tilde{E})$
- **Filtered species and heat diffusion fluxes** $\bar{J}_{j,k}$ in the species equation and $\bar{q}_j$ in the energy equation.
- **Filtered chemical reaction rates** $\bar{\dot{\omega}}_k$

Inviscid terms

The three spatial components of the inviscid flux tensor are the same as in DNS, but based on the filtered quantities:

$$\bar{\mathbf{f}^I} = \begin{pmatrix} \bar{\rho}\tilde{u}^2 + \bar{P} \\ \bar{\rho}\tilde{u}\tilde{v} \\ \bar{\rho}\tilde{u}\tilde{w} \\ \bar{\rho}\tilde{E}\tilde{u} + \overline{Pu} \\ \bar{\rho}\tilde{Y}_k\tilde{u} \end{pmatrix} \tag{2.37}$$

$$\bar{\mathbf{g}^I} = \begin{pmatrix} \bar{\rho}\tilde{u}\tilde{v} \\ \bar{\rho}\tilde{u}\tilde{v}^2 + \bar{P} \\ \bar{\rho}\tilde{v}\tilde{w} \\ \bar{\rho}\tilde{E}\tilde{v} + \overline{Pv} \\ \bar{\rho}\tilde{Y}_k\tilde{v} \end{pmatrix} \tag{2.38}$$

$$\bar{\mathbf{h}^I} = \begin{pmatrix} \bar{\rho}\tilde{u}\tilde{v} \\ \bar{\rho}\tilde{v}\tilde{w} \\ \bar{\rho}\tilde{w}^2 + \bar{P} \\ \bar{\rho}\tilde{E}\tilde{w} + \overline{Pw} \\ \bar{\rho}\tilde{Y}_k\tilde{w} \end{pmatrix} \tag{2.39}$$

Viscous terms

The components of the viscous flux tensor is:

$$\bar{\mathbf{f}^V} = \begin{pmatrix} -\bar{\tau}_{xx} \\ -\bar{\tau}_{xy} \\ -\bar{\tau}_{xz} \\ -(\overline{u\tau_{xx}} + \overline{v\tau_{xy}} + \overline{w\tau_{xz}}) + \bar{q}_x \\ \bar{J}_{x,k} \end{pmatrix} \tag{2.40}$$

$$\mathbf{g}^{\bar{V}} = \begin{pmatrix} -\bar{\tau}_{xy} \\ -\bar{\tau}_{yy} \\ -\bar{\tau}_{yz} \\ -(\overline{u\tau_{xz}} + \overline{v\tau_{yz}} + \overline{w\tau_{yz}}) + \bar{q}_y \\ \bar{J}_{y,k} \end{pmatrix} \tag{2.41}$$

$$\mathbf{h}^{\bar{V}} = \begin{pmatrix} -\bar{\tau}_{xz} \\ -\bar{\tau}_{yz} \\ -\bar{\tau}_{zz} \\ -(\overline{u\tau_{xz}} + \overline{v\tau_{yz}} + \overline{w\tau_{zz}}) + \bar{q}_z \\ \bar{J}_{z,k} \end{pmatrix} \tag{2.42}$$

Filtered stress tensor

The filtered stress tensor $\bar{\tau}_{ij}$ is modelled as (Boussinesq, 1877):

$$\bar{\tau}_{ij} = \overline{2\mu\left(S_{ij} - \frac{1}{3}\delta_{ij}S_{ll}\right)} \approx 2\bar{\mu}\left(\tilde{S}_{ij} - \frac{1}{3}\delta_{ij}\tilde{S}_{ll}\right) \tag{2.43}$$

with $\bar{\mu} \approx \mu\left(\tilde{T}\right)$ and the filtered strain rate tensor:

$$\tilde{S}_{ij} = \frac{1}{2}\left(\frac{\partial \tilde{u}_j}{\partial x_i} + \frac{\partial \tilde{u}_i}{\partial x_j}\right) \tag{2.44}$$

Diffusive species flux

The diffusive is written:

$$\bar{J}_{i,k} = \overline{-\rho\left(D_k\frac{W_k}{W}\frac{\partial X_k}{\partial x_i} - Y_k V_i^c\right)} \approx -\bar{\rho}\left(\bar{D}_k\frac{W_k}{W}\frac{\partial \tilde{X}_k}{\partial x_i} - \tilde{Y}_k\tilde{V}_i^c\right) \tag{2.45}$$

with $\bar{D}_k = \bar{\mu}/(\bar{\rho}\mathrm{Sc}_k)$ and $\tilde{V}_i^c = \sum_{k=1}^{N} \bar{D}_k\frac{W_k}{W}\frac{\partial \tilde{X}_k}{\partial x_i}$

Heat flux

The heat flux term $\bar{q}_i$:

$$\bar{q}_i = -\overline{\frac{\partial T}{\partial x_i}} + \sum_{k=1}^{N}\overline{J_{i,k}h_{sk}} \approx -\frac{\partial \tilde{T}}{\partial x_i} + \sum_{k=1}^{N}\bar{J}_{i,k}\tilde{h}_{sk} \tag{2.46}$$

with $\bar{\lambda} \approx \bar{\mu}\bar{C}_p(\tilde{T})/\mathrm{Pr}$

Sub-grid scale turbulent terms

The filtering operation of the balance equation leads to unclosed quantities to be modelled. So the sub-grid scale flux takes the form of:

$$\bar{\mathbf{f}}^{\mathrm{SGS}} = \begin{pmatrix} \bar{\tau}_{xx}^{\mathrm{sgs}} \\ \bar{\tau}_{xy}^{\mathrm{sgs}} \\ \bar{\tau}_{xz}^{\mathrm{sgs}} \\ \bar{q}_{x}^{\mathrm{sgs}} \\ \bar{J}_{x,k}^{\mathrm{sgs}} \end{pmatrix} \tag{2.47}$$

$$\bar{\mathbf{g}}^{\mathrm{SGS}} = \begin{pmatrix} \bar{\tau}_{xy}^{\mathrm{sgs}} \\ \bar{\tau}_{yy}^{\mathrm{sgs}} \\ \bar{\tau}_{yz}^{\mathrm{sgs}} \\ \bar{q}_{y}^{\mathrm{sgs}} \\ \bar{J}_{y,k}^{\mathrm{sgs}} \end{pmatrix} \tag{2.48}$$

$$\bar{\mathbf{h}}^{\mathrm{SGS}} = \begin{pmatrix} \bar{\tau}_{xz}^{\mathrm{sgs}} \\ \bar{\tau}_{yz}^{\mathrm{sgs}} \\ \bar{\tau}_{zz}^{\mathrm{sgs}} \\ \bar{q}_{z}^{\mathrm{sgs}} \\ \bar{J}_{z,k}^{\mathrm{sgs}} \end{pmatrix} \tag{2.49}$$

The different terms modeled in turn as following:

Reynolds tensor

$$\bar{\tau}_{ij}^{\mathrm{sgs}} = \bar{\rho}(\widetilde{u_i u_j} - \tilde{u}_i \tilde{u}_j) \approx -2\bar{\rho}\nu_{\mathrm{sgs}} \left(\tilde{S}_{ij} - \frac{1}{3}\delta_{ij}\tilde{S}_{kk} \right) \tag{2.50}$$

where ν_{sgs} is the so called sub-grid turbulent viscosity. Its modelling is explained in details in the following section;

Sub-grid scale diffusive species flux vector

$$\bar{J}_{i,k}^{\mathrm{sgs}} = \bar{\rho}\left(\widetilde{u_i Y_k} - \tilde{u}_i \tilde{Y}_k\right) \approx -\bar{\rho}\left(D_k^{\mathrm{sgs}} \frac{W_k}{W} \frac{\partial \tilde{X}_k}{\partial x_i} - \tilde{Y}_k \tilde{V}_i^{c,t} \right) \tag{2.51}$$

with $D_k^{\mathrm{sgs}} = \nu_{\mathrm{sgs}}/\mathrm{Sc}_k^t$. Usually the turbulent Schmidt number is assumed to be the same for all the species. The correction diffusion turbulent velocity is written as:

$$\tilde{V}_i^{c,t} = \sum_{k=1}^{N} \frac{\nu_{\mathrm{sgs}}}{\mathrm{Sc}_k^t} \frac{W_k}{W} \frac{\partial \tilde{X}_k}{\partial x_i} \tag{2.52}$$

sub-grid scale heat flux vector

$$\bar{q}_i^{\text{sgs}} = \bar{\rho}\left(\widetilde{u_i E} - \tilde{u}_i\tilde{E}\right) \approx -\lambda_{\text{sgs}}\frac{\partial\tilde{T}}{\partial x_i} + \sum_{k=1}^{N}\bar{J}_{i,j}^{\text{sgs}}\tilde{h}_{sk} \tag{2.53}$$

with $\lambda_{\text{sgs}} = \mu_{\text{sgs}}\bar{C}_p(\tilde{T})/\text{Pr}^t$. The turbulent Prandtl number is set to $\text{Pr}^t = 0.6$

2.5 LES models for sub-grid stress tensor

The sub-grid scale (SGS) tensors and vectors describe the interaction between the resolved and unresolved structures. The interaction between the resolved and the unresolved structures of the flow is described by the sub-grid scale (SGS) tensor and vectors. The momentum transfer caused by the turbulent eddies is modelled with an eddy viscosity model with the Bussinesq assumption. Equation 2.50 can be written as

$$\bar{\tau}_{ij}^{\text{sgs}} - \frac{1}{3}\bar{\tau}_{ll}^{\text{sgs}}\delta_{ij} = -\bar{\rho}\nu_{\text{sgs}}\left(\frac{\partial\tilde{u}_i}{\partial x_j} + \frac{\partial\tilde{u}_j}{\partial x_i} - \frac{2}{3}\delta_{ij}\frac{\partial\tilde{u}_k}{\partial x_k}\right) = -2\bar{\rho}\nu_{\text{sgs}}\left(\tilde{S}_{ij} - \frac{1}{3}\delta_{ij}\tilde{S}_{kk}\right) \tag{2.54}$$

$\tilde{S}_{ij}$ being the strain rate of the resolved structures. Many models are available in literature for the turbulent viscosity ν_{sgs} (also indicated with ν_T) (Piomelli, 1999; Garnier et al., 2009; Pope, 2000), however, the following description will limited to the ones used in the present work.

2.5.1 Smagorinsky model

The Smagorinsky model was developed for meteorological applications (Smagorinsky, 1963). The turbulent viscosity writes as:

$$\nu_{\text{sgs}} = (C_s\Delta)^2(2\tilde{S}_{ij}\tilde{S}_{ij})^{1/2} = (C_s\Delta)^2|\tilde{S}| \tag{2.55}$$

being Δ the filter characteristic length evaluated as $\Delta = (\Delta x\,\Delta y\,\Delta z)^{1/3}$, C_s is a constant usually set between 0.1 and 0.2 depending on the flow configuration. However the model is known to overpredict the amount of dissipation in anisotropic turbulent zones such as solid boundaries and mixing layers.
An improvement has been introduced by computing the resolved strain rate sensor from an high pass filtered velocity. Ducros and Marcel (1996) improved the model by computing the resolved strain rate tensor from an high pass filtered velocity field $\text{HP}(\tilde{S}_{ij})$:

$$\nu_{\text{sgs}} = (C_F\Delta)^2\sqrt{2\,\text{HP}(\tilde{S}_{ij})\,\text{HP}(\tilde{S}_{ij})}, \tag{2.56}$$

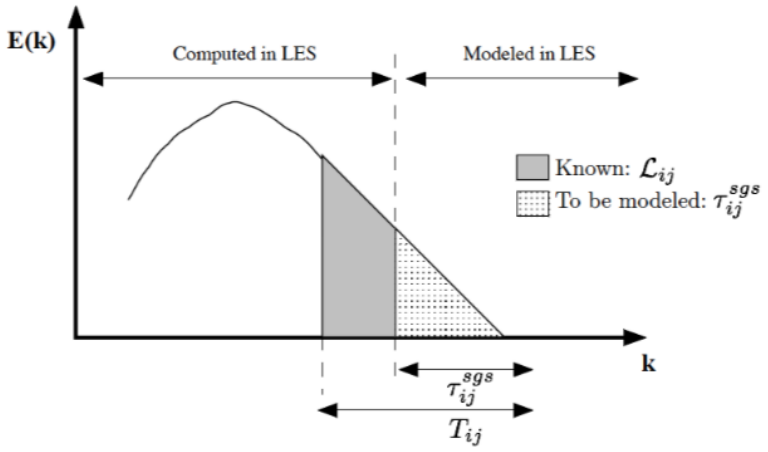

Figure 2.6 – *Graphical representation of the Germano identity in the energy spectrum. The unknown unresolved Reynolds stresses at the filter level τ_{ij}^{sgs} and at the test filter level (T_{ij}) are related through $\mathcal{L}_{ij}$ which is the LES resolved part of the unresolved Reynolds stresses T_{ij} (Poinsot and Veynante, 2012).*

2.5.2 Dynamic Smagorinsky model

The dynamic Smagorinsky formulation differ from the standard one in the fact that the model parameter C_D is no longer fixed, but determined dynamically. The idea is to estimate the small scale dissipation from the knowledge of the resolved eddies. The determination of C_D is based on the Germano identity (Germano et al., 1991) and follows the Lilly (1992)'s procedure.
A test filter $\hat{\phi}$, of width $\hat{\Delta} > \Delta$, is introduced. Numerical tests have shown that an optimal value for the test filter width is $\hat{\Delta} = 2\Delta$ (Spyropoulos and Blaisdell, 1996). The resolved turbulent stress $\mathcal{L}_{ij}$ is related to the sub-grid stress term τ_{sgs} and the sub-grid stress term at the test level $\hat{\Delta}$, T_{ij} as (fig. 2.6):

$$\mathcal{L}_{ij} = T_{ij} - \tau_{ij}^{\text{sgs}} \tag{2.57}$$

where

$$T_{ij} = \widehat{\overline{\rho u_i u_j}} - \widehat{\overline{\rho u_i}}\,\widehat{\overline{\rho u_j}}/\hat{\bar{\rho}} \tag{2.58}$$

$$\mathcal{L}_{ij} = \widehat{\overline{\rho}\tilde{u}_i\tilde{u}_j} - \widehat{\overline{\rho}\tilde{u}_i}\,\widehat{\overline{\rho}\tilde{u}_i}/\hat{\bar{\rho}} \tag{2.59}$$

By assuming that the two sub-grid tensor τ_{ij}^{sgs} and T_{ij} can be modelled with the same constant C_D for both filter levels, according to the Smagorinsky model they can be expressed as:

$$\tau_{ij}^{\text{sgs}} - \frac{\delta_{ij}}{3}\tau_{kk}^{\text{sgs}} = -2C_D\Delta^2|\tilde{S}|\left(\tilde{S}_{ij} - \tfrac{1}{3}\delta_{ij}\tilde{S}_{kk}\right) = C_D\beta_{ij} \tag{2.60}$$

$$T_{ij} - \frac{\delta_{ij}}{3}T_{kk} = -2C_D\hat{\Delta}^2|\hat{\tilde{S}}|\left(\hat{\tilde{S}}_{ij} - \tfrac{1}{3}\delta_{ij}\hat{\tilde{S}}_{kk}\right) = C_D\alpha_{ij} \tag{2.61}$$

where C_D is the parameter to be determined and the tensor α_{ij} and β_{ij} are introduced to simplify the notation. So the Germano identity is finally written

as:

$$L_{ij}^D = L_{ij} - \frac{\delta_{ij}}{3} L_{kk} = C_D \alpha_{ij} - \widehat{C_D \beta_{ij}} \tag{2.62}$$

assuming that C_D is constant over the interval at least equal to the test filter width, $\widehat{C_D \beta_{ij}} = C_D \hat{\beta_{ij}}$. However, this definition consists in six independent relations, which give in turn six values of the constant. So the model parameter is retrieved minimizing the error (Lilly, 1992):

$$E_{ij} = L_{ij}^D - C_D \alpha_{ij} + C_D \hat{\beta_{ij}} \tag{2.63}$$

2.6 Chemistry modelling in LES

One of the primary difficulties for large-eddy simulation in combustion is integrating the chemistry information into the flow solver. The description of chemical reactions at the molecular level is possible only with detailed mechanisms that include a large number of species and reactions. Manipulating such complex mechanisms becomes costly from a computational perspective since an extra equation has to be solved for each species. Then the chemical reaction rates and the transport coefficients are functions of species mass fractions and temperature.

A detailed mechanism can quickly involve hundreds of reactions. For example, the simple reaction of methane-air like the GRI mechanism involves 325 reactions for 53 species, and it accurately performs over the ranges 1000-2500K of temperature, 1.0-1000 kPa of pressure, and equivalence ratios from 0.1 to 5 for premixed systems (Smith et al., 1999). In long hydrocarbons, the number of unknowns further rises. For example, a detailed kerosene-air mechanism by Dagaut and Cathonnet (2006) comprises 206 species and 1673 reversible reactions. Detailed mechanisms are suited to predict auto-ignition and simple planar laminar flows. So many mechanisms to describe the combustion of alkanes, alkynes, and aromatics can be found in literature (Simmie, 2003).

Several techniques have been formulated to reduce those mechanisms. For example, by eliminating reactions and species in a detailed mechanism, it is possible to obtain skeletal mechanisms. Useful methods of reduction are the systematic reaction rate analysis (Nagy and Turányi, 2009), the Jacobian analysis (Tomlin et al., 1997), theory of directed relation graph (Lu and Law, 2005), the singular perturbation model (Massias et al., 1999; Kelley et al., 2011) and the sensitivity analysis (Warnatz et al., 1999). Although the information on the relevant species are not significantly affected and different phenomena are correctly predicted (such as ignition delay, dilution effect, response to stretch), skeletal mechanisms are still too costly for industrial 3D simulation.

Skeletal mechanisms can be further reduced. The idea behind analytical mechanisms is to reduce further the number of the species with the quasi-steady-state approximation (QSS) and the number of reactions with the partial equilibrium

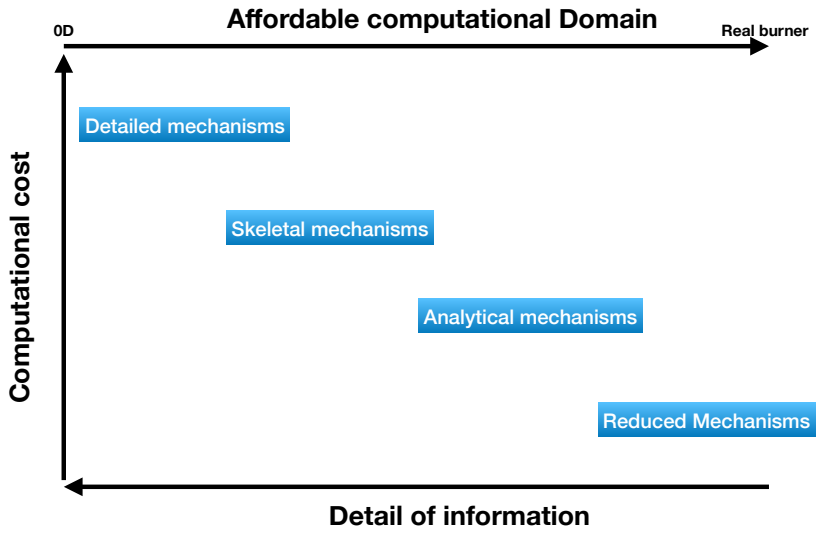

Figure 2.7 – *Summary and classification of chemical mechanisms in term of computational costs, detail of information and affordable domain.*

assumption (Li et al., 1999; Sánchez et al., 2000; Boivin et al., 2011). Examples of analytical schemes for methane are PETERS (Peters, 1985; Chen and Dibble, 1991; Seshadri et al., 2001) and LU (Lu and Law, 2008). This last one is composed of 13 species four quasi-species.
Within certain thermo-physical operating conditions, it is possible to use a reduced mechanism with a minimal number of species (generally around 6) and reactions (from 2 to 4). The reactions do not correspond to elementary reactions but to global reactions, calibrated to reproduce specific features of the flame such as the laminar flame speed or the burnt gas state (Jones and Lindstedt, 1988; Franzelli et al., 2010). Besides, with simple adjustments, reduced schemes can correctly predict the flame's behavior for larger ranges of operating conditions in terms of pressure, fresh gas temperature, and stoichiometry (Franzelli et al., 2010). So due to their affordable computational costs, they are widely used in large-eddy simulations. Figure 2.7 resumes the chemical mechanisms used in reacting flows. A recent strategy, proposed by Cailler et al. (Cailler et al., 2017), consists in gradually increasing the dimensionality by using virtual species whose thermodynamic properties and reaction rate parameters are optimized to reproduce the temperature profiles and the laminar flame speeds of a reference library of laminar flames.

An alternative way to reduce the computational cost of detailed chemistry is to tabulate the parameter representing the chemistry. In order to keep the CPU costs relatively low, the tabulated chemistry methods assume that the chemical evolution in the composition space can be parametrized and tabulated by a reduced set of variables, which are generally combinations of species mass fractions like $\phi_l = \sum_{k=1}^{N} \alpha_{lk} Y_k$. So with the knowledge of ϕ_l all thermo-

chemical variables can be ϕ can be so estimated using a chemical database $\phi^{\text{tab}}(\phi_1; ...; \phi_n)$.
For example, the Intrinsic Low Dimensional Manifold (IDLM) approach proposed by Maas and Pope (Maas and Pope, 1992a,b) take into account only the larger ranges of chemical time scales, where the mass fraction of a species Y_B can be expressed as a function of the species mass fraction Y_A. It provides excellent results at high temperatures close to equilibrium values, but unfortunately, the low-temperature regions are not well described. This inconvenience is not essential for steady flames where the highest temperatures mainly control reaction rates but may lead to difficulties in describing ignition, transient flow, and diffusion phenomena. Then several solutions have been proposed, like the Flame prolongation of ILDM (FPI) (Gicquel et al., 2000; Fiorina et al., 2005) or the "Flamelet generated manifold" FGM (Oijen and Goey, 2000). Those techniques' basic idea is to generate lookup tables from simulations of one-dimensional laminar flames using complex chemical schemes (Oijen and Goey, 2000; Goey et al., 2003). Other methodologies which adopt the same principles are the REDIM (Bykov and Maas, 2007) and ICE-PIC (Ren et al., 2006).
In some circumstances, generating and handling a lookup table can be difficult, and it can lead to memory problems on massively parallel machines, where the table is stored on each core. A solution is to assume the self-similarity behavior of premixed flames (Ribert et al., 2006; Wang et al., 2010) for laminar flame elements or turbulent flames (Veynante et al., 2008; Fiorina et al., 2009).
However, the thesis's scope is to examine the dynamic formulation's benefits by adopting direct chemistry for non-premixed flames.

2.7 LES models for non-premixed flames

The different modelling methodologies of flame/turbulence interaction, used for non-premixed flames, can be classified according to basic principle in flame surface, statistical and mixing formalism (Fiorina et al., 2015). Table 2.3 resumes the different approaches.

Turbulent non-premixed models for LES

Primary concepts	**Flame surface**	**Statistics**	**Mixing**
Models	- TFLES - F-TACLES	- Presumed FDF - Transported FDF - CMC	- EDC - LEM

Table 2.3 – *Summary and classification of LES models used for non-premixed flames. The classification is based on primary concepts such as pdfs, turbulent mixing and flame surface approaches. Since the latters are not able to preserve the flame surface, the flame/turbulence interaction is described through a wrinkling factor or a flame surface density*

2.7.1 Flame surface approaches

Flame surface (or geometrical) formulations, mainly conceived to capture the flame front propagation, well perform in premixed and stratified combustion regimes. Largely used for premixed flames, some of them have been extended to non-premixed configurations, namely filtered one-dimensional flames and thickened flame model. However, those kind of model are not able to predict the flame/turbulence interaction at subgrid scales, then they require an efficiency function to keep into account the wrinkling effect of the flame front at the sub-grid scales, or a transport equation for the flame surface density.

2.7.1.1 Filtered one-dimensional flame

The idea of this modelling approach is to filter the flame front to retrieve the quantities of interest. For example, the application of the LES filter to a reduced progress variable c leads to the filtered balance equation (Fiorina et al., 2015):

$$\frac{\partial \bar{\rho}\tilde{c}}{\partial t} + \nabla \cdot (\bar{\rho}\tilde{\mathbf{u}}\tilde{\psi}) + \nabla \cdot [\bar{\rho}(\widetilde{\mathbf{u}c} - \tilde{\mathbf{u}}\tilde{c})] = \overline{\nabla \cdot (\rho D \nabla c)} + \bar{\dot{\omega}}_c \tag{2.64}$$

For premixed flame, several techniques adopt filtering operation on the progress variable to retrieve the unknown terms of equation (B.17) (Boger et al., 1998; Duwig, 2007). Fiorina et al. (2010) proposed to tabulate the unclosed terms by filtering one-dimensional laminar flames derived from detailed chemistry simulations (FTACLES). Although already used in partially premixed and stratified flames (Auzillon et al., 2011, 2012), Coussement et al. (2015) extended the FTACLES technique to a laminar diffusion flame configuration, without sub-grid wrinkling effects of the flame front. In this case the progress variable c in Eq. (B.17) denotes a chemical database coordinate ψ of filtered mixture fraction $\tilde{z}$ and a progress variable[2] $\tilde{Y}_c$, where $Y_c = Y_{CO_2} + Y_{CO}$ Equation (B.17) rewrites as:

$$\frac{\partial \bar{\rho}\tilde{\psi}}{\partial t} + \nabla \cdot (\bar{\rho}\tilde{\mathbf{u}}\tilde{\psi}) = \nabla \cdot (\rho_0 D_0 \nabla \tilde{\psi}) + \alpha_\psi + \Omega_\psi + \bar{\dot{\omega}}_\psi \tag{2.65}$$

where ρ_0 and D_0 are reference values for the density and molecular diffusion coefficient, and the functions α_ψ, Ω_ψ and $\bar{\dot{\Omega}}_\psi$ are the unresolved diffusion, convective and chemical contributions. Those last terms are properly modelled in order to accurately monitor the filtered flame thickness and the filtered maximal temperature (Coussement et al., 2015). However this model has been used for a simple laminar configuration and several works are still ongoing for more complex geometries. The main difficulty is to keep into account the sub-grid scale wrinkling effects of the flame front. At present, several works are ongoing to keep into account the sub-grid scale wrinkling effects of the flame front for non-premixed flames.

[2] which depends on the case of application

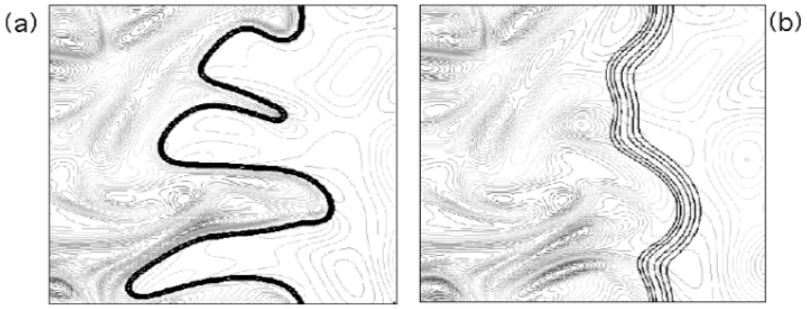

Figure 2.8 – *DNS of flame turbulence interactions. Reaction rate and vorticity fields are superimposed. (a) reference flame; (b) flame artificially thickened by a factor* $F = 5$*. Because of the change in the length scale ratio* l_t/δ_L^0*, combustion/turbulence interaction is changed and the thickened flame is less wrinkled by turbulence motions (Poinsot and Veynante, 2012).*

2.7.1.2 Artificially Thickened Flame Model TFLES

Originally designed for premixed flame by Colin et al. (2000), the TFLES model has been also used for non-premixed (Legier et al., 2000; Schmitt et al., 2007) and two-phase flames (Boileau et al., 2008a,b).
Since the thickness of the flame front happens to be smaller than the grid resolution, the idea is to artificially thicken the flame by preserving the burning laminar velocity (Butler and O'Rourke, 1977; O'Rourke and Bracco, 1979). According to simple theories of the laminar premixed flames, the flame speed S_L and the flame thickness δ_L can be expressed as (Williams, 1985):

$$S_L \propto \sqrt{D_T \dot{\omega}}\,; \qquad \delta_L \propto \frac{D_T}{S_L} \tag{2.66}$$

where D_T is the thermal diffusivity and $\dot{\omega}$ is the mean reaction rate. In practical applications, the thermal diffusivity D_T is linearly related to the mass diffusivity D.
In order to thicken the flame front the diffusivity D is multiplied by a factor F, while the flame speed is preserved by diving the reaction rate by the same factor F (Eq. 2.66). Unfortunately, thickening the flame front δ_L modifies the interaction between turbulence and chemistry (as shown in figure 2.8) since the Damköhler number decreases of a factor F (Da $= \tau_t/\tau_c$, with $\tau_c = S_L/\delta_L$). Colin et al. (2000) investigated this effect by using DNS, and they derived an efficiency function, in fact, a wrinkling factor Ξ_Δ, to counterbalance this effect. In term of formulation, the thickened flame approach consists in changing the diffusivity and the reaction rate (Colin et al., 2000; Charlette et al., 2002a) as:

$$\begin{array}{rccccc} \text{Diffusivity:} & D & \longrightarrow & FD & \longrightarrow & \Xi_\Delta FD \\ \text{Reaction rate:} & \dot{\omega} & \longrightarrow & \dot{\omega}/F & \longrightarrow & \Xi_\Delta\, \dot{\omega}/F \\ & & \text{thickening} & & \text{wrinkling} & \end{array}$$

The model has been successfully used in several configuration with different formulation for the wrinkling factor Ξ_Δ Furthermore, in order to adapt the model to partially premixed and non-premixed configuration, a flame sensor has been used, so that the thickening factor varies according to the flame position. A common expression is given by Legier et al. (2000):

$$F = 1 + (F_{max} - 1)\theta_F \tag{2.67}$$

where θ_F is a parameter between 0 and 1. A classical formulation relates the sensor θ_F to the reaction rate of the 1D premixed laminar flame with hyperbolic tangent relation (Legier et al., 2000). In the work of Legier, the model is used to simulate an experimental burner which consists in two propane steams injected through small slots into an air coflow. The model can predict the phenomenological behaviour of the flame whether it is anchored, lifted and even blow-off.
The use of TFLES in non-premixed configuration is not sustained theoretically. It is part of the present work to analyse the effect of model on a laminar diffusion flame and on a turbulent diffusion jet.

Flame wrinkling

The flame surface models described above, do not take into account the interaction between the flame and the turbulence at subgrid scales. So, as mentioned before, it becomes necessary to couple the model with a wrinkling factor Ξ_Δ or a flame surface density Σ. Those quantities can be deduced from:

- Algebraic expression, these formulations rely on the equilibrium assumption between flame wrinkling and turbulent fluctuations, which is often not valid for early flame developments. Examples of algebraic formulations are given by Colin et al. (2000); Charlette et al. (2002a) or Gouldin (1987)[3].

- Similarity assumption, they take advantage of the knowledge of the resolved scales (Knikker et al., 2002)

- Balance equations for the flame surface density (Boger et al., 1998; Hawkes and Cant, 2000; Richard et al., 2007) Σ , or the wrinkling factor Ξ (Weller et al., 1998)

- Dynamic modelling, where the model parameters entering algebraic expressions are automatically adjusted during the simulation from the knowledge of the resolved flow field. These last strategies are largely treated in the following chapter.

[3]this last derived an expression from a fractal analysis

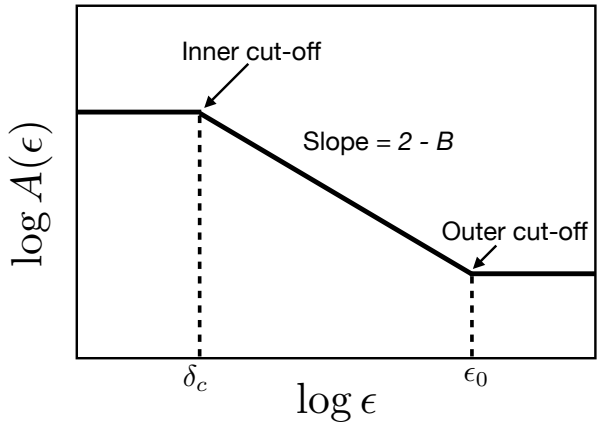

Figure 2.9 – *Graphical description of the area measurement resolution relationship for a fractal surface.*

Fractal formulation

In the present manuscript, the dynamic modelling is applied for a fractal formulation. A lot of complex natural phenomena related to turbulence (Mandelbrot, 1975, 1983, 2004; Sreenivasan and Meneveau, 1986) as well as the behavior of premixed flames can be described by the fractal theory (Peters, 1988; Gouldin, 1987; Gouldin et al., 1989; North and Santavicca, 1990; Gülder, 1991; Gülder and Smallwood, 1995a; Smallwood et al., 1995; Chatakonda et al., 2013).
The geometry characterising a fractal is different from conventional Euclidean one. A self-similar object is composed of smaller pieces, each of which is a replica of the whole itself. The critical point of fractal geometry is that the measured size of a fractal object (L for a curve and A for a surface) varies with the measurement scale ϵ with a power law relationship. For a fractal curve it is:

$$L(\epsilon) \propto \epsilon^{1-B} \ , \quad \text{with} \quad 1 < B \leq 2 \tag{2.68}$$

while for a fractal surface:

$$A(\epsilon) \propto \epsilon^{2-B} \ , \quad \text{with} \quad 2 < B \leq 3 \tag{2.69}$$

where B is the fractal dimension of the curve/surface. However equations 2.68 and 2.69 are valid only in a certain range of ϵ delimited by an inner (δ_c) and outer (ϵ_0) cut-off lengths as shown in figure 2.9. Several studies, numerical and experimental, have been carried out in order to analyse the fractal nature of the flame. (Smallwood et al., 1995) measured the length of the outline of the flame boundary. The fractal behaviour is evident (figure 2.10) and presents an outer cut-off an inner cut-off length. Chatakonda et al. (2013) carried out a numerical investigation. They used direct numerical simulation

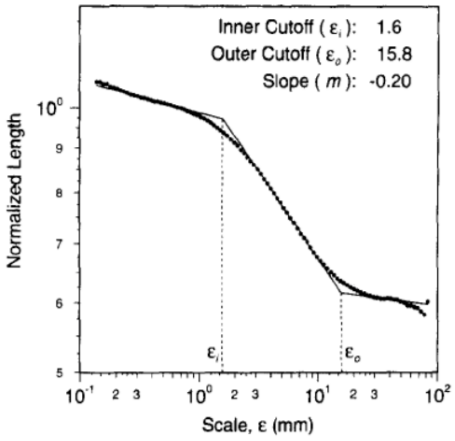

Figure 2.10 – *Normalized length of the outline of the flame boundary as a function of scale for average of 366 images for the CH4-air flame at* $\phi = 0.7$*, mean bulk velocity* $\bar{u} = 5m/s$ *and turbulent velocity* $u'/S_L = 1.22$*. Best-fit three linear segments are shown along with slope and inner and outer cut-offs (Smallwood et al., 1995).*

for a hydrogen-air turbulent premixed plane-jet flames with detailed chemistry and thermonuclear flames. A three-dimensional box-counting method was used to investigate the fractal dimension of the flame surface, characterising the self-similarity of the flame fronts. Also in this work results show the time evolution of the fractal dimension.
Concerning turbulent non-premixed flames, no investigations are present in literature. However, in a turbulent non-premixed regime, it is still legitime to assume the fractal behaviour of the flame because of the nature of turbulence. The work of Favini et al. (2003) gives an example where the fractal model is used to simulate a turbulent CH4/H2/Air non-premixed jet.
In premixed flame, a key point in the fractal formulation is the inner cut-off length which represents the smallest scale of the wrinkled flame. According to the fractal formalism the turbulent flame area A_T and the laminar one A can be related to inner δ_c and outer ϵ_0 cut-off scales as (Gouldin, 1987; Gouldin et al., 1989; Gülder, 1991):

$$\frac{A_T}{A} = \left(\frac{\epsilon_0}{\delta_c}\right)^{B-2} \tag{2.70}$$

In LES, the outer cut-off length is the combustion filter size Δ. The determination of the inner cut-off length is not straightforward and several estimations can be found in literature that relate it to Kolmogorov length scale, laminar flame thickness and also Gibson scale. A list of the main propositions is given in table 2.4. They all show that the inner cut-off scales with the Karlovitz number ($\mathrm{Ka}^{-2} - \mathrm{Ka}^{-1/2}$). Battista et al. (2015), considering laboratory experiments of turbulent premixed jet flames in different regimes, have shown that the in-

Reference	δ_c/δ_L	Comments
Peters (1988)	Ka^{-2}	Physical reasoning
Gouldin (1987)	$f(u'/S_L;\mathrm{Re}_L)\,\mathrm{Ka}^{-2}$	Heuristic approach
MANTZARAS (1992)	$f(u'/S_L)\,\mathrm{Ka}^{-2}$	Curve fit to numerical data
Poinsot et al. (1991b)	$0.74 + 16.4\,\mathrm{Ka}^{-2}$	Curve fit to numerical data
Gülder (1991)	$712\,\mathrm{Re}_L^{-3/4}\,\mathrm{Ka}^{-1/2}$	Physical reasoning
Murayama and Takeno (1989)	$10 - 15$	Experimental result
Roberts et al. (1993)	$7\,\mathrm{Ka}^{-1/2}$	Curve fit to experimental data

Table 2.4 – *Summary of inner cut-off expressions. δ_c inner cut-off; δ_L laminar flame thickness $\delta_L = \nu/S_L$; ν kinematic viscosity of the premixed gases at unburnt mixture temperature; S_L laminar flame velocity; Karlovitz number $Ka(u'/S_L)^{3/2}(L/\delta_L)^{-1/2}$; u' rms velocity; L integral length scale; Re_L Reynolds number based on L (Gülder and Smallwood, 1995b).*

ner cuf-off length scales with the Kolmogorov scale and the Karlovitz number (figure 2.11). In general, it is common practice in literature to rely the cut-off length scale on the laminar flame thickness $\delta_c \propto \delta_L^0$. However, it remains an open question and, at present, no investigations concern non-premixed flames.

2.7.2 Statistical approaches

The statistical formalism hinges on probability density functions (PDF), a concept formulated in RANS context and then expanded to LES.
By considering a thermochemical variable φ, such as species or temperature, depending only on a single variable (for instance, the mixture fraction z for infinitely fast chemistry in non-premixed flames), the Favre filtered quantity is defined as (Gao and O'Brien, 1993):

$$\tilde{\varphi}(\mathbf{x},t) = \frac{1}{\bar{\rho}} \int_{-\infty}^{+\infty} \rho(\mathbf{x}',t)\varphi\left(z(\mathbf{x}',t)\right) G(\mathbf{x}-\mathbf{x}')d\mathbf{x}' \tag{2.71}$$

By introducing the Dirac δ-function, it becomes:

$$\tilde{\varphi}(\mathbf{x},t) = \frac{1}{\bar{\rho}} \int_0^1 \int_{-\infty}^{+\infty} \rho(\Psi)\ \varphi(\Psi)\ \delta\left(z(\mathbf{x}',t)-\Psi\right) G(\mathbf{x}-\mathbf{x}')d\mathbf{x}'d\Psi \tag{2.72}$$

Considering the filtered density function $\tilde{P}$ defined as

$$\tilde{P}(\Psi,\mathbf{x},t) = \frac{1}{\bar{\rho}} \int_{-\infty}^{+\infty} \rho\Psi\ \delta\left(z(\mathbf{x}',t)-\Psi\right)\ G(\mathbf{x}-\mathbf{x}')d\mathbf{x}' \tag{2.73}$$

leads to:

$$\tilde{\varphi}(\mathbf{x},t) = \int_0^1 \varphi(\Psi)\,\tilde{P}(\Psi,\mathbf{x},t)d\Psi \tag{2.74}$$

The filtered density function FDF can be presumed or obtained by solving a transport equation. Furthermore the presumed FDF can be used with a filtered conditional average (Conditional Moment Closure CMC).

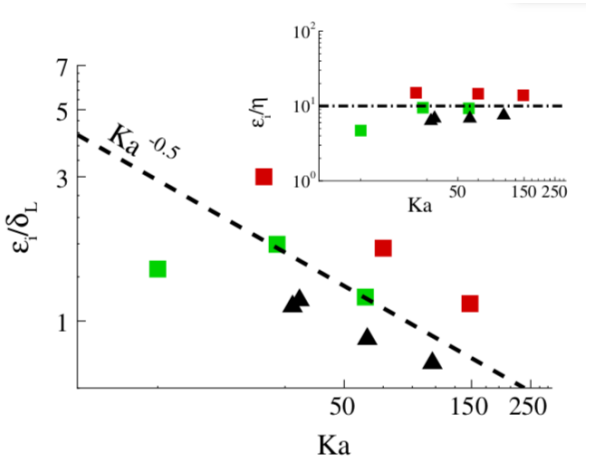

Figure 2.11 – *Inner cut-off (ϵ_i/δ_L) vs Karlovitz number Ka. Dotted line represent the scaling $\epsilon_i/\delta_L \propto Ka^{-1/2}$. In the inset the inner cut-off length normalized by the Kolmogorov scale, ϵ_i/η, is reported against Karlovitz number. The dash-dotted line represent the constant fitting value $\epsilon_i/\eta = 10$ (Battista et al., 2015).*

2.7.2.1 Presumed FDF

The presumed filtered density function is generally modelled with a β-function as suggested by Cook and Riley (1998, 1994).
Olbricht et al. (2012) noted that a β-distribution is expected for temporal statistics but probably not adapted to instantaneous sub-grid scale distributions, suggesting to retain a top-hat function (uniform probability between the minimum and maximum parameter values). Two variables (progress variable and mixture fraction) or multi-variable (adding, for example, strain rate, initial fresh gas temperature, heat losses, exhaust gas recirculation,... dependencies) filtered probability density functions are modelled assuming statistical independence of parameters. In general, progress variable or mixture fraction distribution are described through β-functions while other parameters are assumed constant at the sub-grid scale level (Dirac functions).

2.7.2.2 Transported FDF

The filtered density function FDF can be also calculated as a solution of a balance equation (Gao and O'Brien, 1993; Haworth, 2010), that reads:

$$\begin{aligned}\bar{\rho}\frac{\partial \tilde{P}}{\partial t}+\bar{\rho}\tilde{u}_k\frac{\partial \tilde{P}}{\partial x_k} &= \underbrace{\frac{\partial}{\partial x_k}\left[\bar{\rho}\left(\tilde{u}_k-\overline{\left(u_k|\underline{\varphi}=\underline{\Psi}\right)}\right)\tilde{P}\right]}_{\text{Unresolved transport}} \\ &\underbrace{-\bar{\rho}\sum_{i=1}^{N}\frac{\partial}{\partial \Psi_i}\left[\overline{\left(\frac{1}{\rho}\frac{\partial J_{i,k}}{\partial x_k}|\underline{\varphi}=\underline{\Psi}\right)}\tilde{P}\right]}_{\text{Molecular diffusion}} \\ &\underbrace{-\bar{\rho}\sum_{i=1}^{N}\frac{\partial}{\partial \Psi_i}\left(\frac{1}{\rho}\dot{\omega}_i(\underline{\Psi})\tilde{P}\right)}_{\text{Chemical reaction}}\end{aligned} \tag{2.75}$$

where $(\overline{\mathcal{Q}|\underline{\varphi}=\underline{\Psi}})$ denotes a conditional averaging of $\mathcal{Q}$ for the sampling values Ψ_i on the thermo-chemical variables φ_i. $J_{i,k}$ is the k^{th} component of the diffusion flux of i^{th} thermochemical variable. The LHS terms and the first RHS correspond to the resolved and unresolved transport in physical space, respectively, while the last two LHS terms describe the FDF evolution in the phase space (i.e. φ) due to molecular diffusion and chemical reaction respectively. The formulation of FDF can also include velocity components (Haworth, 2010).

2.7.2.3 CMC

The Conditional Moment Closure approach (CMC) has been first used for RANS simulation (Klimenko, 1990; Bilger, 1993). The filtered quantity can be expressed by using a filtered conditional mean:

$$\tilde{\psi}(\mathbf{x},t)=\int_0^1(\psi|z^*;\mathbf{x},t)\,\tilde{P}(z^*;\mathbf{x},t)dz^z* \tag{2.76}$$

where $(\overline{\psi|z^*;\mathbf{x},t})$ is the filtered conditional mean of ψ for a given value z^* of the mixture fraction and $\tilde{P}(z^*;\mathbf{x},t)$ is the mass-weighted filtered density function of z. However closure schemes are required which easily increase the computational costs of the simulation.
This approach suffers from some drawbacks: it needs a variety of closure schemes, it induces large computational costs (one balance equation per variable ψ and conditional level $z*$ taken into consideration). Anyway it has been successfully used in some situations (Navarro-Martinez and Kronenburg, 2007, 2009; Triantafyllidis and Eggels, 2009; Garmory and Mastorakos, 2011).

2.7.3 Mixing approaches

The idea of describing the flame turbulence interaction with mixing information has been first used in RANS context. The Eddy-Break-Up model proposed by Spalding (1971, 1977) assumes the chemical reaction rate to be inversely proportional to a mixing time. Magnussen and Hjertager (1977) adapted the formulation to non-premixed combustion (Eddy Dissipation Concept), by relating the reaction rate to the reactants mass fractions as well as a turbulent mixing time, estimated from integral length scales. The model is largely used in LES for non-premixed flames (Lysenko et al., 2014)
A more refined formalism is based on a one-dimensional stochastic description of turbulent stirring processes (Linear Eddy model) (Kerstein, 1988, 1989, 1990, 1992, 1991; McMurthy et al., 1992; Menon et al., 1994). In an LES framework, this formulation is used to represent sub-grid scale phenomena.
The turbulent stirring mechanism is modelled by rearranging the 1D scalar field. The initial scalar distribution 2.12a is reshaped on a given segment of size l according to 2.12b ('triplet map'). Then the turbulent mixing is simulated with a stochastic description that considers a given turbulence spectrum to retrieve the values of vortex location x_0, the vortex size l and the vortex frequencies λ. One-dimensional balance equations describe the molecular diffusion and the chemical processes:

$$\frac{\partial \rho Y_i}{\partial t} = \frac{\partial}{\partial x}\left(\rho D_i \frac{\partial Y_i}{\partial x}\right) + \dot{\omega} \tag{2.77}$$

Equation 2.77 can also include complex chemistry. However considering that for each computational cell a one-dimensional DNS calculation is performed, this can easily lead a heavy computational load.
The model has been successfully used to simulate turbulent mixing and LES of non-premixed combustion (Calhoon William and Menon, 1996; Mathey and Chollet, 1997).

2.8 Conclusions

In this chapter, a general overview of LES's turbulent combustion modeling for non-premixed flames is given. The description of chemical reactions can be done by directly computing the transport equations for each species or using parameters (indirect approach). The direct approaches can easily involve a considerable number of species leading to a substantial computational effort. Several techniques aim to reduce the number of species by preserving the ones necessary to predict the target quantity correctly. However, since the combustion phenomenon occurs at the smallest scales, the resolution of LES's computational domain cannot describe the flame/turbulence interaction, and specific models are required. Standard LES model classifications arrange the models according

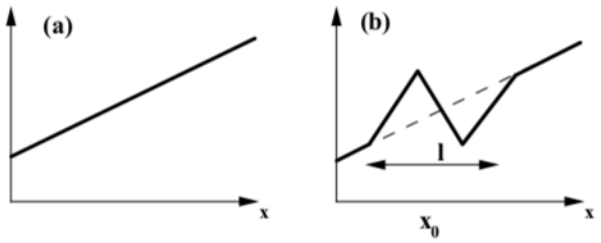

Figure 2.12 – *Map representing the effect of an individual eddy in Linear Eddy Model. (a) Scalar field prior to map. In the example the scalar field is linear in the spatial coordinate. (b) Scalar field after applying the triplet map in a simulated mixing by a vortex of size l.*

to the primary concept. As explained by Veynante and Vervisch (2002), there are exact relations between flame surface densities, filtered density functions, and scalar dissipation rates describing turbulent mixing, and filtered reaction rates may be exactly expressed in terms of each of these quantities. For this reason, there is no absolute advantage of formalism compared to the others, which is not surprising as they only examine the same problem from a different point of view. The only possible advantages lie in the ability to close the unknown terms.

Chapter 3

Dynamic modelling

The dynamic modeling procedure is based on the Germano-like identity initially designed for fluid-dynamic parameters and extended to the flame parameters. This approach aims to compute the model's parameters on the fly instead of adjusting them by hand, detaching them from the specific configuration.
This chapter illustrates the general concepts of dynamic formulations and depicts state of the art by resuming the most relevant related works. The modeling of direct reaction focus is generally related to turbulent premixed flames. Several cases, from turbulent jet flames (Wang et al., 2011; Hosseinzadeh et al., 2016; Volpiani et al., 2016; Schmitt et al., 2015) to explosions configuration (Volpiani et al., 2017a) have been successfully simulated. The promising results encourage the investigation of the possibility of using the dynamic formulation for non-premixed flames. In literature, the dynamic formulation in non-premixed flame has been used to model scalar dissipation rates and not directly reaction rates (Reveillon and Vervisch, 1998; Pierce and Moin, 1998, 2004; Balarac et al., 2008; Kaul et al., 2013).
However, the advantage of using a direct approach to non-premixed flames lies in the fact that such a model can potentially describe reacting flows for applications where both regimes are present.

Contents

3.1 Dynamic formulation

In order to understand the dynamic formulation, it is essential to explain the meaning of the wrinkling factor.
The wrinkling factor Ξ_Δ measures the ratio of total Σ^{tot} to resolved Σ^{res} flame surface density in the filtering volume ν. Under flamelet assumption, it also represents the ratio of the turbulent sub-grid flame speed to the laminar flame speed S_T/S_l (Damköhler, 1940).
The total and resolved flame surface densities can be estimated as (Poinsot and Veynante, 2012; Pope, 1988; Vervisch et al., 1995):

$$\begin{aligned} \Sigma^{tot} &= \overline{|\nabla\psi|} \\ \Sigma^{res} &= \left|\nabla\bar{\psi}\right| \end{aligned} \tag{3.1}$$

where ψ represents a characteristic variable of the flame such as progress variable c in premixed or a mixture fraction z in non-premixed regime. The wrinkling factor over the filtering volume ν writes as (Veynante and Moureau, 2015):

$$\Xi = \frac{\langle\overline{|\nabla\psi|}\rangle}{\langle|\nabla\bar{\psi}|\rangle} \tag{3.2}$$

According to Charlette et al. (2002b), the generic formulation of the filtered reaction rate $\overline{\dot{\omega}(\psi)}$ reads:

$$\overline{\dot{\omega}(\psi)} = \Xi_\Delta \frac{W_\Delta(\tilde{\psi})}{\Delta} \tag{3.3}$$

where $\frac{W_\Delta(\tilde{\psi})}{\Delta}$ corresponds to the resolved reaction rate, estimated from filtered quantities (note that ψ and $\tilde{\psi}$ stands for any quantity entering the reaction rate). Table 3.1 resumes the formulation of Eq. 3.3 for different flame surface models.

A dynamic model introduces a test filter operation, with a filter size $\hat{\Delta}$. For Gaussian filters, combining LES Δ and test filter $\hat{\Delta}$ operators leads to an effective filter width $\gamma\Delta = \sqrt{\Delta^2 + \hat{\Delta}^2}$.

The dynamic formulation can be applied to the reaction rate by considering the generic form of the filtered reaction of eq. 3.3. The test-filtered resolved reaction rate is compared with the reaction rate estimated at the test-filter level as follows:

$$\hat{\overline{\dot{\omega}}} = \widehat{\frac{\Xi_\Delta}{\Delta} W_\Delta(\tilde{\psi})} = \frac{\Xi_{\gamma\Delta}}{\gamma\Delta} W_{\gamma\Delta}(\hat{\tilde{\psi}}) \tag{3.4}$$

Model	$\overline{\dot{\omega}(\psi)}$	$W_\Delta(\tilde{\psi})$
Boger et al.	$4\rho_u S_l \Xi_\Delta \sqrt{\frac{6}{\pi}} \frac{\tilde{\psi}(1-\tilde{\psi})}{\Delta}$	$4\rho_u S_l \sqrt{\frac{6}{\pi}} \tilde{\psi}(1-\tilde{\psi})$
Level set	$\rho_u \Xi_\Delta S_l \lvert\nabla G\rvert$	$\rho_u S_l \Delta \lvert\nabla G\rvert$
TFLES	$\Xi_\Delta \frac{\dot{\omega}(\tilde{\psi})}{F}$	$\delta_l \, \dot{\omega}(\tilde{\psi})$
F-TACLES	$\Xi_\Delta F_l(\tilde{\psi}, \Delta)$	$\Delta \, F_l(\tilde{\psi}, \Delta)$

Table 3.1 – *Generic reaction rate expressions according to Eq. 3.3 for four turbulent premixed combustion LES models. ρ_u is the fresh gases density, S_l and δ_l the laminar flame speed and thickness, respectively. G is the level-set field, usually defined as a signed distance to the flame front, $S_T = \Xi_\Delta S_l$ the sub-grid scale turbulent flame speed, F the TFLES thickening factor and $\dot{\omega}$ the progress variable reaction rate (laminar flame). $F_l(\tilde{\psi}, \Delta)$ is given by filtering one-dimensional laminar premixed flames (Veynante and Moureau, 2015).*

where Favre-filtered quantities at scale Δ are denoted by a tilde $\tilde{}$, and $\hat{}$ denotes the filtering operation with a $\hat{\Delta}$ filter width, so $\hat{\tilde{}}$ is the filtering operation with $\gamma\Delta$ width filter size.
LHS of equation 3.4 is interpreted as the reaction rate at scale Δ which has consequently been test-filtered at scale $\hat{\Delta}$. The RHS instead is interpreted as writing directly the modelled reaction rate at scale $\gamma\Delta$. To determine the model parameters, Charlette et al. (2002a) proposed to average the equation over a given volume:

$$\left\langle \widehat{\frac{\Xi_\Delta}{\Delta} W_\Delta(\tilde{\psi})} \right\rangle = \left\langle \frac{\Xi_{\gamma\Delta}}{\gamma\Delta} W_{\gamma\Delta}(\hat{\tilde{\psi}}) \right\rangle \tag{3.5}$$

where $<.>$ denotes the averaging operation over the finite domain. Averaging over the entire computational domain provides a spatially uniform model parameter evolving only with time (global formulation). When a small local volume is chosen, the model parameter evolves both with time and space coordinates (local formulation).
Furthermore, the averaging operation $<.>$ can be replaceable by a Gaussian filter of size Δ_{avg}, which is easier to implement for unstructured meshes on massively parallel machines than a usual averaging operation over a given volume. Gaussian filters may indeed be written as unsteady diffusion operators (Moureau et al., 2011), which use standard finite-difference or finite-volume schemes. Equation (3.5) is expected to recover unity wrinkling factors when the wrinkling of the flame front is fully resolved by the simulation, i.e.:

$$\left\langle \widehat{W_\Delta(\tilde{\psi})} \right\rangle = \left\langle W_{\gamma\Delta}(\hat{\tilde{\psi}}) \right\rangle \tag{3.6}$$

which is in general not true for algebraic expressions of W_Δ in table 3.1. For the TFLES model, Wang et al. (2011) enforced this condition through a calibration factor. F-TACLES models, based on the explicit filtering of one-dimensional laminar flame elements (Fiorina et al., 2009), fit the condition (3.5) by construction.
The second condition requires that $\widehat{W_\Delta(\tilde{\psi})}$ and $W_{\gamma\Delta}(\tilde{\psi})$ have identical shapes for planar flames, in order to avoid unforeseen bias due to Gaussian filtering replacing the averaging procedure, which is also not verified in general by modeled reaction rates. In the specific context of TFLES, Veynante and Moureau (2015) showed that for an Arrhenius-like law, with a Gaussian filter of width Δ_{avg}, the averaging operations $< \widehat{W_\Delta(\tilde{\psi})} >$ and $< W_{\gamma\Delta}(\hat{\tilde{\psi}}) >$ respectively differ. Then, a unity wrinkling factor would not be correctly predicted by Eq. 3.4. A solution to overcome this difficulty and fit the previous requirements is to recast Eq. (3.4) in term of flame surfaces, so considering relation (3.2):

$$\langle\widehat{\Xi_\Delta|\nabla\bar{\psi}|}\rangle = \langle\Xi_{\gamma\Delta}|\nabla\hat{\tilde{\psi}}|\rangle \tag{3.7}$$

where $|\nabla\bar{\psi}|$, $\Xi_\Delta|\nabla\psi|$, $|\nabla\hat{\tilde{\psi}}|$ and $\Xi_{\gamma\Delta}|\nabla\hat{\tilde{\psi}}|$ measure resolved and total generalized flame surface densities (i.e. flame surface per unit volume) at LES and test-filter scale, respectively. By construction, for one-dimensional flame $\widehat{|\nabla\bar{\psi}|} = |\nabla\hat{\tilde{\psi}}|$ so equation 3.7 is verified for $\Xi_\Delta = \Xi_{\gamma\Delta} = 1$.

3.1.1 Fractal-like model formulation

Among all the wrinkling models present in literature, for the scope of the manuscript, the fractal model is adopted. Section 2.7.1.2 examines in depth the fractal behaviour of the flame.
The fractal formulation of the wrinkling factor writes as:

$$\Xi_\Delta = \left(\frac{\Delta}{\delta_c}\right)^\beta \tag{3.8}$$

where the outer cut-off length scale is represented by the LES filter Δ, δ_c is the inner cut-off length scale. β is a parameter related to the fractal dimension B as (see Eqs 2.68 and 2.69):

$$\beta = \begin{cases} B-1, & \text{for fractal curves} \\ B-2, & \text{for fractal surfaces} \end{cases} \tag{3.9}$$

So the Germano-like identity for flame surfaces (Eq. 3.7) with fractal model becomes:

$$\left\langle\widehat{\left(\frac{\Delta}{\delta_c}\right)^\beta|\nabla\bar{\psi}|}\right\rangle = \left\langle\left(\frac{\gamma\Delta}{\delta_c}\right)^\beta|\nabla\hat{\tilde{\psi}}|\right\rangle \tag{3.10}$$

By assuming β uniform over the averaging volume and independent on the filtering scale, equation 3.10 leads to:

$$\beta = \frac{\ln\left(\langle|\widehat{\nabla\bar{\psi}}|\rangle / \langle|\nabla\hat{\bar{\psi}}|\rangle\right)}{\ln\gamma} \tag{3.11}$$

Unfortunately, equation (3.11) involves unweighted filtered quantities instead of Favre-filtered solved in LES. However, for infinitely thin flame fronts, filtered progress variables are directly linked (Bray and Moss, 1977; Poinsot and Veynante, 2012), and, by analogy for non-premixed flames, eq. (3.11) can be approximated as:

$$\beta \approx \frac{\ln\left(\langle|\widehat{\nabla\tilde{\psi}}|\rangle / \langle|\nabla\hat{\tilde{\psi}}|\rangle\right)}{\ln\gamma} \tag{3.12}$$

The formulation (3.12), already used in numerous works, is adopted in the the following of the manuscript.

Table 3.2 – *Main works dealing with dynamic modelling in direct combustion approach*

Combustion Model	Work	Configuration	Germano identity	Formulation
TFLES	Charlette et al. (2002b)	Academic test case	reaction rate	Global/semi-local
	Wang et al. (2011)	Jet flame	reaction rate	Global
	Hosseinzadeh et al. (2016)	Jet flame	reaction rate	Global/local
	Volpiani et al. (2016)	Jet flame	flame surface	Global/local
	Volpiani et al. (2017b)	PRECCINSTA burner	flame surface	Global/local
	Volpiani et al. (2017a)	Deflagrating flame	flame surface	Local
F-TACLES	Schmitt et al. (2013)	Tecflam	reaction rate	Global/semi-local
	Hosseinzadeh et al. (2015)	Jet flame	reaction rate	Global/local
	Schmitt et al. (2015)	Jet flame	reaction rate	Global/local
FSD	Knikker et al. (2004)	A priori analysis	flame surface	Global
	Gubba et al. (2011)	Deflagrating flame	flame surface	Global
	Wang et al. (2012)	Flame kernel	reaction rate	Global
	Veynante and Moureau (2015)	Turbulent swirl burner	reaction rate / flame surface	Local
	Mouriaux et al. (2017)	Piston Engine	flame surface	Local
Level-set	Im et al. (1997)	Academic test case	flame speed	Global
	Knudsen and Pitsch (2008)	Jet flame	flame speed	Local

3.2 State of the art

In this section, an overall view of LES's dynamic models present in literature is given, and the most significant results are listed. Table 3.2 resumes the main works' features on dynamic modeling with a direct approach. The models mentioned in the following are used for premixed flames. In literature, the dynamic formulation for non-premixed flame has been used with indirect approaches that do not involve direct modeling of the chemical reaction, but they instead describe the flame through mixing or statistical approaches (Kaul et al., 2013; Reveillon and Vervisch, 1998).
However, the advantage to adopting a model designed for premixed flames to non-premixed configurations lies in the fact that such a model can also correctly predict zone where the regime is only partially premixed, which is of utmost importance when it comes to deal with flows inside gas turbines.

3.2.1 TFLES models

In literature, the dynamic formulation has been largely coupled with TFLES in premixed configurations. Charlette et al. (2002b) adopted the dynamic formulation to simulate decaying isotropic turbulence, Wang et al. (2011); Hosseinzadeh et al. (2016) used the formulation to simulate a Bunsen flame. Volpiani et al. (2016) investigated the influence of the dynamic formulation parameters for a pilot stabilized jet. Other successful applications of the formulation concern combustion instabilities (Volpiani et al., 2017b) and explosion flames (Volpiani et al., 2017a).
The determination of the effective combustion filter size Δ (which, for example, representing the outer cut-off length in fractal formulation 3.8) is somewhat tricky. Since the thickening operation is not strictly equivalent to filtering a flame front, a correction parameter α is added:

$$\Delta = \alpha F \delta_L^0 \tag{3.13}$$

where F is the thickening factor, δ_L^0 is the laminar flame thickness. By assuming the Germano formulation for the reaction rate (Eq. 3.5), Wang et al. (2011) found a value of $\alpha = 2.2$ through one-dimensional laminar flame analysis in order to recover $\beta = 0$ and $\Xi_\Delta = 1$ for planar laminar flame. Volpiani et al. (2016), by using the Germano formulation for the flame surface (Eq. 3.7), found a value of $\alpha = 1.4$. Finally, when the model is derived from the flame surface, the condition is automatically enforced, and no correction is required.

3.2.1.1 Charlette et al. (2002b)

Charlette et al. (2002b) adopted the dynamic formulation with the TFLES model by proposing a relation of the wrinkling factor as:

$$\Xi_\Delta = \left(1 + \min\left[\frac{\Delta}{\delta_L^0}, \Gamma_\Delta, \frac{u'_\Delta}{S_L}\right]\right)^\beta \tag{3.14}$$

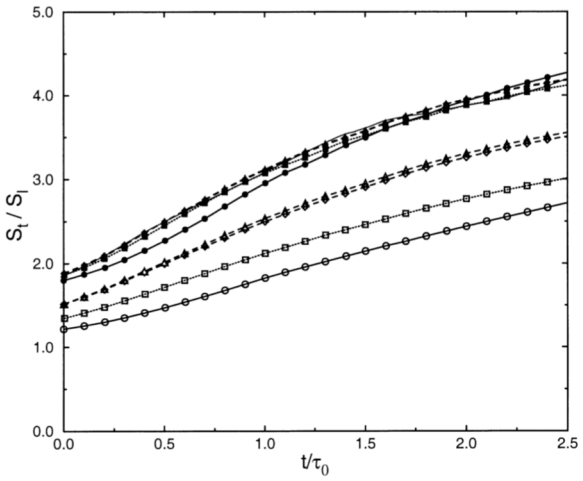

Figure 3.1 – *Time evolution of the turbulent flame speed. A-dimensional time by initial turbulent eddy turn-over-time τ_0. Thick solid line: DNS;* $\bullet, \circ$ $F = 6.6$*;* $\blacksquare, \square$ $F = 4.0$ *;*$\blacklozenge, \lozenge$ $F = 2.8$*; - $\gamma = 2$; $\blacktriangle, \triangle$ $F = 2.8$ - $\gamma = 3$. The empty symbols are for the resolved turbulent speed (computing the reaction rate without wrinkling factor), plain symbols are for the total turbulent speed (with wrinkling factor) (Charlette et al., 2002b).*

where δ_L^0 is the thickness of the laminar premixed flame, u'_Δ is the characteristic turbulent velocity at scale Δ. The effect of the flame stretch on the local flame speed is kept into account by the efficiency function Γ_Δ.
They formulated a Germano-like identity for the reaction rate (eq. 3.5) and the parameter β is retrieved with a global formulation. The dynamic formulation of the wrinkling factor is coupled with the TFLES model, and the test case is a 3D premixed flame in decaying isotropic turbulence. The results are validated against a DNS. As shown in figure 3.1, the prediction of the turbulent flame speed is reasonably accurate over the temporal evolution. The results for the exponent β are shown in figure 3.2. Moreover, considering the Charlette-like formulation, Charlette et al. (2002a) showed both with a priori and a posteriori tests that the formulation is often saturated, which corresponds to the fractal formulation (Eq. 3.8).

In addition they also performed a semi-local formulation by averaging over strips in the direction normal to the flame brush.

3.2.1.2 Wang et al. (2011)

Wang et al. (2011) proposed to modify the Charlette function 3.14 as:

$$\Xi_\Delta \equiv \frac{S_T}{S_L} = \left(1 + \min\left[\frac{\Delta}{\delta_L^0} - 1, \Gamma_\Delta \frac{u'_\Delta}{S_L^0}\right]\right)^\beta \tag{3.15}$$

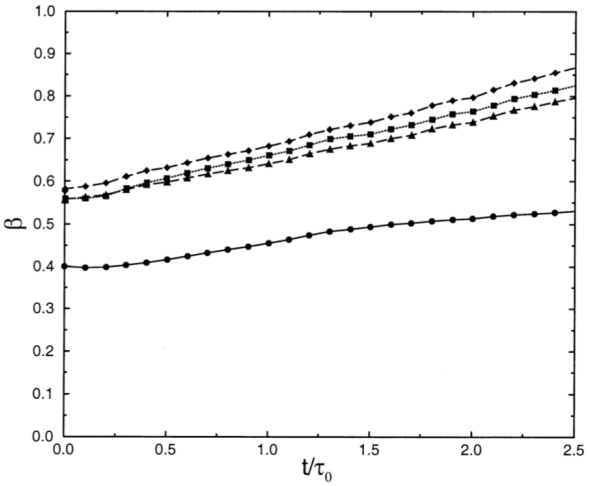

Figure 3.2 – *Time evolution of dynamic parameter β. A-dimensional time as in figure 3.1.* • $F = 6.6$*;* ■ $F = 4.0$*;* ♦ $F = 2.8$ $\gamma = 2$*;i* ▲ $F = 2.8$ - $\gamma = 3$ *(Charlette et al., 2002b).*

They replaced Δ/δ_L^0 by $\Delta/\delta_L^0 - 1$ in the original expression to recover the fractal model $\Xi_\Delta = (\Delta/\delta_L^0)^\beta$ (Gouldin et al., 1989; Gülder, 1991) when saturated. Since the estimation of the turbulence intensity at both filter (u'_Δ) and test-filter ($u'_{\gamma\Delta}$) is not straightforward the parameter β is computed for the limiting case of large turbulence intensities. However, as mentioned before, the Charlette formulation turns to be saturated most of the cases (Veynante and Moureau, 2015). The Germano-identity is then solved for the reaction rate.
Wang et al. (2011) focused on calculating a global value of β, depending only on time, while the averaging volume being the entire computational domain. To note, however, that wrinkling factor is still a local variable because it depends on instantaneous and local conditions through the turbulent intensity u'_Δ.
A dedicated solver computes the test filtering and the parameter calculation, while the AVBP code computes the flow balance equations. A Gaussian test filter is used:

$$G(\mathbf{x}) = \left(\frac{6}{\pi\hat{\Delta}}\right) \exp\left[-\frac{6}{\hat{\Delta}^2}(x^2 + y^2 + z^2)\right] \tag{3.16}$$

Unfortunately, as previously mentioned, thickening a flame in TFLES is not strictly equivalent to filtering a flame front, so the effective combustion filter size Δ is unknown a priori. Then the authors introduced a calibration factor to express an equivalent TFLES filter width as $\Delta = \alpha F \delta_L^0$, with $\alpha = 2.2$ to retrieve $\beta = 0$ and $\Xi_\Delta = 0$ for unstretched laminar flames. They simulated the turbulent Bunsen flame experimentally studied by Chen et al. (1996) over three different operating conditions. The results show that the global parameter depends on the flame Reynolds number. Figure 3.3 shows that for $Re \approx 23000$

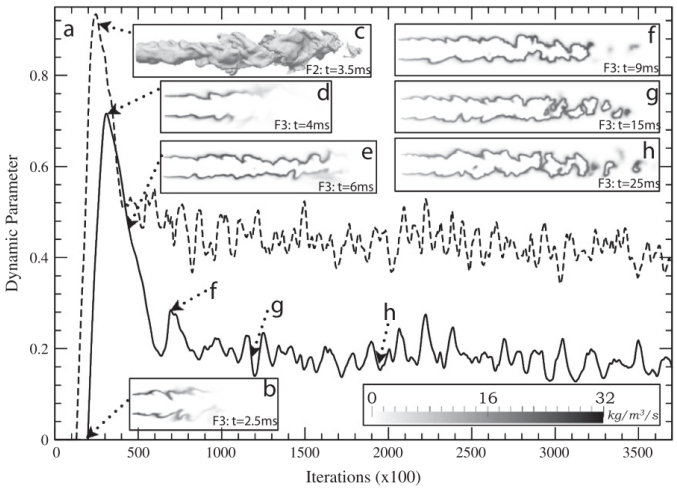

Figure 3.3 – *Time evolution, in terms of number of iterations, of the dynamic parameter β and the flow field for LES of F2 and F3 flame. (a) β evolution for F3 (solid line) and F2 (dashed line) flame; (b) chemical reaction rate term $(\Xi_\Delta/F)\dot{\omega}_{CH_4} \times 8$;(d-h) chemical reaction term; (c) iso-surface of $\tilde{Y}_{CH4} = 0.011$ (Wang et al., 2011).*

(F3) β stabilizes around a mean value of $\beta \approx 0.2$. Increasing the Reynolds number to $Re \approx 40000$, the steady-state value increases in turn to $\beta \approx 0.4$. The simulations are in good agreement with the experimental data. Furthermore, the non-dynamic flame wrinkling factor formulation produces good results with a constant empirical parameter β, correctly estimated with a dynamic formulation.

3.2.1.3 Hosseinzadeh et al. 2016

Hosseinzadeh et al. (2016) used the dynamic formulation coupled with the TFLES model and FGM methodology (Van Oijen et al., 2001; Kuenne et al., 2011). They simulated a lean premixed turbulent Bunsen-type flame with different grid levels. The power law wrinkling model is given by Charlette et al. (2002a) (Eq. 3.14). The flame front is artificially thickened, e.g., by using a flame sensor which guarantees that the regions of pure mixing are not affected by the model parameters. Source terms are extracted from a two-dimensional lookup table based on a progress variable Y_c and the mixture fraction z, $\phi = f(Y_c, z)$ according to the tabulated chemistry.
Then the Germano-like procedure is used over the source term progress variable. Results show that the non-dynamic model with constant values of the parameter β does not predict the correct turbulent velocity. The dynamic formulation improves the predictions. However, the local or global formulation does not significantly influence the prediction of the overall flame characteristics.

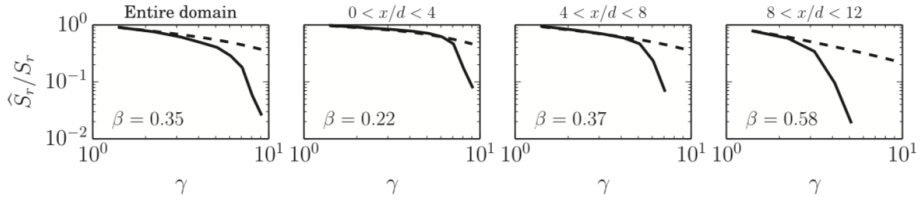

Figure 3.4 – *Pilot stabilized jet flame. Normalized filtered surface flame as a function of the ratio of the test and combustion filter sizes. Results are extracted from the instantaneous resolved field of simulation for a local formulation with test filter size* $\hat{\Delta} = 1.5\Delta$ *and average filter size* $\Delta_{avg} = 3.0\Delta$ *(Volpiani et al., 2016).*

3.2.1.4 Volpiani et al. 2016

Volpiani et al. (2016) made an accurate analysis of the parameters involved in the dynamic formulation. The dynamic model is coupled with TFLES model (Colin et al., 2000) to simulate the F3 pilot stabilized jet experimentally studied by Chen et al. (1996). They carried out simulations for global and local formulation. The main assumption of the model is that the wrinkling factor Ξ_Δ follows a fractal behaviour ($\Xi_\Delta = (\Delta/\delta_c)^\beta$).
By considering the resolved generalised flame surfaces at filter S_r and test-filter $\hat{S}_r$ scales defined as:

$$S_r = \int_V |\nabla \tilde{c}| dV \tag{3.17}$$

$$\hat{S}_r = \int_V |\nabla \hat{\tilde{c}}| dV \tag{3.18}$$

and relating them through the conservation of the total flame surface, $\Xi_\Delta S_r = \Xi_{\gamma\Delta}\hat{S}_r$, it is possible to retrieve a relation for the normalized filtered surface flame:

$$\frac{\hat{S}_r}{S_r} = \frac{\Xi_\Delta}{\Xi_{\gamma\Delta}} = \left(\frac{\gamma\Delta}{\Delta}\right)^{-\beta} = \gamma^{-\beta} \tag{3.19}$$

$\hat{S}_r/S_r$ is expected to follow a straight line slope of $-\beta$ when displayed as a function of the ratio γ of the filter sizes in log-scale as shown in figure 3.4. However, a drop of the slope is observed when two flame fronts interact at the filter test scale, and the relation 3.19 is no longer valid.

3.2.1.5 Volpiani et al. 2017

Volpiani et al. (2017b) adopted the dynamic formulation (both global and local) coupled with TFLES model to simulate the PRECCINSTA burner in both stable and unstable configurations experimentally studied by Meier et al. (2007).

While the local formulation automatically predicts small wrinkling factors near the wall, a simple wall correction is introduced as a first step in the global saturated dynamic formulation. So an ad-hoc damping function is implemented:

$$\Xi_\Delta = \left[1 - \exp\left(\frac{-d_w}{0.5\Delta}\right)\right]\left[\left(\frac{\Delta}{\delta_L^0}\right)^\beta - 1\right] + 1 \tag{3.20}$$

where d_w is the distance to the closest wall. Such an expression affects the wrinkling factor for $d_w < 2\Delta$. They used a simple two-step reduced chemical mechanism where the reaction rates are modeled with Arrhenius laws. The global formulation predicts a time-dependent model parameter β which remain close to 0.5 for the stable flame (figure 3.5) and oscillates strongly around 0.8 for the pulsating flame (figure 3.6). They also analyzed the relation of γ with surface density flame (as in Volpiani et al. (2016), Eq. 3.19), and an instantaneous shot of the resolved and filtered quantities for the progress variable is shown in figure 3.7. The local formulation adapts the parameter locally based on the gradient of the resolved progress variable $\tilde{c}$ all over the domain. The usual non-dynamic formulation with an appropriate constant is sufficient to capture flow and combustion time-averaged and RMS fields with reasonable accuracy in stable configuration. The fractal dimension of the unstable flame is observed to vary locally and depends on the phase within the period of oscillation.
Nevertheless, the self-excited modes of the pulsating flame are predicted only with the dynamic model. Although Franzelli et al. (2012) suggested that methane/air mixing could be associated with the flame pulsation, the details of the exact mechanism controlling the instability itself have not been determined yet.

3.2.2 F-TACLES models

The F-TACLES formulation is based on the description of filtered one dimensional laminar flame. It well fits the combustion filter size requirements Δ, and no correction factor is needed as for the TFLES. The dynamic formulation has been used principally in premixed flames, and, for non-premixed flames, studies are still ongoing at present.
Schmitt et al. (2013) adopted the Germano-identity to the reaction rate:

$$\beta = \frac{\log(<\bar{\dot{\omega}}^{\widehat{\text{tab}}}(\tilde{c},\Delta)> / <\bar{\dot{\omega}}^{\text{tab}}(\hat{\tilde{c}},\gamma\Delta)>)}{\log\gamma} \tag{3.21}$$

where $\bar{\dot{\omega}}^{\text{bar}}$ is the tabulated reaction rate generated with the combustion filter Δ, and c is the progress variable.
They simulated the Tecflam turbulent swirl burner (Schneider et al., 2005; Gregor et al., 2009), firstly by assuming a global parameter spatially independent,

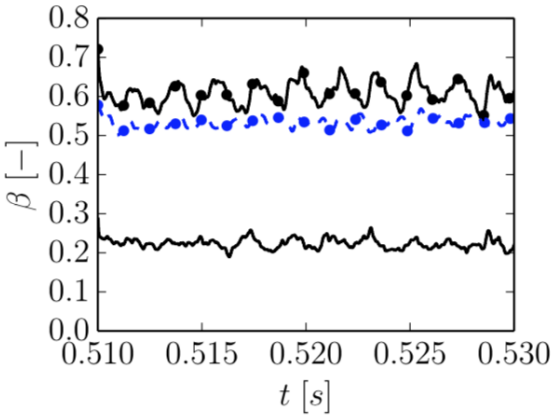

Figure 3.5 – *PRECCINSTA burner stable flame. Temporal evolution of the global parameter $\beta(t)$ (—●—), local average model parameter $\bar{\beta}(t)$ (-●-) and its fluctuation $\beta'(t)$ (——), (Volpiani et al., 2017b).*

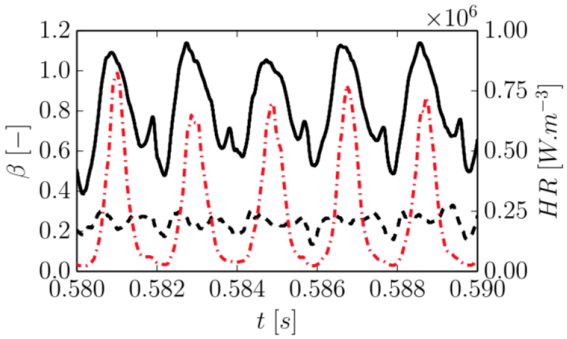

Figure 3.6 – *PRECCINSTA burner pulsating flame. Temporal evolution of the mean model parameter $\bar{\beta}$ (——), its fluctuation β' (- - -) and the total heat release (-·-·-) with a local formulation (Volpiani et al., 2017b).*

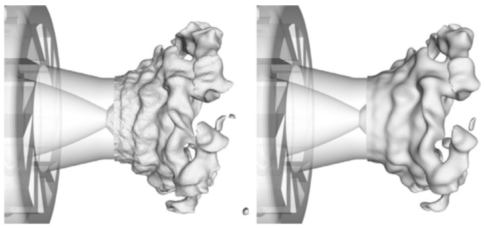

Figure 3.7 – *PRECCINSTA burner. Instantaneous LES resolved fields and corresponding test-filtered quantities. Iso-$\tilde{c}$ surface (left), Iso-$\hat{\tilde{c}}$ surface (right) - $\gamma = 1.5$ (Volpiani et al., 2017b).*

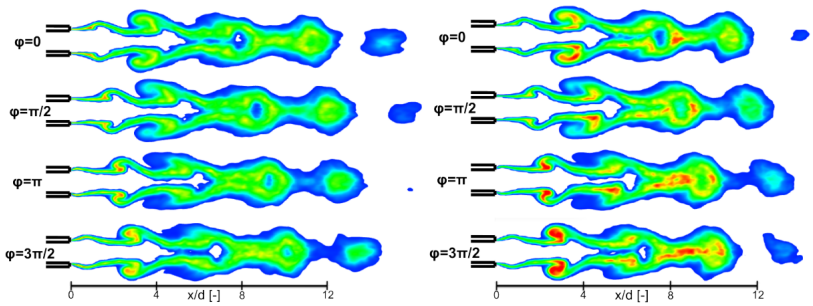

Figure 3.8 – *Phase averaged filtered progress variable reaction rate fields when using global (left) and local (right) model approaches for four phases of the pulsation cycle (from top to bottom) (Schmitt et al., 2015).*

and then considering the dependence of the parameter on the downstream distance from the injector. In both cases, using a dynamic determination of the exponent instead of using the value suggested by Charlette et al. (2002a) improves the simulation's accuracy.

In another work, Schmitt et al. (2015) simulated the turbulent Bunsen flames, investigated by Chen et al. (1996), over three different operating conditions using three different approaches:

- global parameter based on reaction rate (GPRR)
- global parameter based on flame surfaces (GPC)
- local parameter based on flame surfaces (LPC)

Using the LPC model, the dynamic formulation can distinguish zones where the model parameter is close to zero (near the injector) and zones where it presents higher values due to turbulence motions. They also simulated a pulsating flame in order to characterize the model behavior. They show that a spatially uniform parameter produces similar results regarding averages and RMS than a non-dynamic formulation. Furthermore, a local parameter increases from low values near the injector lips, where the flame is quasi-laminar, to large values as the flame is progressively wrinkled by turbulence motions when convected downstream. The amplitude of the reaction rate variations is more significant when using the local approach because maximum reaction rate values are located in the vortexes' highly wrinkled regions as illustrated in figure 3.8. They indicate that dynamic procedures might affect the overall flame dynamics and instantaneous flame behavior and, as a result, they might play an essential role in the prediction of combustion instabilities when strong unsteady motions take place.

3.2.3 Flame surface density models

The dynamic formulation has been largely coupled with Flame Surface density model (FSD) for premixed configurations. A typical formulation of the reaction rate by (Boger et al., 1998) writes as:

$$W_\Delta(\tilde{c}) = 4\rho_u S_L \sqrt{\frac{6}{\pi}} \tilde{c}(1-\tilde{c}) \tag{3.22}$$

where $\tilde{c}$ is the filtered progress variable, ρ_u is the density of the unburnt gases and S_L is the laminar flame speed.
Wang et al. (2012) used the fractal-like model for the efficiency function. Considering the Germano-like identity for the reaction rate, the β parameter is so:

$$\beta = 1 + \frac{\log(<\widehat{\tilde{c}(1-\tilde{c})}> / <\hat{\tilde{c}}(1-\hat{\tilde{c}})>)}{\log\gamma} \tag{3.23}$$

However 3.23 do not recover the case $\beta = 0$, ($\Xi_\Delta = 1$) when the flame wrinkling is fully resolved by the grid resolution. So they used the Germano-like identity for the flame surface density (Eq. 3.7). The formulation has been used to reproduce a flame kernel's growth in a homogeneous and isotropic turbulent flow field in 2D and 3D configurations (figure 3.9 shows the 3D case). Fig 3.10 also shows a proportional relation between the initial turbulence intensity and the model parameter β. Furthermore, in the laminar case ($u' = 0$), β tends towards zero as expected. The numerical results are compared with the experimental data from Renou (1999). Finally, figure 3.11 shows a total radius flame[1] comparison of the present dynamic formulation with the fractal model with constant $\beta = 0.35$ and the Charlette formulation (eq. 3.14) with constant $\beta = 0.35$. The dynamic model fits the experiments much better than the non-dynamic models. This result shows that non-dynamic models assume the equilibrium between the flame surface and the turbulence motion and predict the wrinkling factor's constant values for different turbulence characteristics. The constant fractal model predicts the correct evolution of the total flame radius but overestimates the experimental values because the wrinkling factor is too big at the early stages when the flame has not yet reached equilibrium with turbulence. On the contrary, Charlette et al. (2002a) non-dynamic model reproduces quite well the initial flame development because of a lower wrinkling factor due to a low turbulence intensity u'. Throughout a priori analysis of a DNS simulation of a lean premixed PRECCINSTA burner, Veynante and Moureau (2015) investigated the wrinkling factor's behavior. The show that the Favre filter's approximation with a averaged one is adequate (eq. 3.12). However, a constant fractal dimension ($\beta + 2$) would correspond to a uniform

[1]The total flame radius was defined as the radius of the spherical flame having the same total surface $R_p = \sqrt{S_t(t)/4\pi}$, where S_t is total flame surface $S_t(t) = \int \Xi_\Delta |\nabla \bar{c}| d\nu$

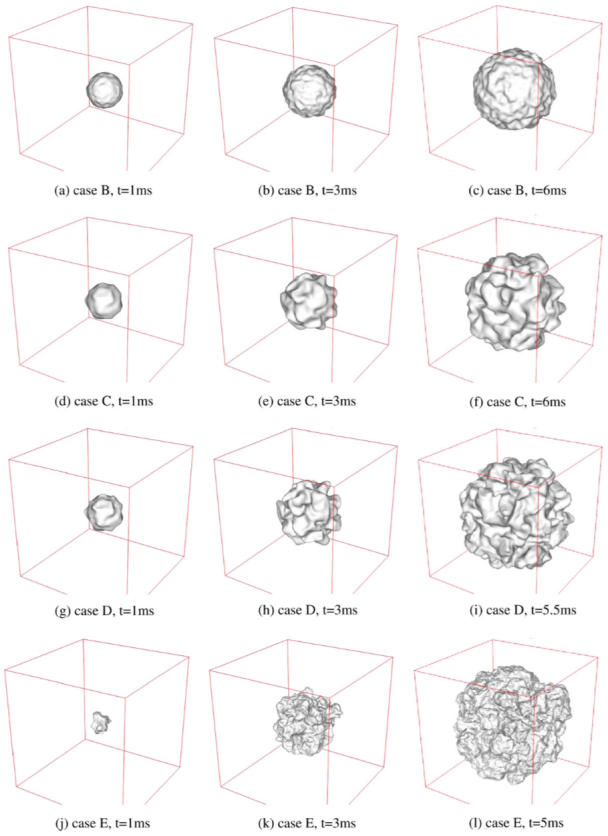

Figure 3.9 – *Iso-surface for* $\tilde{c} = 0.5$ *resolved progress variable for flame kernel growing in different turbulent environments (RMS turbulent velocities u' and integral length scales L). Case A: laminar case, u'= 0 (not shown). Case B: u' = 0.18 m/s; L = 3.0 mm. Case C u' = 0.34 m/s; L = 6.5.0 mm. Case D: u' = 0.51 m/s; L = 6.0 mm. Case E: u' = 3.0 m/s; L = 10.0 mm. The length of computational domain is 60 mm for the low turbulence case B to D, and 120 mm for high turbulence case E. Filter size* $\Delta = 7\Delta x$, Δx *is the mesh size (Wang et al., 2012).*

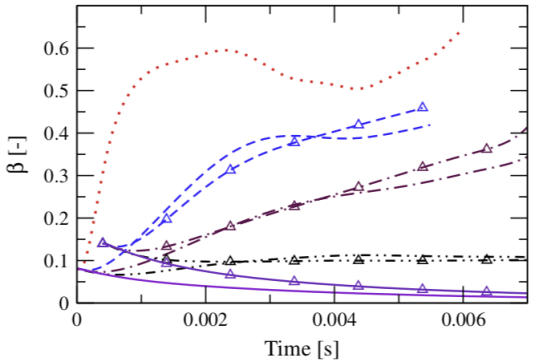

Figure 3.10 – *Dynamic evolution of the model parameter β for different initial turbulent intensities u' and two LES filter size of $\Delta = 7\Delta x$ (without symbols) and $\Delta = 10\Delta x$ (with symbols). Initial turbulence conditions are the same than in figure 3.9 (Wang et al., 2012).*

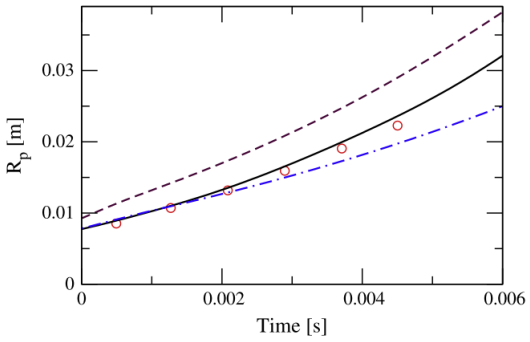

Figure 3.11 – *Evolution of the total flame radius R_p using the dynamic model (solid line), non-dynamic fractal model with constant $\beta = 0.35$ (dashed line) and Charlette formulation model with $\beta = 0.5$ (dotted-dashed line). Symbols denote experimental data shifted by 3.3 ms in time to fit initial conditions. The filter size is $\Delta = 7\Delta x$. Case C (Wang et al., 2012).*

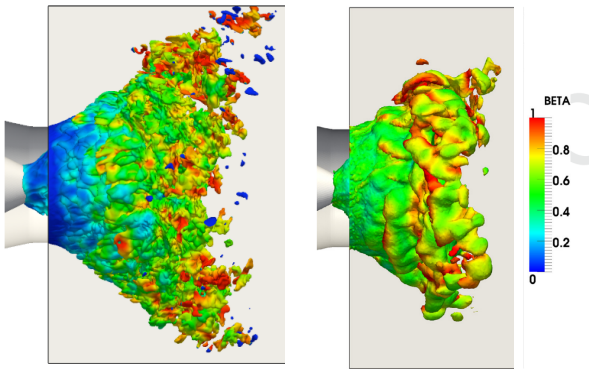

Figure 3.12 – *An instantaneous flame surface obtained is colored by the value of the model parameter β. DNS a priori computation of β (left). LES colored by the values parameter β computed a posteriori (right) (Veynante and Moureau, 2015).*

wrinkling factor over the flow-flied, which is not necessarily verified. They also show that the Charlette formulation of the wrinkling factor (eq. 3.14) is saturated most of the time.
Preliminary a posteriori tests were also presented, proving the robustness of the dynamic model. Figure 3.12 compares an instantaneous field of the progress variable iso-surface colored by the value of the model parameter β computed a priori and a posteriori. Mouriaux et al. (2017) improved and validated the dynamic model in an engine configuration. They emphasized that interaction of flame fronts and interaction with solid boundaries can be problematic once they induce large non-physical values of β. They explained that contrary to flames at the atmospheric condition, the combustion filter to flame thickness ratio Δ/δ_c can be critical and difficult to treat numerically. In piston engines, the flame front is very thin ($\approx 10\mu m$), the ratio Δ/δ_c is very high (≈ 200) leading to high unexpected values of Ξ_Δ when $\beta > 0.9$. Based on 1D laminar flames, they proposed two adaptations, one for the interaction between two flame fronts and one for the interaction of the flame fronts with solid boundaries (Mouriaux et al., 2017).

3.2.4 Indirect approaches for non-premixed flames

In large eddy simulation of non-premixed combustion, instead of solving transport equations for all of the numerous species in a typical chemical mechanism and modeling the unclosed chemical source terms, the detailed chemical processes can be reduced to a system of tracking scalars. Typically, two scalars are considered: a mixture fraction variable, which tracks the mixing of fuel and oxidizer, and a progress variable, which tracks the global extent of reaction of the local mixture (Pierce and Moin, 2004) (Pierce and Moin 2004). Accurate prediction of non-premixed turbulent combustion using LES requires detailed modeling of the mixing between fuel and oxidizer at scales smaller than

the LES filter resolution. In flamelet models of non-premixed combustion, the small-scale mixing process is quantified by two parameters: the subfilter scalar variance and the subfilter scalar dissipation rate (Kaul et al., 2013). Thus, the dynamic formalism has also been employed to compute these sub-grid quantities that enter non-premixed combustion models (Reveillon and Vervisch, 1998; Pierce and Moin, 1998, 2004; Balarac et al., 2008; Kaul et al., 2013). These procedures are denoted "indirect approaches" to differ from the previous one that involves reaction rate terms directly. Reveillon and Vervisch (1998) have proposed extensions of the PDF method to LES, and a dynamic approach was used to close the turbulent micro-mixing term in the PDF transport equation. Pierce and Moin (1998) proposed a simple scaling relation for the sub-grid scale variance where the scaling coefficient was computed dynamically. The variance dissipation rate was also obtained using a dynamic procedure assuming equilibrium with the local variance production rate. Based on their previous work, Pierce and Moin (2004) simulate a methane-fuelled coaxial jet combustor and captured the unsteady, lifted flame dynamics observed in the experiment, and obtained good agreement with the experimental data. Balarac et al. (2008) carried out a priori tests based on 5123 direct numerical simulation data of forced homogeneous isotropic turbulence and evaluate several subfilter variance models for the mixture fraction. They proposed a new dynamic procedure that improves predictive accuracy. Kaul et al. (2013) developed a dynamic non-equilibrium model for variance and dissipation rate, based on a scale similarity assumption, and simulated a turbulent lifted ethylene flame. They concluded that the use of the dynamic procedure increases the accuracy of the non-equilibrium modeling approach.

3.3 Conclusions

In this chapter, the dynamic formulation for the wrinkling flame factor Ξ_Δ has been explained. Several questions come up when it comes to couple the formulation with a combustion model: the Germano-like identity formulation or the parameters entering the wrinkling model. In literature, the dynamic formulation has been coupled with flame surface models in premixed configurations. Charlette et al. (2002b) used the dynamic formulation, coupled with the TFLES model, to simulate a 3D premixed flame in decaying isotropic turbulence by validating results against a DNS. Wang et al. (2011) simulated a Bunsen flame with a global formulation. They showed that the value of the parameter β increases with the Reynolds number of the jet. Hosseinzadeh et al. (2016) proposed a dynamic formulation coupled with Flame Generated Manifolds (FGM) combined with the TFLES model to simulate a lean premixed jet. They focus on the influence of the local and global formulation for such a configuration. Detailed and rigorous analysis of the formulation's parameters has

been done by Volpiani et al. (2016). In another work, Volpiani et al. (2017b) simulated the PRECCINSTA burner in stable and unstable conditions. They used local and global formulation and introduced a wall correction to predict low wrinkling factors near the wall.
The dynamic formulation has also been used with the FTACLES model. Schmitt et al. (2013) adopted the dynamic formulation with a global and semi-local formulation to simulate the Tecflam burner. Then, Schmitt et al. (2015) simulated the turbulent Bunsen flame over different operating conditions using global and local formulation and the Germano-like identity for the reaction rate and the flame surface density. Other significant works have been carried out with the flame surface density models (FSD). Wang et al. (2012) simulated a flame kernel, while Veynante et al. (2012) investigated a turbulent swirl burner. Mouriaux et al. (2017) used the dynamic formulation for a Piston Engine configuration. The results encourage the idea to investigate the possible benefits of the model to non-premixed configurations.

Part II

Model Development

Chapter 4

Counter Flow Laminar Diffusion Flame

Although designed for premixed flame, the Thickened Flame Model (TFLES) has been used for non-premixed configurations without a theoretical foundation. The objective of this chapter is to investigate the effects of the model for a non-premixed flame. The study is carried out by considering the analytical solutions of a constant density laminar counter-flow diffusion flame. The density variation's impact due to the thermal expansion is then taken into account by solving numerical simulation with a compressible solver. Comparisons with analytical solutions are possible by using the Howarth-Dorodnitzyn transformation. Furthermore, the effect of the application of a flame sensor is analyzed. For such a configuration, the prediction of significant quantities such as the global heat release and species distribution turns to be misleading because of the model's mathematical formulation. However, predictions for the particular configuration are still possible to a certain extent, and possible solutions are examined.

Contents

4.1 Introduction

As discussed in section 2.7.1.2, the Thickened Flame Model (Colin et al., 2000) has been used and validated for several applications. Designed for premixed flames, it consists in thickening the flame front by conserving the laminar flame speed. It has been successfully used for premixed and partially premixed (Angelberger et al., 1998; Colin et al., 2000), and also non-premixed configurations but without theoretical support (Legier et al., 2000).
To understand non-premixed flames' behavior, it becomes essential to choose a reference diffusion flame for the investigation. The literature on diffusion flame is abundant (Linan and Crespo, 1976; Bilger, 1980; Peters, 1984), and the most straightforward steady-state non-premixed configuration is the laminar counter-flow diffusion flame. This flame does not present any laminar flame speed, while its thickness depends on the strain rate. Those characteristics are inconsistent with the TFLES formulation, based on the conservation of laminar flame speed.
Shum-Kivan (2017) tried to quantify the effects of the grid refinement of the diffusion flame front to obtain an estimation of the required value of F. He also investigated the effect of the interaction with the turbulence, identifying two main impacts: the variation of the strain rate and the wrinkling of flame resulting in a gain of flame surface (Poinsot and Veynante, 2012). In the present work, the thickening operation's impact is investigated independently of the grid size to understand the exact behavior of the model.
In section 4.2, the analytical formulation of the TFLES model for a counter-flow flame is derived by assuming constant density with and without a flame sensor. In section 4.3, the computational configuration is presented. Results are presented and discussed for the TFLES application and the flame sensor adoption in section 4.3.3. Section 4.4 proposes solutions for the laminar counterflow configuration. For each one of them, suggestions and drawbacks are discussed.

4.2 Analytical formulation

4.2.1 Thickened counter-flow steady strained planar flame

In the context of LES of premixed flame, the flame thickness is too tiny, compared to the size of the cell grid, to be resolved. As mentioned in section 2.7.1.2, a common technique consists in thickening the flame front artificially, while preserving the laminar flame speed (O'Rourke and Bracco, 1979; Butler

and O'Rourke, 1977). Following simple theories of laminar premixed flame, the flame speed S_L and the flame thickness δ_L^0 (Williams, 1985; Kuo, 2005):

$$S_L \propto \sqrt{D_T \dot{\omega}} \quad ; \quad \delta_L \propto \frac{D_T}{S_L} \propto \sqrt{\frac{D_T}{\dot{\omega}}} \tag{4.1}$$

where D_T is the thermal diffusivity and $\dot{\omega}$ is the reaction rate. By increasing the thermal diffusivity by a factor F and decreasing the reaction rate by the same factor:

$$D_T \rightarrow F\ D_T \tag{4.2}$$

$$\dot{\omega} \rightarrow \frac{\dot{\omega}}{F} \tag{4.3}$$

the flame speed S_L remains unchanged. The model is so applied to a laminar steady counter-flow diffusion flame as shown in figure 4.1 So, by considering:

- infinitely fast chemistry assumption;
- neglecting the gradient along the flame front (Williams, 1985; Peters, 2000);
- constant diffusion D for all the species

the global mass balance equation for the mixture fraction z (Eq. 1.60 in section 1.3) with the thickened flame formulation rewrites as:

$$\rho u_1 \frac{\partial z}{\partial x_1} = \frac{\partial}{\partial x_1}\left(\rho F D \frac{\partial z}{\partial x_1}\right) \tag{4.4}$$

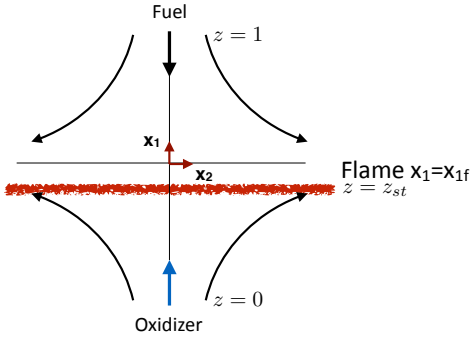

Figure 4.1 – *Planar counter flow flame domain.*

Since the analysis is carried out for a steady strained planar counterflow diffusion flame configuration, shown in figure 4.1, the flow is characterised by the potential flow relationship (Lamb and Caflisch, 1993):

$$\frac{\partial \rho u_2}{\partial x_2} = -\frac{\partial \rho u_1}{\partial x_1} = \rho a \tag{4.5}$$

where a is the strain rate.
By considering constant strain rate a and constant density ρ, from equation 4.5 one can write:

$$\begin{aligned} u_1 &= -a\, x_1 \\ u_2 &= a\, x_2 \end{aligned} \tag{4.6}$$

Substituting in Eq. (4.4) leads to:

$$-ax_1 \frac{\partial z}{\partial x_1} = FD \frac{\partial^2 z}{\partial x_1^2} \tag{4.7}$$

The boundary conditions of equation 4.7 for a counter flow diffusion flame, shown in figure 4.1, are:

$$z(x_1 \to +\infty) = 1 \tag{4.8}$$
$$z(x_1 \to -\infty) = 0 \tag{4.9}$$

By considering the a-dimensional axial coordinate:

$$\zeta = x_1 \sqrt{\frac{a}{2D}} \tag{4.10}$$

equation 4.7 can be further reshaped as:

$$\frac{\partial^2 z}{\partial \zeta} + \frac{2\zeta}{F} \frac{\partial z}{\partial \zeta} = 0 \tag{4.11}$$

A general solution of equation 4.11 writes as:

$$z = \kappa \operatorname{erf}\left(\frac{\zeta}{\sqrt{F}}\right) + \theta \tag{4.12}$$

where κ and θ are two constant that depend on the boundary conditions and the exponential error function is defined as:

$$\operatorname{erf}(\zeta) = \frac{2}{\sqrt{\pi}} \int_0^{\zeta} \exp\left(-\zeta^2\right) d\zeta \tag{4.13}$$

and it verifies $\operatorname{erf}(-\infty) = -1$ and $\operatorname{erf}(+\infty) = 1$.
The solution of equation 4.11 and its gradient, with boundary conditions (4.8) and (4.9), are respectively:

$$z = \frac{1}{2}\left(1 + \operatorname{erf}(\frac{\zeta}{\sqrt{F}})\right) = \frac{1}{2}\left[1 + \operatorname{erf}\left(x_1 \sqrt{\frac{a}{2FD}}\right)\right] \tag{4.14}$$

and

$$\frac{\partial z}{\partial \zeta} = \frac{1}{\sqrt{\pi F}} \exp\left(-\frac{\zeta^2}{F}\right) \qquad \text{and} \qquad \frac{\partial z}{\partial x_1} = \sqrt{\frac{a}{2\pi FD}}\, \exp\left(-x_1^2 \frac{a}{2FD}\right) \tag{4.15}$$

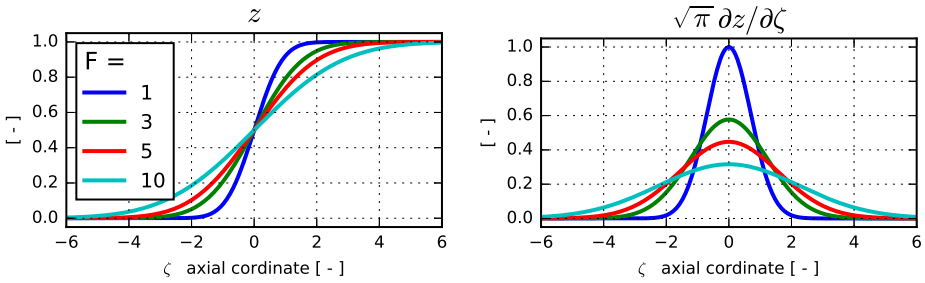

(a) (b)

Figure 4.2 – *Analytical solution of counter-flow laminar flame. (a) Distribution of the mixture fraction z; (b) Distribution of the non-dimensional gradient of the mixture fraction defined as* $\sqrt{\pi}(\partial z)/(\partial \zeta)$.

The distribution of the mixture fraction (Eq. 4.14) and its gradient (Eq. 4.15) are shown in figures 4.2(a) and 4.2(b). The thickening factor smoothens the distribution of the mixture and decreases the gradients.
The diffusion thickness can be related to the gradient of the passive scalar (Poinsot and Veynante, 2012). So considering eq 4.15 leads to:

$$\delta_F = \frac{1}{\max(\partial z/\partial x_1)} = \sqrt{\frac{2\pi DF}{a}} \propto \sqrt{F} \tag{4.16}$$

So, the scalar dissipation rate (from Eq. 1.80) becomes:

$$\chi_F = 2FD\left(\frac{\partial z}{\partial x_1}\right)^2 = \frac{a}{\pi}\exp\left(-x_1^2\frac{a}{FD}\right) \tag{4.17}$$

Another significant quantity is the heat released by the flame per unit surface. For a 1-step chemical reaction mechanism, it is linearly related to the reaction rate integrated over the flame front. This last quantity can be expressed like the molecular diffusion rate of the fuel towards the reaction zone (Poinsot and Veynante, 2012):

$$\dot{\Omega}_F = \int_{x_{1f}-}^{x_{1f}+} \dot{\omega}\ dx_1 = \left[\rho FD\frac{\partial Y_F}{\partial x_1}\right]_{x_{1f}^-}^{x_{1f}^+} = \rho FD\left[\frac{\partial Y_F}{\partial x_1}\right]_{x_1=x_{1f}^+} \tag{4.18}$$

$$\dot{\Omega}_F = \rho FD\left[\frac{\partial Y_F}{\partial z}\right]_{x_1=x_{1f}^+}\left[\frac{\partial z}{\partial x}\right]_{x_1=x_{1f}^+} \tag{4.19}$$

In infinitely fast chemistry fuel and oxidizer cannot coexist at the same location. So the fuel mass fraction on the fuel side can be written as ($z > z_{st}$) is (Burke and Schumann, 1928; Poinsot and Veynante, 2012):

$$Y_F = Y_F^1\left(\frac{z - z_{st}}{1 - z_{st}}\right) \tag{4.20}$$

where Y_F^1 is the fuel mass fraction on the fuel tank side ($z = 1$).
Substituting equations (4.20) and (4.15) in equation (4.19) gives

$$\dot{\Omega}_F = -\rho \frac{Y_F^1}{1 - z_{st}} \sqrt{\frac{aFD}{2\pi}} \exp\left(-\frac{\zeta_f^2}{F}\right) \tag{4.21}$$

where ζ_f corresponds to the flame location:

$$\zeta_f = \sqrt{F}\,\mathrm{erf}^{-1}(1 - 2z_f)$$

and:

$$\dot{\Omega}_F = -\rho \frac{Y_F^1}{1 - z_{st}} \sqrt{\frac{aFD}{2\pi}}\, g(z_{\mathrm{st}}) \quad \text{with} \quad g(z_{\mathrm{st}}) = \exp\left(-\left[(\mathrm{erf}^{-1}(1 - 2z_{\mathrm{st}}))^2\right]\right) \tag{4.22}$$

Considering the integral reaction rate of the non-thickened solution

$$\dot{\Omega}_0 = -\rho \frac{Y_F^1}{1 - z_{\mathrm{st}}} \sqrt{\frac{aD}{2\pi}}\, g(z_{\mathrm{st}}) \tag{4.23}$$

leads to

$$\frac{\dot{\Omega}_F}{\dot{\Omega}_0} = \sqrt{F} \tag{4.24}$$

Equation 4.24 indicates that the thickening operation increases the heat released by the flame by a factor $\sqrt{F}$. Furthermore, equation (4.22) states that the thickened flame burns like a non-thickened flame with a strain rate aF.
Finally, table 4.1 resumes the formulation for the mixture fraction z, scalar dissipation χ_F and the reaction rate integrated over the flame front $\dot{\Omega}_F$.

Quantity	Expression
mixture fraction	$\frac{1}{2}\left[1+\operatorname{erf}\left(x_1\sqrt{\frac{a}{2FD}}\right)\right]$
scalar dissipation	$\chi_F = \frac{a}{\pi}\exp\left(-x_1^2\frac{a}{FD}\right)$
global reaction rate	$\dot{\Omega}_F = -\rho\frac{Y_F^1}{1-z_{st}}\sqrt{\frac{aFD}{2\pi}}g(z_{st})$, with $g(z_{\mathrm{st}}) = \exp\left(-\left[(\operatorname{erf}^{-1}(1-2z_{\mathrm{st}}))^2\right]\right)$

Table 4.1 – *TFLES model for laminar counter-flow non-premixed flame. Expressions for mixture fraction, scalar dissipation and reaction rate integrated over the flame front (global reaction rate).*

4.2.2 Sensor Formulation

Multiplying the diffusivity by a factor F modifies the physical properties of the entire domain. In premixed flames, fuel and oxidizer are mixed before burning, so the diffusivity does not influence the mixture's composition. Unfortunately, for non-premixed and partially premixed regimes, the flame strongly depends on the species' diffusion transport towards the flame front. As already mentioned in section 2.7.1.2, the flame can be thickened locally to preserve the diffusion fluxes outside the flame front. Following Legier et al. (2000), the thickening factor is related to a flame sensor as: :

$$F(z) = 1 + (F-1)\theta_F \tag{4.25}$$

where $theta_F$ is the flame sensor which varies from 0 (outside the flame front) to 1 (inside the flame front). To allow a simple analytical analysis, the sensor is modeled here as a rectangular function over z. For sake of simplicity the position of the flame is assumed to be at $\zeta = 0$, so that $z(0) = z_{\mathrm{st}}$. By considering a span of $2\Delta z$ (shown in figure 4.3) the sensor is modelled as:

$$F(z) = \begin{cases} 1\,, \theta_F = 0 & \text{for } z < z_{st} - \Delta z \text{ or } z > z_{st} + \Delta z \\ F\,, \theta_F = 1 & \text{for } z_{st} - \Delta z < z < z_{st} + \Delta z \end{cases} \tag{4.26}$$

where Δz represents half span of the sensor in the mixture fraction space.
In order to simplify the analysis (and to better visualize the comparison with the simulations) the composition of the mixture is supposed to be stoichiometric at $z_{st} = 0.5$, and figure 4.3 shows the respective shape of the sensor.
Equation (4.7) can be written for the thickened and the non-thickened zone in a piecewise-like function in non-dimensional coordinate ζ (Eq. 4.10), which

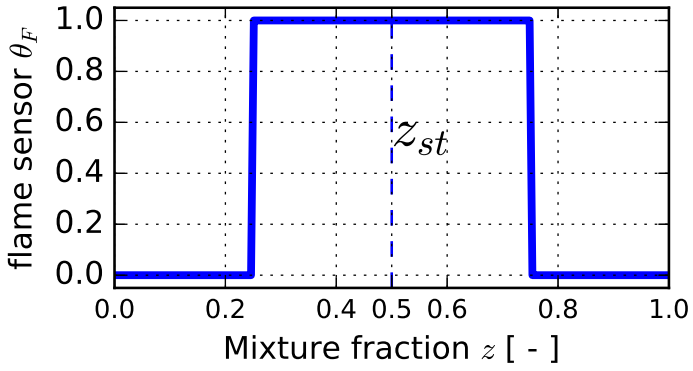

Figure 4.3 – *Rectangular function of the flame sensor θ_F as a rectangular function over the mixture fraction z centered in $z_{st} = 0.5$, with a span $2\Delta z = 0.5$.*

gives :

$$z = \lambda \operatorname{erf}(\zeta/\sqrt{F}) + \mu \qquad \text{for } z_{\text{st}} - \Delta z < z < z_{\text{st}} + \Delta z \tag{4.27}$$

$$z = \lambda' \operatorname{erf}(\zeta) + \mu' \qquad \text{for } z < z_{\text{st}} - \Delta z \text{ or } z > z_{\text{st}} + \Delta z \tag{4.28}$$

where λ' and λ are coefficients proportional to the slopes of the mixture passive distribution for the non-thickened and thickened zone, respectively. μ' and μ are two constant to be determined.
Due to the symmetry of problem, the solution is considered for $z > z_{\text{st}}$, and the part for $z < z_{\text{st}}$ can be retrieved analogously.
The boundary condition of system 4.27-4.28 are the same of Eq. 4.7 ($z_{\zeta \to +\infty} = 0$). So $\mu = z_{\text{st}}$ and $\mu' + \lambda' = 1$ lead to:

$$z = \lambda \operatorname{erf}(\zeta/\sqrt{F}) + z_{\text{st}} \qquad \text{for } z_{\text{st}} < z < z_{\text{st}} + \Delta z \tag{4.29}$$

$$z = \lambda' \operatorname{erf}(\zeta) + 1 - \lambda' \qquad \text{for } z > z_{\text{st}} + \Delta z \tag{4.30}$$

and the gradients:

$$\frac{\partial z}{\partial \zeta} = \frac{2\lambda}{\sqrt{\pi F}} \exp\left(-\frac{\zeta^2}{F}\right) \qquad \text{for } z_{\text{st}} < z < z_{\text{st}} + \Delta z \tag{4.31}$$

$$\frac{\partial z}{\partial \zeta} = \frac{2\lambda'}{\sqrt{\pi}} \exp\left(-\zeta^2\right) \qquad \text{for } z > z_{\text{st}} + \Delta z \tag{4.32}$$

Defining ζ_L as the junction position for which eq. (4.29) = eq. (4.30) allows to write the continuity conditions in term of mixture fraction distribution and in term of mass flux respectively:

$$z(\zeta_L^-) = z(\zeta_L^+) = z_{\text{st}} + \Delta z \tag{4.33}$$

$$FD \left.\frac{\partial z}{\partial \zeta}\right|_{\zeta_L^-} = D \left.\frac{\partial z}{\partial \zeta}\right|_{\zeta_L^+} \tag{4.34}$$

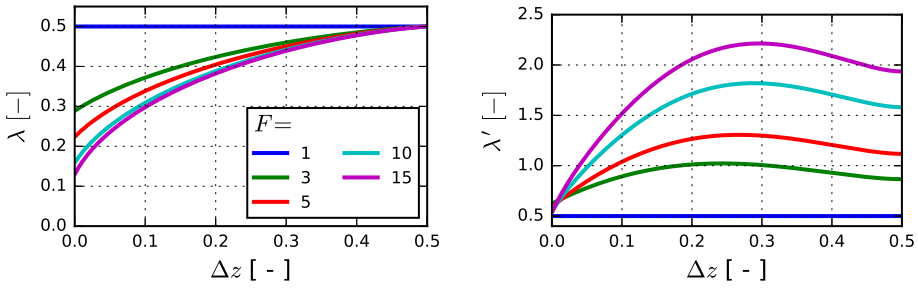

(a) (b)

Figure 4.4 – *(a): values of λ of solution of equation (4.38). λ is related to the slope of mixture fraction's profile at the flame position ζ_f; (b) values of λ' obtained from Eq.(4.36). λ' is related to the slope of the mixture fraction's profile ot the junction position η_L.*

By considering equations (4.29), (4.30), (4.31) and (4.32), system 4.33-4.34 can be written as:

$$\lambda \,\mathrm{erf}\left(\frac{\zeta_L}{\sqrt{F}}\right) + z_{\mathrm{st}} = \lambda' \left[\mathrm{erf}(\zeta_L) - 1\right] + 1 \tag{4.35}$$

$$\lambda\sqrt{F}\exp\left(-\frac{\zeta_L^2}{F}\right) = \lambda' \exp(-\zeta_L^2) \tag{4.36}$$

which leads to:

$$\lambda\sqrt{F}\exp\left(-\frac{\zeta_L^2}{F}\right) = \frac{\lambda \mathrm{erf}\left(\frac{\zeta_L}{\sqrt{F}}\right) + z_{\mathrm{st}} - 1}{\mathrm{erf}(\zeta_L) - 1}\exp\left(-\zeta_L^2\right) \tag{4.37}$$

and by considering eq. (4.29), one can write:

$$\begin{aligned} &\lambda = \frac{z_{\mathrm{st}} + \Delta z - 1}{\sqrt{F}} \frac{\exp\left[-\zeta_L^2\left(1 - \frac{1}{F}\right)\right]}{\mathrm{erf}(\zeta_L) - 1} \quad \text{with} \quad \zeta_L = \sqrt{F}\,\mathrm{erf}^{-1}\left(\frac{\Delta z}{\lambda}\right) \\ &\lambda = f(\Delta z, F) \end{aligned} \tag{4.38}$$

Equation 4.38 does not admit an explicit solution, and it can only be solved recursively. However, it directly relates the slopes of the distribution λ (and consequently λ' and the junction position ζ_J) to the thickening factor F and the size of the sensor Δz.
Figure 4.4(a) shows a graphical representation of the solution of equation 4.38, whether 4.4(b) plots the values of λ' from equation (4.36). The increasing of thickening factor decreases the slope of the thickened part (λ) while increases the slope at the junction position (λ'). This fact means that the gradient of z at the junction position increases.
Figures 4.5(a) and 4.5(b) show the solution z and its gradient for a fixed value

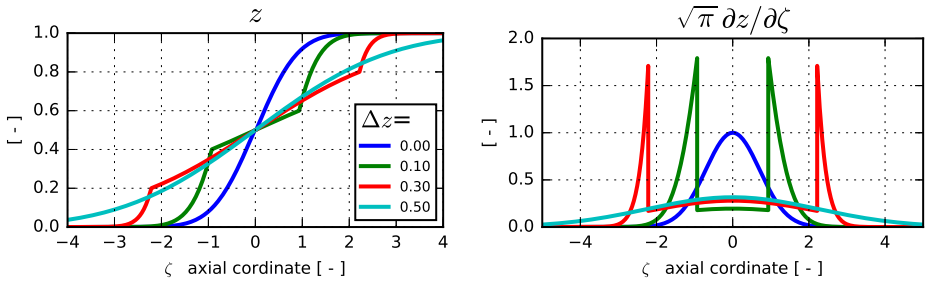

(a) (b)

Figure 4.5 – *Analytical solution of counter-flow laminar flame with the application of a flame sensor. The plots are considered for a fixed value of the thickening factor* $F = 10$. *(a) Mixture fraction* z *profile; (b) Profile of the non-dimensional gradient of the mixture fraction defined as* $\sqrt{\pi}(\partial z)/(\partial \zeta)$.

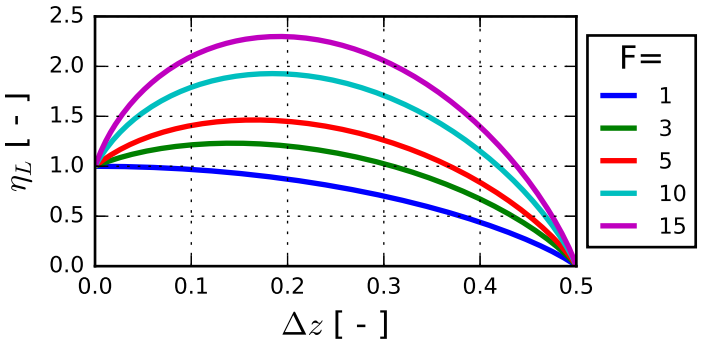

Figure 4.6 – *Representation of* η_L, *from equation (4.39), for different values of the thickening factor* F *and sensor size* Δz. *It represents the gradient of the mixture fraction evaluated at the junction position* ζ_L.

of the thickening factor and different values of the sensor size Δz. Although the thickening operation reduces the gradient on the thickened zone, it drastically increases the gradient at the junction position, where it is maximal.
The gradient peak at the junction position can be determined from equation (4.32) by considering the gradient the junction position as:

$$\eta_L = \sqrt{\pi}\frac{\partial z}{\partial \zeta}\bigg|_{\zeta=\zeta_L^+} = 2\lambda' \exp\left(-\zeta_L^2\right) \quad \text{with} \quad \zeta_L = \sqrt{F}\,\mathrm{erf}^{-1}\left(\frac{\Delta z}{\lambda}\right) \tag{4.39}$$

The solution of equation (4.39) is shown in figure (4.6). The gradient peak increases with F while decreases with large values of the sensor size Δz in line with the fact that the maximum size of sensor Δz corresponds to no sensor at all, i.e., simple thickening operation.
Finally, the integrated reaction rate over the flame front is estimated from

equation (4.19) by considering Eqs. (4.20) and (4.31):

$$\dot{\Omega}_F = \rho \frac{Y_F^1}{1 - z_{st}} 2\lambda \sqrt{\frac{aDF}{2\pi}} \tag{4.40}$$

which leads to

$$\frac{\dot{\Omega}_F}{\dot{\Omega}_0} = \lambda\sqrt{2\,F} = f(\Delta z, F) \tag{4.41}$$

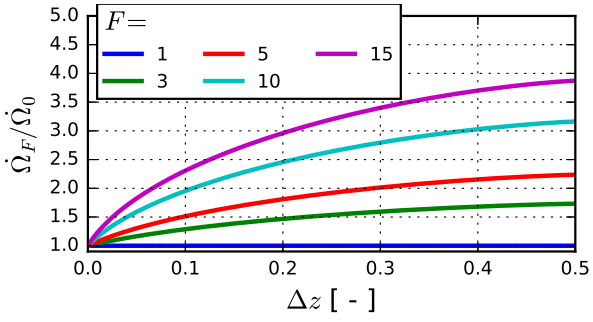

(a)

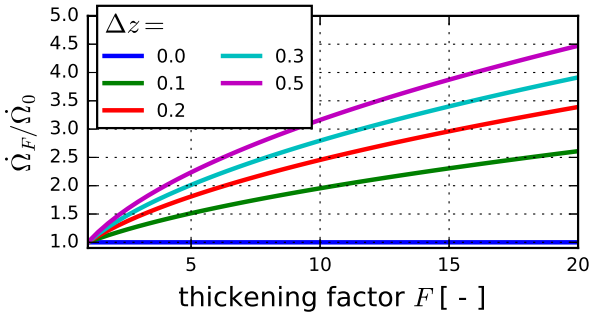

(b)

Figure 4.7 – *Graphical representation of equation (4.41). The non-dimensional reaction rate is plotted over the filter size Δz and the thickening factor F. (a) plots the curves over Δz for different values of F; (b) plots the curves over F for different values of Δz.*

Figure 4.7 displays the solution of equation (4.41).
The value of $\dot{\Omega}_F/\dot{\Omega}_0$ increases with the thickening factor F, and with the sensor size Δz. This means that a small over-prediction can be obtained with small thickening factor F (see Fig. 4.7(a)) and sensor size Δz (see Fig. 4.7(b)). However, by considering the gradients shown in figure 4.6, small sensor size values drastically increase the gradient's peaks opposite to the thickening operation's purpose.

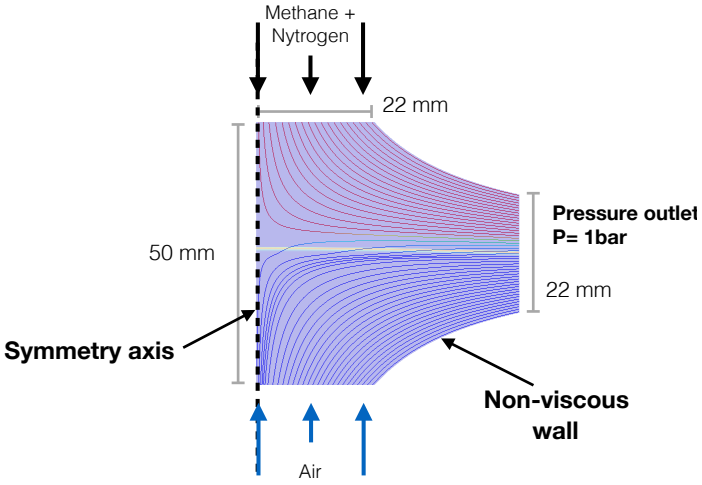

Figure 4.8 – *Computational domain. The central axis is considered as symmetry axis and treated as a non viscous wall. The boundary walls of the domain are non-viscous and shaped like the streamlines of potential counter flow.*

4.3 Simulations

The computations have been run for a planar domain with symmetry axis as shown in figure 4.8. The axial speed at both inlets is $U = 5m/s$, so that the global strain rate a_g defined as the sum of the velocities over the distance between the inlets $L = 5$ cm is:

$$a_g = \frac{U_{\text{Fuel}} + U_{\text{Oxidizer}}}{L} = 200s^{-1} \tag{4.42}$$

The shape of the domain is designed to follow the streamlines of a counter-flow fitly.
The reactants are injected both at the temperature of 300 K. Methane is injected on the fuel side diluted with nitrogen (fuel mass compositions: $Y_{CH_4} = 0.1$, $Y_{N_2} = 0.9$), while on the oxidizer the air is enriched in oxygen (oxidizer mass composition: $Y_{O_2} = 0.4$, $Y_{N_2} = 0.6$). The resulting stoichiometric mixture fraction is $z_{st} = 0.5$, which simplifies the visual comparisons with the analytical results.
The chemical reaction mechanism is a simple one-step forward reaction: $CH_4 + 2\,O_2 \longrightarrow CO_2 + 2\,H_2O$. The rate progress of the reaction $\mathcal{Q}$ is modelled with the Arrhenius law (from Eq. 1.42):

$$\mathcal{Q} = A \exp\left(\frac{E_a}{RT}\right)[CH_4][O_2]^2 \tag{4.43}$$

where the pre-exponential factor is $A = 1.1 \times 10^{10}$mol/(s cm^3), the activation energy $E_a = 20000$cal/mol, $R = 8.314$J/(mol T) is the gas constant, and $[CH_4]$

and $[O_2]$ are the species molar concentrations. The molecular viscosity μ is modelled with a linear law in function of temperature as:

$$\mu = \mu_0 \left(\frac{T}{T_0} \right) \tag{4.44}$$

where $\mu_0 = 1.8410^{-5}$kg/(ms) is a reference value at temperature $T_0 = 300$K.
The grid consists of 1.8 million triangular elements with a characteristic length size of the cell of 0.05 mm, that, considering the thickness of the non-thickened flame 0.8 mm, assures the resolution of the flame front with around 15 points.
The simulations have been run with the compressible solver AVBP (Schönfeld and Rudgyard, 1999) with a Lax-Wendroff finite volume convection scheme (Lax and Wendroff, 1960), and no artificial viscosity has been used.
The computation has been initialized with the analytical solution at constant density (Eqs. 4.6 and 4.14).
The inlet boundary conditions are velocity-imposed, while the outlet is constant pressure at 1 bar and the boundary walls are non-viscous.

4.3.1 Results with constant thickening

The profiles are extracted along the symmetry axis. Figure 4.9 shows the species mass fractions and temperature profiles extracted along the symmetry axis of the domain for thickening factor up to $F = 10$. Monotonous profiles, such as mixture fraction z, methane, and oxygen mass fractions, are spread by the thickening operation, and the value at the center position (axial coordinate = 0) remains unchanged, while intermediate species mass fraction, such as CO_2 H_2O, and temperature profile preserve their peaks. The thickening operation smoothens the distribution and preserves the peaks.
Figure 4.10 evidences the effects of thermal expansion on density and consequently on the axial speed, strain rate and scalar dissipation.
Equation (4.14), from the analytical investigation, suggests that the mixture fraction profiles scale with the axial coordinate as $x_1/\sqrt{F}$. This is still verified by the simulation and the species as shown in figure 4.11.
Density profiles are also found to scale with the same factor (analytical derivation assumes constant density), as shown in 4.12(a). However, the local strain rate increases in the center position, as shown in Fig. 4.12(b).
Equation (4.17) states that the scalar dissipation rate scales only in space, while the peak remains unchanged. Figure 4.13 shows the results of the simulation. All the curves collapse on each other. However, the center position peak rises with F since the local strain rate is not constant across the flame front.

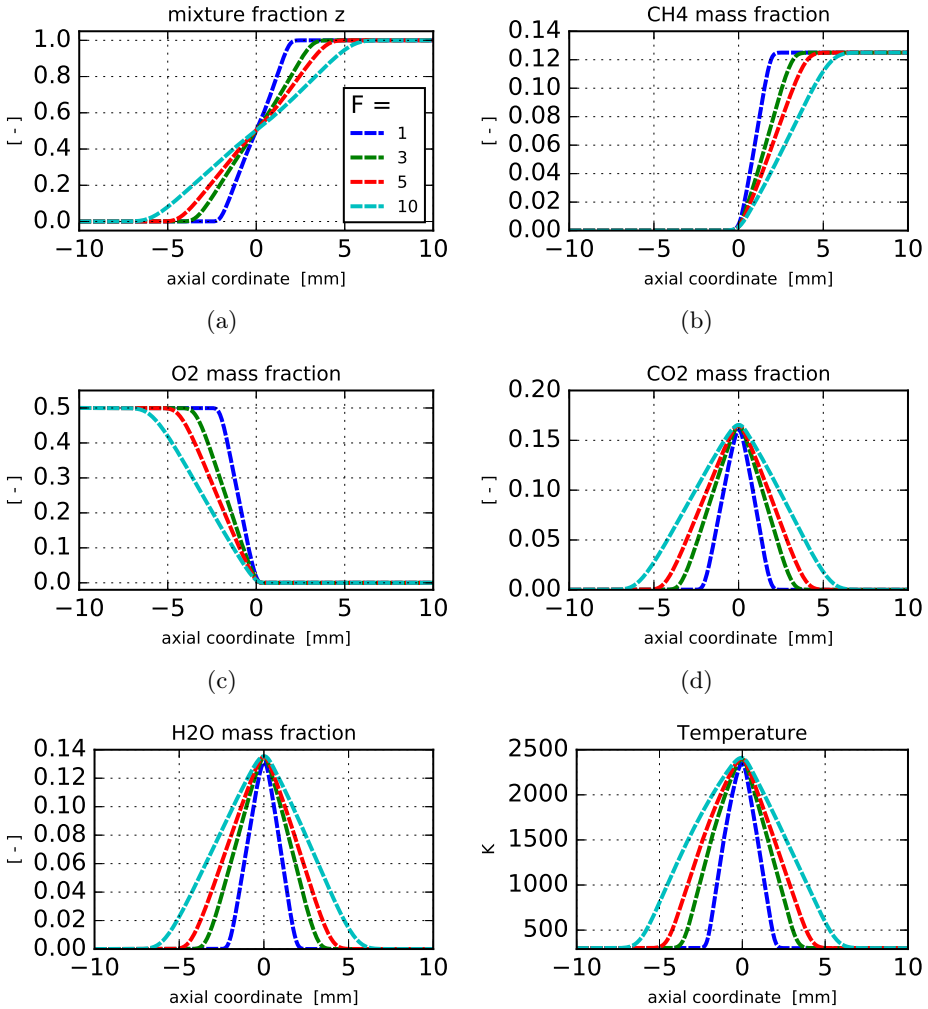

Figure 4.9 – *Profiles of species mass fractions and temperature along the symmetry axis of the computational domain with different value of the thickening factor F.*

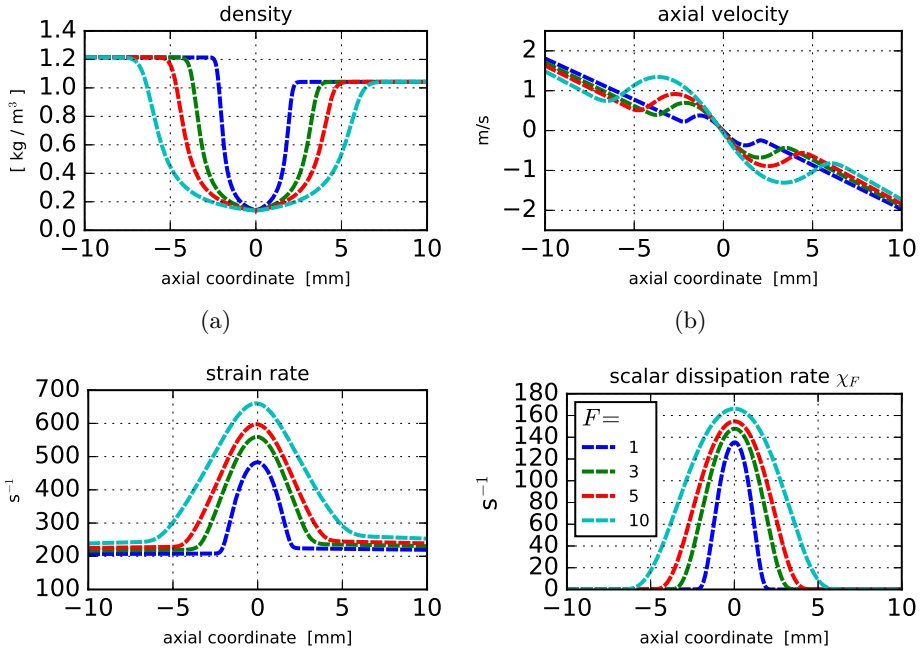

Figure 4.10 – *Profiles of density (a), axial velocity (b), strain rate (c) and scalar dissipation (d) along the symmetry axis of the computational domain for different values of the thickening factor F.*

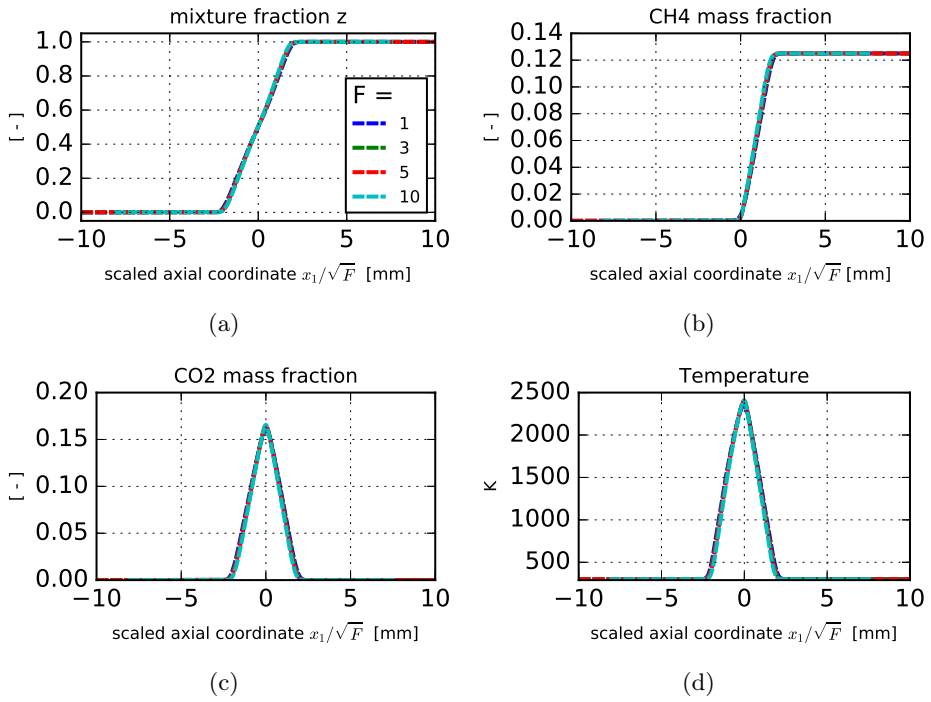

Figure 4.11 – *Profiles of species mass fractions and temperature along the scaled axial coordinate $x_1/\sqrt{F}$ for different value of the thickening factor F.*

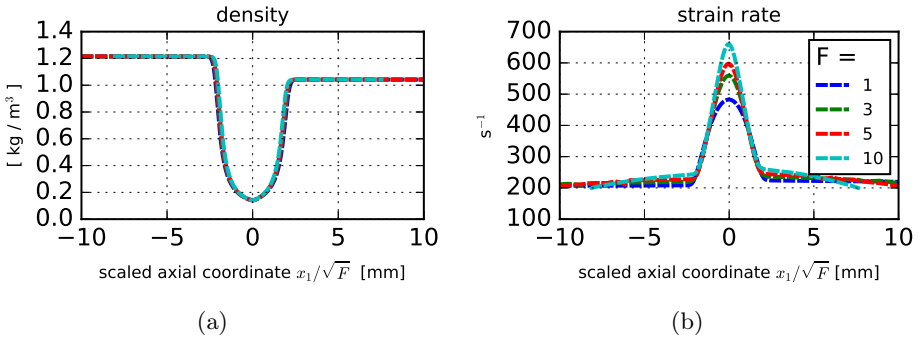

Figure 4.12 – *Profiles of density (a), and strain rate (b) along scaled axial coordinate $x_1/\sqrt{F}$ for different value of the thickening factor F.*

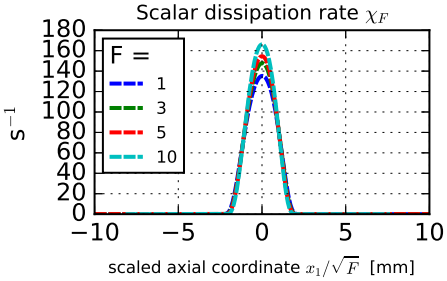

Figure 4.13 – *Profile of scalar dissipation rate χ_F over the scaled coordinate $x_1/\sqrt{F}$ for different values of the thickening factor F.*

4.3.2 Use of a flame sensor

Species mass fractions and temperature profiles obtained by using the flame sensor defined by relation (4.26) are shown in figure 4.14 for a fixed value of the thickening value $F = 10$.
As already discussed in the analytical formulation, small sensor values Δz preserve the profiles. However, the application of a flame sensor increases the gradients at the junction positions.

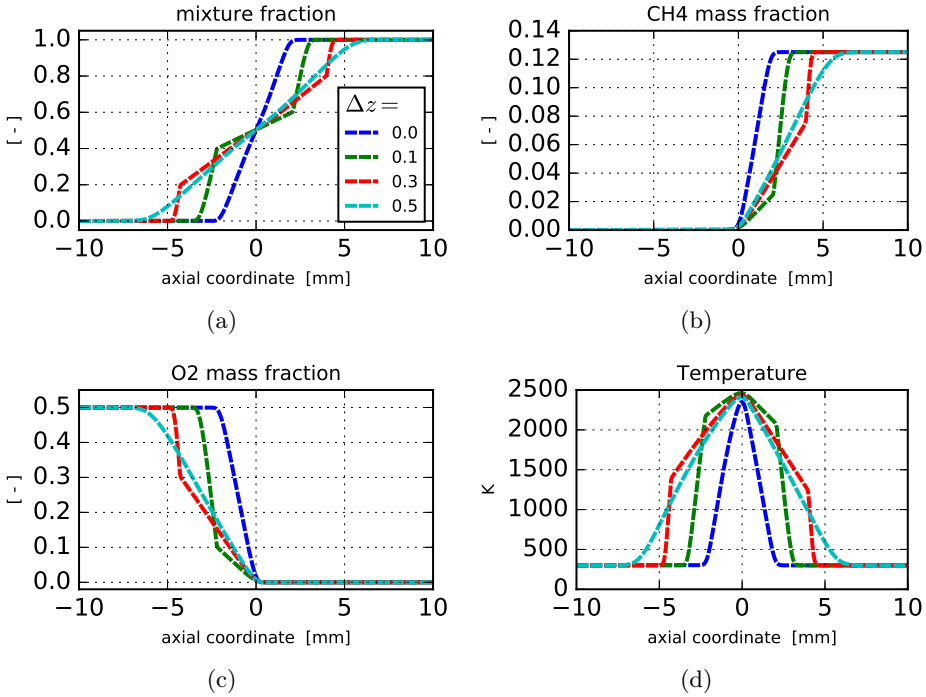

Figure 4.14 – *Profiles of mixture fraction, species mass fractions CH_4 O_2 and temperature along the symmetry axis of the computational domain with sensor application with fixed value of thickening factor $F = 10$ and different values of the sensor size Δz.*

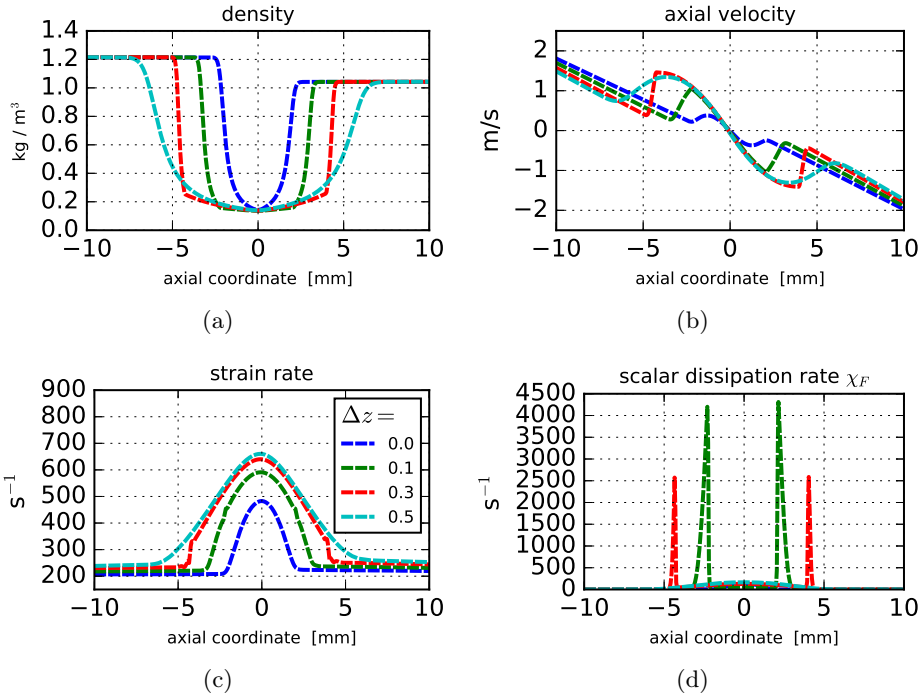

Figure 4.15 – *Profiles of density (a), axial velocity (b), strain rate (c) and scalar dissipation rate χ_F (d) along the symmetry axis of the computational domain with sensor application with fixed value of thickening factor $F = 10$ and different values of the sensor size F.*

Figure 4.15 evidences the sensor's effect on density, axial speed, and strain rate. The quantities are impacted solely in the domain portion delimited by the sensor. Furthermore, there is a significant impact on the scalar dissipation rate since the relation (4.17) is no longer valid.
The thickening operation with the sensor drastically reduces the scalar dissipation (and the gradients) at the flame position x_f, but unfortunately, sharp peaks appear at the junction positions in accordance with the analytical investigation.

4.3.3 Comparisons with analytical solutions

The simulations are here compared with the analytical investigation discussed in section 4.2. The thermal expansion, present in the simulations, can be taken into consideration by using the Howarth-Dorodnitzyn transformation. A new space-variable X is defined as (Linan and Crespo, 1976; Williams, 1985; Cuenot and Poinsot, 1996):

$$X = \frac{1}{\rho_0} \int_{x_0}^{x_1} \rho(x')dx' \tag{4.45}$$

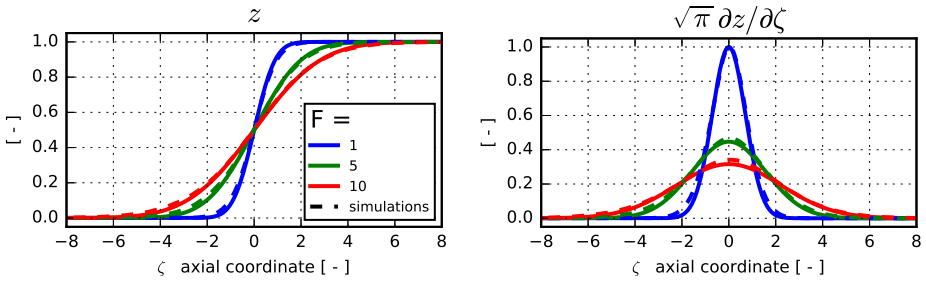

(a) (b)

Figure 4.16 – *Thickening operation comparison for the mixture fraction (a) and mixture fraction gradient (b) profiles. Continuous lines represent the analytical solutions, dashed lines represent results from simulation in the Howarth-Dorodnitzyn axial coordinate.*

where x_0, corresponding to ρ_0, is a reference location, namely the stagnation point. Replacing x_1 by X equation 4.45 leads to:

$$\frac{\partial}{\partial x_1} = \frac{\partial X}{\partial x_1}\frac{\partial}{\partial X} = \frac{\rho}{\rho_0}\frac{\partial}{\partial X} \tag{4.46}$$

By assuming $\rho^2 D = \rho_0^2 D_0$ and considering relations (4.45) and (4.46), it possible to recast the mixture fraction balance equation (Eq. 4.4) as[1]:

$$-aX\frac{\partial z}{\partial X} = FD_0\frac{\partial^2 z}{\partial X^2} \tag{4.47}$$

which is exactly equation 4.7 with the same boundary conditions, so all the solutions retrieved at constant density can be applied to the new density-space variable X.

Figure 4.16 compares mixture fraction and mixture fraction gradient profiles. The agreement between analytical and numerical solutions is fine.

Figure 4.17 shows that simulation well matches the analytical dependence in $\sqrt{F}$ of the integrated reaction rate over the flame front (Eq. 4.24). The slight deviation from the analytical solution for higher values of F is probably due to the thermal expansion or the interaction with the domain boundaries. Figure 4.18 compares mixture fraction and mixture fraction gradient profiles when using different values of the flame sensor thickness Δz for a fixed value $F = 10$ of the thickening factor. Once again, the agreement is excellent. Lastly, figure

[1] the assumption of constant $\rho^2 D$ is physically related to the viscosity law of the mixture. By assuming constant Schmidt number $\mathrm{Sc} = \mu/(\rho D)$ and a linear dependence of the dynamic viscosity with the temperature $\mu = (\mu_0 T)/T_0$, one can write: $\mathrm{Sc} = (\mu_0 T_0)/(T\rho D)$, and considering the perfect gas law for the mixture: $p = \rho RT/W$, with W the mean molecular weight of the mixture, leads to the relation: $\rho^2 D = (\mu_0 pW)/(T_0 R)$. The condition is verified when the variation of W is negligible.

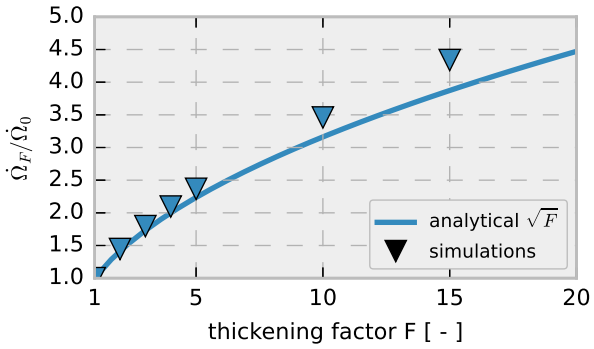

Figure 4.17 – *Integrated reaction rate $\dot{\Omega}_F/\dot{\Omega}_0$ as a function of the thickening factor F. The line represents the analytical relation $\sqrt{F}$, while triangles correspond to numerical simulations.*

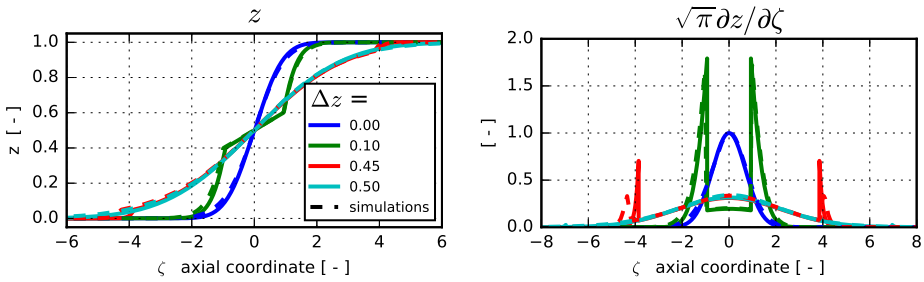

(a) (b)

Figure 4.18 – *Thickening operation with sensor with fixed value of $F = 10$ and different values of sensor size Δz. Comparison for the mixture fraction (a) and mixture fraction gradient (b) profiles. Continuous lines represent the analytical solutions, dashed line represent results from simulation in the Howarth-Dorodnitzyn axial coordinate.*

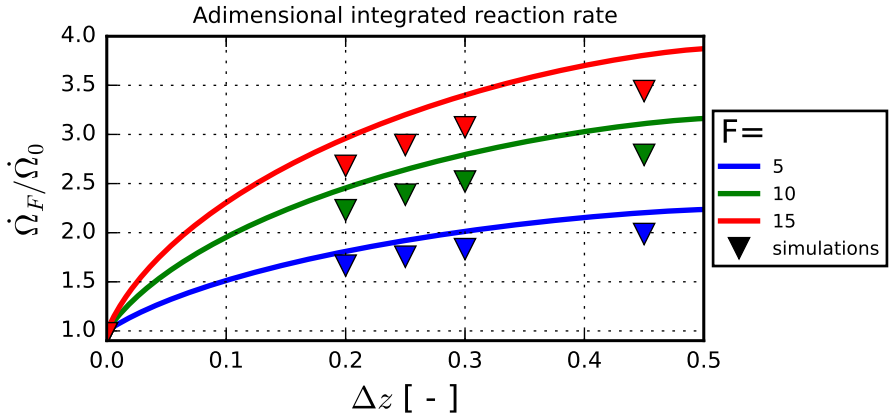

Figure 4.19 – *Integral reaction rate $\dot{\Omega}_F/\Omega_0$ as function of thickening factor and filter size Δz.*

4.19 displays the evolution of the integrated reaction rate as a function of the sensor width for various thickening factor F values. Again, the simulations match the analytical solution, and all the conclusions retrieved in section 4.2 are valid also in the case of variable density.

4.3.4 Outcomes

Analytical investigation and simulations point to the same conclusions. For infinitely fast chemistry, the reaction rate strongly depends on the molecular diffusion (Eq. 4.21), so increasing the diffusion by a factor F necessarily leads to an overestimation. Furthermore, limiting the thickening operation to the flame front by adopting a flame sensor cannot improve the prediction significantly and, unfortunately, introduces high gradients around the thickened zone.
Viable solutions, restricted to the laminar case, can be based on controlling the diffusion outside the thickened zone or shaping the reaction rate directly, or, even more, by modifying the strain rate.

4.4 Solution attempts

Even with the application of a flame sensor, the overestimation of the integral reaction rate persists.
In non-premixed flames, the reaction is regulated by the species' molecular diffusion towards the flame front.
The mathematical formalism of the TFLES model for non-premixed flames presents an intrinsic overestimation of the reaction rate, which can be overcome only with further modeling adjustments.

4.4.1 Modified diffusion coefficient in the outer region

The idea of this method is to control the mass flow of reactants towards the flame front by reducing the diffusion outside the thickened zone of a factor $\alpha < 1$ in order to preserve $\dot{\Omega}_F/\dot{\Omega}_0 = 1$. Since the aim is to modify the diffusion leading to further increase gradients, the methodology is unpractical for real application.
However, A graphical representation of the method is shown in figure 4.20. The balance equation for the mixture fraction (Eq. 4.7) becomes:

$$-ax_1\frac{\partial z}{\partial x_1} = FD\frac{\partial^2 z}{\partial x_1^2} \quad \text{for } z_{\text{st}} - \Delta z < z < z_{\text{st}} + \Delta z \tag{4.48}$$

$$-ax_1\frac{\partial z}{\partial x_1} = \alpha D\frac{\partial^2 z}{\partial x_1^2} \quad \text{for } z < z_{\text{st}} - \Delta z \quad \text{and} \quad z > z_{\text{st}} + \Delta z \tag{4.49}$$

By considering:

- symmetry ($z_{x=0} = z_{st} = 0.5$)

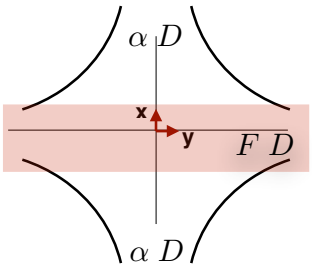

Figure 4.20 – *Graphical representation of the diffusion adjustment method. The idea is to multiply the diffusion coefficient by a factor $\alpha < 1$ outside the thickened zone in order to control the flux of the reactant towards the flame front. Inside the thickened region, the diffusion remains multiplied by the thickening factor F.*

- dimensionless axial coordinate $\zeta = x_1\sqrt{a/\,2D}$
- boundary condition $z(x \to +\infty) = 1$
- continuity condition at a given junction position x_L or ζ_L so that $z^-(\zeta_L) = z^+(\zeta_L)$

it is possible to solve the system (4.48) and (4.49), with mathematical passages similarly to section 4.2.2, which leads to the solution for the mixture fraction profile z and mixture fraction derivative shown in figure 4.21.

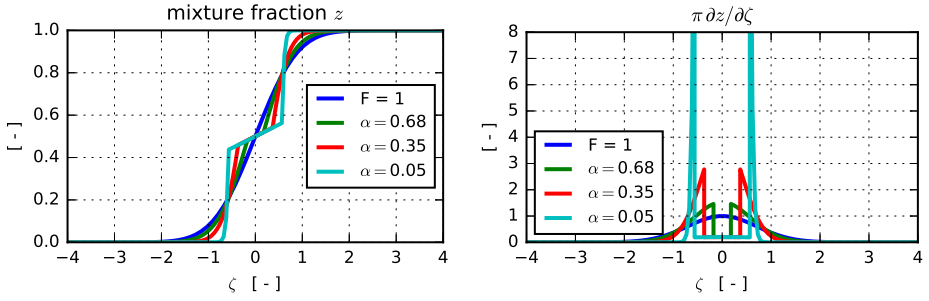

(a) (b)

Figure 4.21 – *Solution of the Diffusion Adjustment method for the mixture fraction distribution (a) and its gradient (b). The thickening factor is fixed at $F = 5$. Different values of α are plotted*

Although theoretically compelling, the modification of the diffusion further increases the gradient at the junction position ζ_L between the thickened and non-

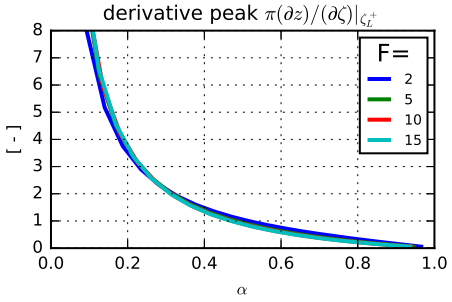

Figure 4.22 – *Derivative peak profile on the junction position ζ_L as function of α with different values of the thickening factor F.*

thickened zone as shown in figure 4.22. Computations with this methodologies have not been possible because of the gradient peaks and the restricted range of values of α applicable, which does not cover the reaction flame thickness. This methodology is sharply limited by mathematical construction.

4.4.2 Modified Reaction Rate

The idea of this methodology is to directly modify the governing law of the reaction rate in order to preserve its integral over the flame front. The species balance equation of diffusion flame (Eq. 1.65) in TFLES formulation writes as:

$$\rho\frac{\partial Y_k}{\partial t} = \frac{\dot{\omega}_k}{F} + \frac{1}{2}\rho F\chi\frac{\partial^2 Y_k}{\partial z^2} \tag{4.50}$$

So for steady solution, the reaction rate $\dot{\omega}_k/F$ can be written:

$$\frac{\dot{\omega}_k}{F} = -\frac{1}{2}F\rho D\left(\frac{\partial z}{\partial x}\frac{\partial z}{\partial x}\right)\frac{\partial Y_k}{\partial z^2} \tag{4.51}$$

So the thickened integrated reaction rate writes as:

$$\dot{\Omega}_F = \int_{x_{1f}^-}^{x_{1f}^+}\frac{\dot{\omega}_k}{F}dx_1 = \int_0^1 -\frac{1}{2}\rho F D\frac{\partial z}{\partial x_1}\frac{\partial Y_k}{\partial z^2}\,dz \tag{4.52}$$

where x_{1f} is the flame position.
By assuming infinitely fast chemistry (i.e. the reaction take places in a small neighbourhood of the flame position x_f where $z = z_{st}$), the quantity $\partial z/\partial x$ inside the integral of equation (4.52) can be approximated with its value at $z = z_{\mathrm{st}}$. So from equation (4.15), one can write:

$$\frac{\partial z}{\partial x} \approx \sqrt{\frac{a}{\pi 2DF}} \tag{4.53}$$

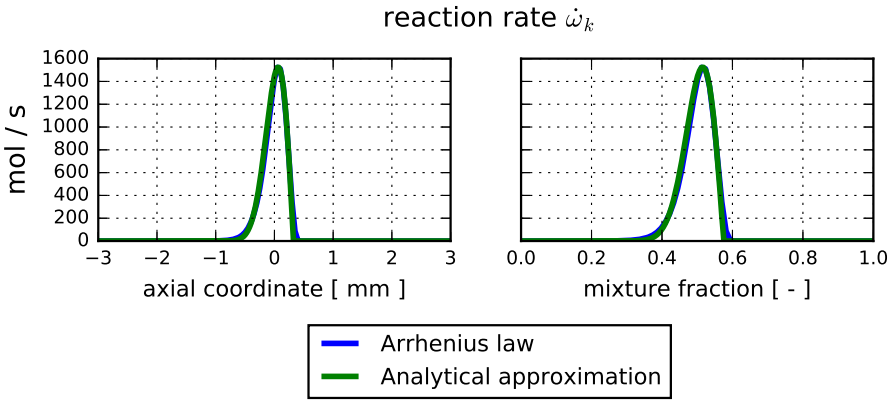

Figure 4.23 – *Comparison of the Arrhenius law for the reaction rate distribution with the analytical expression (Eq. 4.55).*

So equation (4.52) becomes:

$$\dot{\Omega}_F = \int_{-\infty}^{+\infty} \rho \sqrt{\frac{DF}{2\pi}} \frac{\partial Y_k^2}{\partial^2 z} \partial z \propto \sqrt{F} \tag{4.54}$$

A way to remove the dependence of the $\dot{\Omega}_F$ from $\sqrt{F}$ is to modify the shape of the term $\partial Y_k^2/\partial^2 z$ with a function of $1/\sqrt{F}$. This can be done by rewriting the reaction rate as:

$$\dot{\omega}_{kF} = -\rho F D \left(\frac{\partial z}{\partial x}\right)^2 \frac{f(z)}{\sqrt{F}} \tag{4.55}$$

where $f(z)$ is a function properly shaped to overlap the Arrhenius law when no thickening is applied preserving the quantity $\dot{\Omega}_F$, and it is equal to:

$$f(z) = \max\left[0, g(z)\right] \tag{4.56}$$

where $g(z)$ is an analytical function which follows a Rayleigh distribution as:

$$g(z) = k\frac{z'}{\delta} \exp\left(-\frac{z'^2}{2\delta^2}\right) \qquad \text{with} \qquad z' = 1 - z - z_{\text{st}} + \delta\sqrt{\frac{\pi}{2}} \tag{4.57}$$

k and δ are two constants numerically computed in order to retrieve the integrated reaction of the non-thickened solution with a thickening factor $F = 1$ ($\dot{\Omega}_{F=1} = \dot{\Omega}_0$). The resulting analytical function of the reaction rate (Eq. 4.55) is compared with the numerical one (without thickening) in figure 4.23.
By integrating equation 4.55 over the flame front domain, there is no more dependence of the integral reaction rate from the thickening factor F, to a certain extent. The resulting reaction rate distributions are shown in figure 4.24.
Since the modified reaction rate does not depend anymore on species conservation, the species' conservation law is not respected anymore. Hence unburnt gases are present in the domain, as shown for the fuel mixture fraction in figure 4.25. The fuel is present even on the oxidizer side ($z < z_{\text{st}}$), so the infinitely fast chemistry assumption is no more valid.

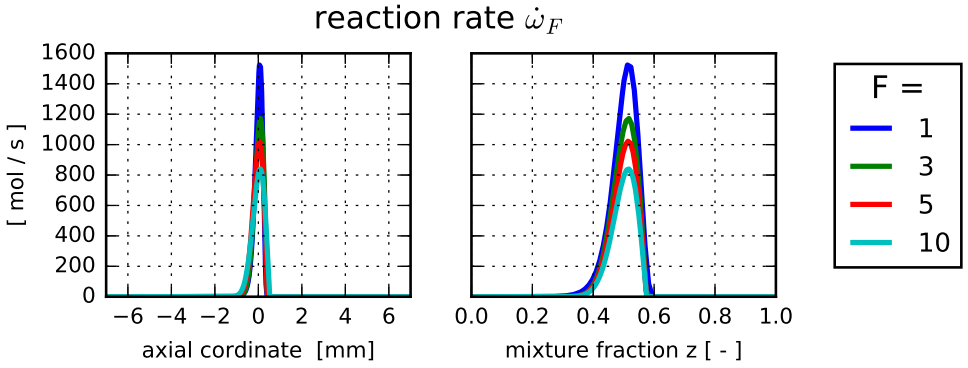

Figure 4.24 – *Reaction rate distribution for the Modified Reaction Rate methodology. Distribution over the mixture fraction space and along the axial coordinate of the flame.*

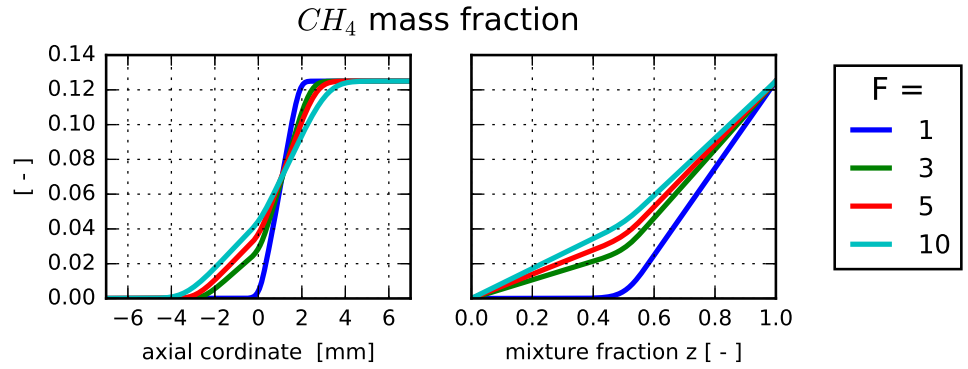

Figure 4.25 – *Fuel mass fraction distribution for the Modified Reaction Rate methodology. Distribution over the mixture fraction space and along the axial coordinate of the flame.*

4.4.3 Fictitious Strain Rate

Still by considering equation 4.22, this methodology consists in changing strain rate a, so that:

$$\frac{\dot{\Omega}_F}{\dot{\Omega}_0} = \sqrt{F\frac{a_F}{a}} = 1 \tag{4.58}$$

and:

$$a_F = \frac{a}{F} \tag{4.59}$$

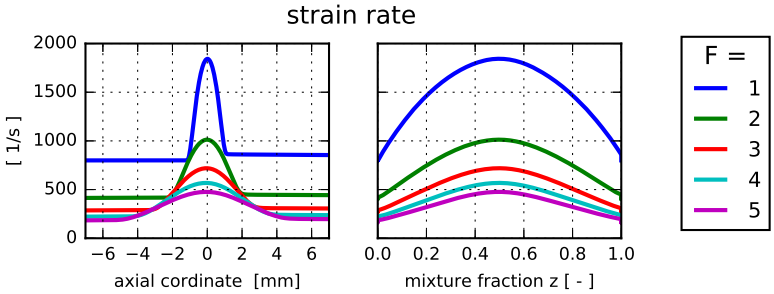

Figure 4.26 – *Distribution of strain rate for the Modified Strain Rate Methodology. For the purpose the reference flame in non-thickened solution presents a global strain rate of 1000 s^{-1}.*

However, besides the constant density hypothesis, this model is strongly affected because the strain rate is not constant all along the flame front (as shown in Fig. 4.26), which can be a non-negligible source of error in the predictions. Figure 4.27 represents the distribution of the reaction rate $\dot{\omega}_F$ for this last methodology. Although it can be attractive for a simple counter-flow configuration, this methodology cannot be applied for a more general case such as a turbulent diffusion flame since there is no way to control the strain rate.

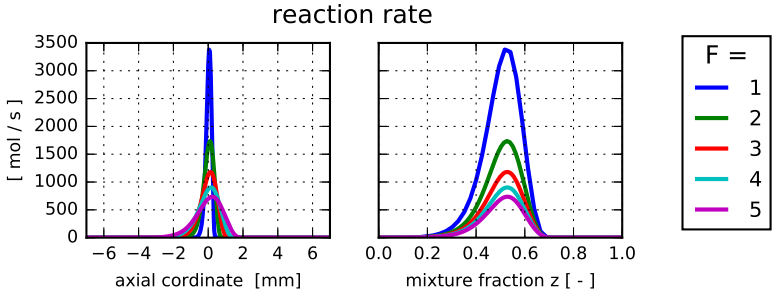

Figure 4.27 – *Distribution of the reaction rate $\dot{\omega}_F$ for the Modified Strain Rate Methodology.*

Figure 4.28 shows the prediction of $\dot{\Omega}_F/\dot{\Omega}_0$ over the thickening factor F for the modified reaction rate and the modified Strain Rate methodologies. Modifying the reaction rate underestimates the global reaction rate for high values of thickening factor, whether the modified strain rate leads to an overestimation.

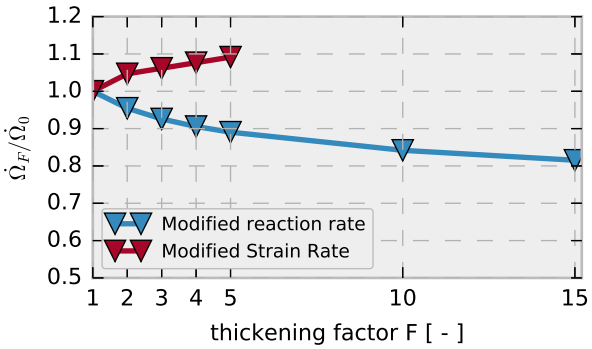

Figure 4.28 – *Comparison of the modified reaction rate and modified strain rate methodologies against the integral reaction rate over the thickening factor*

4.5 Conclusions

In this chapter, the application of the thickened flame model to a laminar counter-flow flame has been investigated. The analytical investigation outcomes are in good agreement with the ones from the simulations, which take into account the density variations due to the thermal expansion.
Nonetheless, the integral heat release across the flame front cannot be preserved since it depends on $\sqrt{F}$. The application of a flame sensor can slightly improve the predictions but induces gradients, at the opposite of the thickened flame formalism's objective.
For infinitely fast chemistry, the molecular diffusion of the species controls the reaction rate. In order to decrease the gradients, the TFLES formalism modifies the diffusion by a factor F, which inevitably leads to a wrong prediction of the reaction rates. Several solutions have been proposed to preserve the target quantity, but none is feasible for practical application.
However, in literature, the TFLES model has been successfully used for non-premixed turbulent flames. The reason lies in the fact that the reaction rate is controlled essentially by the species' turbulent transport towards the flame front. In this case, the application of a flame sensor is beneficial, and the total reaction rate is not significantly affected by the model. Another reason is that often in industrial burners, non-premixed flames react in a partially premixed regime, limiting the thickening model (Legier et al., 2000; Schmitt et al., 2007).
Finally, the analysis has been carried out only for a steady counter-flow flame. An unsteady strained diffusion flame can explain the dynamic of the thickened flame when unsteady conditions are considered since the flame's response can

also play an essential role in the interaction with the turbulence.

Chapter 5

Planar Jet Diffusion Flame

Dynamic models, where model parameters are automatically adjusted from known resolved fields, represent an attractive formulation for large-eddy simulations. Widely used for unresolved momentum transport, this approach has been applied to describe the interaction between turbulence and flame in premixed flames with encouraging results (see chapter 3 details). In this chapter, the model is applied to a diffusion flame configuration. First, a planar jet case is adequately set up as a reference DNS case for the investigation, and the flame structure is investigated. Second, the TFLES model is applied without any efficiency function. The model's effects are investigated qualitatively and quantitatively with the estimation of the heat release and the resolved flame surfaces. Then, the model is coupled with a dynamic formulation for the efficiency function to keep into account the loss of flame surface. The influence of physical (flame wrinkling inner cut-off length scale) and numerical (test filter width, averaging procedure, updating frequency) characteristics of the dynamic model is then investigated. Results are discussed in terms of flame structure and local effects. The behavior of the model is then discussed, and the computational costs are measured.

Contents

5.1 Introduction

Dynamic models have shown to be a convincing tool in large-eddy simulations (LES). The basic idea of such models initially developed to describe sub-grid scale momentum transport (Germano et al., 1991), is to automatically take advantage of the known instantaneous resolved large scales to adjust model parameters automatically. State of the art is explained in section 3.2 of the manuscript.
This chapter aims to investigate the possibility of coupling the dynamic formulation with the TFLES model for turbulent diffusion flame.
Shum-Kivan (2017) has shown that in turbulent non-premixed thickened flames, the heat release is affected by the thickening factor, the local strain rate, and the loss of flame surface due to the thickening flame operation. The heat release increases with the thickening factor and the local strain rate (under the effects on the laminar diffusion flame discussed in the present work chapter 4) and decreases with the loss of flame surface. Shum-Kivan (2017) also tried to quantify those effects with DNS of diffusion counter-flow homogeneous turbulent flames. The effective correction factor is computed by considering the thickening factor, the strain rate correction, and flame surface loss. The correction value is computed as the global heat release ratio of the unrefined case over the DNS reference case. Therefore, it is dependent on the characteristic grid size. Corrections values have been then used to simulate the Sandia D flame (Barlow et al., 2005; Barlow and Frank, 2007). This methodology leads to accurate correction factors and includes the possibility to account for correction factors minor than unity where no wrinkling is present. Furthermore, besides the enormous computational effort to retrieve correction from DNS, the methodology of Shum-Kivan (2017) relates the correction coefficient to the resolution of the grid and flame thickness itself. Instead, the purpose of the dynamic formulation is to retrieve the information from the resolved scales without dependence on the grid resolution.
For the present work, a planar turbulent jet test case is set up. Because of the prohibitive cost of three-dimensional reacting flow computations, two-dimensional simulations turn to be a convenient tool when dealing with flame-vortex interactions (Laverant and Candel, 1989; Poinsot et al., 1991a; Ashurst,

1993) or to evaluate the turbulent transport (Veynante et al., 1997). Furthermore, the relatively light computational effort allows performing a sensitivity analysis of the model by exploring different ranges of values for each parameter. The study is organized as follows:

- a turbulent jet flame test case is set up without a combustion model, where the mesh grid fully resolves the flame front. The simulation, running as LES, turns out to be a quasi-DNS;
- the TFLES model is applied without any efficiency function, and the effects are analyzed and explained;
- the TFLES is applied with a dynamic formulation and the sensitivity analysis of the various parameters is presented;
- finally, conclusions are drawn.

5.2 Test case description

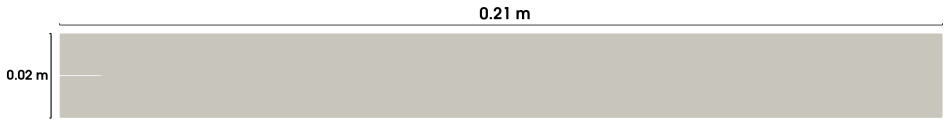

Figure 5.1 – *Computational domain*

The test case is a planar turbulent jet where the computational domain's size is 0.02×0.21 (see figure 5.1), and the splitter plate length is $L = 0.01$ m, and L is considered as reference length all along with the following of the analysis. The configuration reproduces a standard shear turbulent flame. Pure methane is injected from the upper side of the splitter plate at 30 m/s, while pure oxygen is injected on the lower side at 15 m/s.
A viscous mask is applied to correctly evacuate the flow from the domain (shown in figure 5.2). Figure 5.2 shows an instantaneous solution of three main species over the domain and the effect of the viscous mask, which is significant for an axial coordinate of $x/L > 10$.

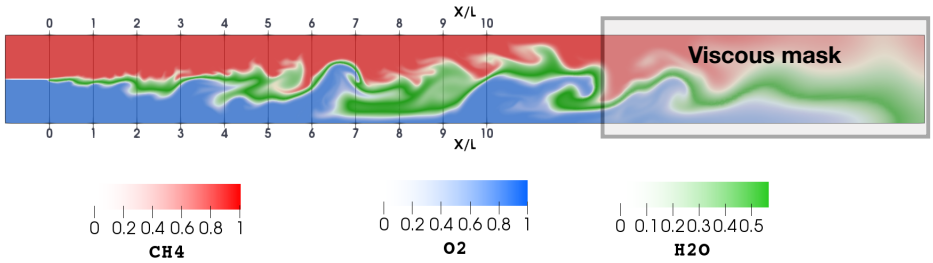

Figure 5.2 – *Instantaneous snapshot of the planar jet test case. Red colour represent CH_4 mass fraction, while blue colour the O_2 mass fraction and green colour the H_2O mass fraction. A viscous mask is applied to a distance of 14 characteristic lengths from the edge of the splitter plate.*

The turbulent fluctuations are injected from both fuel and oxidizer inlet with a superimposed perturbation with a set of modes randomly chosen from a normal distribution (Smirnov et al., 2001). The integral length scale, which represents the most energetic scale in the turbulent spectrum, is chosen one-third of the injection duct width (i.e., $L/3$), while the root mean square of the velocity is set to $u_{rms} = 3$ m/s. The velocity at the splitter plate walls is set to zero to better stabilize the flame. At the peripheral walls, only the velocity normal to the wall is set to zero (slipping condition). All the walls are considered adiabatic. The mesh grid consists of 542'965 triangular cell elements with 273'073 nodes. The triangular cells' characteristic size is 0.1 mm at the splitter plate and remains constant up to an axial distance of $x/L = 12$, where the viscous starts. Figure 5.3 displays the grid resolution at the splitter plate tip, which presents a width of 0.2 mm. A flow-through time is defined as the ratio of axial domain span of 10 L over the mean inlet velocity as $\tau_f = 5$ms.

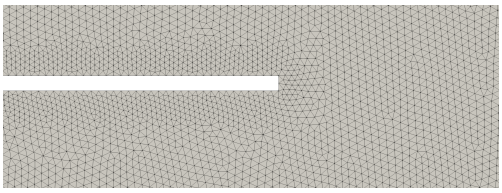

Figure 5.3 – *Mesh resolution zoom on the splitter plate tip.*

For the sake of the analysis, a simple one-step chemical mechanism is adopted to avoid any side complications. The reaction is chosen as the first reaction of the 2S-CM2 simplified mechanism for methane (Bibrzycki and Poinsot, 2010):

$$\mathrm{CH_4} + \frac{3}{2}\,\mathrm{O_2} \longrightarrow \mathrm{CO} + 2\,\mathrm{H_2O} \tag{5.1}$$

The reaction rate is modelled with the Arrhenius law as:

$$k_f = A \exp\left(-\frac{E_a}{R\,T}\right) [\mathrm{CH_4}]^{n_{\mathrm{CH_4}}} [\mathrm{O_2}]^{n_{\mathrm{O_2}}} \tag{5.2}$$

The pre-exponential factor A, activation energy E_a and the reaction exponents $n_{\mathrm{CH_4}}$ and $n_{\mathrm{CH_4}}$ are listed in table:

A [moles of CH_4/(s cm^3)]	E_a [cal/mol]	$n_{\mathrm{CH_4}}$	$n_{\mathrm{O_2},j}$
4.9×10^9	3.50×10^4	0.9	1.1

A unique unity Lewis number is assumed, and the Schmidt number is constant and equal to $Sc = 0.75$ for all the species. Consequently, a mixture fraction z is defined as:

$$z = \frac{sY_{CH_4} - Y_{O_2} + 1}{s + 1} \tag{5.3}$$

where $s = 3$ is a coefficient depending on the molecular mass fraction of the reactants (W_{O_2} and W_{CH4}) and the their respective reaction coefficient in Eq. 5.1 so that:

$$s = \frac{1.5\,W_{O_2}}{W_{CH_4}} = 3 \tag{5.4}$$

The corresponding stoichiometric mixture fraction is $z_{st} = 0.25$.
The computations have been run with the compressible solver AVBP (Schönfeld and Rudgyard, 1999) in finite element formulation with a two-step Taylor-Galerkin convection scheme[1] (Colin and Rudgyard, 2000) and a dynamic Smagorinsly LES model for the subgrid stress tensor (Lilly, 1992).

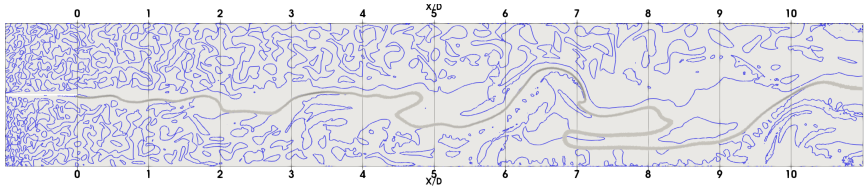

Figure 5.4 – *Iso-contours of vorticity overlapping the reaction rate (gray lines).*

Figure 5.4 shows a snapshot of the vorticity overlapping the reaction rate field. The injected turbulent motions rapidly decay along the first two-length L in the axial direction.

5.2.1 Local flame structure analysis

The flame structure analysis is carried out by extracting quantities from 100 cuts normal to the flame front from a single snapshot, along with the axial

[1] third order in space and time

distance up to 10 characteristic lengths L. The flame front is considered to lie on the iso-line of the stoichiometric mixture fraction $z = 0.25$, and the position along the cuts is determined with a uniform random position generator (Ayachit et al., 2017). The data set extracted from the cuts is then grouped by the cut's length position and the mixture fraction, giving information about the average values in space and mixture fraction framework. Figure 5.5 sketches the cuts over the flame front.

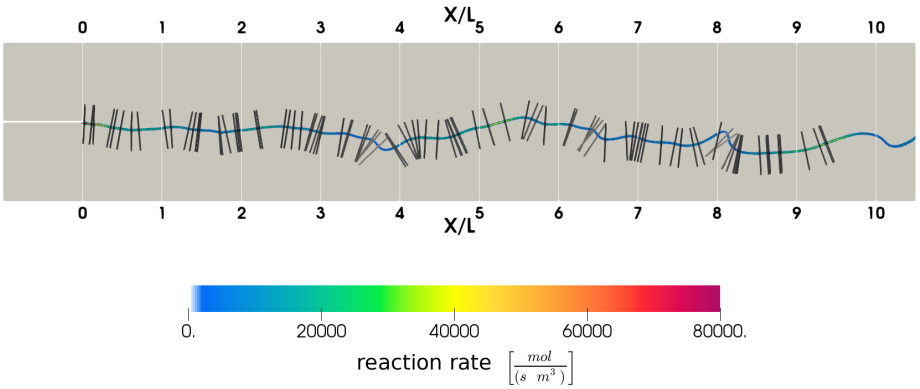

Figure 5.5 – *Positions of cuts for the analysis of the flame structure. The cuts are overlapped with the reaction rate (coloured).*

As a first check, figure 5.6 compares laminar, turbulent, and artificial viscosities. Since the laminar viscosity is much higher than the turbulent one, the simulation turns to be close to a DNS, at least on the flame front. Figure 5.7 shows the scatter plots for the front flame profiles of mass fraction of CH_4 and O_2, while the reaction rate is shown in figure5.8. By considering the species scatter plots, the flame presents a structure compatible with infinitely fast chemistry assumption, which is confirmed by the distribution of reaction rate, close to a Dirac function. It is possible to conclude that the chosen case fulfills the infinitely fast chemistry requirements, and the analytical formulation (see chapter 4) is expected to predict the flame dynamics with good approximation.

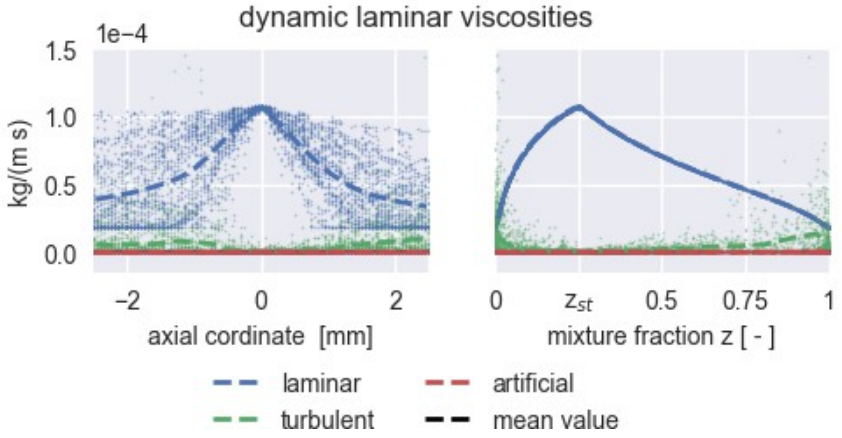

Figure 5.6 – *Flame Front Analysis: comparison of laminar and turbulent viscosities over the flame fronts.*

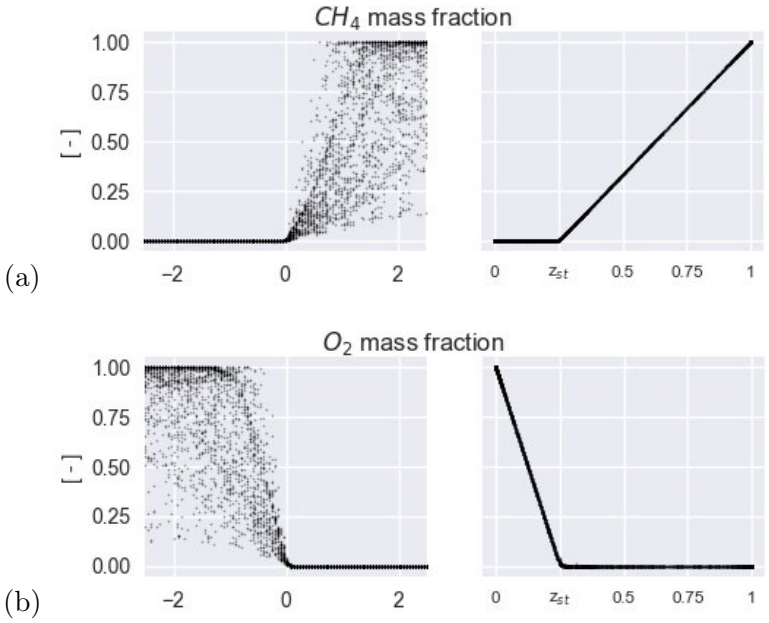

Figure 5.7 – *Scatter plots over the flame front neighbourhood: mass fraction species profiles of CH_4(a) and O_2(b).*

5.2.2 Global flame structure analysis

The global quantities such as heat release and flame surface are here analyzed. The evolution of the global heat release as a function of the downstream x -

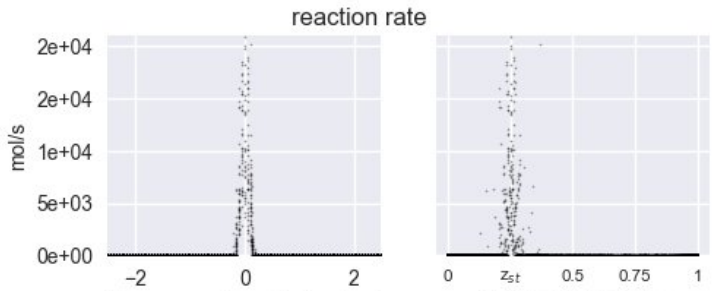

Figure 5.8 – *Reaction rate scatter plot over the flame front neighbourhood.*

coordinate is estimated as:

$$hr_S(x) = \frac{1}{S}\int_{\nu_S} [\dot{\omega}_t]\, d\nu \tag{5.5}$$

where ν_S denotes a volume strip normal to the axial direction with a given width S and [.] represents a time average operator. Figure 5.9 shows the influence of width strip S for different values. The value of averaging strip S does not influence the value of the heat release.

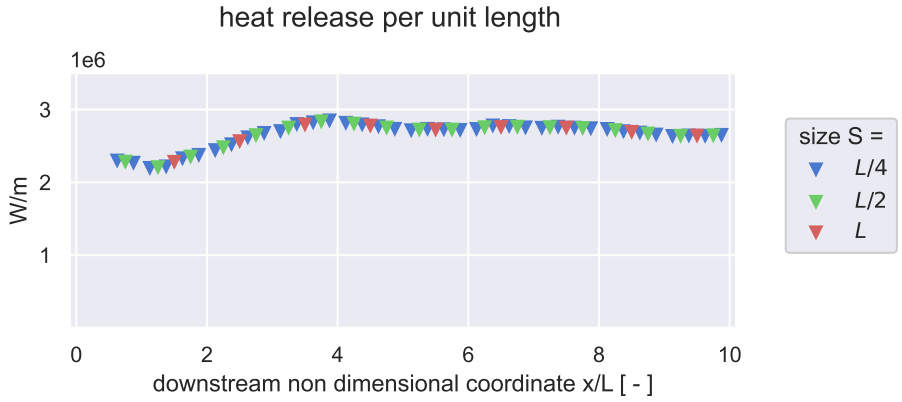

Figure 5.9 – *Evolution of heat release per unit length along the axial direction. The size S represents the width of the volume strip used for the integration and L is the reference length of the domain.*

The flame surface can be investigated with a surface density function. Pope (1988) proposed a formulation based on the conditional surface means. A generalized flame surface density has been proposed by Boger et al. (1998) for turbulent premixed flames. This last formulation is acceptable if the quantity's iso-value surfaces are parallel, which is likely not the case in non-premixed flames. For diffusion flames, the flame surfaces match the stoichiometric iso-surface. In the present work, the flame surface is computed by considering a

portion of the domain defined by a small volume of the neighborhood of stoichiometric mixture fraction z_{st} surface. For a given volume, the resolved flame surface S_{res} is estimated as:

$$S_{res} = \frac{1}{\Delta z} \int_{\nu_{S\Delta z}} |\nabla z| d\nu \tag{5.6}$$

where $\nu_{S\Delta z}$ is the portion of volume strip with a width S and defined where:

$$z_{st} - \frac{1}{2}\Delta z < z < z_{st} + \frac{1}{2}\Delta z$$

The size of Δz should be as small as possible to be close to the correct estimation of the stoichiometric iso-surface, but at the same time large enough to assure a minimum number of grid points to get relevant statistics. Figure 5.10 shows the influence of Δz from a snapshot of the test case. The stoichiometric mixture fraction surface is retrieved for a longitudinal strip of the domain with a 'diving cubes' contouring algorithm (Cline et al., 1988), and then compared with its estimation from equation 5.6 for different values of Δz. This is done for three strips placed at the splitter plate tip and axial coordinate $4L$ and $9L$ respectively. By calling S_{res}^{interp} the flame surface computed with the contouring algorithm, the error of the estimation done by using equation (5.6) is[2]:

$$err = \frac{S_{res} - S_{res}^{\text{interp}}}{S_{res}^{\text{interp}}} \tag{5.7}$$

[2]the data treatment pipelines have been developed by using the C++ open-source library VTK (Schroeder et al., 2016). The library includes a large set of tools for grid based databases. Details can be found at `https://vtk.org`

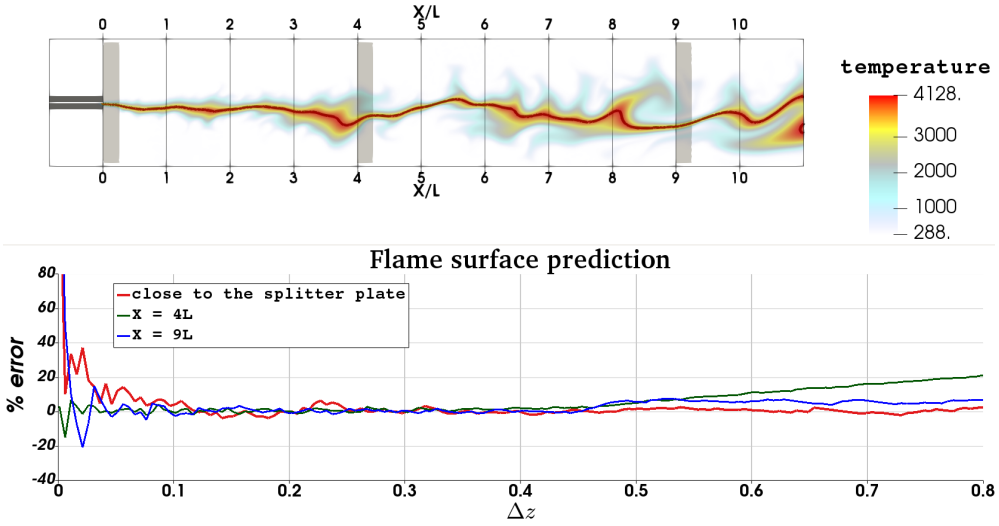

Figure 5.10 – *Estimation of an optimal value of Δz for the test case configuration. Upper figure: instantaneous snapshot ot the temperature field with the iso-line $z = z_{st}$ and position of the considered strips. Lower figure: Representation of the error for the prediction of the flame front for different values of Δz (Eq. 5.7)*

For values of $\Delta z < 0.1$ the error is noising because of the low number of sampled points, especially close to the splitter plate. The accepted range of Δz is between 0.1 and 0.3.
Figure 5.11 shows the axial evolution of the mean resolved wrinkling factor computed as the flame surface into a domain strip over its projection on the longitudinal axis (S) as:

$$\Xi_{res}^{m} = \left[\frac{S_{res}}{S}\right] \tag{5.8}$$

where S is the width of the domain strip considered and the square brackets the average operation over the time. Three different values of Δz are compared with the generic estimation which considers the gradient for the entire range of mixture fraction. Considering the entire range of mixture fraction gradient overpredicts the flame surface in accordance with the analysis of an instantaneous solution shown in figure 5.10. Figure 5.12 represents the flame surface wrinkling for a fixed value $\Delta z = 0.1$ by using different strip's width S for the computation of S_{res} showing the independence of results from S.

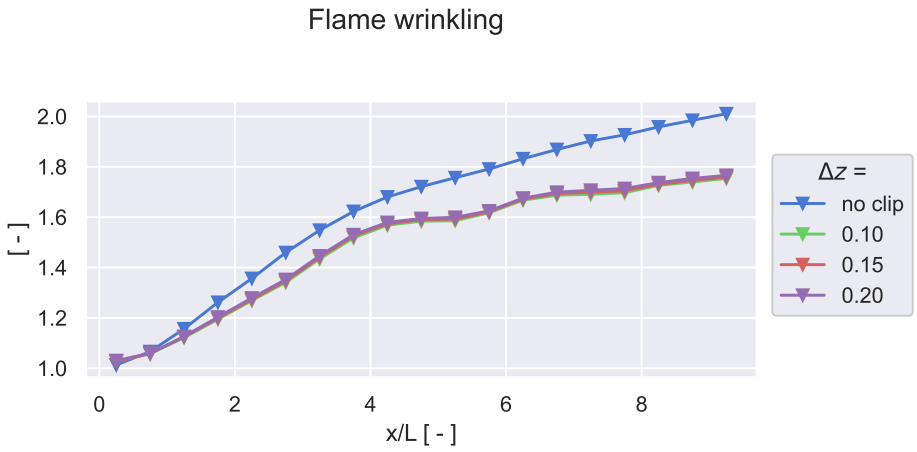

Figure 5.11 – *Evolution of the flame surface in term of flame wrinkling by considering the projection over the longitudinal axis. The results for different values af* Δz *are compared with the general formulation which consider the gradient* ∇z *over the entire domain. The averaging strip width is* $S = L/2$.

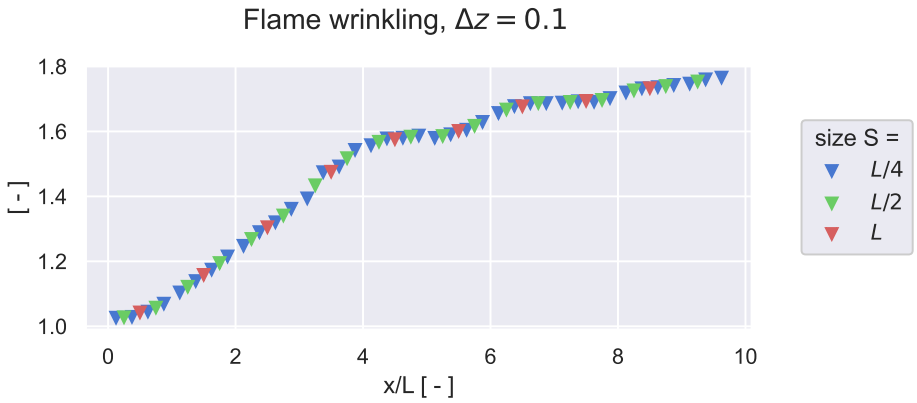

Figure 5.12 – *Evolution of the resolved flame surface wrinkling. The size* S *represent the strip width used for the integration and* L *is the reference length of the domain.*

The following results of the analysis are about the flame thickness. Diffusion flames present two main thicknesses: reaction thickness and diffusive thickness. Figure 5.13 shows the evolution over the stoichiometric iso-line arc length coordinate of those thicknesses. The quantities are computed along the normals to the stoichiometric iso-line. The reaction thickness is computed as the cut's portion where the heat release is greater than 5% of its maximum over the cut itself. The diffusive thickness, instead, is computed as the inverse of the mixture fraction gradient on the flame front ($1/\left|\nabla z\right|_{|z=z_{st}}$). The figure evidences

a considerable difference between reaction and diffusion thickness in a turbulent flame. The reaction thickness size is way much smaller than the diffusive one, and it remains pretty constant.

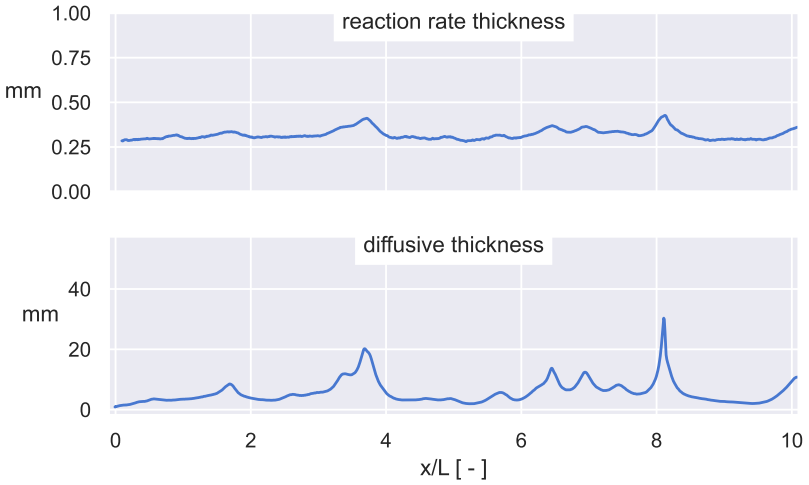

Figure 5.13 – *Reaction and diffusive thicknesses over the stoichiometric iso-line $z = z_{st}$. The snapshot is represented in figure 5.10.*

5.3 TFLES application

The thickened flame model is adopted here with a flame sensor without any efficiency function in order to investigate the effect of the purely thickening operation on a turbulent diffusion jet.
The adoption of a flame sensor affects thickening factor F so that:

$$F = 1 + (F_{max} - 1)\,\theta_F \tag{5.9}$$

where F_{max} is the maximum value in the reaction zone. In the present the value of the maximum thickening factor is set to $F_{max} = 5$.

5.3.1 Flame sensor analysis

The detection of the reaction zone is based on an "Arrhenius-like" expression:

$$\Omega = Y_{\mathrm{CH_4}}^{\nu_{\mathrm{CH_4}}}\; Y_{\mathrm{O_2}}^{\nu_{\mathrm{O_2}}} \exp\left(-\Gamma \frac{E_a}{R\,T}\right) \tag{5.10}$$

where Γ is a parameter that artificially decreases the effect of the activation temperature $T_a = E_a/R$ and it is assumed $\Gamma = 0.5$ by default. The flame sensor

θ_F is so determined with the hyperbolic tangent function (Legier et al., 2000):

$$\theta_F = \tanh\left(\Gamma' \frac{\Omega}{\Omega_0}\right) \tag{5.11}$$

where Γ' is a parameter controlling the thickness of the transition layer between the thickened and non-thickened zone, and Ω_0 represents the maximum value of Ω in the flame. As done in literature, its value is retrieved from the stoichiometric premixed flame, with $\Omega_0 = 1.5 \times 10^{-5}$. Figure 5.14 shows the influence of the parameter Γ' in determining the flame sensor for a counter flow laminar diffusion flame. For a wide range of Γ' the flame sensor overlaps the heat release. Furthermore by looking at the influence in term of global heat release, table 5.1 shows that its influence is minimal. However for the following of the analysis Γ' is set to 20.

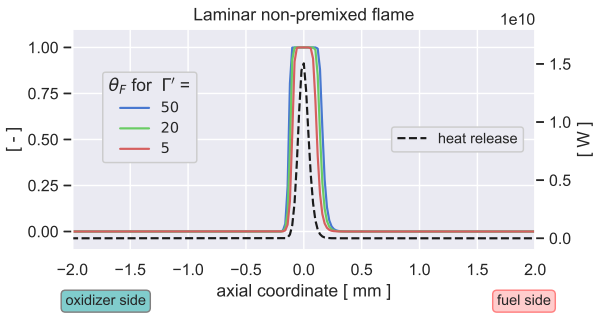

Figure 5.14 – *Axial evolution of the flame sensor θ_F over the axis of counter flow laminar diffusion flame at strain rate $500s^{-1}$. Results are shown for different values of Γ' parameter. The dashed line represent the heat release that tracks the reaction thickness.*

Γ' **[-]**	**50**	**20**	**5**
global heat release MW	2.43	2.36	2.37

Table 5.1 – *Global heat release per unit length along the axes of the diffusion laminar flames for the reference cases.*

A snapshot of the flame sensor overlapping the heat release of for the turbulent thickened solution flame is shown in figure 5.15 as a qualitative check.

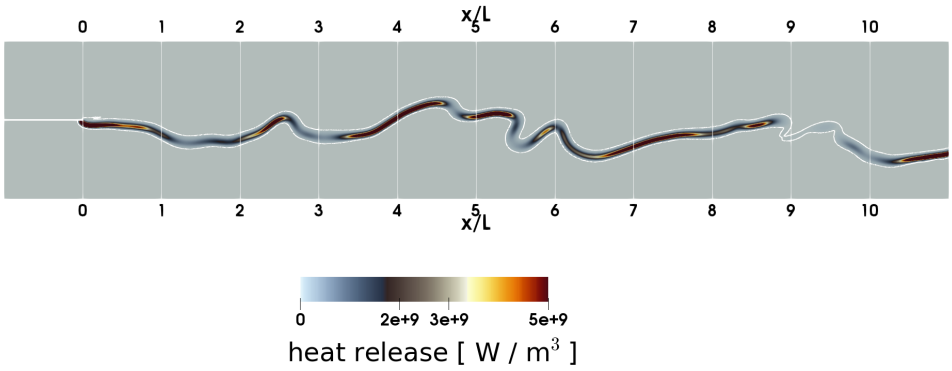

Figure 5.15 – *Instantaneous solution of heat release for the thickened turbulent flame with maxiumum thickening factor $F_{max} = 5$. Blank contour represent iso-line for the flame sensor $\theta_F = 0.5$.*

As explained in chapter 4, the presence of the sensor affects the global reaction rate. Figure 5.16 shows the axial evolution of the heat release per unit length for the non thickened solution, the thickened with sensor and thickened without sensor computed as:

$$hr_S(x) = \frac{1}{S} \int_{\nu_S} \left[\frac{\dot{\omega}_t}{F} \right] d\nu \tag{5.12}$$

The presence of sensor drastically reduces the heat release at the splitter plate exit, compared to the thickened solution without sensor, even though it does not recover the value of the reference DNS flame.

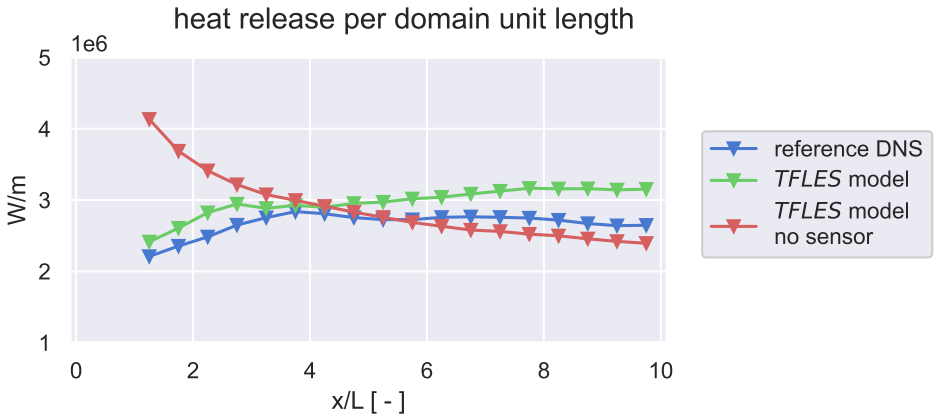

Figure 5.16 – *Axial evolution of heat release per domain unit length. The strip width S is set to half the reference length ($L/2$).*

The effect of the sensor can be even more appreciated by considering the heat release per resolved flame surface unit as:

$$hr_{\Xi_{res}}(S) = \frac{hr_S(x)}{\Xi_{res}(x)} \tag{5.13}$$

Figure 5.17 confirms that the presence of the sensor reduces the heat release per flame surface unit, especially close to the splitter plate where the flame is expected to be laminar.

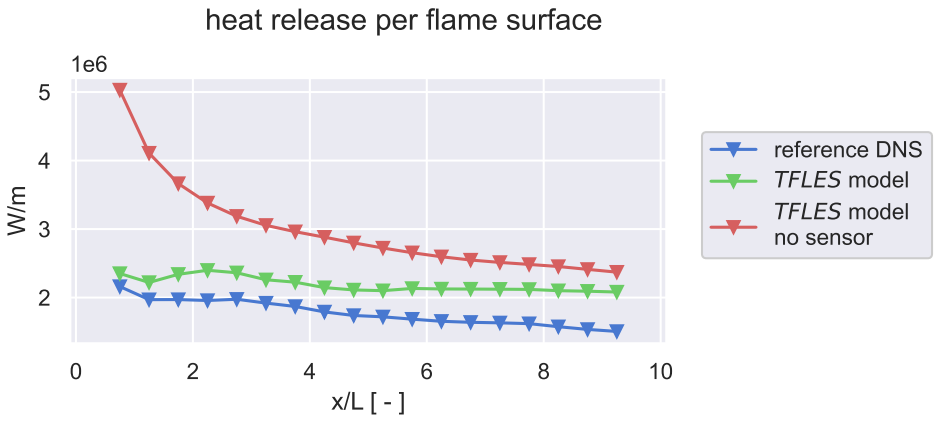

Figure 5.17 – *Axial evolution of heat release per flame surface. The strip width S is set to half the reference length ($S = L/2$).*

The primary effect of the flame sensor is related to the flow field dynamic. Comparing two instantaneous shots of the thickened flames without and with sensor, as in figure 5.18, shows a considerable difference of the flame surfaces. Without a sensor, the flame is almost not wrinkled anymore, and the flow regime is close to being laminar. In the presence of the sensor, the Reynolds number is affected only locally, and the main flow regime remains predominantly turbulent.

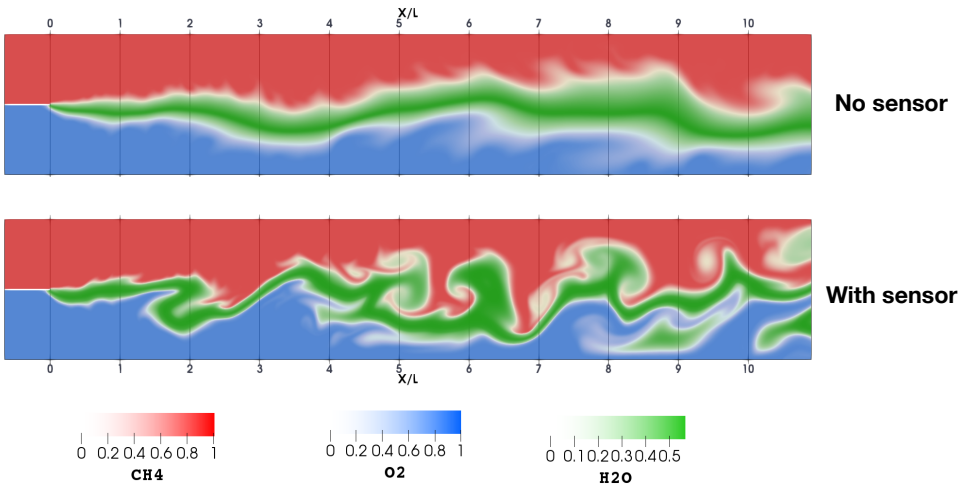

Figure 5.18 – *Instantaneous snapshot of species mass fraction for the solution without sensor (upper) and with sensor (lower).*

However, as shown in section 4.2, the presence of the flame sensor induces non-physical peaks in the mixture fraction field (see figure from 4.5(b) from section 4.2), which require to be properly handled for further modeling. For the following analysis, the flame sensor is adopted.

5.3.2 Flame structure

The flame front analysis, applied over an axial coordinate between 2 and 8 L for the methane/oxygen (Fig. 5.19) and temperature (Fig. 5.20), shows that although the gradients of the main species are smoothed, the structure of the flame does not change significantly in the mixture fraction framework, and the reaction rate is still close to a Dirac function (Fig. 5.21). So, the assumption of infinitely fast chemistry can still be considered for the thickened flame.

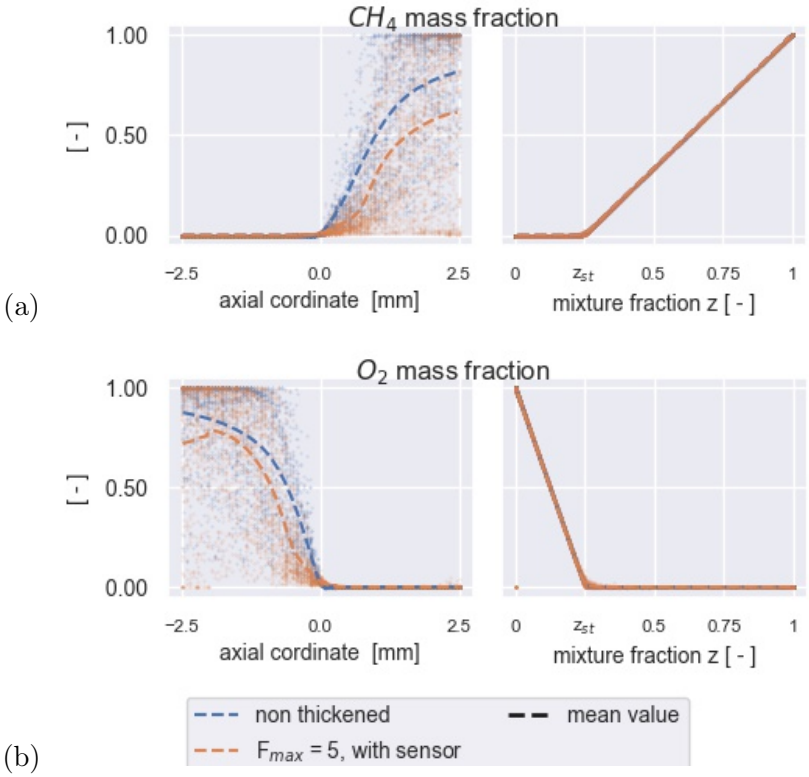

Figure 5.19 – *flame front analysis: comparison of non-thickened and thickened flames. reaction rate (a). Mass fraction profiles of CH_4(a) and O_2(b).*

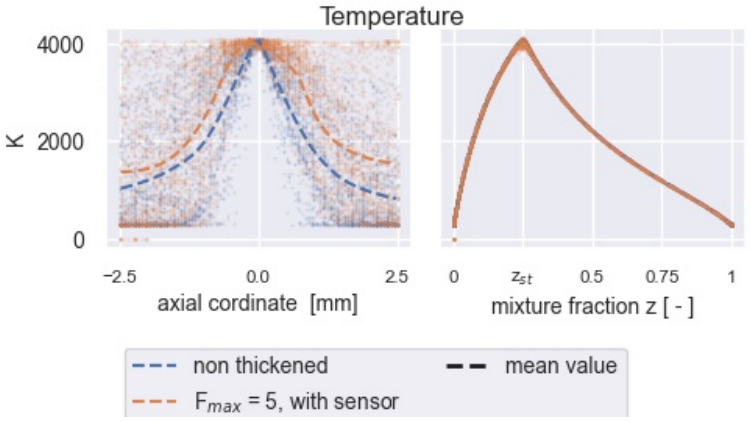

Figure 5.20 – *flame front analysis: comparison of non-thickened and thickened flames. Mass fraction profiles of temperature.*

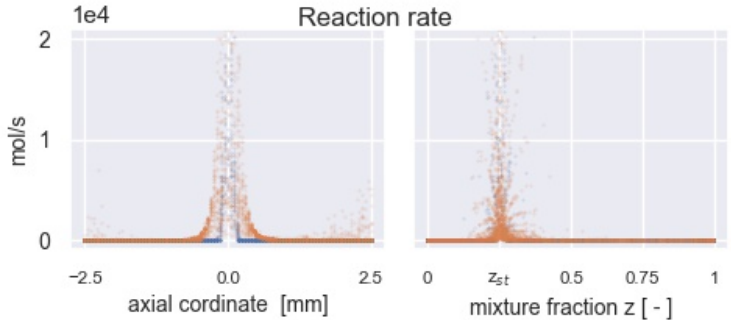

Figure 5.21 – *flame front analysis: comparison of non-thickened and thickened flames for the reaction rate.*

5.3.3 Flame dynamics

Analogously to the reference solution, the resolved surface flame is estimated through the gradient of the mixture fraction z in the neighborhood of the iso-line $z = z_{st}$ with equation 5.6. The lower bound of Δz is considered the same as for the reference DNS flame. Figure 5.22 shows the axial evolution of the resolved flame surface wrinkling for different values of Δz compared with the estimation considering the entire range of z. Considering the gradient of z over the entire domain overpredicts the flame surface's value almost by a factor of two in the case of the thickened flame.

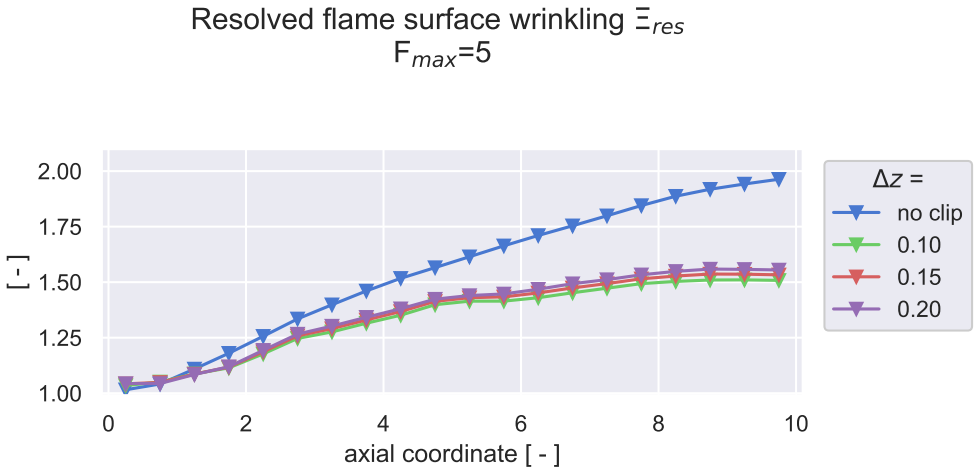

Figure 5.22 – *Axial evolution of the flame surface in term of flame wrinkling by considering the projection over the longitudinal axis. The results for different values af Δz are compared with the general formulation which consider the gradient ∇z over the entire domain. The average strip width is $S = L/2$*

Figure 5.23 shows the axial evolution of the resolved flame surface wrinkling between the DNS reference case and thickened solution with the flame sensor. Besides, figure 5.23 shows the ratio of two flame surfaces, which corresponds roughly to the efficiency factor required to counterbalance the loss of flame

surface due to the thickened model application.

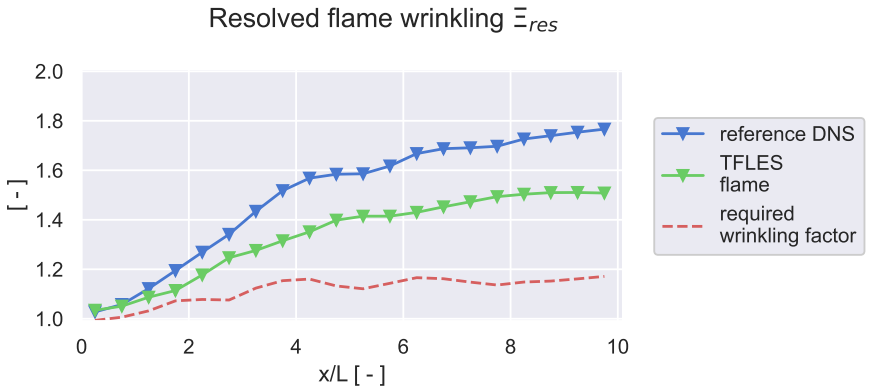

Figure 5.23 – *Axial evolution of resolved flame surface wrinkling Ξ_{res} for the reference DNS and thickened flame. The dashed line represent the ratio which is the required wrinkling expected from the formulation. The strip width S is set to the reference length ($S = L/2$).*

5.4 Dynamic model Application

The loss of flame surface justifies the need for a sub-grid efficiency model proposed in the present analysis through a dynamic formulation. The efficiency function is computed by assuming a fractal behavior (Eq. 3.8) where the inner cut-off length is assumed as the laminar flame thickness δ_L and the outer cut-off length as the resolved flame thickness $F\delta_L$, so that equation (3.8) becomes:

$$\Xi_\Delta = F^\beta \tag{5.14}$$

5.4.1 Quantities of interests

The computation of the parameter β is based on an estimation of a flame surface density-like quantity Ψ as:

$$\Psi = \begin{cases} \frac{|\nabla\tilde{z}|}{\Delta z}\,\theta_F & \text{if } z_{st} - \frac{\Delta z}{2} < \tilde{z} < z_{st} + \frac{\Delta z}{2} \\ 0 & \text{elsewhere} \end{cases} \tag{5.15}$$

The flame sensor θ_F is introduced to cut off the peaks of mixture fraction gradients due to the presence of the sensor itself (see figure from 4.5(b) from section 4.2). Those peaks lead to non-physical effects when filtering the quantities, which lead to incorrect values of the parameter β.
Analogously, a filtered surface density-like quantity $\dot{\Psi}$, conditioned over the flame reaction,is defined as:

$$\dot{\Psi} = \begin{cases} \frac{|\nabla\hat{\tilde{z}}|}{\Delta z}\,\theta_F & \text{if } z_{st} - \frac{\Delta z}{2} < \hat{z} < z_{st} + \frac{\Delta z}{2} \\ 0 & \text{elsewhere} \end{cases} \tag{5.16}$$

where the hat symbol " ˆ " denotes the filtering operation at test filter scale $\hat{\Delta}$. So from equation 3.12 the parameter β becomes:

$$\beta = \frac{\log\left(<\widehat{\Psi}> / <\dot{\Psi}>\right)}{\log\gamma} \tag{5.17}$$

where γ is a parameter that depends on the TLFES filter Δ and test filter size $\hat{\Delta}$ as:

$$\gamma = \sqrt{1 + \left(\frac{\hat{\Delta}}{\Delta}\right)^2} \tag{5.18}$$

The flame surface at the filtered test scale S_{filt} is computed as:

$$S_{filt} = \int_{\nu_{\Delta z}} \frac{\left|\nabla\hat{\tilde{z}}\right|}{\Delta z} d\nu \tag{5.19}$$

The time evolution of total flame surface S_{tot}, analogously to Eq. 5.6, is computed as:

$$S_{tot} = \int_{\nu_{\Delta z}} \Xi_{\Delta} \frac{|\nabla\tilde{z}|}{\Delta z} d\nu \tag{5.20}$$

and a total surface wrinkling Ξ_{tot}, analogously to the resolved one (Eq. 5.8), over a volume strip ν_S, is:

$$\Xi_{tot}^{m} = \left[\frac{S_{tot}}{S}\right] \tag{5.21}$$

where S is the length of the axial projection of the volume strip considered. The instantaneous global heat released per unit length is:

$$hr_S(x,t) = \frac{1}{S}\int_{\nu_S} \frac{\Xi_{\Delta}\dot{\omega}_t}{F} d\nu \tag{5.22}$$

and the the corresponding time averaged quantity is

$$hr_S^m(x) = [hr_S(x,t)] \tag{5.23}$$

The spatial mean at a given time stamp t of β for a volume strip ν_S is:

$$\bar{\beta}(t,x) = \frac{\int_{\nu_S} \beta(x',y',t)\,\Psi\,d\nu}{\int_{\nu_S} \Psi d\nu} \tag{5.24}$$

where x' and y' are the spatial coordinates domain volume ν_S. The corresponding RMS is given by:

$$\beta'(t,x) = \sqrt{\overline{\beta^2} - \left(\bar{\beta}(t)\right)^2} \tag{5.25}$$

The time averaged downstream evolution of β is:

$$\beta^S_{avg}(x) = \frac{\int_{\nu_S} [\beta(x', y', t)\, \Psi]\, d\nu}{\int_{\nu_S} [\Psi]\, d\nu} \tag{5.26}$$

and the corresponding RMS by:

$$\beta^S_{rms}(x) = \sqrt{\frac{\int_{\nu_S} \left[(\beta(x', y', t))^2\ \Psi\right] d\nu}{\int_{\nu_S} [\Psi]\, d\nu} - \left(\beta^S_{avg}(x)\right)^2} \tag{5.27}$$

and ν_S denotes the domain strip centred in x with S width.
Analogously, the spatial mean at a given time stamp t of the efficiency function Ξ_Δ is computed as:

$$\bar{\Xi}_\Delta(t, x) = \frac{\int_{\nu_S} \Xi_\Delta(x', y', t)\, \Psi\, d\nu}{\int_{\nu_S} \Psi d\nu} \tag{5.28}$$

The corresponding RMS is given by:

$$\Xi'_\Delta(t, x) = \sqrt{\overline{\Xi^2_\Delta} - \left(\bar{\Xi}_\Delta(t)\right)^2} \tag{5.29}$$

The time averaged downstream evolution of the mean parameter is:

$$\Xi^S_{\Delta,\, avg}(x) = \frac{\int_{\nu_S} [\Xi_\Delta(x, y, t)\, \Psi]\, d\nu}{\int_{\nu_S} [\Psi]\, d\nu} \tag{5.30}$$

and the corresponding RMS by:

$$\Xi^S_{\Delta,\, rms}(x) = \sqrt{\frac{\int_{\nu_S} \left[(\Xi_\Delta(x, y, t))^2\ \Psi\right] d\nu}{\int_{\nu_S} [\,\Psi]\, d\nu} - \left(\Xi^S_{\Delta,\, avg}(x)\right)^2} \tag{5.31}$$

and ν_S denotes the domain strip centred in x with S width.

Variable	Integration over space	Integration over time
β	$\bar{\beta}(t,x) = \frac{\int_{\nu_S} \beta\, \Psi d\nu}{\int_{\nu_S} \Psi d\nu}$	$\beta^S_{avg}(x) = \frac{\int_{\nu_S} [\beta\, \Psi] dS}{\int_{\nu_S} [\Psi] dS}$
	$\beta'(t,x) = \sqrt{\overline{\beta^2} - \left(\bar{\beta}(t)\right)^2}$	$\beta^S_{rms}(x) = \sqrt{\frac{\int_{\nu_S} [\beta^2\ \Psi\ ] dS}{\int_{\nu_S} [\Psi] dS} - \left(\beta^S_{avg}(x)\right)^2}$
Ξ_Δ	$\bar{\Xi}_\Delta(t,x) = \frac{\int_{\nu_S} \Xi_\Delta\, \Psi d\nu}{\int_{\nu_S} \Psi d\nu}$	$\Xi^S_{\Delta,\,avg}(x) = \frac{\int_{\nu_S} [\Xi_\Delta\ \Psi] dS}{\int_{\nu_S} [\Psi] dS}$
	$\Xi'_\Delta(t,x) = \sqrt{\overline{\Xi^2_\Delta} - \left(\bar{\Xi}_\Delta(t)\right)^2}$	$\Xi^S_{\Delta,\,rms}(x) = \sqrt{\frac{\int_{\nu_S} \left[\Xi^2_\Delta\ \Psi\right] dS}{\int_{\nu_S} [\Psi] dS} - \left(\Xi^S_{\Delta,\,avg}(x)\right)^2}$
Resolved surface wrinkling	$\Xi_{res}(t,x) = \frac{S_{res}}{S}$	$\Xi^m_{res}(x) = \left[\frac{S_{res}}{S}\right]$
Total surface wrinkling	$\Xi_{tot}(t,x) = \frac{S_{tot}}{S}$	$\Xi^m_{tot}(x) = \left[\frac{S_{tot}}{S}\right]$
heat release	$hr_S(t,x) = \frac{1}{S}\int_{\nu_S} \Xi_\Delta \frac{\dot{\omega}_t}{F} d\nu$	$hr^m_S(x) = \frac{1}{S}\int_{\nu_S} \left[\Xi_\Delta \frac{\dot{\omega}_t}{F}\right] d\nu$

Table 5.2 – *Summary of statistic definitions. [.] denotes a time average operation, while ν_S denotes the volume strip centred in x.*

Furthermore, since the computation of the parameter β is costly in terms of CPU time, it is not computed at each iteration. The code time step is based on the acoustic CFL number, and the model parameter evolves with convection times so that β is updated every n iterations. The influence of the parameter n is investigated in section 5.4.6. However, for the following analysis, n is set to 500.

5.4.2 Fractal behavior

The current model assumes that the wrinkling factor Ξ_Δ scales as an exponent of the filter width Δ (Eq. 3.8). As a recall, the efficiency function in fractal formulation writes as:

$$\Xi_\Delta = \left(\frac{\Delta}{\delta_c}\right)^\beta \tag{5.32}$$

Resolved flame surface at LES filter (S_{res}) and test-filter scales (S_{filt}) are related through the conservation of the total flame surface, $\Xi_\Delta S_{res} = \Xi_{\gamma\Delta} S_{filt}$, leading to:

$$\frac{S_{filt}}{S_{res}} = \frac{\Xi_\Delta}{\Xi_{\gamma\Delta}} = \left(\frac{\gamma\Delta}{\Delta}\right)^{-\beta} = \gamma^{-\beta} \tag{5.33}$$

Accordingly, the normalized filtered surface flame S_{filt}/S_{res} over a portion of domain is expected to follow a straight line of slope $-\beta$ when displayed as a function of the ratio γ of the filter sizes in log-scale. Figure 5.24 shows

the relation for an instantaneous solution of the thickened flame without efficiency model. The value of the TFLES filter width is $\Delta = F_{max}\,\delta_L^0$, where $\delta_L^0 = 0.45$ mm is estimated through the flame thickness of a freely propagating laminar premixed flame as:

$$\delta_L^0 = \frac{T_2 - T_1}{\max\left(\left|\frac{\partial T}{\partial x}\right|\right)} \tag{5.34}$$

where T_1 is the temperature of fresh and T_2 of the burnt gases. So the TFLES filter size Δ is:

$$\Delta = F_{max}\delta_L^0 = 2.25\,mm = 0.225L$$

The slope of the curve is constant for values of the test filter size up to $\hat{\Delta} \approx 2.5\Delta$, which validates the use of a fractal-like model. This limitation is given by the integral length scale of the turbulence.

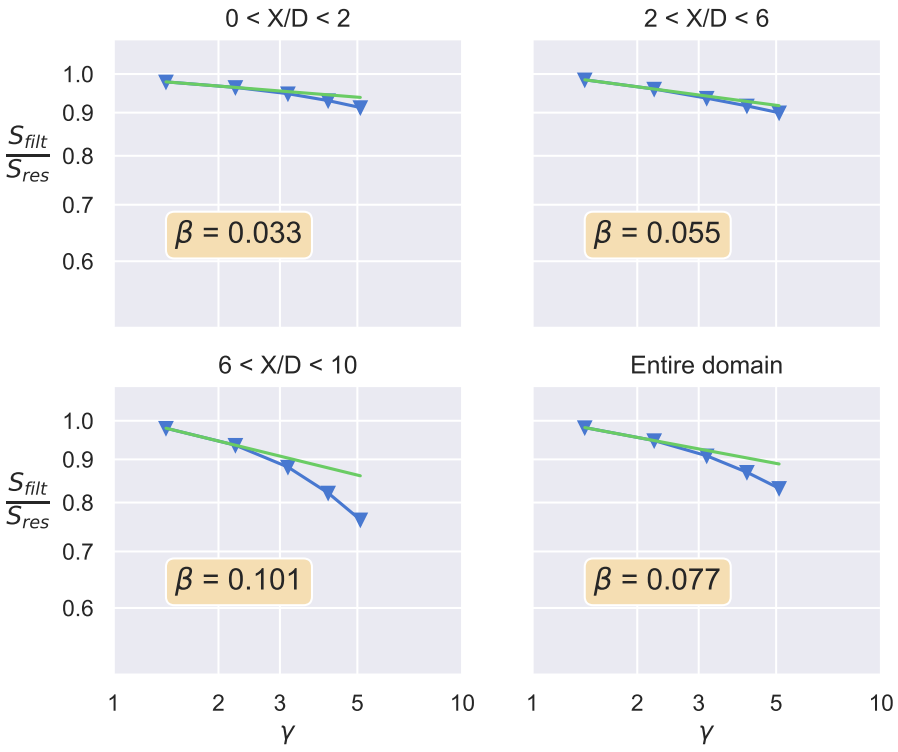

Figure 5.24 – *Normalized filtered surface flame S_{filt}/S_{res} as a function of the ratio of the test and combustion filter sizes in log-scale for values of the filter size $\hat{\Delta}$ from 1Δ to 5Δ, with $\Delta = 0.225L = 2.25\,mm$. Results are extracted from the instantaneous field of the thickened flame.*

A fractal formulation requires defining an outer to inner cut-off length ratio. By considering the inner cut-off length as the thickness of the non-thickened

flame, the outer cut-off length is assumed the thickened flame thickness so that the ratio outer to inner cut-off length is the thickening factor F_{max}. This assumption, purely made as standard practice, turns accurate when comparing the reaction thicknesses of the DNS reference with the TFLES one, as shown in figure 5.25, which shows the thicknesses and ratio thickened to non-thickened one. The thicknesses are computed as the portion of the cut, normal to the stoichiometric iso-line, where the reaction rate is higher than five percent of its maximum over the cut itself. Since the thickness of the TFLES flame does not change in the order of magnitude, the assumption $\Delta/\delta_c = F$ can be accepted.

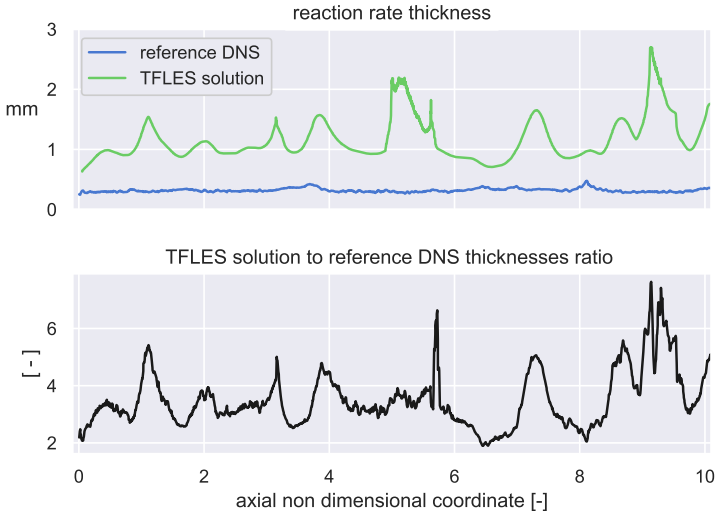

Figure 5.25 – *Upper figure: Comparison of reaction rate thickness of the reference DNS and thickened solution from 2 instantaneous solutions. The thickness is computed as the portion of the cut normal to the flame front where the value is higher than five percent of its maximum over the cut itself. Lower figure: ratio thickened to non thickened thicknesses.*

5.4.3 Discussion

The model parameters, such as filter sizes, inner cut-off length scale, and updating frequency, are here varied to characterize the model behavior and its robustness. Table 5.3 summarizes the different cases studied. By assuming a reference case, the other cases vary from it by a single parameter. The TFLES filter size Δ is related to the laminar flame thickness δ_L^0, according to:

$$\Delta = F_{max}\delta_L^0 = 2.25\,mm = 0.225\,L \tag{5.35}$$

Case	$\hat{\Delta}$	Δ_{avg}	δ_c	γ
$C^{1.5\Delta}_{3.0\Delta}$ (ref.)	1.5 Δ	3.0 Δ	δ^0_L	1.80
$C^{1.5\Delta}_{4.0\Delta}$	1.5 Δ	4.0 Δ	δ^0_L	1.80
$C^{2.0\Delta}_{3.0\Delta}$	2.0 Δ	3.0 Δ	δ^0_L	2.24
$C_{2.0\delta^0_L}$	1.5 Δ	3.0 Δ	2 δ^0_L	1.80

Table 5.3 – *Summary of simulated cases. Superscript α_1 and subscript α_2 in $C^{\alpha_1}_{\alpha_2}$ denote test and averaging filter sizes, respectively. The subscript α_3 in C_{α_3} stands for the inner cut-off length scale. The combustion filter size is set to $\Delta = 2.25\ mm = 0.225L$. The maximum thickening factor is set to $F_{max} = 5$ for all cases.*

Figure 5.26 shows an instantaneous snapshot of the model parameter β for the case $C^{1.5\Delta}_{3.0\Delta}$ overlapped with the reaction rate. The parameter β presents peaks where the reaction rate is wrinkled as expected.

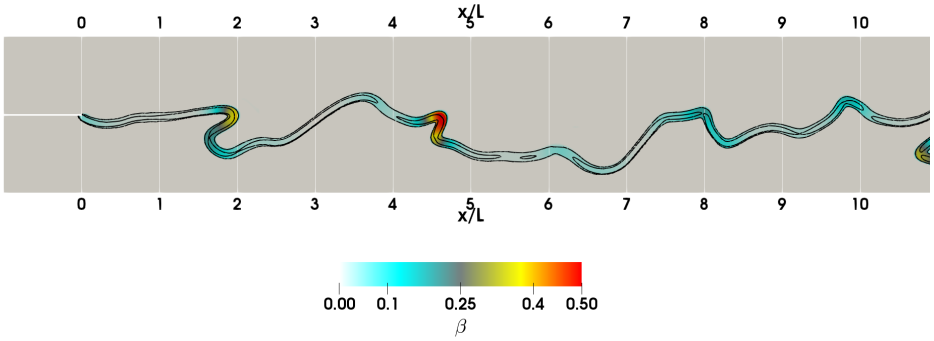

Figure 5.26 – *Instantaneous solution of the turbulent diffusion flame case $C^{1.5\Delta}_{3.0\Delta}$ representing the parameter β. Black lines represent iso-contour of reaction rate for* 300 *and* 3000 $mol/(s\,m^3)$

Figure 5.27 displays snapshots of the instantaneous LES resolved fields and the corresponding test filtered and averaged filtered quantities illustrating the dynamic procedure to determine the model parameter. The flame surface density Ψ from Eq. 5.15 (shown in Fig. 5.27a) is filtered at the test scale $\hat{\Delta}$ (Fig. 5.27b) and averaged (Fig. 5.27d) at Δ_{avg} scale. The filtered surface density $\dot{\Psi}$, at test filter $\hat{\Delta}$ from equation 5.16, is shown in (Fig 5.27c) and it is then filtered (Fig. 5.27e) at average scale Δ_{avg}. Then equation (5.17) is applied obtaining the β-field displayed in figure 5.27g.

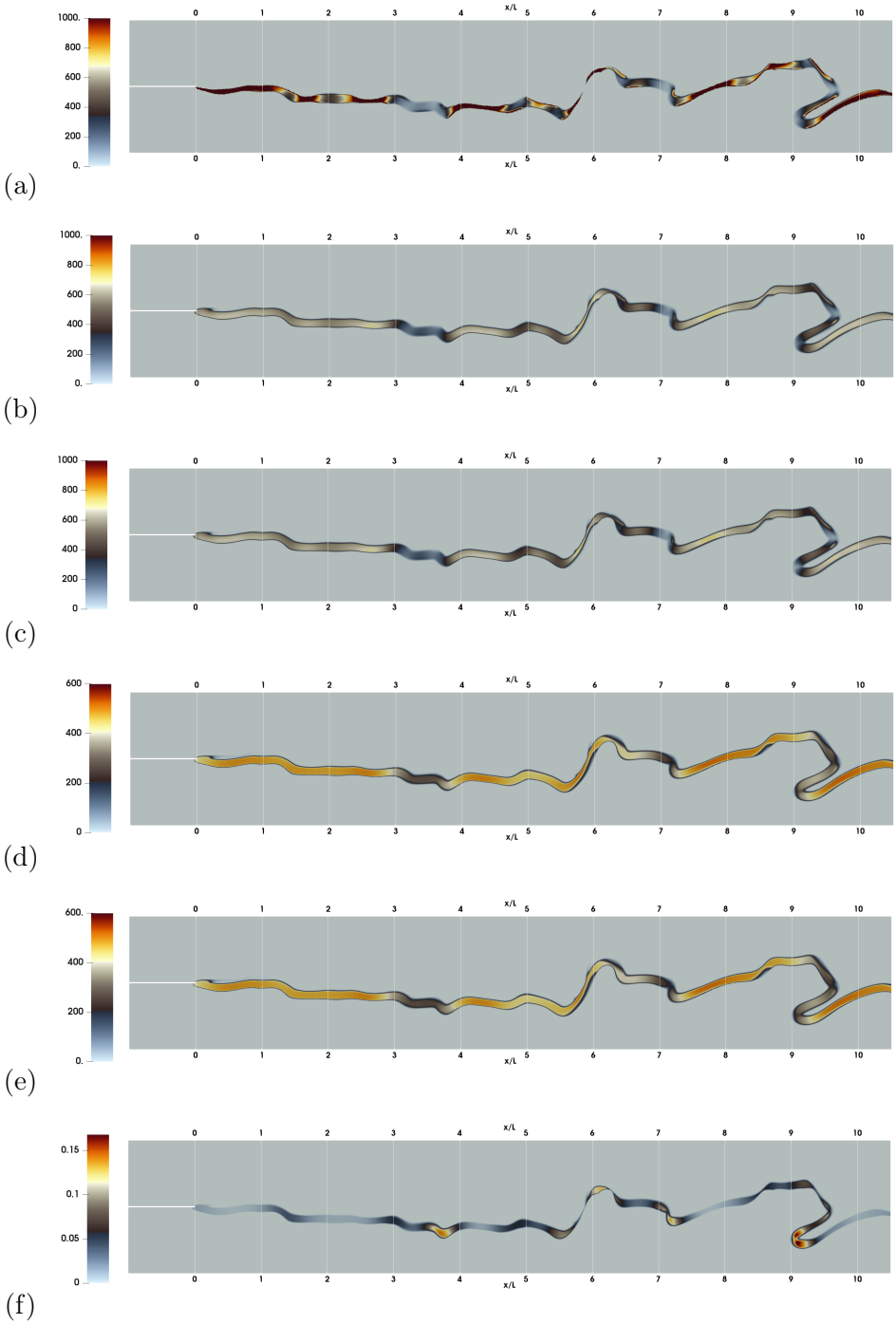

Figure 5.27 – *Instantaneous LES resolved field and corresponding test-filtered quantities for the turbulent diffusion jet. (a) Ψ; (b) $\hat{\Psi}$; (c) $\dot{\Psi}$; (d) $<\hat{\Psi}>$;(e) $<\dot{\Psi}>$; (f) β-field. Snapshot corresponds to simulation $C^{1.5\Delta}_{3.0\Delta}$*

Figure 5.28 shows the axial evolution of β^S_{avg} and β^S_{rms} for different values of the

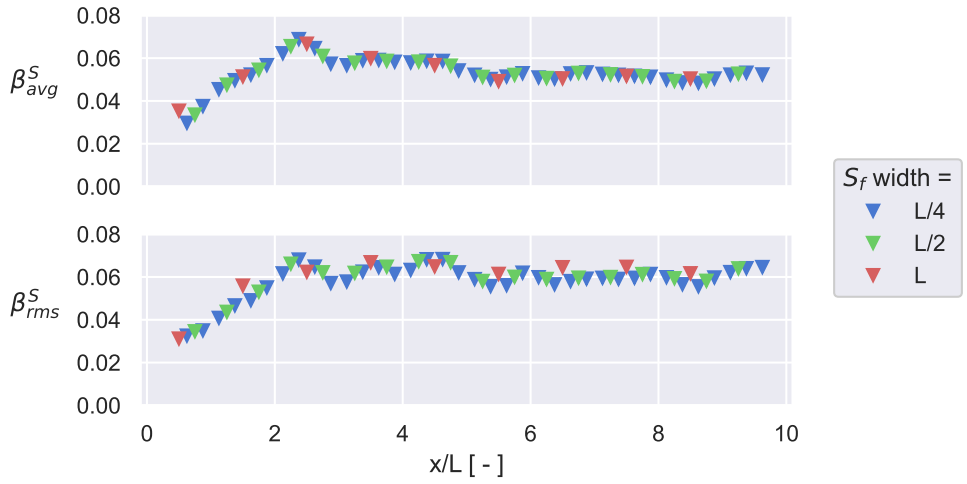

Figure 5.28 – *Axial evolution of β^S_{avg} and β^S_{rms} for different values of the averaging strip width S for the reference case $C^{1.5\Delta}_{3.0\Delta}$. The results are averaged over 6 convective times, where a convective time is estimated to 5 milliseconds.*

averaging strip width S. The average value of β increases in the first $2\,L$ along the axial coordinate and then tends to a constant value of 0.05. The RMS turns to be close to the β average value and follows a similar evolution. Figure 5.29 shows the values of the resolved flame wrinkling Ξ_{res} (Eq. 5.8), the averaged efficiency factor $\bar{\Xi}_\Delta$ (Eq. 5.28) and the corresponding averaged parameter $\bar{\beta}$ (Eq. 5.24) for strips of $S = L$ normal to the axial direction along the domain for the case $C^{1.5\Delta}_{3.0\Delta}$. The evolution of β follows the evolution of resolved flame surface wrinkling along the axis.

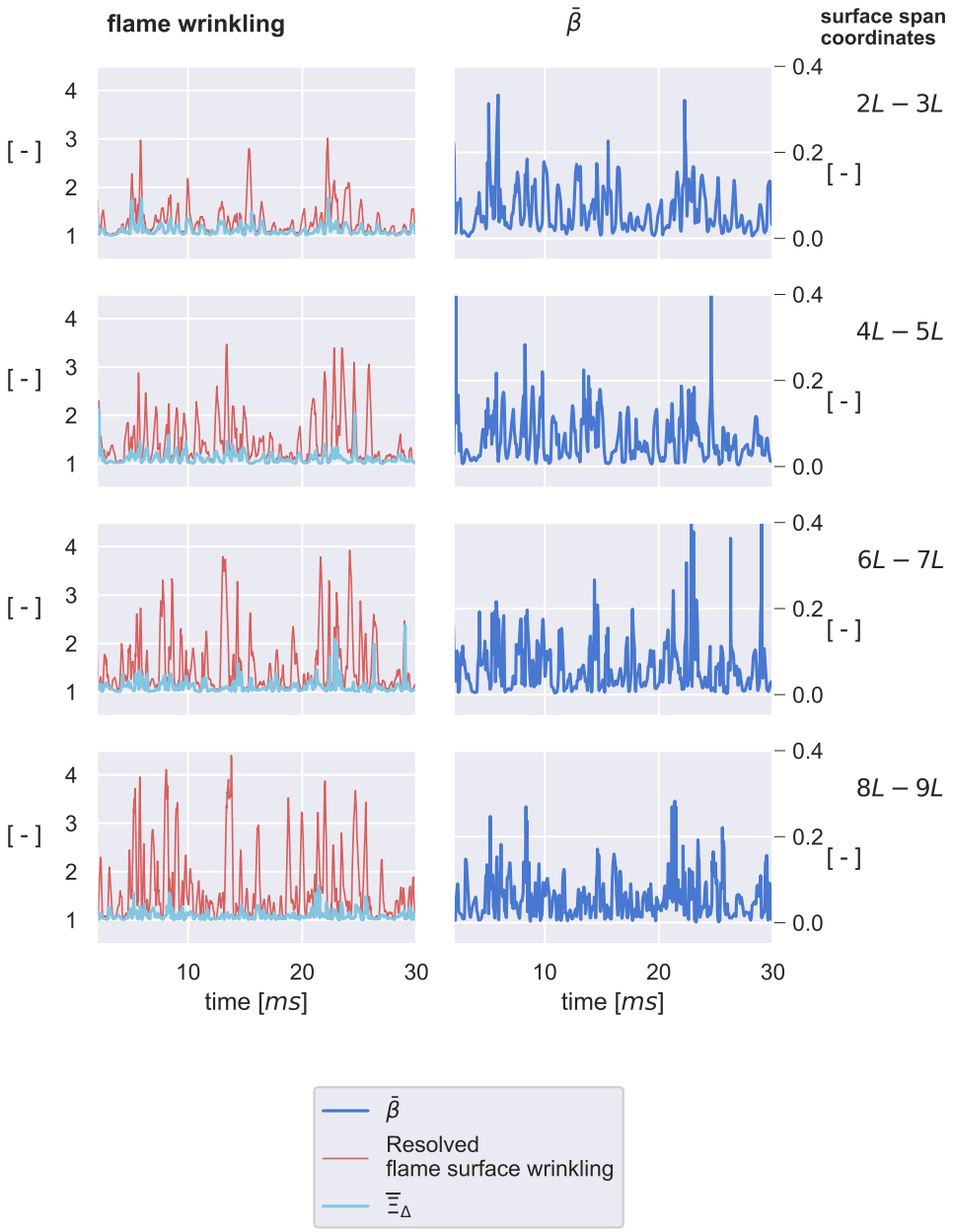

Figure 5.29 – *Temporal evolution of resolved flame surface wrinkling* Ξ_{res} *(Eq. 5.8), average flame wrinkling factor* $\bar{\Xi}_\Delta$ *(Eq. 5.28) and parameter* $\bar{\beta}(t)$ *(Eq. 5.24) for different strips along the domain for the reference case* $C^{1.5\Delta}_{3.0\Delta}$.

5.4.4 Influence of model parameters

Test filter and averaging filter sizes

The following results are averaged over six convective times, where a convective time is estimated to 5 milliseconds[3]. Figure 5.30 compares the conditional downstream evolution of mean β^S_{avg} (Eq. 5.26), and its RMS (Eq.5.27) varying test and averaging filter widths. A filtering size of$\hat{\Delta} = 2.0\Delta$ does not impact the value of β significantly. On the other hand, the average filter increase mainly decreases the β_{rms}. Ideally, with large values of Δ_{avg}, the formulation should tend to a global formalism where β depends only on time.

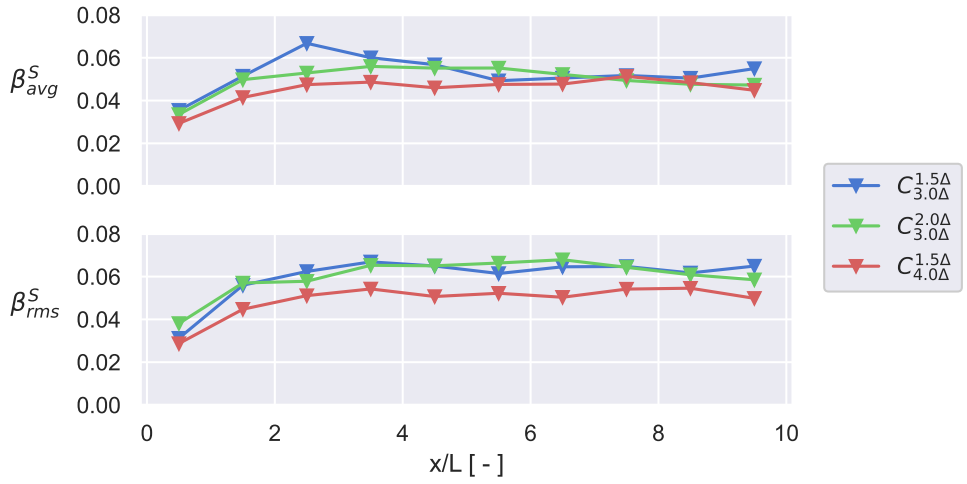

Figure 5.30 – *Axial evolution of $\beta^S_{avg}(x)$ and $\beta^S_{rms}(x)$ for simulations varying test and averaging filter. The averaging strip width is the characteristic length $S = L$.*

cut-off length scale

The inner cut-off length scales δ_c, entering equation 5.32, is unknown a priori. For premixed flames, several formulations can be found in literature (Gülder, 1991; Smallwood et al., 1995). For example Smallwood et al. (1995) suggested that the inner cut-off is linked to the Karlovitz number.
In the present work, the cut-off length scale is assumed to be constant. According to Eq. 5.32, by increasing δ_c the wrinkling factor Ξ_Δ decreases if the the parameter β remain constant. Figure 5.31 shows the variation of β^S_{avg} and its RMS due to the inner cut-off length. Increasing the cut-off length by a factor of two slightly decreases the average value β and the RMS. As expected for the efficiency factor instead, Figure 5.32 shows that the impact on the efficiency is not negligible, and the average value of Ξ_Δ decreases by increasing the cut-off

[3]computed as the time to flow of a particle for a domain portion of 10 L at average inlet speed of 20 m/s

length δ_c with the same factor. This effect turns into a reduction in the total flame surface as shown in figure 5.33.

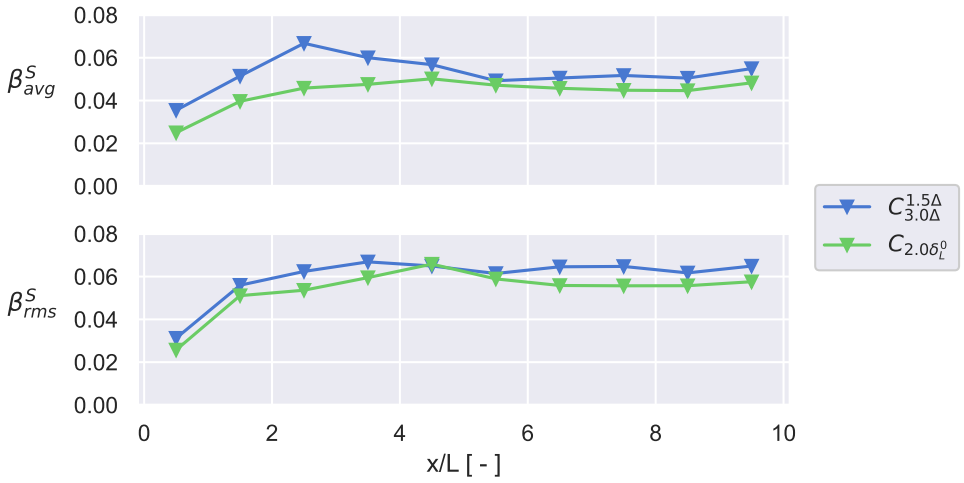

Figure 5.31 – *Axial evolution of $\beta^S_{avg}(x)$ and $\beta^S_{rms}(x)$ for simulations varying the cut-off length δ_c. The averaging strip width is the characteristic length $S = L$.*

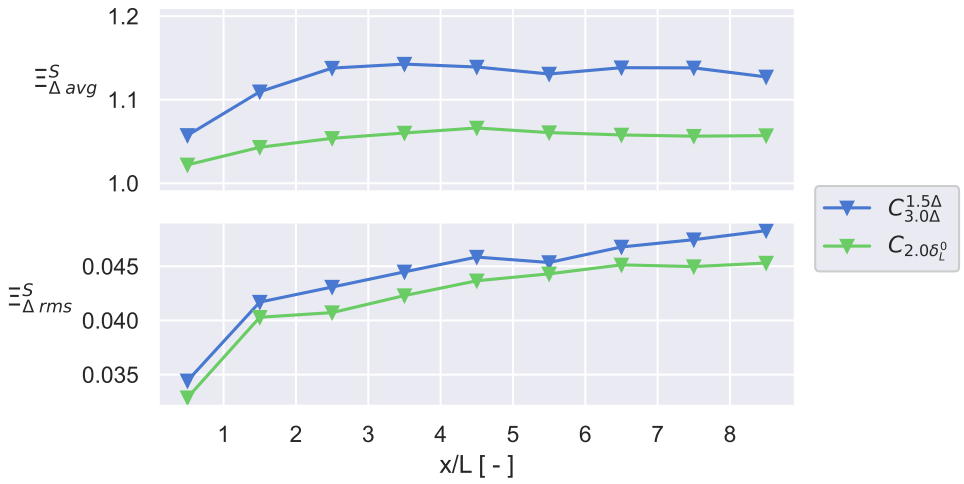

Figure 5.32 – *Axial evolution of $\Xi^S_{\Delta,\,avg}(x)$ and $\Xi^S_{\Delta,\,rms}$ for simulation varying the cut-off length δ_c.*

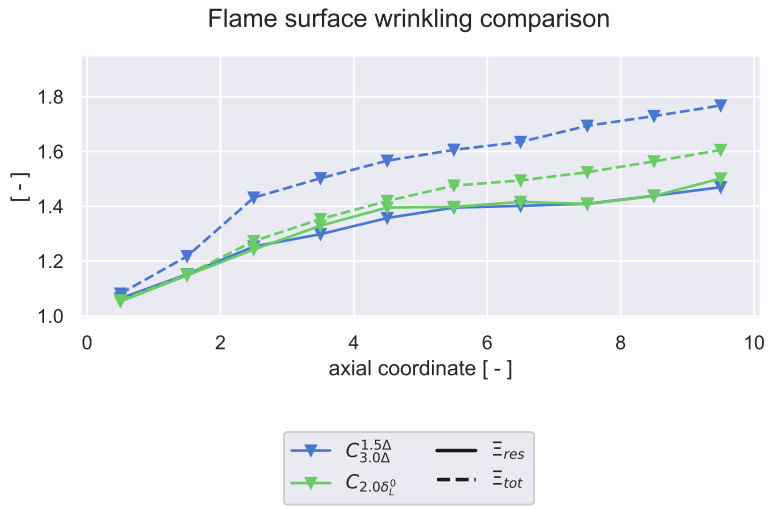

Figure 5.33 – *Axial evolution of* $\Xi_{res}^m(x)$ *and* $\Xi_{tot}^m(x)$ *for simulation varying the cut-off length* δ_c*. The averaging strip width is the characteristic length* $S = L$*.*

5.4.5 Comparison with the reference case

The dynamic formulation is compared with the fully resolved jet case and the thickened solution without efficiency function. Total and resolved flame surfaces (Ξ_{res} and Ξ_{tot}) are compared in figure 5.34 by showing the dynamic formulation, the reference DNS and thickened flame surfaces without the dynamic model. The dynamic formulation recovers the total flame surface at least after a certain distance from the splitter plate ($x/L > 3$) where the model activates. However, for distance $x/L > 3$ the model activates gradually but overpredicts the total flame surface.

Figure 5.35 shows the comparison of total flame surfaces evolution for the reference DNS, dynamic solution $C_{3.0\Delta}^{1.5\Delta}$ and a thickened flame with constant efficiency $\Xi_\Delta = 1.08$ and $\beta = 0.05$, which is approximately the average value of β resulting from the previous analysis (see figure 5.30). It shows that a constant efficiency model can be adopted in the zone where the flow is fully developed ($x/L > 3$).

For diffusion flames and infinitely fast chemistry, according to the analytical theory for laminar flame in chapter 4, the TFLES model cannot compensate the over-prediction of heat realease. The application of dynamic formulation for the efficiency function leads to a further over prediction of the heat release compared to the DNS reference solution shown in Fig. 5.36, where the heat per unit length is compared.

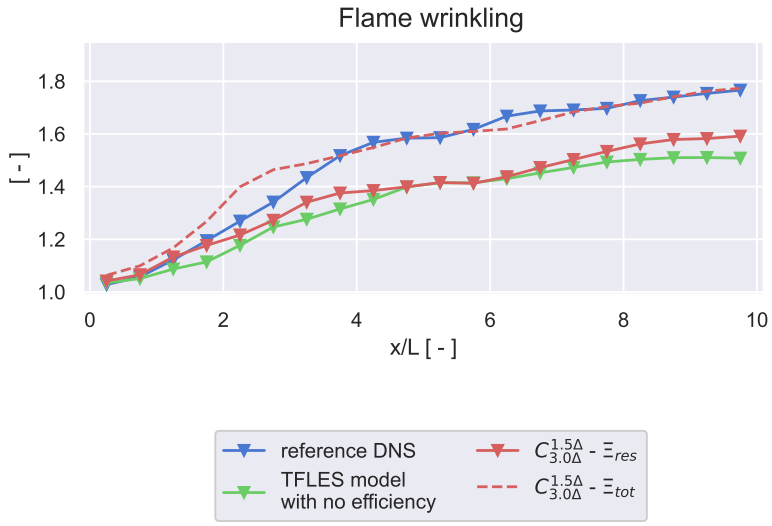

Figure 5.34 – *Axial evolution of resolved (Ξ_{res}) and total (Ξ_{tot}) flame surface wrinkling. Comparison of reference DNS, TFLES without efficiency and dynamic model formulation $C_{3.0\Delta}^{1.5\Delta}$. The average strip width is $S = L/2$.*

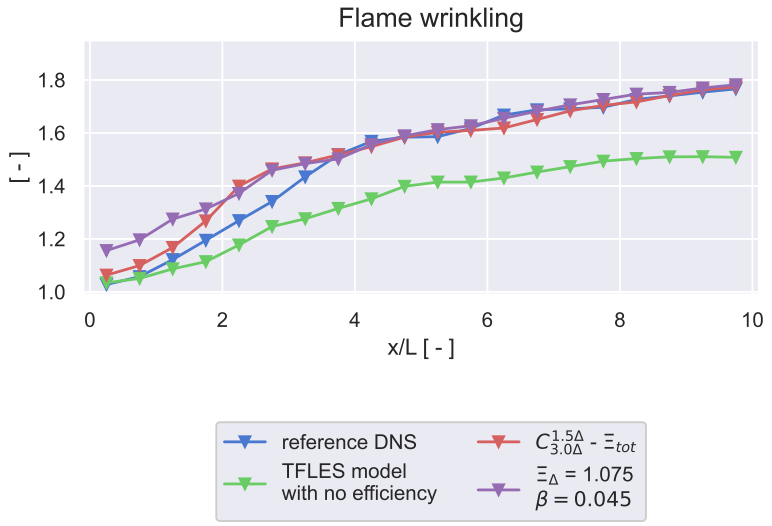

Figure 5.35 – *Axial evolution of total (Ξ_{tot}) flame surfaces. Comparison of reference solution, only thickening, dynamic model and TFLES model with constant efficiency. The average strip width is $S = L/2$.*

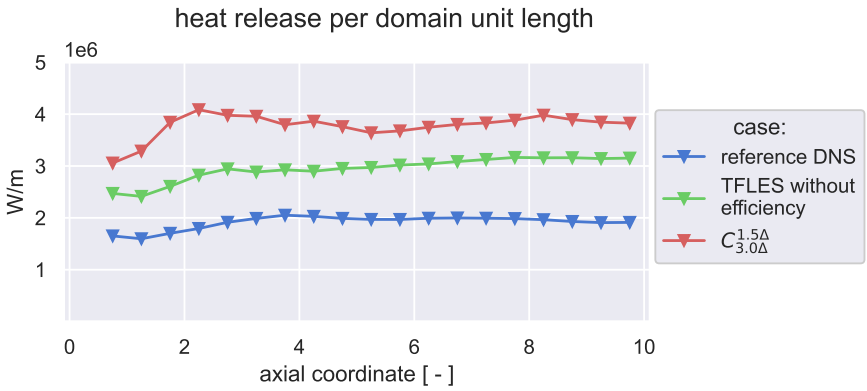

Figure 5.36 – *Axial evolution of heat release per domain unit length. The averaging strip width S is set to half the reference length ($L/2$). Comparison of reference DNS, TFLES flame without efficiency and dynamic model formulation $C_{3.0\Delta}^{1.5\Delta}$.*

5.4.6 Influence of updating iteration

The dynamic model could be computationally expensive because of the filtering operations involved if computed every time step. The code time step is based on the acoustic CFL number, and the model parameter is expected to evolve with convection times, so the dynamic procedure is not applied every time step but every n iterations. The physical time for a single iteration is around $\tau_i = 0.02\mu s$. A value of the parameter $n = 500$ iterations, used in the previous analysis, corresponds to a physical time $\tau_n = n\tau_i = 10\mu s$. By considering the bulk velocity of the fuel inlet $U_0 = 20m/s$ (averaged velocity of fuel and oxidizer inlet), the distance travelled by a convected fluid particle can be estimated as $\delta_n = U_0\tau_n$. For $n = 500$, $\delta_n = 0.20$ mm. Since the filter sizes are bigger than this length ($\Delta = 2.25$ mm), this updating frequency seems acceptable. Optimizing this parameter is essential to achieve the best CPU performance. The size of δ_n has to be considered with the TFLES filter width and the reference length L. Table 5.4 represents the physical time τ_n and its respective length δ_n for different values of number of updating iterations n, and relates δ_n to the TFLES filter size Δ and the reference length L.
By considering the value of the TFLES filter size $\Delta = 2.25$ mm, the updating frequency of $n = 1000$ is relevant. The updating convective length δ_n is not negligible for values higher than the TFLES filter size.

n	τ_n $[\mu s]$	δ_n $[mm]$	δ_n/Δ	δ_n/L
200	4	0.08	3.6%	0.8%
500	10	0.20	8.9%	2.0%
1000	20	0.40	17.8%	4%
2000	40	0.80	35.6%	8%

Table 5.4 – *Values of updating frequency n and corresponding updating time step τ_n and equivalent average distance travelled by a particle flow between two model updates δ_n computed by considering the bulk velocity of the fuel inlet $U_b = 15m/s$. δ_n is compared to the combustion TFLES filter size $\Delta = 2.25$ mm and the reference length $L = 10$ mm.*

Figure 5.37 represents the evolution of the average wrinkling factor $\Xi^S_{\Delta\,avg}$ in different strip locations for different periods between updates n. The procedure adapts the value of the local wrinkling factor independently of n. For $n = 1000$, the efficiency value barely follows the refined one, and for $n = 2000$, the steps in the computation steps become important.

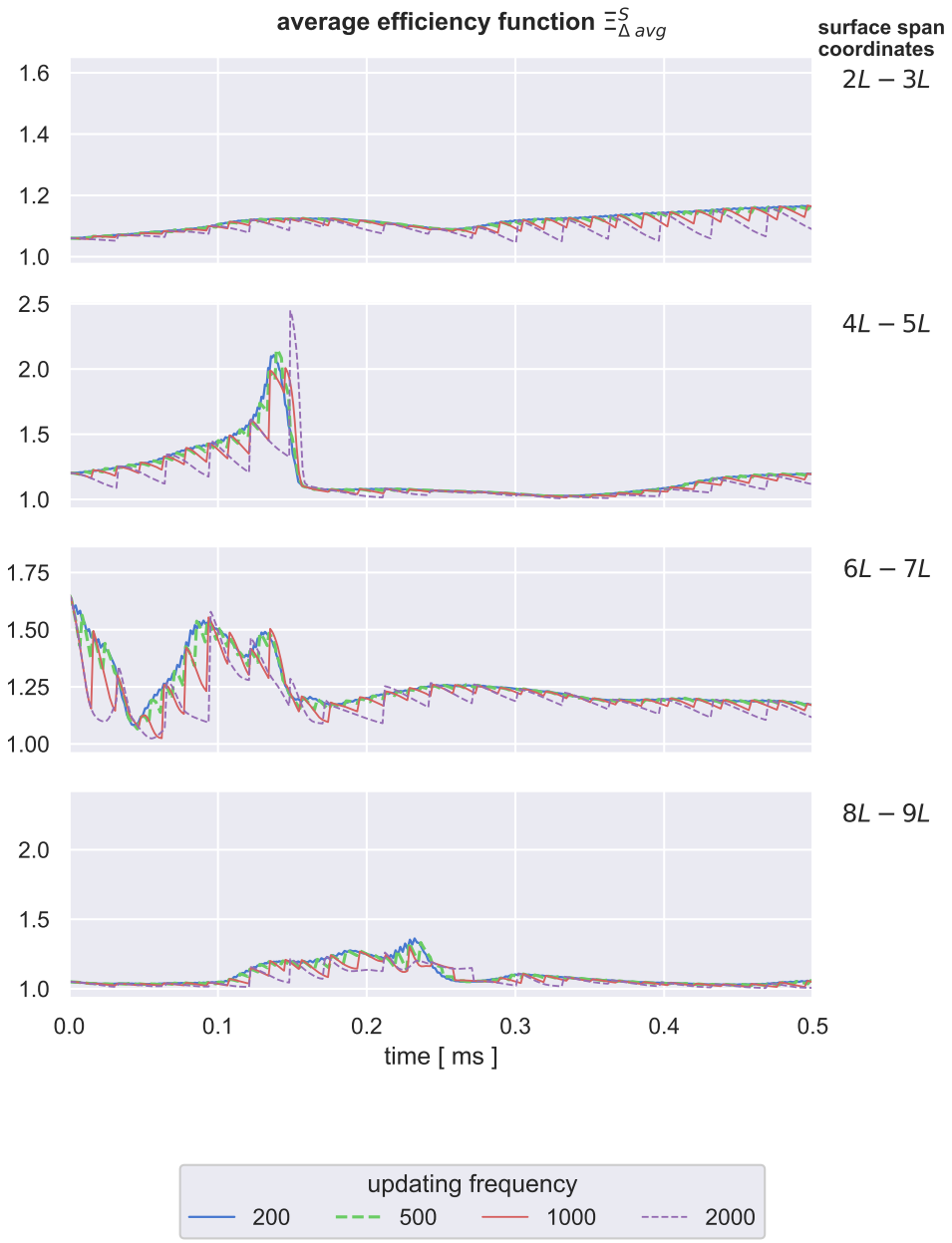

Figure 5.37 – *Time evolution of the wrinkling factor* $\Xi_\Delta(x,t)$ *at different domain strip and numbers of updating iterations* n.

5.4.7 Computational Costs

The simulations were performed on 240 cores on an SGI ICE X machine through computational time slots of 4 hours. Simulations without the model computed a physical time of 18 ms during a single time slot, while the thickened solution without the dynamic model performed a physical time of 19 ms. Table 5.5

resumes all the cases' computational costs and compares them to a solution with constant efficiency. The application of the dynamic model, for the specific case, doubles the computational cost compared to the thickened solution with constant efficiency. The dynamic model reference case $C_{1.5\Delta}^{3.0\Delta}$ with an updating iterations $n = 500$ computes a physical time span of $8\,ms$. The filter widths determine an extra over-cost related to the filtering operation. Increasing average filter width from 3.0Δ to 4.0Δ increases the computational cost by 60%. The increase of test filter width from 1.5Δ to 3.0Δ raises the cost by 33 %. Generally, the cost increases with the size of the filter widths. For this reason, test and average filter sizes should be kept as small as possible, with the only limitation to ensure that the resolved flame wrinkling at the test filter level is well captured. Increasing the updating iterations from 500 to 1000 decreases the computational costs by 20 %. The updating iterations n should be kept as small as possible so that the distance traveled by a particle between two updates does not interact with the TFLES filter and the integral length scale. On the other side, small values increase the computational times.

case	$\hat{\Delta}$	Δ_{avg}	n	CPU time per physical time (hours/ms)	Base 100
reference DNS	-	-		53	96
constant efficiency	-	-		55	100
$C_{3.0\Delta}^{1.5\Delta}$	1.5Δ	3.0Δ	500	120	218
$C_{4.0\Delta}^{1.5\Delta}$	1.5Δ	4.0Δ	500	192	349
$C_{3.0\Delta}^{2.0\Delta}$	3.0Δ	3.0Δ	500	160	290
$C_{3.0\Delta}^{1.5\Delta}$	1.5Δ	3.0Δ	1000	96	175

Table 5.5 – *Comparisons of computational costs for the analyzed cases.*

5.5 Conclusion

The thickened flame model TFLES applied to non-premixed turbulent combustion has been investigated. A planar test case has been set up to carry on the

investigation properly. The flame structure has been investigated for the fully resolved jet in terms of local quantities (scatter plots) and global (heat release, flame surfaces, and heat release per flame surfaces). The setup case fulfills the requirements of infinitely fast chemistry assumption.
Next, the TFLES model has been applied to the flame without any efficiency function. The application of a flame sensor is required to preserve the flame dynamic in a turbulent state. Although the flame's local structure does not change when the flame is thickened, the global quantities are impacted. The dynamic formulation has been so investigated in order to account for the loss of flame surface. The heat release a priori cannot be recovered by the TFLES model as shown by the analytical formulation in chapter 4. The use of the flame sensor slightly improves the prediction, but on the other hand, it induces non-physical parasitic effects that alter the correct operation of the model and have to be accurately managed to avoid spurious values. Therefore for the dynamic formulation of the wrinkling factor, the exponential parameter β is obtained by considering a progress variable conditioned by the flame sensor value (Eq. 5.15). The flame's fractal behavior, stated in the analysis, allows a fractal formulation of the wrinkling factor to recover the loss of the flame surface. The inner cut-off length also plays a relevant role in the model formulation. In the present work, its size has been estimated from the reaction thickness of the non-thickened flame. An over-sizing of the inner cut-off length can quickly turn off the model values.
By choosing the filter size $\hat{\Delta}$ within a limited range of the flame thickness size, the dynamic formulation recovers the total flame surface satisfyingly, at least after a certain distance from the splitter plate, where the flow is fully developed. Nevertheless, the model's activation at the splitter plate tip requires more accurate analysis and specific formulation.
The computational cost of the dynamic formulation is strictly related to the filter sizes of the filtering operations. An accurate choice of the number of iterations between two updates of the model can be estimated by considering the respective distance traveled by a flow particle in between, which has to be small enough to not interact with the TFLES filter size Δ. A technique to further reduce the computational cost could be to compute the dynamic formulation only in a well-bounded portion of the domain where the flame dynamic's correct prediction is required.
Conclusively, the dynamic formulation for diffusion flame can accurately recover the loss of flame surface, but not the overprediction of the heat release, advocating its application on a flame surface-based combustion model to correctly predict the reaction rate per flame surface.

Conclusion and perspectives

This work's objective was to investigate a dynamic formulation for the flame surface wrinkling factor coupled with the thickened flame model (TFLES) to perform large-eddy simulations of turbulent diffusion flames.
The influence of the TFLES formalism is first tested in a laminar steady counter-flow non-premixed flame using analytical and numerical studies. The analysis has shown the model limitations in predicting global quantities such as heat release rates which depend on the thickening factor as $\sqrt{F}$. The introduction of a flame sensor can improve the prediction to a certain extent but induces species mass fraction gradient peaks that have to be properly handled. It should be pointed out that, as long as the chemistry is sufficiently fast, reaction rates are primarily controlled by molecular diffusion processes, and any change in diffusion characteristics, as done in the TFLES framework, affects them. Nevertheless, we examined several solutions to adapt the model to diffusion flames, but none can be practically used for real applications. For example, using tabulated chemistry or analytical relations to reduce reaction rates to counter-balance overestimated diffusion fluxes leads to unphysical unburnt reactants. However, it is expected that the model performs well when reaction rates are mainly controlled by turbulent transport, or reactants are burning in a partially premixed combustion regime, as suggested by results reported in the literature.
The counter-flow flame configuration was also used to investigate simplified chemical mechanisms in view of simulating the Sandia D flame, one of our primary goals (Annex A). Unfortunately, this study highlighted several difficulties which led to giving up this objective. Therefore, a planar turbulent jet has been considered to investigate the thickened flame model's behavior coupled with a dynamic determination of the flame surface wrinkling factor. For the sake of optimizing computational time, the set-up assumes a two-dimensional flow and is designed to provide a fully resolved reference solution without a combustion model (direct numerical simulation limit).
The validity of the infinitely fast chemistry limit is first assessed from a local analysis of the reference direct numerical simulation and the thickened flame. Then, the flame surface wrinkling factor, describing flame/turbulence interactions, is modeled by a dynamic formulation of a fractal-like expression determining the unresolved flame surface from the knowledge of the resolved one.

The influence of the physical and numerical parameters entering the dynamic formalism is first examined to verify the model's correct behavior, while the inner cut-off length scale is identified to the reaction zone thickness. The dynamic model is found to correctly predict the total flame surface without adjusting model parameters. However, due to the enhancement of reaction rates per unit of flame area induced by the thickening procedure, the overall reaction rate remains significantly overestimated.

These results suggest two main directions as perspectives. The first direction points to investigate the behavior of the thickened flame model in situations where reaction rates are mainly controlled by the turbulent transport of reactants towards the flame and when the combustion regime is more related to the burning of partially premixed reactants than displaying ideal diffusion flame structure, as observed in highly turbulent lifted flames. In these cases, the local increase of diffusive transport in the flame front might have a negligible influence on overall reaction rates explaining the good results reported in the literature when using the thickened flame model for non-premixed turbulent flames.

The second route is to take advantage of the ability of the dynamic formulation to predict the total flame surface, replacing the thickened flame model in the estimation of local reaction rates by another approach, for example, a flamelet formalism, possibly coupled with tabulated chemistry. Certainly, three-dimensional large-eddy simulations of non-premixed flames of practical interest are mandatory to go further.

Appendix A

Reduced Chemical Mechanisms for Methane

Nowadays, simulations of reacting flows of practical interest still require substantial computational effort. Reacting species goes through hundreds of reactions producing, in turn, hundreds of final and intermediate products. For example, a detailed mechanism (GRI) for methane includes 325 reactions and 53 species. All those equations become a non-neglecting burden that has to be added to the flowfield equations making the computation prohibitive. However, to predict global quantities such as temperature distribution, flame speed, or the dominant species' distribution, detailed mechanisms can be reduced to a reasonable cost.
The purpose of this chapter is to accurately select a reduced mechanism for methane that can be used to carry on large-eddy simulations of non-premixed and partially premixed mixtures and ultimately evaluate the feasibility to simulate a real operating burner, namely the Sandia D burner (Barlow et al., 2005; Barlow and Frank, 2007). The most suitable mechanism is chosen from simulations of a laminar counter-flow flame. The reduced mechanisms are compared with the results of a detailed one, namely the GRI 3.0 (Smith et al., 1999) mechanism.
First, the BFER mechanism developed by Franzelli et al. (2012) is tested, then a modified BFER is proposed. Finally, within a considerable computational over cost, an analytical scheme, namely LU (Lu and Law, 2008), is examined.

A.1 Introduction

Combustion involves, in reality, thousands of elementary reactions that produce, in turn, as many species. When the purpose is to describe global flame characteristics such as flame speed, temperature distribution, or heat release, detailed mechanisms are unnecessary and can be replaced by reduced ones. However, a reduced mechanism behaves well for a limited range of operating

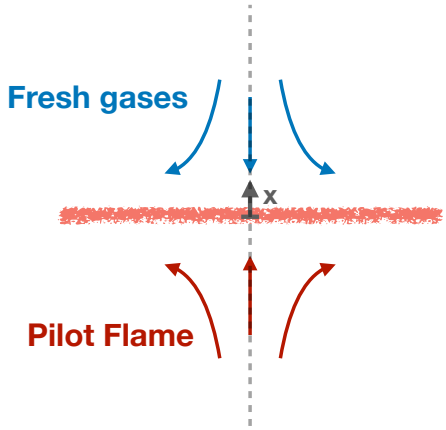

Figure A.1 – *Laminar counter-flow testing flame configuration. Fresh gases: rich mixture methane/air. Pilot flame: burnt gases lean mixtures methane/air. x indicates the axial coordinate.*

conditions, so a reference configuration is essential to correctly choose the most suitable one. The chosen configuration is related to the reference diffusion flame Sandia D (Barlow et al., 2005; Barlow and Frank, 2007). This flame is characterized by the presence of a pilot flame which ignites the combustion. In order to reproduce this process, the configuration chosen for the present analysis is a counter-flow flame of the fresh gas ($300K$) methane/air rich mixture (Φ=3.17) pushed against pilot flame gases as shown in figure A.1. The composition of the pilot flame is determined by the equilibrium of a lean mixture of air-gas (Φ=0.77) related to the chemical mechanism. Table A.1 resumes the compositions of the reactants. The mean strain rate imposed is $200s^{-1}$.
Along the symmetry axis (shown in figure A.1) the flow can be considered one-dimensional. The simulations with the detailed GRI mechanism have been run with the REGATH code (Darabiha, 1992), an in-house solver for reacting one-dimensional NS equations[1]. Instead, the computations with the reduced mechanism have been run for a planar domain, shown in figure A.2, with AVBP solver (Schönfeld and Rudgyard, 1999). The inlets are velocity-imposed, while the output is constant pressure at 1 bar. The size of a cell grid is 0.05 mm, while the entire mesh comprises 1.8 million triangular elements. The convection term's numerical scheme is a finite volume Lax-Wendroff, and the computations are run without any artificial viscosity.

[1] All the computations with REGATH code have been gently run by my friend and PhD collegue at École CentraleSupélec Giampaolo Maio

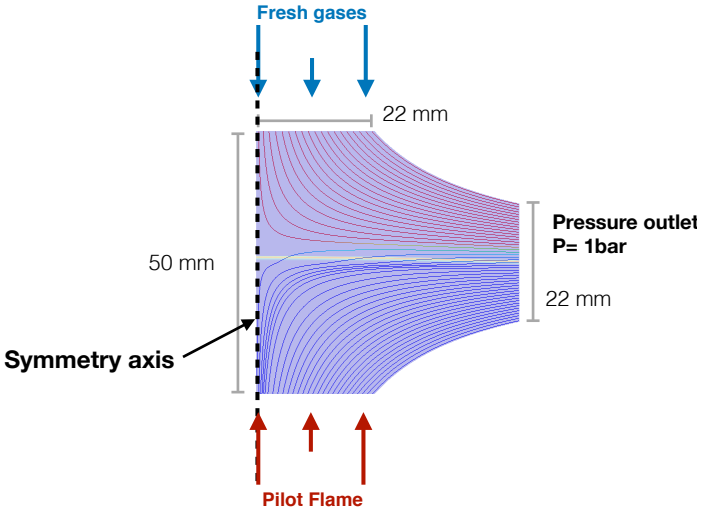

Figure A.2 – *Computational domain. The central axis is considered as symmetry axis and treated as a non viscous wall. The boundary walls of the domain are shaped like the streamlines of potential counter flow.*

	Fresh Gases	Pilot Flame
stoichiometry ϕ	3.17	0.77
composition	$Y_{CH_4} = 0.1561$, $Y_{O_2} = 0.1966$, $Y_{N_2} = 0.6473$	Determined by the chemical mechanism
temperature	300 K	

Table A.1 – *Reactants inlet conditions of the reference counter-flow laminar flame. The temperature and composition of the pilot flame are determined by the equilibrium of the chemical mechanism considered.*

A.2 BFER Mechanism

The first mechanism analyzed is the BFER (Franzelli et al., 2010). The methodology of the BFER mechanism is based on a parameter best fitting in order to reproduce the behavior of the flame on a relatively wide range of equivalence ratio, pressure and temperature. It has been first validated with premixed flames with GRI mechanism and then used for gas fueled swirled burner (Franzelli et al., 2012). The BFER mechanism accounts for 6 species and 2 reactions namely:

$$CH_4 + \frac{3}{2} O_2 \longrightarrow CO + 2\,H_2O \tag{A.1}$$

$$CO + \frac{1}{2} O_2 \longleftrightarrow CO_2 \tag{A.2}$$

	A_j [mol/(s cm^3)]	E_{aj} [cal/mol]	n_{CH_4}	n_{CO}	$n_{O_2,j}$
j=1	4.9×10^9	3.55×10^4	0.5	-	0.65
j=2	2×10^8	1.2×10^4	-	1	0.5

Table A.2 – *Pre-exponential factors A_j, activation energies E_{aj} and reaction exponents $n_{k,j}$ for the BFER mechanism.*

The laminar flame speed is directly related to the fuel consumption rate, and it is mainly determined by the reaction (A.1). The second reversible reaction (A.2) represents the equilibrium of CO and CO_2, and it is mandatory to predict the burnt gas temperature for rich mixtures.
The idea is to correct the forward reaction rates of the classical Arrhenius law (Eq. 1.42) by multiplying by a factor f_j, based on the equivalence ratio[2] ϕ, each reaction j:

$$k_{f1} = A_1 f_1(\phi) \exp\left(-\frac{E_{a,1}}{RT}\right) [CH_4]^{n_{CH_4}} [O_2]^{n_{O_2,1}} \tag{A.3}$$

$$k_{f2} = A_2 f_2(\phi) T^{0.7} \exp\left(-\frac{E_{a,2}}{RT}\right) [CO]^{n_{CO}} [O_2]^{n_{O_2,2}} \tag{A.4}$$

where A_j is the pre-exponential factor of reaction j, $E_{a,j}$ is the activation energy and $n_{k,j}$ is the reaction exponent for species k in reaction j. Those parameters are resumed in table A.2. The correction factor f_1 allows decreasing the laminar flame speed for rich flames, while f_2 is calibrated to adjust the post-flame zone's thickness and quickly reach the equilibrium state. They depend on the equivalence ratio of the mixture and they are given by:

$$f_1(\phi) = \frac{2}{\left[1 + \tanh\left(\frac{\phi_{0,1}-\phi}{\sigma_{0,1}}\right)\right] + B_1\left[1 + \tanh\left(\frac{\phi-\phi_{1,1}}{\sigma_{1,1}}\right)\right] + C_1\left[1 + \tanh\left(\frac{\phi-\phi_{2,1}}{\sigma_{2,1}}\right)\right]} \tag{A.5}$$

$$f_2(\phi) = \frac{1}{2}\left[1 + \tanh\left(\frac{\phi_{0,2}-\phi}{\sigma_{0,2}}\right)\right] + \frac{B_2}{2}\left[1 + \tanh\left(\frac{\phi-\phi_{1,2}}{\sigma_{1,2}}\right)\right] + \frac{C_2}{2}\left[1 + \tanh\left(\frac{\phi-\phi_{2,2}}{\sigma_{2,2}}\right)\right]\left[1 + \tanh\left(\frac{\phi_{3,2}-\phi}{\sigma_{3,2}}\right)\right] \tag{A.6}$$

The values of the coefficients are listed in table A.3 and the resulting functions f_1 and f_2 are plotted in figure A.3.

[2]defined as the fuel-to-oxidizer ratio to the stoichiometric fuel-to-oxidizer ratio (Poinsot and Veynante, 2012): $\phi = \left(\frac{Y_F}{Y_O}\right) / \left(\frac{Y_F}{Y_O}\right)_{st}$

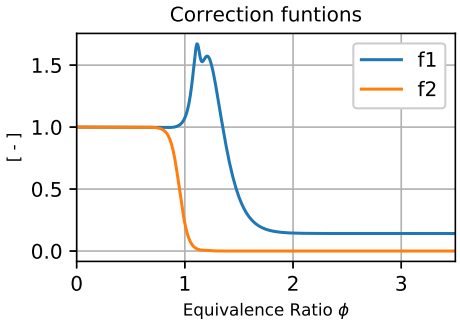

Figure A.3 – *Evolution of the correction functions f_1 and f_2 of the BFER mechanism versus the equivalence ratio* Φ.

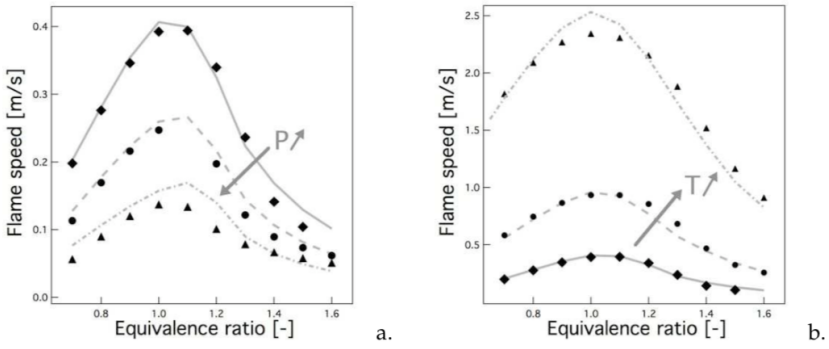

Figure A.4 – *a) Pressure and equivalence ratio dependence of the flame speed for fresh gas temperature $T_f = 300K$ and pressure P =1,3,10 atm. b) Temperature and equivalence ratio dependence of flame speed for P = 1atm and Tf =300,500,700 K. Comparison between a detailed GRI 3.0 (Smith et al., 1999) (black symbols) and reduced BFER (grey lines) mechanisms (Franzelli et al., 2012).*

	$\phi_{0,j}$	$\sigma_{0,j}$	B_j	$\phi_{1,j}$	$\sigma_{1,j}$	C_j	$\phi_{2,j}$	$\sigma_{2,j}$	$\phi_{3,j}$	$\sigma_{3,j}$
$j=1$	1.1	0.09	0.37	1.13	0.03	6.7	1.6	0.22	-	-
$j=2$	0.95	0.08	2.5×10^{-5}	1.3	0.04	0.0087	1.2	0.04	1.2	0.05

Table A.3 – *Coefficients for the two correction function f_1 and f_2 in the BFER scheme (Franzelli et al., 2012).*

The corrections are derived from simulations of freely propagating planar laminar flames. The mechanism has been tested and validated in literature for several values of fresh gas temperature and pressure as shown in figure A.4. However, the range of equivalence ratio validated (ϕ=0.7-1.6), and it has not been used for diffusion flames. In the present work, the BFER mechanism has been first used to check the consistency between the two solvers (compressible AVBP and 1-D REGATH) for premixed freely propagating methane/air flames

at different equivalence ratio ϕ by comparing the laminar flame speed[3] and the flame thickness[4]. As shown in figure A.5, the solutions with AVBP solver perfectly overlap the ones from REGATH solver both for the laminar flame speed and the laminar flame thickness.

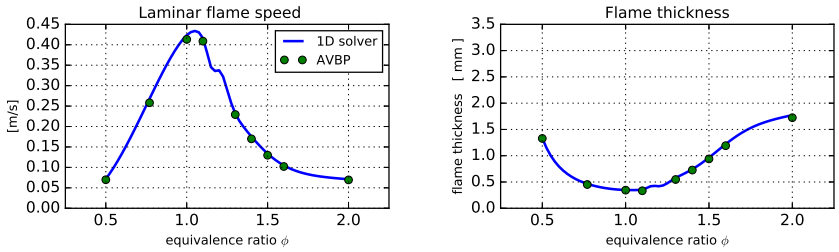

(a) (b)

Figure A.5 – *Premixed freely propagating 1D flame simulation of methane/air mixture over the equivalence ratio with BFER mechanism. Comparison of compressible solver AVBP with 1-D Regath solver. (a) Laminar flame speed; (b) Laminar flame thickness computed with the progress variable c based on the temperature profile as* $\delta_L = 1/|\Delta c|_{max}$.

A.2.1 Simulation with BFER

The BFER mechanism is here used to simulate the counter-flow test case shown in figure A.2. For diffusion flames because of the correction factors $f_1(\phi)$ and $f_2(\phi)$, it is necessary to define a local equivalence ratio as (Poinsot and Veynante, 2012):

$$\phi = \left(\frac{z}{1-z}\right)\left(\frac{1-z_{st}}{z_{st}}\right) \tag{A.7}$$

where the mixture fraction z is referred to the a pure methane-air diffusion flame, with $z = 1$ in pure methane and $z = 0$ in pure air conditions, and $z_{st} = 0.055$.
A first set of simulations is run to compare the BFER mechanism with the detailed GRI 3.0.
Figure A.6 shows the comparison for the heat release profile along the axis in both spatial axial coordinate and local equivalence ratio ϕ. The BFER mechanism overpredicts the rich zone for $\phi > 1.6$ and the overprediction is consequently found for the temperature shown in figure A.7.

[3] the laminar flame speed is computed with the burning rate of the fuel across the flame brush as $S_L = \frac{1}{\rho_0}\int_{-\infty}^{+\infty} \dot{\omega}_{CH_4} dx$

[4] the flame thickness is computed with the progress variable c based on the temperature as $\delta_L = 1/\max\left|\frac{\partial c}{\partial x}\right|$

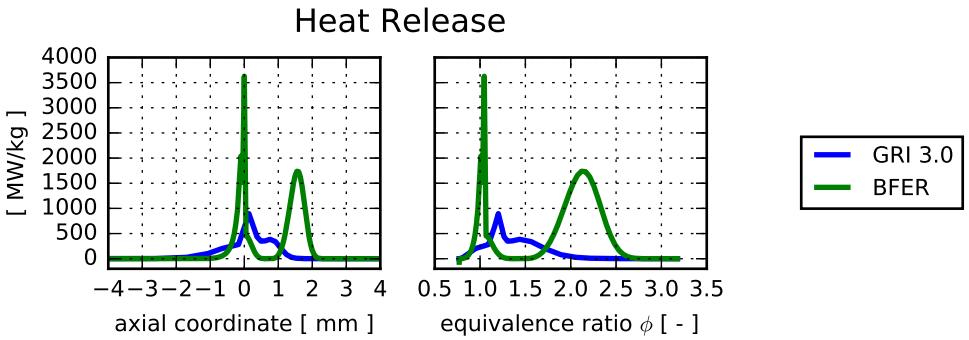

Figure A.6 – *Comparison of the BFER with the detailed GRI 3.0 mechanism. Distribution of heat release per unit mass over the axial coordinate and the equivalence ratio ϕ.*

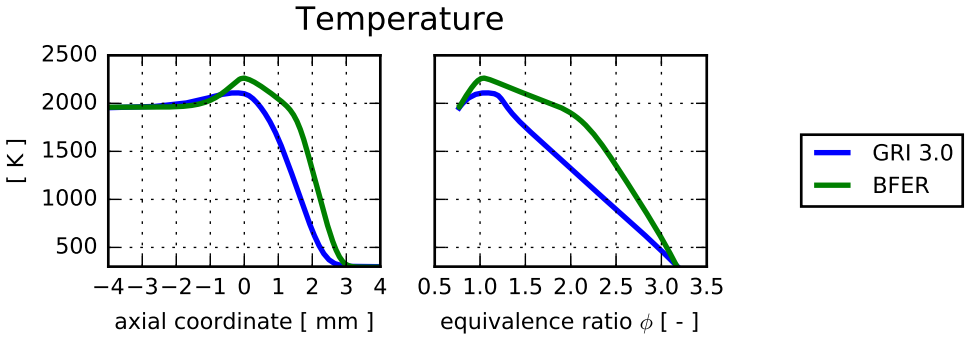

Figure A.7 – *Comparison of the BFER mechanism with the detailed GRI 3.0 mechanism. Temperature profile over the axial coordinate and the equivalence ratio ϕ.*

Consequently, the distributions of the species shown in figure A.8 are mismatching, particularly the oxygen. This is most likely due to the fact that the consumption rate of the methane is over-predicted (in absolute value) by the BFER mechanism as shown in figure A.9. In the BFER mechanism, the first reaction (Eq. A.3) involves the methane. By further reducing the reaction rate with the coefficient f_1, it could be possible to recover the mismatching. This solution is used in the following section.

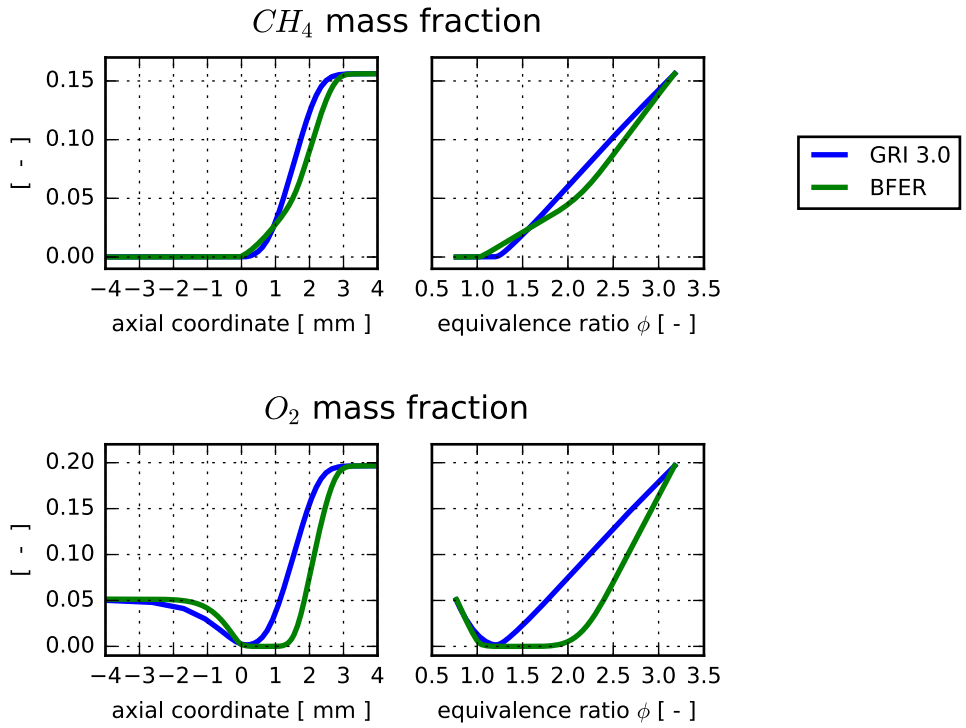

Figure A.8 – *Comparison BFER mechanism with the detailed GRI 3.0 mechanism. Mass fraction profiles of CH_4 and O_2 over the axial coordinate and the equivalence ratio ϕ.*

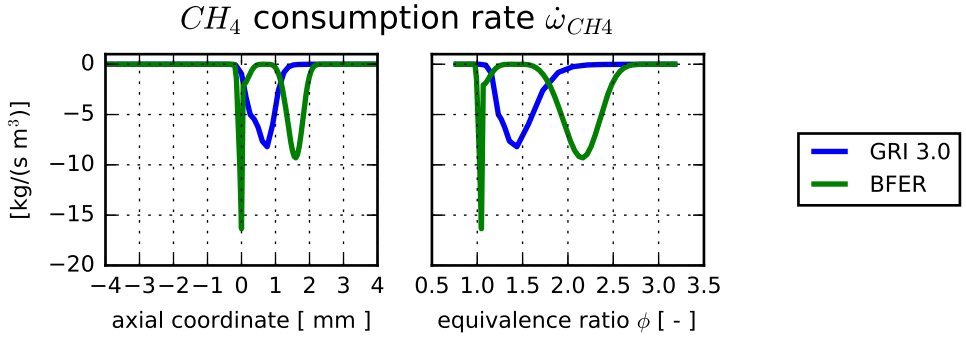

Figure A.9 – *Comparison of the BFER mechanism with the detailed GRI 3.0 mechanism. Methane consumption rate profile $\dot{\omega}_{\mathrm{CH_4}}$ over the axial coordinate and the equivalence ratio ϕ.*

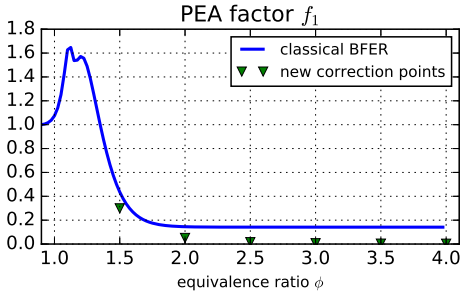

Figure A.11 – *comparison of the value of the coefficient correction f_1 for the classical BFER and the Modified BFER.*

A.3 Modified BFER Mechanism

Since the BFER mechanism has been optimized for a limited equivalence ratio range, the proposed solution is to further extend the correction function to a broader range of values. Since the flame speed is controlled by the consumption rate of the fuel (reaction A.1), only the function f_1 is modified.
So, by considering a freely propagating 1-D premixed flame, simulations are run with the BFER model and compared in terms of flame speed with results of detailed GRI 3.0 mechanism. The discrepancies of results are used to determine the corrections to obtain the new function f_1, and the procedure goes on iteratively until the new flame speed corresponds to the reference speed obtained with GRI 3.0. The procedure's result is displayed in figure A.10(a), while figure A.10(b) shows the resulting flame thickness. Figure A.11 compares the values of the new function f_1 with the old one. The new function overlaps the classical one for $\Phi < 1.5$.

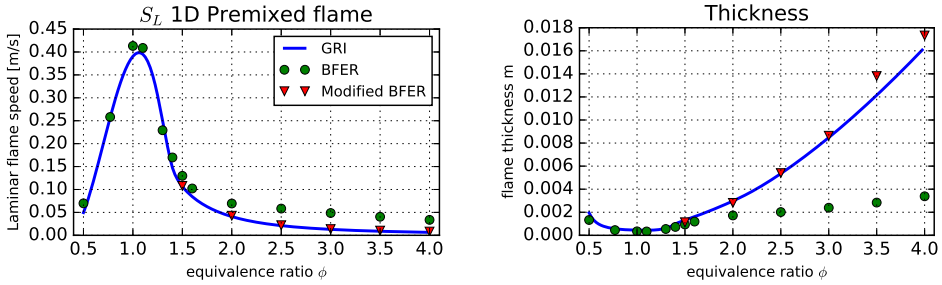

(a) (b)

Figure A.10 – *Comparison of the classical BFER mechanism and the modified BFER with the detailed GRI 3.0 mechanism. (a) laminar flame speed, (b) laminar flame thickness.*

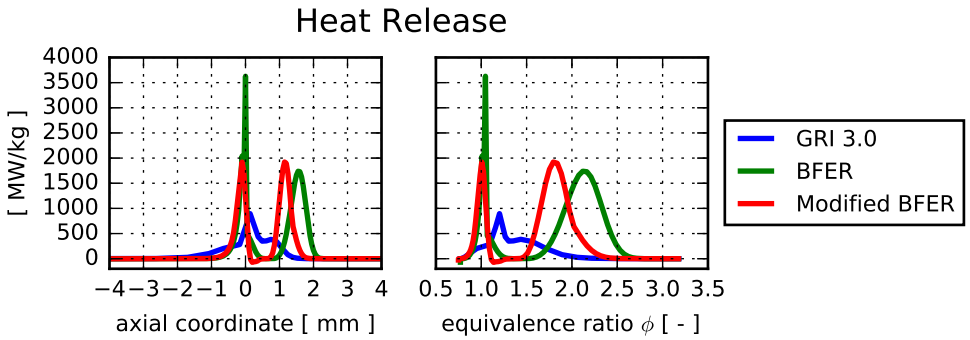

Figure A.12 – *Comparison of the BFER and modified BFER mechanism with the detailed GRI 3.0 mechanism. Profiles of heat release per unit mass over the axial coordinate and the equivalence ratio ϕ.*

A.3.1 Simulations with Modified BFER mechanism

By considering the heat release (Fig. A.12), the rich zone's peak is slightly shifted and remains too high. The global heat release[5] of the classical BFER, listed in table A.4, is almost twice the one from the GRI, and no significant improvement is observed for the modified BFER.

Chemical Mechanism	Global heat release [W m /g]
GRI 3.0	857
BFER	1594
Modified BFER	1359

Table A.4 – *Global heat release for GRI 3.0, BFER and Modified BFER mechanims.*

Consequently, the temperature profile is still far from the detailed mechanism (Fig. A.13) as well as the species profiles (Fig. A.14). The methane consumption, shown in figure A.15, slightly improves, and the Modified BFER mechanism perfectly recovers the global consumption rate of methane[6] shown in table A.5.

Chemical Mechanism	Global methane consumption rate [g /m^2]
GRI 3.0	6.42
BFER	7.4
Modified BFER	6.3

Table A.5 – *Global methane consumption release for GRI 3.0, BFER and Modified BFER mechanims.*

[5] the heat release per unit mass integrated across the flame front
[6] the consumption rate integrated across the flame front

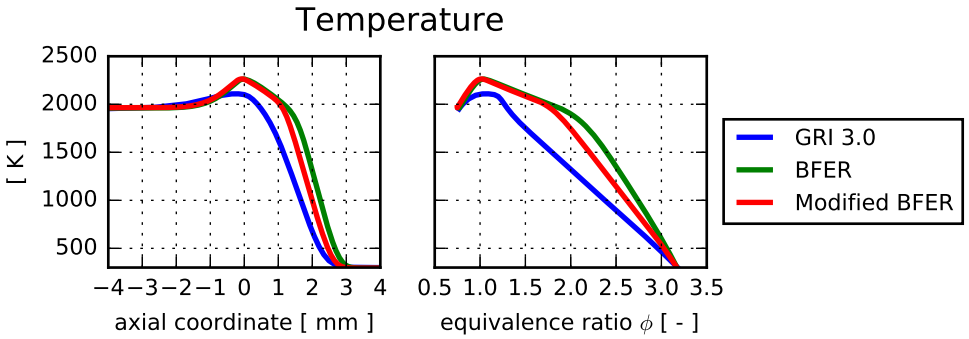

Figure A.13 – *Comparison of the BFER and modified BFER mechanism with the detailed GRI 3.0 mechanism. Temperature profiles over the axial coordinate and the equivalence ratio ϕ*

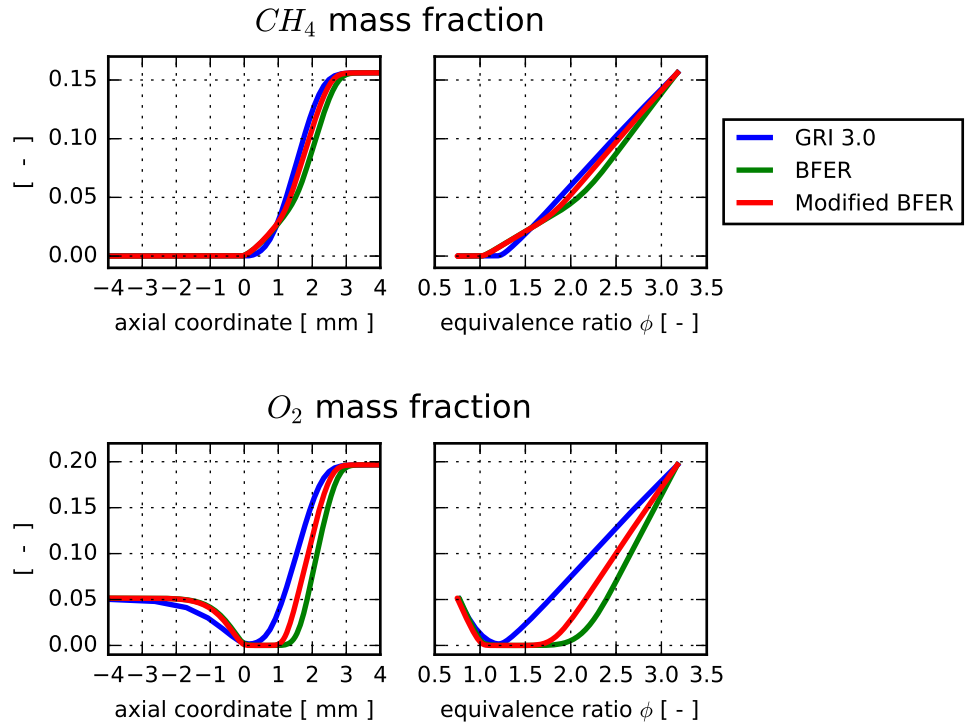

Figure A.14 – *Comparison of the BFER and modified BFER mechanism with the detailed GRI 3.0 mechanism. Mass fraction profiles of CH_4 and O_2 over the axial coordinate and the equivalence ratio ϕ.*

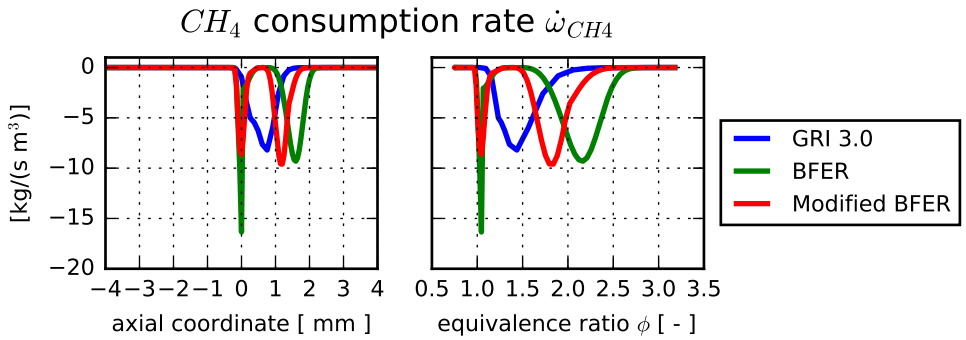

Figure A.15 – *Comparison of the BFER and modified BFER mechanism with the detailed GRI 3.0 mechanism. CH_4 consumption rate over the axial coordinate and the equivalence ratio ϕ*

The discrepancy of the heat release and the fuel consumption's accordance suggests that for rich mixture, the methane recombines in intermediate species through low energy reactions before reacting with oxygen. A simple 2-step mechanism such as the BFER does not consider those intermediate products and considers the fuel's oxidation instead.

A.4 The LU Mechanism

Because even by further investigating the correction functions, the BFER mechanism is not suited for very rich mixtures, we consider adopting an analytical mechanism (Li et al., 1999; Sánchez et al., 2000; Boivin et al., 2011; Lu and Law, 2008). The smallest one found in the literature for methane is the LU scheme (Lu and Law, 2008). It comes from the reduction of skeletal schemes by using a quasi-steady-state (QSS) for some species and the partial equilibrium assumption for some reactions. The LU mechanism is obtained by reducing the GRI 1.2 (Frenklach et al., 1995), with the directed relation graph method, the sensitivity analysis, and the computational singular perturbation approach (Lu and Law, 2008). It takes into account 13 resolved species (CH_4, O_2, CO_2, CO, H_2O, N_2, H_2, H, OH, O, HO_2, CH_3 and CH_2O), 4 QSS species (CH2, CH2S, HCO and CH2OH) and 73 elementary reactions. Simplified transport properties are assumed with constant Lewis numbers (relation 1.38) summarized in table A.6.

CH_4	O_2	CO_2	CO	H_2O	H_2	N_2	H	O	OH	HO_2	CH_3	CH_2O
0.0967	1.0557	1.35	1.07	0.777	0.29	1.036	0.17	0.69	0.7	1.07	0.97	1.25

Table A.6 – *Species Lewis numbers of the LU scheme.*

As shown in figure A.16, the distribution of the heat release is very close to the

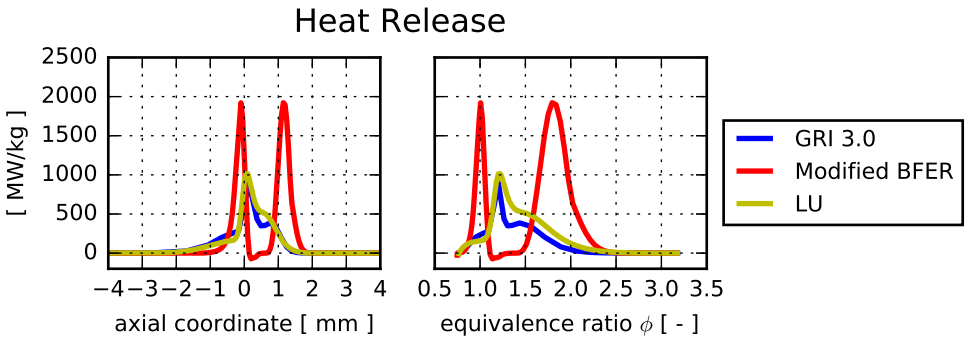

Figure A.16 – *Comparison of the LU and modified BFER mechanism with the detailed GRI 3.0 mechanism. Profiles of heat release per unit mass over the axial coordinate and the equivalence ratio ϕ.*

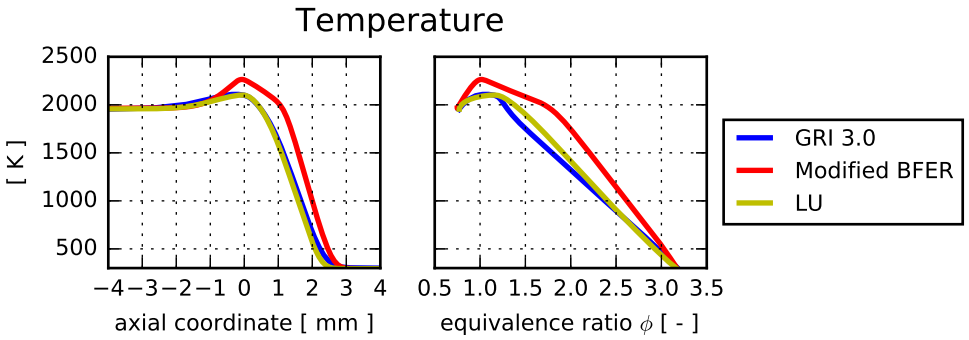

Figure A.17 – *Comparison of the LU and modified BFER mechanism with the detailed GRI 3.0 mechanism. Temperature profiles over the axial coordinate and the equivalence ratio ϕ.*

GRI 3.0, unlikely the modified BFER, as well as the global heat release shown in table A.7.

Chemical Mechanism	Global heat release [W m /g]
GRI 3.0	857
Modified BFER	1359
LU	946

Table A.7 – *Global heat release for GRI 3.0, Modified BFER and LU mechanisms.*

Accordingly, also the distribution of the temperature (Fig. A.17) and the species mass fractions (Fig. A.18) are well predicted with the LU mechanism.

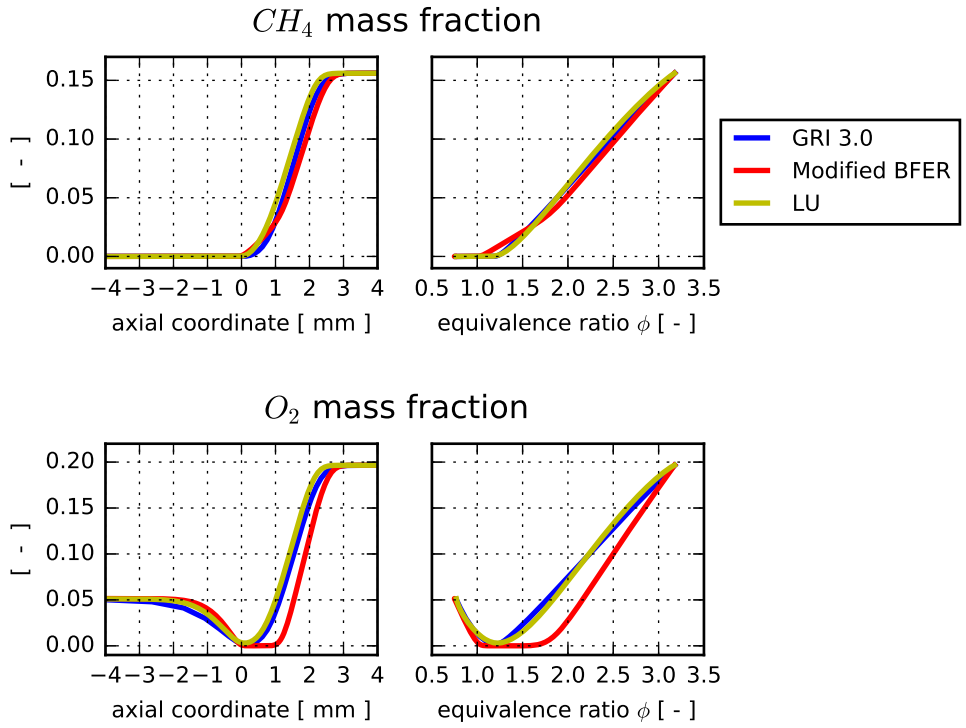

Figure A.18 – *Comparison of the LU and modified BFER mechanism with the detailed GRI 3.0 mechanism. Distribution mass fraction of CH_4 and O_2 over the axial coordinate and the equivalence ratio ϕ.*

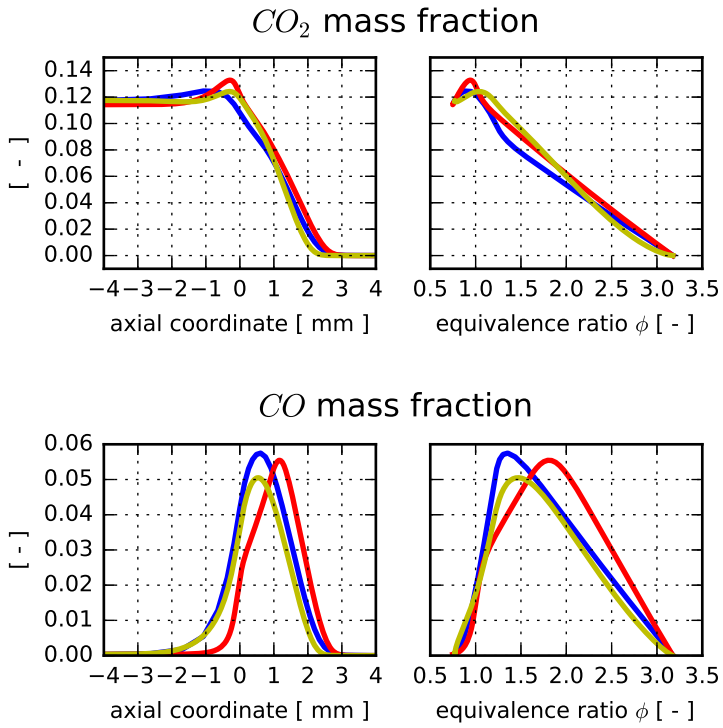

Figure A.19 – *Comparison of the LU and modified BFER mechanism with the detailed GRI 3.0 mechanism. Distribution mass fraction of CO_2 and CO over the axial coordinate and the equivalence ratio ϕ.*

The LU mechanism predicts the flame in rich conditions because it considers intermediate species that are products of methane recombination in rich conditions. Figure A.20 shows the CH_3 and CH_2O mass fraction profiles. The production and extinction of those species happen in a range of equivalence ratio $1.5 < \phi < 3$, where the oxygen is not supposed to react. By looking at the fuel consumption distribution (figure A.21), the recombination of methane in the LU mechanism shifts the peak to overlap the GRI profile.
We can finally presume that the LU mechanism is better suited to simulate rich flames.

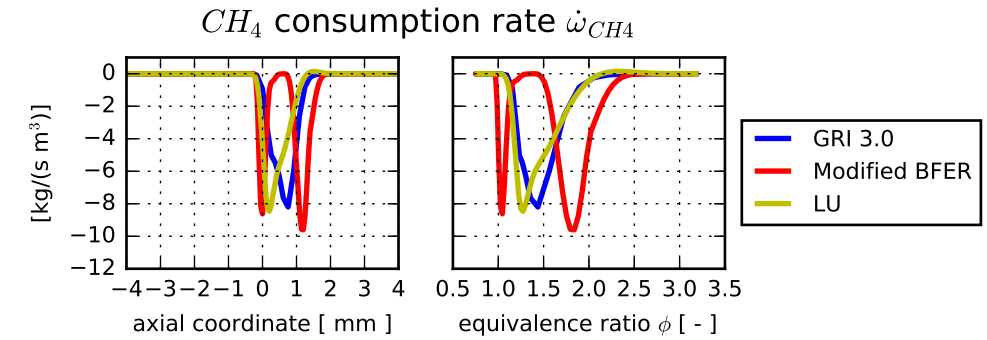

Figure A.21 – *Comparison of the LU and modified BFER mechanism with the detailed GRI 3.0 mechanism. Profiles of methane consumption rate over the axial coordinate and the equivalence ratio ϕ.*

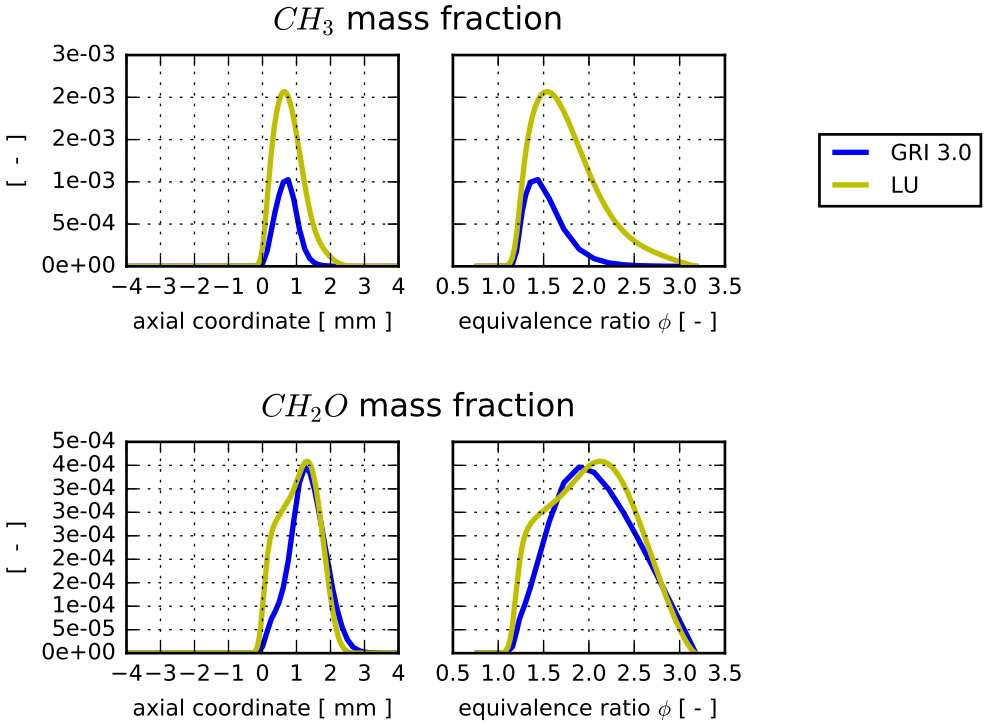

Figure A.20 – *Comparison of the LU and modified BFER mechanism with the detailed GRI 3.0 mechanism. Profiles of mass fraction for the major species over the axial coordinate and the equivalence ratio ϕ.*

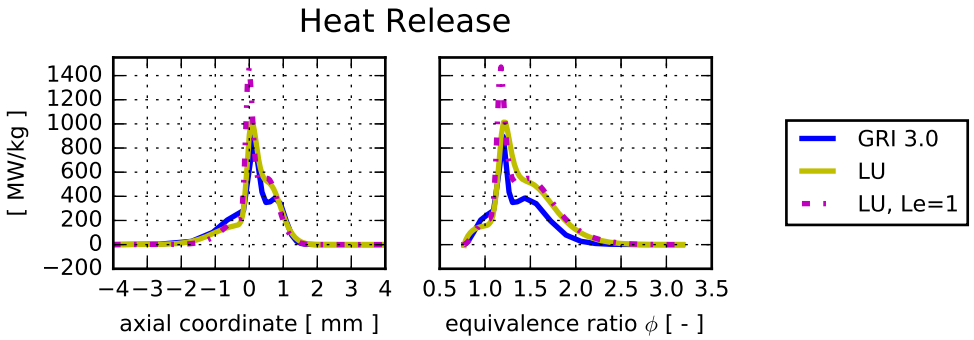

Figure A.22 – *Comparison of LU mechanism and LU with unity Lewis number for the species with the detailed GRI 3.0 mechanism. Profiles of heat release per unit mass over the axial coordinate and the equivalence ratio ϕ.*

A.4.1 Lewis number influence

Since the GRI 3.0 mechanism assumes unity Lewis for all the species, it is interesting to verify the effect of adopting a unity Lewis number for the LU mechanism. So a further simulation is run with the LU mechanism with unity Lewis number Le = 1 for all the species and meta-species. By considering the heat release, a unity Lewis number increases the value at the flame position (see figure A.22), and, consequently, the global heat release slightly increases (table A.8). This results because the original Lewis number of LU mechanism is less than 1 (0.097 see table A.6)

Chemical Mechanism	**Global heat release [W m /g]**
GRI 3.0	857
LU	946
LU Le_k=1	988

Table A.8 – *Global heat release for GRI 3.0, Modified BFER and LU mechanisms.*

In figure A.23 it is possible to note that the temperature is not affected as well as for the fuel and oxizider species (Fig. A.24). A small impact can be viewed for CO_2 and CO in figure A.25.
We can conclude that the Lewis numbers does not affect significantly the predictions of the LU mechanism.

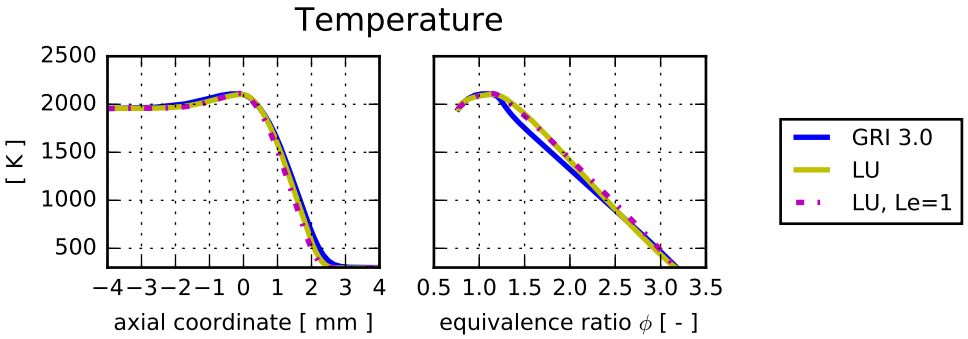

Figure A.23 – *Comparison of LU mechanism and LU with unity Lewis number for the species with the detailed GRI 3.0 mechanism. Temperature profiles over the axial coordinate and the equivalence ratio ϕ.*

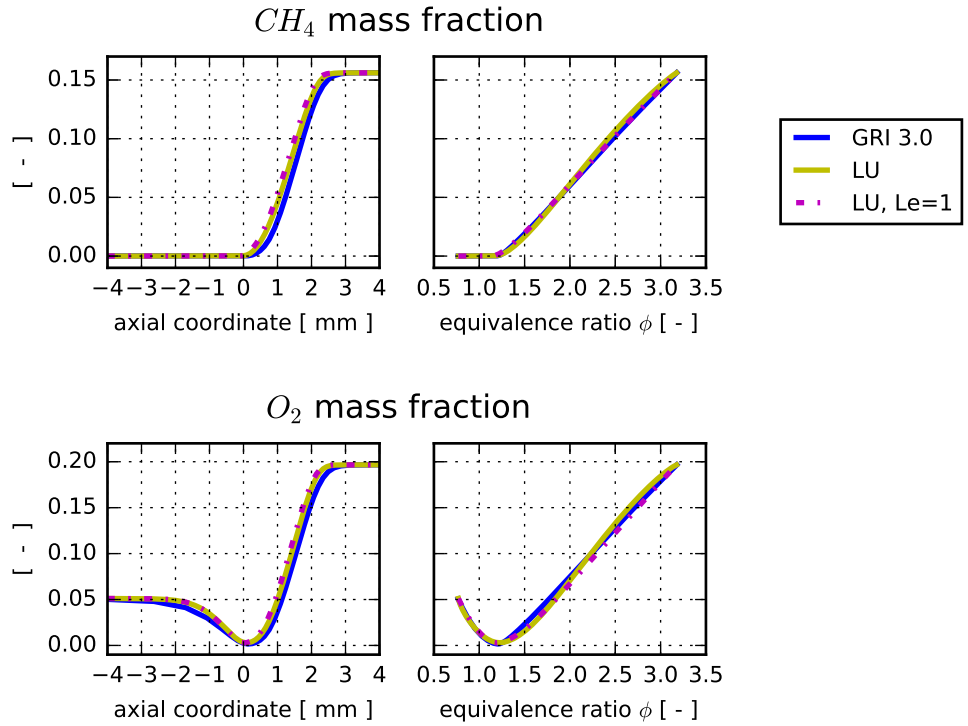

Figure A.24 – *Comparison of LU mechanism and LU with unity Lewis number with the detailed GRI 3.0 mechanism. Mass fraction profiles of CH_4 and O_2 the major species over the axial coordinate and the equivalence ratio ϕ.*

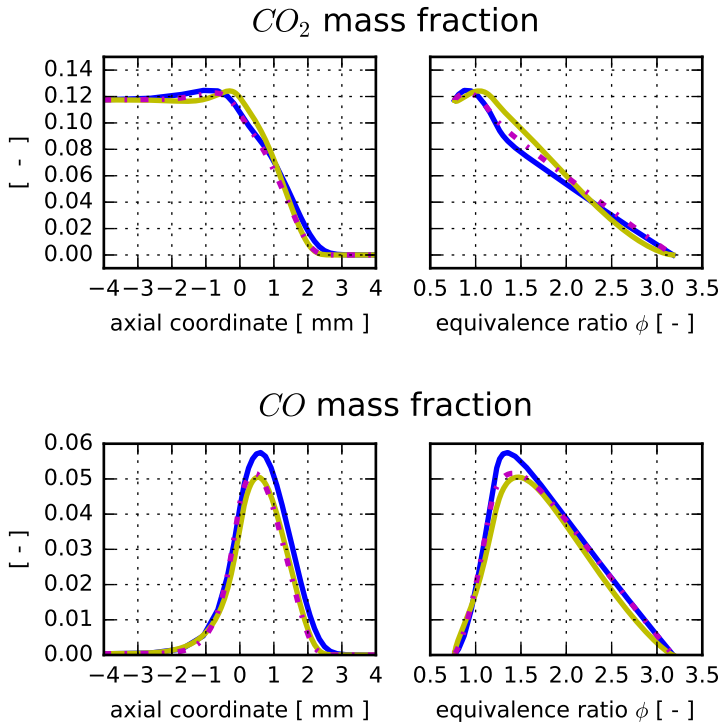

Figure A.25 – *Comparison of LU mechanism and LU with unity Lewis number with the detailed GRI 3.0 mechanism. Mass fraction profiles of CO_2 and CO the major species over the axial coordinate and the equivalence ratio ϕ.*

A.5 Conclusions

This chapter aims to properly select a reduced methane mechanism to conduct LES simulation for diffusion and partially premixed flames. Several mechanisms have been compared to the detailed GRI 3.0 reference mechanism in predicting a representative counter-flow flame configuration.
The BFER mechanism (Franzelli et al., 2010), designed to predict the laminar flame speed for premixed flames up to an equivalence ratio $\phi \approx 1.4$, turns out to not be accurate to describe diffusion flames, even by expanding the correction coefficients to a broader range of equivalence ratio.
A Modified BFER mechanism has been proposed by extending the correction function to higher values of equivalence ratio. Unfortunately, heat release, temperature, and mass fraction profiles are only slightly adjusted, and GRI predictions are still not recovered.
The result is not surprising since the methane-air mixture's reaction at rich conditions involves many minor species, not accounted for in a simple two-step mechanism.
Then the analytical mechanism (Lu and Law, 2008), obtained by reduction of the detailed mechanism GRI 1.2 (Frenklach et al., 1995), has been so adopted, resulting in better predictions. However, it is still too costly for an actual application due to the grid resolution required by some intermediate species due to their small chemical time.
For this reason, the idea of a real flame application simulation such as the Sandia D has been abandoned.

Appendix B

Comparison of filtered and thickened flames for LES in non-premixed combustion

The purpose of this appendix is to show the relation between the filtering and thickening operation over for a non-premixed flame and determine a coefficient correction α to relates them. The analysis focuses on the diffusion thickness impact.

B.1 Laminar non-premixed flame

The mixture fraction balance equation for laminar counter-flow steady strained one-dimensional diffusion flame, with usual notation,writes as:

$$-ax\frac{\partial z}{\partial x} = D\frac{\partial^2 z}{\partial^2 x^2} \tag{B.1}$$

where D is the diffusion coefficient and a the strain rate, and x is the direction normal to the flame front. By considering the boundary conditions $z(+\infty) = 0$ and $z(-\infty) = 1$, the solution of Eq. B.1 is:

$$z = \frac{1}{2}\left[1 - \mathrm{erf}\left(x\sqrt{\frac{a}{2D}}\right)\right] \tag{B.2}$$

The laminar diffusive thickness δ_L can be estimated by the derivative of z in Eq. B.2 along the x direction as:

$$\delta_L = \frac{1}{\max\left(\left|\frac{\partial z}{\partial x}\right|\right)} \tag{B.3}$$

so:

$$\delta_L = \sqrt{\frac{2\pi\, D}{a}} \tag{B.4}$$

B.2 Thickened non-premixed flame

For sake of clarity, the thickened flame model is considered with a constant thickening factor F without any flame sensor. The balance equation for a steady strained one dimensional diffusion flame is:

$$-ax\frac{\partial z}{\partial x} = F\,D\frac{\partial^2 z}{\partial^2 x^2} \tag{B.5}$$

with the same boundary conditions $z(-\infty) = 0$ and $z(+\infty = 1)$, the solution of Eq. B.5 is:

$$z = \frac{1}{2}\left[1 - \mathrm{erf}\left(x\sqrt{\frac{a}{2\,F\,D}}\right)\right] \tag{B.6}$$

Analogously, a diffusive TFLES flame thickness δ_F is retrieved from the derivative of Eq. B.6:

$$\delta_F = \sqrt{\frac{2\pi\,F\,D}{a}} = \sqrt{F}\delta_L \tag{B.7}$$

B.3 Filtered non-premixed flame

The mixture fraction profile can be rewritten from Eq. B.3 as:

$$z = \frac{1}{2}\left[1 - \mathrm{erf}\left(x\sqrt{\frac{a}{2D}}\right)\right] = \frac{1}{2}\left[1 - \mathrm{erf}\left(\frac{\sqrt{6}x}{\sqrt{\frac{12D}{a}}}\right)\right] \tag{B.8}$$

Then, considering relation B.4 leads to:

$$z = \frac{1}{2}\left[1 - \mathrm{erf}\left(\frac{\sqrt{6}x}{\sqrt{\frac{6}{\pi}}\,\delta_L}\right)\right] \tag{B.9}$$

By considering a Gaussian filter function with filter size σ:

$$G(x) = \sqrt{\frac{6}{\pi\sigma^2}}\exp\left(-\frac{6x^2}{\sigma^2}\right) \tag{B.10}$$

equation B.9 corresponds to a step function filtered with a Gaussian filter of size $\delta_L\sqrt{\frac{6}{\pi}}$. Filtering Eq. B.10 with a Gaussian filter of size Δ is equivalent to filtering the step function with a filter size $\sqrt{\Delta^2 + \frac{6}{\pi}\delta_L^2}$. So, the filtered

mixture fraction profile $\tilde{z}$ is

$$\tilde{z} = \frac{1}{2}\left[1 - \mathrm{erf}\left(\frac{\sqrt{6}x}{\sqrt{\Delta^2 + \frac{12D}{a}}}\right)\right] \tag{B.11}$$

A filtered diffusive thickness δ_f can be estimated as:

$$\delta_f = \frac{1}{\max\left(\left|\frac{\partial\tilde{z}}{\partial x}\right|\right)} = \sqrt{\delta_L^2 + \frac{\pi\Delta^2}{6}} \tag{B.12}$$

B.4 Comparison of filtered and thickened diffusive thickness

By considering the thickness of the thickened flame (Eq. B.7), the filter size is related to the equivalent thickening factor F_{eq}:

$$\Delta = \alpha\sqrt{F_{eq}}\,\delta_L \tag{B.13}$$

where α is coefficient to be determined. An equivalent thickening factor F_{eq} for the filtering operation, should fulfill the balance equation of the thickened flame (Eq. B.5). So, by considering Eq. B.6, the filtered mixture profile can be rewritten as:

$$z = \frac{1}{2}\left[1 - \mathrm{erf}\left(x\sqrt{\frac{a}{2\,F_{eq}\,D}}\right)\right] \tag{B.14}$$

Comparing relations B.14 and B.11, after few simple passages, leads to:

$$\delta_L\sqrt{F_{eq}} = \sqrt{\delta_L^2 + \frac{\pi}{6}\Delta^2} \tag{B.15}$$

then:

$$\Delta = \delta_L\sqrt{\frac{6}{\pi}\left(F_{eq} - 1\right)} = \sqrt{\frac{6}{\pi}}\sqrt{F_{eq} - 1}\,\delta_L \tag{B.16}$$

For values of F_{eq} sufficiently large, Eq.B.16 becomes:

$$\Delta = \sqrt{\frac{6}{\pi}}\sqrt{F_{eq}}\,\delta_L \tag{B.17}$$

Then, comparing Eq. B.17 to Eq. B.13 leads to the determination of α:

$$\alpha = \sqrt{\frac{6}{\pi}} \approx 1.4 \tag{B.18}$$

Bibliography

Angelberger, C., D. Veynante, F. N. Egolfopoulos, and T. Poinsot
1998. Large eddy simulations of combustion instabilities in premixed flames. *Proceedings of the Summer Program, Center for Turbulence Research*, Pp. 61–82. *(p. 78)*

Arrhenius, S.
1889. Über die Dissociationswärme und den Einfluss der Temperatur auf den Dissociationsgrad der Elektrolyte. *(p. 16)*

Ashurst, W. M. T.
1993. Flame Propagation Through Swirling Eddies, A Recursive Pattern. *Combustion Science and Technology*, 92(1-3):87–103. *(p. 106)*

Auzillon, P., B. Fiorina, R. Vicquelin, N. Darabiha, O. Gicquel, and D. Veynante
2011. Modeling chemical flame structure and combustion dynamics in LES. *Proceedings of the Combustion Institute*, 33(1):1331–1338. *(p. 45)*

Auzillon, P., O. Gicquel, N. Darabiha, D. Veynante, and B. Fiorina
2012. A Filtered Tabulated Chemistry model for LES of stratified flames. *Combustion and Flame*, 159(8):2704–2717. *(p. 45)*

Ayachit, U., B. Geveci, C. Quammen, D. Demarle, K. Moreland, A. Bauer, B. Boeckel, D. Lipsa, M. Westphal, J. Pouderoux, S. Waldon, A. Choudhary, S. Philip, G. Zagaris, B. Loring, T. Maxwell, J. Patchett, J. Ahrens, B. Nouanesengsy, and B. Sherman
2017. *The ParaView Guide*. *(p. 110)*

Balarac, G., H. Pitsch, and V. Raman
2008. Development of a dynamic model for the subfilter scalar variance using the concept of optimal estimators. *Physics of Fluids*. *(p. 5, 55, 73)*

Barlow, R. and J. Frank
2007. Piloted CH4/Air Flames C, D, E, and F; Release 2.1. *http://www.sandia.gov/TNF/DataArch/FlameD/SandiaPilotDoc21.pdf*, (June):1–12. *(p. 28, 106, 145, 146)*

Barlow, R., J. H. Frank, A. N. Karpetis, and J. Y. Chen
2005. Piloted methane/air jet flames: Transport effects and aspects of scalar structure. *Combustion and Flame*, 143(4):433–449. *(p. 106, 145, 146)*

Batchelor, G. K.
2000. *An Introduction to Fluid Dynamics*, Cambridge Mathematical Library.

Cambridge University Press. *(p. 26)*

Battista, F., G. Troiani, and F. Picano

2015. Fractal scaling of turbulent premixed flame fronts: Application to LES. *International Journal of Heat and Fluid Flow*, 51:78–87. *(p. 49, 51)*

Benocci, C. and D. Olivari

2014. *An Introduction to Mechanics of Turbulence, Notes from 1998/98 to 2010/2011 Lectures*. von Karman Institute for Fluid Dynamics. *(p. 27)*

Bibrzycki, J. and T. Poinsot

2010. Reduced chemical kinetic mechanisms for methane combustion in O 2 / N 2 and O 2 / CO 2 atmosphere. *Working note ECCOMET WN/CFD/10/17, CERFACS*. *(p. 108)*

Bilger, R. W.

1980. *Turbulent flows with nonpremixed reactants*, Pp. 65–113. Berlin, Heidelberg: Springer Berlin Heidelberg. *(p. 78)*

Bilger, R. W.

1988. The structure of non-premixed flame. Pp. 475–488. *(p. 9, 17, 24)*

Bilger, R. W.

1989. Turbulent Diffusion Flames. *Annual Review of Fluid Mechanics*, 21(1):101–135. *(p. 9, 17, 24)*

Bilger, R. W.

1993. Conditional moment closure for turbulent reacting flow. *Physics of Fluids A: Fluid Dynamics*, 5(2):436–444. *(p. 52)*

Bird, R.

1961. Transport phenomena. *AIChE Journal*, 7(2):5J–6J. *(p. 15)*

Boger, M., D. Veynante, H. Boughanem, and A. Trouvé

1998. Direct numerical simulation analysis of flame surface density concept for large eddy simulation of turbulent premixed combustion. *Symposium (International) on Combustion*, 27(1):917–925. *(p. 4, 45, 47, 69, 112)*

Boileau, M., S. Pascaud, E. Riber, B. Cuenot, L. Y. Gicquel, T. J. Poinsot, and M. Cazalens

2008a. Investigation of two-fluid methods for large eddy simulation of spray combustion in gas turbines. *Flow, Turbulence and Combustion*, 80(3):291–321. *(p. 46)*

Boileau, M., G. Staffelbach, B. Cuenot, T. Poinsot, and C. Bérat

2008b. LES of an ignition sequence in a gas turbine engine. *Combustion and Flame*, 154(1):2–22. *(p. 46)*

Boivin, P., C. Jiménez, A. Sánchez, and F. Williams

2011. An explicit reduced mechanism for H2–air combustion. *Proceedings of the Combustion Institute*, 33:517–523. *(p. 43, 156)*

Borghi, R.

1988. Turbulent combustion modelling. *Progress in Energy and Combustion Science*, 14(4):245–292. *(p. 35)*

Boussinesq, J.

1877. *Essai sur la théorie des eaux courantes*. Imprimerie Nationale. *(p. 38)*

Bray, K. N. C. and J. B. Moss
1977. A unified statistical model of the premixed turbulent flame. *Acta Astronautica*, 4(3):291–319. *(p. 59)*

Burke, S. P. and T. E. W. Schumann
1928. Diffusion Flames. *Industrial & Engineering Chemistry*, 20(10):998–1004. *(p. 21, 23, 81)*

Butler, T. D. and P. J. O'Rourke
1977. A numerical method for two dimensional unsteady reacting flows. *Symposium (International) on Combustion*, 16(1):1503–1515. *(p. 46, 78)*

Bykov, V. and U. Maas
2007. The extension of the ILDM concept to reaction–diffusion manifolds. *Combustion Theory and Modelling*, 11(6):839–862. *(p. 44)*

Cailler, M., N. Darabiha, D. Veynante, and B. Fiorina
2017. Building-up virtual optimized mechanism for flame modeling. *Proceedings of the Combustion Institute*, 36(1):1251–1258. *(p. 43)*

Calhoon William, J. and S. Menon
1996. Subgrid modeling for reacting large eddy simulations. In *34th Aerospace Sciences Meeting and Exhibit*, Aerospace Sciences Meetings. American Institute of Aeronautics and Astronautics. *(p. 53)*

Charlette, F., C. Meneveau, and D. Veynante
2002a. A Power-Law Flame Wrinkling Model for LES of Premixed Turbulent Combustion Part I: Non-Dynamic Formulation and Initial Tests. Technical report. *(p. 4, 46, 47, 57, 62, 64, 68, 69)*

Charlette, F., C. Meneveau, and D. Veynante
2002b. A Power-Law Flame Wrinkling Model for LES of Premixed Turbulent Combustion Part II: Dynamic Formulation. Technical report. *(p. 5, 56, 60, 61, 62, 63, 73)*

Chatakonda, O., E. R. Hawkes, A. J. Aspden, A. R. Kerstein, H. Kolla, and J. H. Chen
2013. On the fractal characteristics of low Damköhler number flames. *Combustion and Flame*, 160(11):2422–2433. *(p. 48)*

Chen, J. Y. and R. W. Dibble
1991. *Application of reduced chemical mechanisms for prediction of turbulent nonpremixed methane jet flames*, Pp. 193–226. Berlin, Heidelberg: Springer Berlin Heidelberg. *(p. 43)*

Chen, Y. C., N. Peters, G. A. Schneemann, N. Wruck, U. Renz, and M. S. Mansour
1996. The detailed flame structure of highly stretched turbulent premixed methane-air flames. *Combustion and Flame*, 107(3):223–244. *(p. 63, 65, 68)*

Cline, H. E., W. E. Lorensen, S. Ludke, C. R. Crawford, and B. C. Teeter
1988. Two algorithms for the three dimensional reconstruction of tomograms. *Medical Physics*, 15(3):320–327. *(p. 113)*

Colin, O., F. Ducros, D. Veynante, and T. Poinsot
2000. A thickened flame model for large eddy simulations of turbulent pre-

mixed combustion. *Physics of Fluids*, 12(7):1843–1863. *(p. 4, 46, 47, 65, 78)*

Colin, O. and M. Rudgyard

2000. Development of High-Order Taylor–Galerkin Schemes for LES. *Journal of Computational Physics*, 162(2):338–371. *(p. 109)*

Cook, A. W. and J. J. Riley

1994. A subgrid model for equilibrium chemistry in turbulent flows. *Physics of Fluids*, 6(8):2868–2870. *(p. 51)*

Cook, A. W. and J. J. Riley

1998. Subgrid-scale modeling for turbulent reacting flows. *Combustion and Flame*, 112(4):593–606. *(p. 51)*

Coussement, A., T. Schmitt, and B. Fiorina

2015. Filtered Tabulated Chemistry for non-premixed flames. *Proceedings of the Combustion Institute*, 35(2):1183–1190. *(p. 45)*

Cuenot, B. and T. Poinsot

1994. Effects of curvature and unsteadiness in diffusion flames. Implications for turbulent diffusion combustion. *Symposium (International) on Combustion*, 25(1):1383–1390. *(p. 30, 31, 34)*

Cuenot, B. and T. Poinsot

1996. Asymptotic and numerical study of diffusion flames with variable Lewis number and finite rate chemistry. *Combustion and Flame*, 104(1-2):111–137. *(p. 29, 30, 94)*

Dagaut, P. and M. Cathonnet

2006. The ignition, oxidation, and combustion of kerosene: A review of experimental and kinetic modeling. *Progress in Energy and Combustion Science*, 32(1):48–92. *(p. 42)*

Damköhler, G.

1940. Der Einfluss der Turbulenz auf die Flammengeschwindigkeit in Gasgemischen. *Zeitschrift für Elektrochemie und angewandte physikalische Chemie*, 46(11):601–626. *(p. 56)*

Darabiha, N.

1992. Transient Behaviour of Laminar Counterflow Hydrogen-Air Diffusion Flames with Complex Chemistry. *Combustion Science and Technology*, 86(1-6):163–181. *(p. 146)*

Ducros, P. and L. Marcel

1996. Large-eddy simulation of transition to turbulence in a boundary layer developing spatially over a flat plate. *Journal of Fluid Mechanics*, 326:1–36. *(p. 40)*

Duwig, C.

2007. Study of a Filtered Flamelet Formulation for Large Eddy Simulation of Premixed Turbulent Flames. Pp. 433–454. *(p. 45)*

Favini, B., C. Bruno, F. Picchia, N. Arcidiacono, and E. Giacomazzi

2003. LES of CH4/H2/Air Turbulent Non-Premixed Flame Turbulent Non-Premixed Flame. *(p. 49)*

Favre, A. J. A.
1969. *Formulation of the Statistical Equations of Turbulent Flows with Variable Density*, Pp. 324–341. New York, NY: Springer New York. *(p. 36)*

Ferziger, J. H.
1999. *Introduction to the Physics and Simulation of Turbulence*. Rhode-Saint-Genèse: von Karman Institute for Fluid Dynamics. *(p. 26)*

Fiorina, B., O. Gicquel, L. Vervisch, S. Carpentier, and N. Darabiha
2005. Premixed turbulent combustion modeling using tabulated detailed chemistry and PDF. *Proceedings of the Combustion Institute*, 30(1):867–874. *(p. 44)*

Fiorina, B., O. Gicquel, and D. Veynante
2009. Turbulent flame simulation taking advantage of tabulated chemistry self-similar properties. *Proceedings of the Combustion Institute*, 32(2):1687–1694. *(p. 44, 58)*

Fiorina, B., D. Veynante, and S. Candel
2015. Modeling Combustion Chemistry in Large Eddy. Pp. 3–42. *(p. 44, 45)*

Fiorina, B., R. Vicquelin, P. Auzillon, N. Darabiha, D. Veynante, B. Fiorina, R. Vicquelin, P. Auzillon, N. Darabiha, and O. Gicquel
2010. A filtered tabulated chemistry model for LES of premixed combustion To cite this version : A filtered tabulated chemistry model for LES of premixed combustion. *Combustion and Flame*, 157(3):465–475. *(p. 45)*

Franzelli, B., E. Riber, L. Y. Gicquel, and T. Poinsot
2012. Large Eddy Simulation of combustion instabilities in a lean partially premixed swirled flame. *Combustion and Flame*, 159(2):621–637. *(p. 66, 145, 147, 149)*

Franzelli, B., E. Riber, M. Sanjosé, and T. Poinsot
2010. A two-step chemical scheme for kerosene–air premixed flames. *Combustion and Flame*, 157(7):1364–1373. *(p. 43, 147, 164)*

Frenklach, M., H. Wang, C.-L. Yu, M. Goldenberg, C. Bowman, R. Hanson, D. Davidson, E. Chang, G. Smith, D. Golden, W. Lissianski, and V. Gardiner
1995. GRI-mech 1.2. *(p. 156, 164)*

Gao, F. and E. E. O'Brien
1993. A large eddy simulation scheme for turbulent reacting flows. *Physics of Fluids A: Fluid Dynamics*, 5(6):1282–1284. *(p. 50, 52)*

Garmory, A. and E. Mastorakos
2011. Capturing localised extinction in Sandia Flame F with LES–CMC. *Proceedings of the Combustion Institute*, 33(1):1673–1680. *(p. 52)*

Garnier, E., N. Adams, and P. Sagaut
2009. *Large Eddy Simulation for Compressible Flows*, Scientific Computation. Springer Netherlands. *(p. 40)*

Germano, M., U. Piomelli, P. Moin, and W. H. Cabot
1991. A dynamic subgrid scale eddy viscosity model. *Physics of Fluids A: Fluid Dynamics*, 3(7):1760–1765. *(p. 4, 41, 106)*

Geurts, B. J. and J. Fröhlich
2002. A framework for predicting accuracy limitations in large-eddy simulation. *Physics of Fluids*, 14(6):L41–L44. *(p. 35)*

Ghosal, S.
1996. An Analysis of Numerical Errors in Large-Eddy Simulations of Turbulence. *Journal of Computational Physics*, 125(1):187–206. *(p. 35)*

Gicquel, O., N. Darabiha, and D. Thévenin
2000. Liminar premixed hydrogen/air counterflow flame simulations using flame prolongation of ILDM with differential diffusion. *Proceedings of the Combustion Institute*, 28(2):1901–1908. *(p. 44)*

Giovangigli, V.
1999. Modeling and Simulation in Science, Engineering and Technology. *(p. 14)*

Goey, P., J. van Oijen, H. Bongers, and G. R A Groot
2003. New flamelet based reduction methods: the bridge between chemical reduction techniques and flamelet methods. *(p. 44)*

Gouldin, F. C.
1987. An application of fractals to modeling premixed turbulent flames. *Combustion and Flame*, 68(3):249–266. *(p. 47, 48, 49, 50)*

Gouldin, F. C., K. N. C. Bray, and J.-Y. Chen
1989. Chemical closure model for fractal flamelets. *Combustion and Flame*, 77(3):241–259. *(p. 48, 49, 63)*

Gregor, M. A., F. Seffrin, F. Fuest, D. Geyer, and A. Dreizler
2009. Multi-scalar measurements in a premixed swirl burner using ID Raman/Rayleigh scattering. *Proceedings of the Combustion Institute*, 32 II(2):1739–1746. *(p. 66)*

Gubba, S. R., S. S. Ibrahim, W. Malalasekera, and A. R. Masri
2011. Measurements and LES calculations of turbulent premixed flame propagation past repeated obstacles. *Combustion and Flame*, 158(12):2465–2481. *(p. 60)*

Gülder, Ö. L.
1991. Turbulent premixed combustion modelling using fractal geometry. *Symposium (International) on Combustion*, 23(1):835–842. *(p. 48, 49, 50, 63, 133)*

Gülder, Ö. L. and G. J. Smallwood
1995a. Inner cutoff scale of flame surface wrinkling in turbulent premixed flames. *Combustion and Flame*, 103(1):107–114. *(p. 48)*

Gülder, Ö. L. and G. J. Smallwood
1995b. Inner cutoff scale of flame surface wrinkling in turbulent premixed flames. *Combustion and Flame*, 103(1-2):107–114. *(p. 50)*

Haselbacher, A. and O. Vasilyev
2003. Commutative discrete filtering on unstructured grids based on least-squares techniques. *Journal of Computational Physics*, 187:197–211. *(p. 36)*

Hawkes, E. R. and R. S. Cant

2000. A flame surface density approach to large-eddy simulation of premixed turbulent combustion. *Proceedings of the Combustion Institute*, 28(1):51–58. *(p. 4, 47)*

Haworth, D. C.

2010. Progress in probability density function methods for turbulent reacting flows. *Progress in Energy and Combustion Science*, 36(2):168–259. *(p. 52)*

Hirschfelder, C. and F. Curtiss

1954. Molecular Theory of Gases and Liquids. Joseph O. Hirschfelder, Charles F. Curtiss, and R. Byron Bird. Wiley, New York; Chapman & Hall, London, 1954. xxvi + 1219 pp. Illus. $20. *Science*, 120(3131):1097. *(p. 14, 15)*

Hosseinzadeh, A., A. Sadiki, and J. Janicka

2016. Assessment of the Dynamic SGS Wrinkling Combustion Modeling Using the Thickened Flame Approach Coupled with FGM Tabulated Detailed Chemistry. *Flow, Turbulence and Combustion*, 96(4):939–964. *(p. 55, 60, 61, 64, 73)*

Hosseinzadeh, A., T. Schmitt, A. Sadiki, and J. Janicka

2015. Application of the Dynamic F-TACLES Combustion Model to a Lean Premixed Turbulent Flame. *Flow, Turbulence and Combustion*, 95(2-3):481–500. *(p. 60)*

Im, H. G., T. S. Lund, and J. H. Ferziger

1997. Large eddy simulation of turbulent front propagation with dynamic subgrid models. *Physics of Fluids*, 9(12):3826–3833. *(p. 60)*

Inernational Energy Agency

2016. Key world Energy Statistics 2016. Technical Report. *(p. 1, 2)*

Jones, W. P. and R. P. Lindstedt

1988. Global reaction schemes for hydrocarbon combustion. *Combustion and Flame*, 73(3):233–249. *(p. 43)*

Kaul, C. M., V. Raman, E. Knudsen, E. S. Richardson, and J. H. Chen

2013. Large eddy simulation of a lifted ethylene flame using a dynamic nonequilibrium model for subfilter scalar variance and dissipation rate. *Proceedings of the Combustion Institute*, 34(1):1289–1297. *(p. 5, 55, 61, 73)*

Kelley, A. P., W. Liu, Y. X. Xin, A. J. Smallbone, and C. K. Law

2011. Laminar flame speeds, non-premixed stagnation ignition, and reduced mechanisms in the oxidation of iso-octane. *Proceedings of the Combustion Institute*, 33(1):501–508. *(p. 42)*

Kerstein, A. R.

1988. A Linear- Eddy Model of Turbulent Scalar Transport and Mixing. *Combustion Science and Technology*, 60(4-6):391–421. *(p. 53)*

Kerstein, A. R.

1989. Linear-eddy modeling of turbulent transport. II: Application to shear layer mixing. *Combustion and Flame*, 75(3):397–413. *(p. 53)*

Kerstein, A. R.

1990. Linear-eddy modelling of turbulent transport. Part 3. Mixing and differential molecular diffusion in round jets. *Journal of Fluid Mechanics*,

216:411–435. *(p. 53)*

Kerstein, A. R.

1991. Linear-eddy modelling of turbulent transport. Part 6. Microstructure of diffusive scalar mixing fields. *Journal of Fluid Mechanics*, 231:361–394. *(p. 53)*

Kerstein, A. R.

1992. Linear-Eddy Modeling of Turbulent Transport. Part 4. Structure of Diffusion Flames. *Combustion Science and Technology*, 81(1-3):75–96. *(p. 53)*

Kerstein, A. R., W. T. Ashurst, and F. A. Williams

1988. Field equation for interface propagation in an unsteady homogeneous flow field. *Phys. Rev. A*, 37(7):2728–2731. *(p. 4)*

Klimenko, A. Y.

1990. Multicomponent diffusion of various admixtures in turbulent flow. *Fluid Dynamics*, 25(3):327–334. *(p. 52)*

Knikker, R., D. Veynante, and C. Meneveau

2002. A priori testing of a similarity model for large eddy simulations of turbulent premixed combustion. *Pci*, 29:2105–2111. *(p. 47)*

Knikker, R., D. Veynante, and C. Meneveau

2004. A dynamic flame surface density model for large eddy simulation of turbulent premixed combustion. *Physics of Fluids*, 16(11):L91–L94. *(p. 60)*

Knudsen, E. and H. Pitsch

2008. A dynamic model for the turbulent burning velocity for large eddy simulation of premixed combustion. *Combustion and Flame*, 154(4):740–760. *(p. 60)*

Kolmogorov, A. N.

1941. The Local Structure of Turbulence in Incompressible Viscous Fluid for Very Large Reynolds Numbers. *Proceedings of the Royal Society A: Mathematical, Physical and Engineering Sciences*, 434(1890):9–13. *(p. 26)*

Kothe, D.

2007. Science Prospects And Benefits with Exascale Computing. *(p. 3)*

Kuenne, G., A. Ketelheun, and J. Janicka

2011. LES modeling of premixed combustion using a thickened flame approach coupled with FGM tabulated chemistry. *Combustion and Flame*, 158(9):1750–1767. *(p. 64)*

Kuo, K. K.

2005. *Principles of combustion*, second edi edition. Hoboken, New Jersey: [publisher unknown]. *(p. 9, 17, 24, 79)*

Lamb, H. and R. Caflisch

1993. *Hydrodynamics*, Cambridge Mathematical Library. Cambridge University Press. *(p. 79)*

Laurendeau, N. M.

2005. *Statistical Thermodynamics: Fundamentals and Applications*. Cambridge University Press. *(p. 11)*

Laverant, A. M. and S. M. Candel

1989. Computation of diffusion and premixed flames rolled up in vortex structures. *Journal of Propulsion and Power*, 5(2):134–143. *(p. 106)*

Lax, P. and B. Wendroff

1960. Systems of conservation laws. *Communications on Pure and Applied Mathematics*, 13(2):217–237. *(p. 89)*

Legier, J. P., T. Poinsot, and D. Veynante

2000. Dynamically thickened flame LES model for premixed and non-premixed turbulent combustion. *Proceedings of the Summer Program, Centre for Turbulence Research*, Pp. 157–168. *(p. 4, 46, 47, 78, 83, 103, 117)*

Lele, S. K.

1992. Compact finite difference schemes with spectral-like resolution. *Journal of Computational Physics*, 103(1):16–42. *(p. 36)*

Leonard, A.

1975. Energy Cascade in Large-Eddy Simulations of Turbulent Fluid Flows. In *Turbulent Diffusion in Environmental Pollution*, F. N. Frenkiel and R. E. Munn, eds., volume 18 of *Advances in Geophysics*, Pp. 237–248. Elsevier. *(p. 35)*

Li, S. C., F. A. Williams, and K. Gebert

1999. A simplified, fundamentally based method for calculating NOx emissions in lean premixed combustors. *Combustion and Flame*, 119:367–373. *(p. 43, 156)*

Lilly, D. K.

1992. A proposed modification of the Germano subgrid scale closure method. *Physics of Fluids A: Fluid Dynamics*, 4(3):633–635. *(p. 41, 42, 109)*

Liñán, A.

1974. The asymptotic structure of counterflow diffusion flames for large activation energies. *Acta Astronautica*, 1(7):1007–1039. *(p. 29, 30, 33)*

Linan, A. and A. Crespo

1976. An Asymptotic Analysis of Unsteady Diffusion Flames for Large Activation Energies. *Combustion Science and Technology.* *(p. 9, 17, 24, 78, 94)*

Lu, T. and C. K. Law

2005. A directed relation graph method for mechanism reduction. *Proceedings of the Combustion Institute*, 30(1):1333–1341. *(p. 42)*

Lu, T. and C. K. Law

2008. A criterion based on computational singular perturbation for the identification of quasi steady state species: A reduced mechanism for methane oxidation with NO chemistry. *Combustion and Flame*, 154:761–774. *(p. 43, 145, 156, 164)*

Lund, T.

1999. On the Use of Discrete Filters for Large Eddy Simulation. *(p. 36)*

Lysenko, D. A., I. S. Ertesvåg, and K. E. Rian

2014. Numerical Simulations of the Sandia Flame D Using the Eddy Dissipation Concept. *Flow, Turbulence and Combustion*, 93(4):665–687. *(p. 53)*

Maas, U. and S. B. Pope
1992a. Implementation of simplified chemical kinetics based on intrinsic low-dimensional manifolds. *Symposium (International) on Combustion*, 24(1):103–112. *(p. 44)*

Maas, U. and S. B. Pope
1992b. Simplifying chemical kinetics: Intrinsic low-dimensional manifolds in composition space. *Combustion and Flame*, 88(3):239–264. *(p. 44)*

Magnussen, B. F. and B. H. Hjertager
1977. On mathematical modeling of turbulent combustion with special emphasis on soot formation and combustion. *Symposium (International) on Combustion*, 16(1):719–729. *(p. 53)*

Mandelbrot, B.
1983. *The Fractal Geometry of Nature*, volume 51, P. 468 p. *(p. 48)*

Mandelbrot, B. B.
1975. On the geometry of homogeneous turbulence, with stress on the fractal dimension of the iso-surfaces of scalars. *Journal of Fluid Mechanics*, 72(3):401–416. *(p. 48)*

Mandelbrot, B. B.
2004. *Fractals*. American Cancer Society. *(p. 48)*

MANTZARAS, J.
1992. Geometrical Properties of Turbulent Premixed Flames: Comparison Between Computed and Measured Quantities. *Combustion Science and Technology*, 86(1-6):135–162. *(p. 50)*

Massias, A., D. Diamantis, E. Mastorakos, and D. A. Goussis
1999. An algorithm for the construction of global reduced mechanisms with CSP data. *Combustion and Flame*, 117(4):685–708. *(p. 42)*

Mathey, F. and J. P. Chollet
1997. Subgrid-Scale Model of Scalar Mixing for Large Eddy Simulations of Turbulent Flows. In *Direct and Large-Eddy Simulation II*, J.-P. Chollet, P. R. Voke, and L. Kleiser, eds., Pp. 103–114, Dordrecht. Springer Netherlands. *(p. 53)*

McMillan, . J. and J. H. Ferziger
1979. Direct Testing of Subgrid-Scale Models. *AIAA Journal*, 17(12):1340–1346. *(p. 35)*

McMurthy, P. A., S. Menon, and A. R. Kerstein
1992. A linear eddy sub-grid model for turbulent reacting flows: Application to hydrogen-AIR combustion. *Symposium (International) on Combustion*, 24(1):271–278. *(p. 53)*

Meier, W., P. Weigand, X. R. Duan, and R. Giezendanner-Thoben
2007. Detailed characterization of the dynamics of thermoacoustic pulsations in a lean premixed swirl flame. *Combustion and Flame*, 150(1-2):2–26. *(p. 65)*

Menon, S., J.-Y. Chen, A. Kerstein, and P. Mcmurtry
1994. Prediction of NO(x) production in a turbulent hydrogen-air jet flame.

Journal of Propulsion and Power - J PROPUL POWER, 10:161–168. *(p. 53)*

Meuert, H., E. Strohmaier, J. Dongarra, H. Simon, and M. Meuer
2018. Top500 The list. *(p. 2, 3)*

Meyers, J., B. J. Geurts, and M. Baelmans
2005. Optimality of the dynamic procedure for large-eddy simulations. *Physics of Fluids*, 17(4):45108. *(p. 35)*

Morton, K. W.
1993. Computational Fluid Dynamics: An Introduction. Edited by J. F. Wendt. Springer, 1992. 291 pp. DM128. Numerical Solutions of the Euler Equations for Steady Flow Problems. *Journal of Fluid Mechanics*, 252:722–723. *(p. 4)*

Moureau, V., P. Domingo, and L. Vervisch
2011. From Large-Eddy Simulation to Direct Numerical Simulation of a lean premixed swirl flame: Filtered laminar flame-PDF modeling. *Combustion and Flame*, 158(7):1340–1357. *(p. 3, 57)*

Mouriaux, S., O. Colin, and D. Veynante
2017. Adaptation of a dynamic wrinkling model to an engine configuration. *Proceedings of the Combustion Institute*, 36(3):3415–3422. *(p. 60, 72, 74)*

Murayama, M. and T. Takeno
1989. Fractal-like character of flamelets in turbulent premixed combustion. *Symposium (International) on Combustion*, 22(1):551–559. *(p. 50)*

Nagy, T. and T. Turányi
2009. Reduction of very large reaction mechanisms using methods based on simulation error minimization. *Combustion and Flame*, 156(2):417–428. *(p. 42)*

Navarro-Martinez, S. and A. Kronenburg
2007. LES-CMC simulations of a turbulent bluff-body flame. *Proceedings of The Combustion Institute - PROC COMBUST INST*, 31:1721–1728. *(p. 52)*

Navarro-Martinez, S. and A. Kronenburg
2009. LES–CMC simulations of a lifted methane flame. *Proceedings of the Combustion Institute*, 32(1):1509–1516. *(p. 52)*

North, G. L. and D. A. Santavicca
1990. The Fractal Nature of Premixed Turbulent Flames. *Combustion Science and Technology*, 72(4-6):215–232. *(p. 48)*

Oijen, J. and L. Goey
2000. Modelling of Premixed Laminar Flames using Flamelet-Generated Manifolds. *Combustion Science and Technology*, 161(1):113–137. *(p. 44)*

Olbricht, C., O. T. Stein, J. Janicka, J. A. V. Oijen, S. Wysocki, and A. M. Kempf
2012. LES of lifted flames in a gas turbine model combustor using top-hat filtered PFGM chemistry. *Fuel*, 96:100–107. *(p. 51)*

O'Rourke, P. J. and F. V. Bracco
1979. Two scaling transformations for the numerical computation of multidimensional unsteady laminar flames. *Journal of Computational Physics*,

33(2):185–203. *(p. 46, 78)*

Peters, N.

1984. Laminar diffusion flamelet models in non-premixed turbulent combustion. *Progress in Energy and Combustion Science*, 10(3):319–339. *(p. 78)*

Peters, N.

1985. Numerical and asymptotic analysis of systematically reduced reaction schemes for hydrocarbon flames. In *Numerical Simulation of Combustion Phenomena*, R. Glowinski, B. Larrouturou, and R. Temam, eds., Pp. 90–109, Berlin, Heidelberg. Springer Berlin Heidelberg. *(p. 43)*

Peters, N.

1988. Laminar flamelet concepts in turbulent combustion. *Symposium (International) on Combustion*, 21(1):1231–1250. *(p. 9, 48, 50)*

Peters, N.

2000. *Turbulent Combustion*, Cambridge Monographs on Mechanics. Cambridge University Press. *(p. 20, 24, 35, 79)*

Pierce, C. D. and P. Moin

1998. A dynamic model for subgrid-scale variance and dissipation rate of a conserved scalar. *(p. 5, 55, 73)*

Pierce, C. D. and P. Moin

2004. Progress-variable approach for large-eddy simulation of non-premixed turbulent combustion. *Journal of Fluid Mechanics*, 504:73–97. *(p. 5, 55, 72, 73)*

Piomelli, U.

1999. Large eddy simulation: achievements and challenges. *Progress in Aerospace Sciences*, 35(4):335–362. *(p. 40)*

Pitsch, H.

2006. Large-eddy simulation of turbulent combustion. *Annual Review of Fluid Mechanics*, 38(1):453–482. *(p. 4)*

Poinsot, T. and D. Veynante

2012. *Theoretical and Numerical Combustion Third Edition*, third edit edition. *(p. 4, 9, 11, 14, 18, 20, 22, 23, 24, 28, 29, 30, 32, 33, 34, 41, 46, 56, 59, 78, 81, 148, 150)*

Poinsot, T., D. Veynante, and S. Candel

1991a. Diagrams of premixed turbulent combustion based on direct simulation. *Symposium (International) on Combustion*, 23(1):613–619. *(p. 106)*

Poinsot, T. J., D. Veynante, and S. Candel

1991b. Quenching processes and premixed turbulent combustion diagrams. *Journal of Fluid Mechanics Digital Archive*, 228:561. *(p. 50)*

Pope, S. B.

1988. The evolution of surfaces in turbulence. *International Journal of Engineering Science*, 26(5):445–469. *(p. 56, 112)*

Pope, S. B.

2000. *Turbulent Flows*. Cambridge University Press. *(p. 40)*

Raman, V. and H. Pitsch

2007. A consistent LES/filtered-density function formulation for the simulation of turbulent flames with detailed chemistry. *Proceedings of the Combustion Institute*, 31 II:1711–1719. *(p. 4)*

Ren, Z., S. B. Pope, A. Vladimirsky, and J. M. Guckenheimer

2006. The invariant constrained equilibrium edge preimage curve method for the dimension reduction of chemical kinetics. *The Journal of Chemical Physics*, 124(11):114111. *(p. 44)*

Renou, B.

1999. *Contribution a l'etude de la propagation d'une flamme de premelange instationnaire dans un ecoulement turbulent. Influence du nombre de lewis.* PhD thesis. *(p. 69)*

Réveillon, J. and L. Vervisch

1998. Subgrid-scale turbulent micromixing: Dynamic approach. *AIAA Journal*, 36(3):336–341. *(p. 5)*

Reveillon, J. and L. Vervisch

1998. Subgrid-Scale Turbulent Micromixing: Dynamic Approach. 36(3). *(p. 55, 61, 73)*

Ribert, G., O. Gicquel, N. Darabiha, and D. Veynante

2006. Tabulation of complex chemistry based on self-similar behavior of laminar premixed flames. *Combustion and Flame - COMBUST FLAME*, 146:649–664. *(p. 44)*

Richard, S., O. Colin, O. Vermorel, A. Benkenida, C. Angelberger, and D. Veynante

2007. Towards large eddy simulation of combustion in spark ignition engines. *Proceedings of the Combustion Institute*, 31(2):3059–3066. *(p. 4, 47)*

Roberts, W. L., J. F. Driscoll, M. C. Drake, and L. P. Goss

1993. Images of the quenching of a flame by a vortex to quantify regimes of turbulent combustion. *Combustion and Flame*, 94(1):58–69. *(p. 50)*

Sánchez, A. L., A. Lépinette, M. Bollig, A. Liñán, and B. Lázaro

2000. The reduced kinetic description of lean premixed combustion. *Combustion and Flame*, 123(4):436–464. *(p. 43, 156)*

Sawyer, R. F.

2009. Science based policy for addressing energy and environmental problems. *Proceedings of the Combustion Institute*, 32(1):45–56. *(p. 1)*

Schmitt, P., T. Poinsot, B. Schuermans, and K. P. Geigle

2007. Large-eddy simulation and experimental study of heat transfer, nitric oxide emissions and combustion instability in a swirled turbulent high-pressure burner. *Journal of Fluid Mechanics*, 570:17–46. *(p. 4, 46, 103)*

Schmitt, T., M. Boileau, and D. Veynante

2015. Flame Wrinkling Factor Fynamic Modeling for Large Eddy Simulations of Turbulent Premixed Combustion. *Flow, Turbulence and Combustion.* *(p. 5, 55, 60, 68, 74)*

Schmitt, T., A. Sadiki, B. Fiorina, and D. Veynante

2013. Impact of dynamic wrinkling model on the prediction accuracy using

the F-TACLES combustion model in swirling premixed turbulent flames. *Proceedings of the Combustion Institute*. *(p. 5, 60, 66, 74)*

Schneider, C., A. Dreizler, and J. Janicka

2005. Fluid dynamical analysis of atmospheric reacting and isothermal swirling flows. *Flow, Turbulence and Combustion*, 74(1):103–127. *(p. 66)*

Schönfeld, T. and M. Rudgyard

1999. Steady and unsteady flows simulations using the hybrid flow solver AVBP. *AIAA Journal*. *(p. 89, 109, 146)*

Schroeder, W., K. Martin, and B. Lorensen

2016. *The Visualization Toolkit: an Object-Oriented approach to 3D Graphics*. *(p. 113)*

Sengissen, A. X., A. V. Giauque, G. S. Staffelbach, M. Porta, W. Krebs, P. Kaufmann, and T. J. Poinsot

2007. Large eddy simulation of piloting effects on turbulent swirling flames. *Proceedings of the Combustion Institute*, 31 II:1729–1736. *(p. 4)*

Seshadri, K., X. S. Bai, and H. Pitsch

2001. Asymptotic structure of rich methane-air flames. *Combustion and Flame*, 127(4):2265–2277. *(p. 43)*

Shum-Kivan, F.

2017. *Simulation des Grandes Echelles de flamme de spray et modélisation de la combustion non-prémélangée*. PhD thesis, Univeristé de Toulouse. *(p. 78, 106)*

Simmie, J. M.

2003. Detailed chemical kinetic models for the combustion of hydrocarbon fuels. *Progress in Energy and Combustion Science*, 29(6):599–634. *(p. 42)*

Smagorinsky, J.

1963. General circulation experiments with the primitive equations. Part I: The basic experiment. *Monthly Weather Review*, 91(3):99–164. *(p. 40)*

Smallwood, G. J., Ö. L. Gülder, D. R. Snelling, B. M. Deschamps, and I. Gökalp

1995. Characterization of flame front surfaces in turbulent premixed methane/Air combustion. *Combustion and Flame*, 101(4):461–470. *(p. 48, 49, 133)*

Smirnov, A., S. Shi, and I. Celik

2001. Random Flow Generation Technique for Large Eddy Simulations and Particle-Dynamics Modeling. *Journal of Fluids Engineering*, 123(2):359. *(p. 108)*

Smith, G. P., D. M. Golden, M. Frenklach, N. W. Moriarty, B. Eiteneer, M. Goldenberg, C. T. Bowman, R. K. Hanson, S. Song, C. J. William, V. V. Lissianski, and Z. Qin

1999. GRI-mech 3.0. *(p. 42, 145, 149)*

Spalding, D. B.

1971. Mixing and chemical reaction in steady confined turbulent flames. *Symposium (International) on Combustion*, 13(1):649–657. *(p. 53)*

Spalding, D. B.

1977. Development of the eddy-break-up model of turbulent combustion. *Symposium (International) on Combustion*, 16(1):1657–1663. *(p. 53)*

Spyropoulos, E. T. and G. A. Blaisdell

1996. Evaluation of the dynamic model for simulations of compressible decaying isotropic turbulence. *AIAA Journal*, 34(5):990–998. *(p. 41)*

Sreenivasan, K. R. and C. Meneveau

1986. The fractal facets of turbulence. *Journal of Fluid Mechanics*, 173:357–386. *(p. 48)*

Sutherland, W.

1893. LII. The viscosity of gases and molecular force. *The London, Edinburgh, and Dublin Philosophical Magazine and Journal of Science*, 36(223):507–531. *(p. 15)*

Tennekes, H.

1972. *A first course in turbulence*. Cambridge, Mass. : MIT Press, [1972]. *(p. 28)*

Tomlin, A. S., T. Turányi, and M. J. Pilling

1997. Chapter 4 Mathematical tools for the construction, investigation and reduction of combustion mechanisms. In *Low-Temperature Combustion and Autoignition*, M. J. Pilling, ed., volume 35 of *Comprehensive Chemical Kinetics*, Pp. 293–437. Elsevier. *(p. 42)*

Triantafyllidis, A. and B. Eggels

2009. Large Eddy Simulations of forced ignition of a non-premixed bluff-body methane flame with Conditional Moment Closure. *(p. 52)*

van Beeck, J. and C. Benocci

2014. *Introduction to the Mechanics of Turbulence: Spectral Analysis of Turbulent Flows*. Rhode-Saint-Genèse: von Karman Institute for Fluid Dynamics. *(p. 28)*

Van Oijen, J. A., F. A. Lammers, and L. P. De Goey

2001. Modeling of complex premixed burner systems by using flamelet-generated manifolds. *Combustion and Flame*, 127(3):2124–2134. *(p. 64)*

Vasilyev, O. V., T. S. Lund, and P. Moin

1998. A General Class of Commutative Filters for LES in Complex Geometries. *Journal of Computational Physics*, 146(1):82–104. *(p. 36)*

Vervisch, L., E. Bidaux, K. N. C. Bray, and W. Kollmann

1995. Surface density function in premixed turbulent combustion modeling, similarities between probability density function and flame surface approaches. *Physics of Fluids*, 7(10):2496–2503. *(p. 56)*

Vervisch, L. and T. Poinsot

1998. Direct numerical simulation of non-premixed turbulent flames. *Annual Review of Fluid Mechanics*, 30(1):655–691. *(p. 29, 30)*

Veynante, D., B. Fiorina, P. Domingo, and L. Vervisch

2008. Using self-similar properties of turbulent premixed flames to downsize chemical tables in high-performance numerical simulations. *Combustion Theory and Modelling*, 12(6):1055–1088. *(p. 44)*

Veynante, D. and V. Moureau
2015. Analysis of dynamic models for large eddy simulations of turbulent premixed combustion. *Combustion and Flame*, 162(12):4622–4642. *(p. 56, 57, 58, 60, 63, 69, 72)*

Veynante, D., T. Schmitt, M. Boileau, and D. V. Moureau
2012. Analysis of dynamic models for turbulent premixed combustion. Technical report. *(p. 74)*

Veynante, D., A. Trouvé, K. N. C. Bray, and T. Mantel
1997. Gradient and counter-gradient scalar transport in turbulent premixed flames. *Journal of Fluid Mechanics*, 332:263–293. *(p. 107)*

Veynante, D. and L. Vervisch
2002. Turbulent combustion modeling. *Progress in Energy and Combustion Science*, 28(3):193–266. *(p. 54)*

Volpiani, P. S., T. Schmitt, O. Vermorel, P. Quillatre, and D. Veynante
2017a. Large eddy simulation of explosion deflagrating flames using a dynamic wrinkling formulation. *Combustion and Flame*, 186:17–31. *(p. 55, 60, 61)*

Volpiani, P. S., T. Schmitt, and D. Veynante
2016. A posteriori tests of a dynamic thickened flame model for large eddy simulations of turbulent premixed combustion. *Combustion and Flame*, 174:166–178. *(p. 5, 55, 60, 61, 65, 66, 74)*

Volpiani, P. S., T. Schmitt, and D. Veynante
2017b. Large eddy simulation of a turbulent swirling premixed flame coupling the TFLES model with a dynamic wrinkling formulation. *Combustion and Flame*. *(p. 5, 60, 61, 65, 67, 74)*

Wang, G., M. Boileau, and D. Veynante
2011. Implementation of a dynamic thickened flame model for large eddy simulations of turbulent premixed combustion. *Combustion and Flame*, 158(11):2199–2213. *(p. 5, 55, 58, 60, 61, 62, 63, 64, 73)*

Wang, G., M. Boileau, D. Veynante, and K. Truffin
2012. Large eddy simulation of a growing turbulent premixed flame kernel using a dynamic flame surface density model. *Combustion and Flame*, 159(8):2742–2754. *(p. 5, 60, 69, 70, 71, 74)*

Wang, K., G. Ribert, P. Domingo, and L. Vervisch
2010. Self-similar behavior and chemistry tabulation of burnt-gas diluted premixed flamelets including heat-loss. *Combustion Theory and Modelling*, 14(4):541–570. *(p. 44)*

Warnatz, J., U. Mass, and R. W. Dibble
1999. Combustion: Physical and Chemical Fundamentals, Modeling and Simulation, Experiments, Pollutant Formation, 2nd edn. By J. WARNATZ, U. MAAS & R. W. DIBBLE. Springer, 1999. 299 pp. ISBN 3540 65228 0. £34.00. *Journal of Fluid Mechanics*, 401:378–381. *(p. 42)*

Weller, H. G., G. Tabor, A. D. Gosman, and C. Fureby
1998. Application of a flame-wrinkling les combustion model to a turbu-

lent mixing layer. *Symposium (International) on Combustion*, 27(1):899–907. *(p. 4, 47)*

Williams, F. A.

1985. *Combustion Theory*. Menlo Park, CA: Benjamin Cummings. *(p. 9, 12, 20, 23, 46, 79, 94)*

ÉCOLE DOCTORALE
Sciences mécaniques et énergétiques, matériaux et géosciences (SMEMAG)

Titre : Développement de modèles dynamiques pour la simulation aux grandes échelles de la combustion turbulente non-prémélangée

Mots clés : flammes de diffusion, combustion turbulente, flamme jet, simulation aux grandes échelles LES, modèle de flamme épaissie, modèles dynamiques

Résumé : Le présent travail se concentre sur la formulation d'un modèle LES dynamique pour simuler des flammes de diffusion turbulentes. De nos jours, le DNS n'est toujours pas abordable pour les applications pratiques et LES représente un bon compromis en termes d'informations récupérées et de coût de calcul. Le modèle de flamme épaissie pour la simulation de grands tourbillons (TFLES), initialement formulé pour les flammes prémélangées, a également été utilisé pour prédire le com portement qualitatif des flammes turbulentes non prémélangées sans fondements théoriques clairs. Le manuscrit fournit la formulation analytique des effets du modèle TFLES sur les flammes non prémélangées.

La deuxième partie de l'étude se concentre sur une formulation dynamique pour prédire la surface de la flamme dans les flammes à diffusion turbulente. Cette approche de modélisation a été largement utilisée pour décrire le transport turbulent non résolu.
Dans le présent travail, la formulation dynamique est couplée au modèle TFLES, et ses implications sur les flammes non pré mélangées sont étudiées pour un jet turbulent planaire.
La précision de ces prévisions dépend du modèle des effets de plissement de la surface de la flamme aux échelles non résolues.

Title : : Development of a dynamic LES model for turbulent diffusion flames

Keywords : Diffusion flames, turbulent non-premixed combustion, turbulent jet flame, large eddy simulation LES, thickened flame model TFLES, dynamic models

Abstract : The present work focuses on the formulation of a dynamic LES model to simulate turbulent diffusion flames. Nowadays, DNS is still not affordable for practical applications and LES represents a good compromise in terms of information retrieved and computational cost. The Thickened Flame Model for Large Eddy Simulation (TFLES), initially formulated for premixed flame, has also been used for predicting the qualitative behavior of non-premixed turbulent flames without clear theoretical foundations. The manuscript provides the analytical formulation of the TFLES model effects on non-premixed flames.

The second part of the study focuses on a dynamic formulation to predict the flame surface in turbulent diffusion flames.
This modeling approach has been widely used to described unresolved turbulent transport. In the present work, the dynamic formulation is coupled with the TFLES model, and its implications on non-premixed flames are investigated for a planar turbulent jet. The accuracy of such predictions depends on the model of the flame surface's wrinkling effects at the non-resolved scales.

Maison du doctorat de l'Université Paris-Saclay
2ème étage aile ouest, Ecole normale supérieure Paris-Saclay
4 avenue des Sciences,
91190 Gif sur Yvette, France